The Stability of Short-Period Extrasolar Giant Planets

Tommi Tapio Koskinen

Submitted for the degree of Doctor of Philosophy

Atmospheric Physics Laboratory
Department of Physics and Astronomy
University College London
August 2008

I, Tommi Tapio Koskinen, confirm that the work presented in this thesis is my own. Where information has been derived from other sources, I confirm that this has been indicated in the thesis.

Abstract

A three-dimensional coupled thermosphere-ionosphere model for extrasolar giant planets (EXOTIM) has been developed. This is the first such model reported in the literature. This thesis contains an extensive description of the model and the methods adopted in modelling the different physical processes expected in the upper atmospheres and ionospheres of extrasolar giant planets. Modelling the upper atmosphere is important because the stability of the atmosphere against thermal evaporation is controlled by the conditions in the thermosphere. The thermosphere is heated by the absorption of EUV and X ray (XUV) radiation emitted by the host star. The radiation also ionises the neutral species in the upper atmosphere, which is expected to be composed mainly of molecular and atomic hydrogen, and atomic helium. Ionisation and subsequent photochemistry leads to the formation of the H^+, H_2^+, H_3^+, and He^+ ions (and small quantities of HeH^+). H_3^+ emits strongly in the infrared and may act as a significant coolant in gas giant thermospheres. Assuming photochemical equilibrium, the absorption of XUV radiation and ion photochemistry were modelled in a self-consistent fashion. The 3D model can also simulate strong winds affecting the upper atmosphere, and account for both advection and diffusion of the neutral species around the planet. The results indicate that within 1.0 AU from a solar-type host star, the upper atmospheres of Jupiter-type EGPs can be substantially cooler and more stable than implied by studies that ignore the possibility of radiative (H_3^+) cooling. In this context, a limiting distance, or a stability limit, was identified for such EGPs that depends on the composition of the upper atmosphere and ionosphere, and within which the atmospheres of the planets undergo hydrodynamic escape. Under restricted conditions, this limit is located around 0.15 AU from a Sun-like host star. The model was also used to simulate a newly found transiting planet HD17156b, which orbits its host star on a highly eccentric orbit.

Acknowledgements

I would like to thank my girlfriend and flatmate Stephanie for her patience in listening to my frequent rants about atmospheric dynamics that may not always have seemed so relevant to her. I am grateful to my supervisor, Alan Aylward, for his advice and support throughout this project. I would also like to thank Steve Miller for supporting and persistently promoting my work, and Chris Smith for his brilliant modelling insights that helped me to get started with this project.

God does not care about our mathematical difficulties.
He integrates empirically.

A. Einstein

Contents

List of Figures

List of Tables

Chapter 1

Introduction

A little over a decade has passed since Mayor and Queloz [1995] announced the discovery of 51 Peg b, the first known extrasolar planet orbiting a solar-type star. Now, at the time of writing of this thesis, more than 290 extrasolar planets have been discovered[1], including 25 multi-planet systems. Most of these planets have been detected indirectly by using the Doppler method, which is based on deducing radial velocity variations induced by the planet in the spectrum of the host star. In addition, gravitational microlensing searches have led to the discovery of seven exoplanets, five planets have been imaged directly, and a number of planets have been detected by transit searches and using astrometric methods. Most of the known exoplanets orbit F, G, K, or M type stars but four planets have also been detected orbiting pulsar stars. Indeed, the first exoplanets were found around the millisecond pulsar PSR 1257+12 by Wolszczan and Frail [1992].

The radial velocity method is limited to detecting massive planets that orbit their host stars at relatively close-in distances. Due to this bias, most of the known exoplanets are massive gas giants, generally known as extrasolar giant planets (EGPs). Some of these planets orbit very close to their host stars. For instance, 51 Peg b has an orbital semi-major axis of 0.052 AU, and a period of only 4.23 days. In general, around 25 % of the known exoplanets orbit within 0.1 AU from the host star. These planets are sometimes referred to as *Hot Jupiters*. The probability of transit, i.e. the planet passing across the disk of the host star, is highest for these close-in EGPs. Transits have been detected for more than 40 known EGPs, most of which are Hot Jupiters. Analysing transit light curves and secondary eclipse data has allowed for the characterisation of EGP atmospheres both in the visible and in the infrared. A review of these observations is presented in Chapter 2.

The discovery of close-in EGPs was controversial. Already, Mayor and Queloz [1995] suggested that 51 Peg b is under such extreme stellar irradiation that its atmosphere must have been affected by evaporation. Modelling indicates that the atmospheres of Hot Jupiters are likely to undergo thermal hydrodynamic escape [eg. Lammer et al., 2003, Yelle, 2004, 2006, Tian et al., 2005, García Muñoz, 2007, Koskinen et al., 2007a], and observations imply that this is the case for the well-known transiting

---

[1] May 2008: Schneider, J., The Extrasolar Planet Encyclopaedia, http://exoplanet.eu/

planet HD209458b, which orbits a Sun-like host star at 0.045 AU [Vidal-Madjar et al., 2003, Ballester et al., 2007, Vidal-Madjar et al., 2008]. Evaporation affects the evolution of planetary atmospheres and interiors, and thus it is important that it is properly quantified. This thesis is concerned with the stability of EGP atmospheres against thermal evaporation at different orbital distances from different host stars. One of the primary aims of this project was to generalise a model of Jupiter's upper atmosphere to extrasolar gas giants and move it gradually towards a solar-type host star.

The discovery of Hot Jupiters presents other problems as well. According to current understanding, gas giants form around an icy planetesimal that accretes gas and other material from the surrounding planetary nebula. According to this core accretion model, giant planets cannot form at close-in distances, and instead are thought to form between 5 and 20 AU from the host star. Thus it is now assumed that close-in EGPs form further out from the host star, and then migrate towards it [eg. Papaloizou and Terquem, 2006].

During the last decade, much effort has gone into modelling both the evolution of planetary systems and the atmospheres of extrasolar giant planets. The discovery of Hot Jupiters and other exoplanets has already changed our understanding of how planetary systems form and evolve, and exposed the limitations of using the solar system as a template for other planetary systems. With rapidly developing technology and detection methods, we will soon be able to detect and characterise terrestrial exoplanets as well as gas giants. More than likely, then, we can expect still further surprises in the near future.

Several models of EGP atmospheres have been developed recently to complement and interpret the available observations. Some of these models and the observations are discussed in detail in Chapter 2. Most of the models are one-dimensional, and the majority of them concentrate on the 'photospheric' altitudes in the middle or lower atmosphere where most of the thermal infrared emissions are generated. As such, they are used to simulate radiative transfer and chemical equilibrium in the atmosphere, and the results are employed in predicting the observed spectra of different EGPs. The composition of the EGPs in the models is based on their assumed similarity with either solar system giants or, in some cases, brown dwarfs. In the lower atmosphere of Jupiter and Saturn, the equilibrium mixing ratios arise from complicated chemical reaction chains. These reactions have been studied in great detail but many uncertainties remain even for these relatively well-known planets. Brown dwarf models, on the other hand, suffer from the fact that they often ignore stellar irradiation, which is a crucial factor affecting EGP atmospheres. Also, due to uncertainties over cloud opacities, scattering of radiation, and sources of radiative cooling, accurate modelling of radiative transfer and atmospheric P-T profiles is difficult.

One-dimensional models cannot accurately reproduce the effects that horizontal variations and circulation may have on the temperature and composition of EGP atmospheres. Judging by the few existing models of EGP meteorology [eg. Showman and Guillot, 2002, Cho et al., 2003, 2008, Cooper and Showman, 2005, Burkert et al., 2005, Dobbs-Dixon and Lin, 2008], circulation is likely to be significant and characterised by fast winds. Thus three-dimensional hydrodynamic models are needed to complement our understanding of EGP atmospheres. However, self-consistent modelling of the dynamics, radiative transfer, chemistry, and photochemistry at the photospheric level in 3D is computationally prohibitive. Some of the problems and complications involved can be avoided in modelling the neutral upper atmosphere.

The density of the upper atmosphere, or the thermosphere-ionosphere region, is relatively low, and on gas giants the composition is likely to be dominated by H_2, He, and H. In the absence of complicated plasma interactions, the dynamics of the neutral thermosphere is likely to be determined by the net radiative heating rate and the Coriolis force, which arises from the rotation of the planet around its axis. In contrast, dynamics in the lower atmosphere is affected by turbulent eddies and wave motions that can have a significant influence on the large-scale circulation. In general, turbulence is less significant in the upper atmosphere where, for instance, the vertical distribution of neutral species is largely determined by molecular diffusion. Diffusive separation filters out heavier elements such as oxygen and carbon, and thus photochemistry and radiative transfer are much simpler in the thermosphere than in the lower atmosphere. While such assumptions apply to the planets in the solar system, both gas giants and terrestrial planets, they may not hold generally for exoplanets. Nevertheless, they provide a useful platform for early investigations of EGP thermospheres and ionospheres.

Modelling the thermosphere-ionosphere system is also important because the evaporation rates for EGPs are determined by the conditions in the upper atmosphere, which is often much hotter than the lower atmosphere. This thesis introduces the first attempt to develop a three-dimensional, coupled thermosphere-ionosphere model for extrasolar giant planets (EXOTIM). The details of the model are discussed in Chapter 3. As mentioned above, the model was used to explore the stability of EGP atmospheres at different orbital distances. The results of the simulations are discussed extensively in Chapters 4 and 5. The model was also extended to simulate EGPs orbiting in eccentric orbits, and used to explore the stability and the upper atmosphere of the transiting extrasolar planet HD17156b, which orbits its host star in a highly eccentric orbit.. The extension and the results of the simulations for HD17156b are discussed in Chapter 6. Finally, suggestions at future improvements to the model and ideas about the future direction of this investigation are discussed in Chapter 7.

1.1 Basic Atmospheric Physics

This investigation is concerned with the thermospheres of extrasolar giant planets. The thermosphere is the outermost layer of the atmosphere, situated between the mesosphere and the exobase. On Earth, the thermosphere begins at the altitude of 85 km and extends to about 500 km. It is characterised by a positive vertical temperature gradient, which becomes isothermal at high altitudes. This is due to the absorption of high energy solar X-ray and UV (XUV) photons by oxygen and nitrogen [Salby, 1996]. There are no radiatively active species in the Earth's thermosphere and thus the heating is mainly balanced by downward heat conduction and thermospheric winds. As a result, the thermosphere is very hot and kinetic temperatures of over 1000 K are measured in the upper part. The prefix 'thermo' comes from the Greek word '$\theta\epsilon\rho\mu\omega s$' ('thermos') that means 'warm, hot'.

The upper atmospheres of gas giants are of course very different to Earth. The thermosphere of Earth is dominated by O, N_2 and O_2 while the dominant species in gas giant thermospheres are H_2, He and H. Solar system giants are much further away from the Sun than the Earth and the XUV flux incident on them is thus greatly diminished. Also, many of them have radiatively active species in the upper atmosphere, such as hydrocarbons or H_3^+ ions, that reradiate the absorbed energy in the infrared. For instance, infrared emissions from H_3^+ have been detected from Jupiter, Saturn and Uranus [Drossart et al., 1989, Trafton et al., 1993, Geballe et al., 1993] and H_3^+ appears to be an important coolant at least in the thermospheres of Jupiter and Saturn [Miller et al., 2000].

Despite the differences, on both Jupiter and Saturn the temperature gradients in the upper atmosphere are positive and relatively high temperatures have been measured in the upper layers. In fact, as will be explained in section 1.3, these temperatures are too high to be explained solely by solar heating. This provides a loose justification for extending the concept of a thermosphere to the analysis of gas giant atmospheres, although one should never lose sight of the fact that this definition is only based on thermal character, not on what may be causing it.

The thermal structure of the Earth's atmosphere is shown in Figure 1.1. The definitions of the different atmospheric layers are based on their thermal characteristics. These definitions can be applied to other planetary atmospheres if the *thermal* characteristics are similar. The dominant species in Earth's atmosphere are molecular nitrogen and molecular oxygen, and trace gases include water vapour, carbon dioxide and ozone along with other minor species. The layer closest to the surface is called the *troposphere*, which extends to the *tropopause* at around 10 km. In this layer the temperature decreases with altitude at a nearly constant *lapse rate* of 6.5 K km^{-1}. The troposphere is unstable and characterised by convective overturning. Thus the name *troposphere*, which means 'turning sphere'.

The layer above the tropopause is known as the *stratosphere* or 'layered sphere'. It extends to the *stratopause* at 50 km. The stratosphere contains significant quantities of ozone, which absorbs solar UV radiation. The temperature in the stratosphere is nearly constant up to the altitude of $\sim$20 km, but then the temperature increases sharply with altitude reaching $\sim$275 K at 50 km. The maximum ozone concentration within the ozone layer in the stratosphere is found between 20 and 30 km. Radiative heating in the stratosphere prevents convective overturning and the layer is said to be in radiative-convective equilibrium with the troposphere [Salby, 1996].

The third layer of the atmosphere is known as the *mesosphere*. It extends to the *mesopause* at 85 km and it is characterised by temperature decreasing with altitude. Both convective motions and radiative processes are important in this layer. Unfortunately the mesosphere has not been studied in great detail. It is located between the stratosphere and the thermosphere, and its altitude is too high to be reached by balloons but too low to be probed by satellites.

The thermosphere is limited from above by the exobase, located at the altitude of $\sim$500 km. Above the exobase, in the *exosphere*, particles move on ballistic trajectories. At the exobase, or 'critical level',

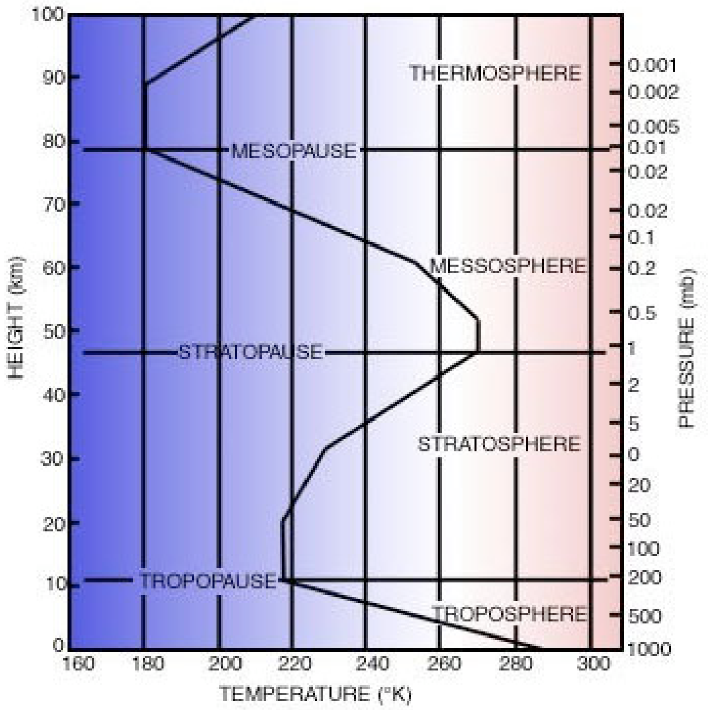

Figure 1.1: The thermal structure of the Earth's atmosphere. Different layers are characterised by the variation of temperature with altitude. (Source: The Met Office, UK, 2007)

particles with enough thermal kinetic energy overcome the gravitational potential of the planet and enter the exosphere. Some of these particles escape to space, while others are drawn back by gravity.

The thermosphere coincides with the ionosphere and thus it is not electrically neutral. Molecules and atoms are ionised by solar XUV radiation and form a partly ionised plasma of free electrons and ions that react to Earth's electric and magnetic fields. The ionosphere ranges from the altitude of 80 km to 400 km and consists of three layers of different ion densities. These layers, from bottom to top, are known as the D, E and F layers. The D and E layers diminish greatly at night, while the plasma density decreases less in the F layer, which is significant both day and night. The plasma densities in these layers are displayed in Figure 1.2.

In addition to thermal layering, another important distinction in the atmosphere is defined its composition at different altitudes. Above 100 km the density of the atmosphere is relatively low and consequently the mean free paths of the particles become larger than displacements driven by turbulent motions or *eddies*. This means that transfer mechanisms arising from molecular diffusion become important and turbulent transfer is suppressed. The transition layer between the two regimes is known as the *homopause*. The region between the homopause and the exobase is known as the *heterosphere*. Due to molecular diffusion, the concentrations of heavier species in the heterosphere decrease with altitude more rapidly than the concentrations of lighter species and the species are said to be diffusively separated. The layers below the homopause are known as the *homosphere*. The homosphere contains the bulk of

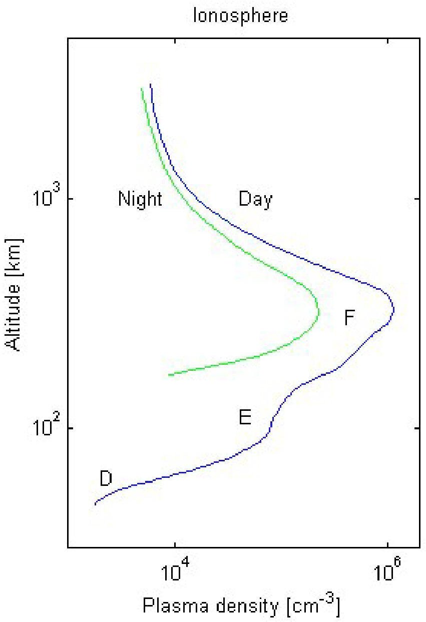

Figure 1.2: The structure of the Earth's ionosphere shown for daytime and night time under solar maximum conditions. The plasma density reaches a maximum in the F layer at the altitude of about 300 km.

the atmosphere, and there the concentrations of all species decrease at the same rate with altitude.

The labels used for different layers in the Earth's atmosphere can be generalised to other planets, and it is convenient to refer back to these definitions while discussing the atmospheres of Jupiter or extrasolar planets. Jupiter, due to its assumed similarity with some of the known extrasolar giant planets (EGP), has become a convenient solar system analogue for such planets. The knowledge of Jupiter's atmosphere works as a valuable reference point for most studies of EGP atmospheres. Thus we will proceed to describe its atmosphere in detail in Section 1.3. However, before we can do so, we need to develop a few basic concepts of atmospheric physics in more detail and derive some basic equations summarising these concepts.

1.1.1 The Equation of State

The thermodynamic state of the neutral atmosphere at a given point is described in terms of pressure, density and temperature. These variables are related to each other by the equation of state, in this case the ideal gas law [Holton, 2004]:

$$p\alpha = (\frac{R*}{m})T \ or \ p = \rho RT \tag{1.1}$$

where $R*$ is the universal gas constant, m is the mean molecular weight of the gas in the atmosphere (i.e. the volume weighted average of the molecular weights of the constituents), ρ is the mass density of the gas, and $\alpha = 1/\rho$ is the specific volume. In meteorology, equation (1.1) is known as the equation of state for dry air. In the presence of humidity or condensation this equation does not hold and must be modified to take them into account. In general, the thermosphere is free of either humidity or any condensation. Thus in this investigation the equation of state for dry air is used in all developments.

1.1.2 The Hydrostatic Equation

At the heart of atmospheric physics lies the assumption of hydrostatic equilibrium. The atmosphere is in hydrostatic equilibrium if at any point in the atmosphere, the force of gravity is balanced by the vertical pressure gradient and the net vertical acceleration can be considered negligible. Mathematically, this statement translates into:

$$\frac{dp}{dz} = -\rho g \tag{1.2}$$

where z is the vertical coordinate. It is convenient to express gravity in terms of the *geopotential* Φ, defined as [Holton, 2004]:

$$\nabla\Phi = -\mathbf{g} \tag{1.3}$$

It should be noted that $\mathbf{g} = g\hat{\mathbf{e}}_z$ where $\hat{\mathbf{e}}_z$ is the unit vector parallel to the local vertical. It follows from this that $\Phi = \Phi(z)$ and that $d\Phi/dz = g$. This implies that horizontal surfaces on a planet are surfaces of constant geopotential.

The assumption of hydrostatic equilibrium can be used to derive a convenient relation between pressure and height in the neutral atmosphere. Substituting equation (1.1) into equation (1.2) and integrating between two pressure levels yields the *hypsometric* equation [Holton, 2004]:

$$Z_2 - Z_1 = \frac{R}{g_o}\int_{p_2}^{p_1} T \; d\ln\ p \tag{1.4}$$

where $Z \equiv \Phi(z)/g_o$ is the *geopotential height*, often close to or identical to geometric height, and g_o is the globally averaged gravity at some agreed reference level.

The mean layer temperature is defined as [Holton, 2004]:

$$\langle T\rangle = \int_{p_2}^{p_1} T \; d\ln\ p[\int_{p_2}^{p_1} d\ln\ p]^{-1}$$

With the aid of this definition we can define a quantity known as vertical scale height:

$$H \equiv \frac{R\langle T\rangle}{g_o} \tag{1.5}$$

Using equation (1.4) and integrating between pressure p and a reference pressure p_o at which the geopotential height $Z_o = 0$, we obtain the following relation between pressure and height:

$$p(z) = p_o exp(-z/H) \tag{1.6}$$

This equation tells us that pressure decreases by a factor of e^{-1} per one vertical scale height.

It is worth noting that vertical scale height is inversely proportional to the mean molecular mass. In the heterosphere, where diffusive separation dominates, a separate value for the scale height can be ascribed for each individual species. In equation (1.5) the mean molecular mass is then replaced by the mass of the constituent. Partial pressures of the constituents are related to their densities by Dalton's law, and thus the density of heavier species decreases with height more rapidly than the density of lighter species.

The situation is much more complex in the ionosphere where free electrons and ions present a significant complication to these basic ideas. However, even charged particles can be thought to have separate scale heights, although obviously these are much more difficult to derive than the corresponding neutral scale heights.

1.1.3 The Energy Equation and Potential Temperature

The fundamental thermodynamic relation (per unit mass) for a moving parcel of gas in the neutral atmosphere can be expressed as:

$$TdS = dU + pdV \tag{1.7}$$

where S is the entropy, and U is the internal thermal energy of the gas. This relation is generally valid for reversible changes between neighbouring equilibrium states that are infinitesimally close to each other. The specific enthalpy (i.e. enthalpy per unit mass) of the gas is given by:

$$H = U + pV \tag{1.8}$$

Differentiating equation (1.8) and using equation (1.7) together with the equation of state (1.1) yields:

$$TdS = C_p dT - \alpha dp$$

where we have also used the fact that for an ideal gas $R = C_p - C_v$. Differentiating with respect to time in the inertial frame of reference leads to a form of the thermodynamic energy equation common in atmospheric physics [Holton, 2004]:

$$T\frac{DS}{Dt} = C_p\frac{DT}{Dt} - \alpha\frac{Dp}{Dt} \tag{1.9}$$

The time derivative in the inertial frame is defined as:

$$\frac{D}{Dt} \equiv \frac{\partial}{\partial t} + \mathbf{u}\cdot\nabla \tag{1.10}$$

where $\mathbf{u}$ is the flow velocity of the gas. This form of the time derivative is also known as the Lagrangian or advective derivative. It describes the rate of change of any quantity within the parcel of gas that is moving with the bulk flow.

If the parcel is undergoing adiabatic change the time evolution is reversible and there is no heat exhange with the environment. In such cases the entropy of the gas does not change and equation (1.9) can be written as:

$$C_p D \ln T - R D \ln p = 0$$

Integrating this equation from a state characterised by pressure p and temperature T to a state with pressure p_s and temperature θ, we obtain the *Poisson's equation* [Holton, 2004]:

$$\theta = T(\frac{p_s}{p})^{R/C_p} \tag{1.11}$$

where the quantity θ is known as the *potential temperature.* It is the temperature that a parcel would have if it was expanded or compressed adiabatically from its surroundings to a given reference pressure p_s. For dry adiabatic motion the potential temperature is conserved. This leads to a handy measure of the stability of the atmosphere.

1.1.4 The Stability of the Atmosphere

Consider a small parcel of gas that is displaced vertically by a tiny distance δz from its surroundings at pressure p_o and density ρ_o. Assuming that the displacement is adiabatic and on such a small scale that that it does not disturb the surroundings, the vertical acceleration of the parcel can be written as:

$$\frac{D^2(\delta z)}{Dt^2} = -g - \alpha \frac{\partial p}{\partial z}$$

where p and ρ are the pressure and density of the parcel. If the parcel is displaced without disturbing the surroundings, the pressure inside the parcel must adjust instantenously to the pressure of the surroundings, i.e. $p_o = p$. Using equations (1.2) and (1.11) we obtain:

$$\frac{D^2(\delta z)}{Dt^2} = g[\frac{\theta - \theta_o(z)}{\theta_o(z)})]$$

where $\theta_o(z)$ is the potential temperature of the environment.

For an adiabatic displacement the potential temperature of the parcel of gas is conserved. Also, we can expand the potential temperature of the surroundings as a linear Taylor expansion about the initial level z_o and then write $\theta - \theta_o(z_o + \delta z) = -(d\theta_o/dz)\delta z$. Using this expression we obtain the equation of motion for buoyancy oscillations in the atmosphere:

$$\frac{D^2(\delta z)}{Dt^2} = -N^2 \delta z \tag{1.12}$$

where

$$N^2 = g \frac{d \ln \theta_o}{dz}$$

The frequency N is known as the buoyancy frequency or Brunt-Väisälä frequency. One solution to equation (1.12) is $\delta z = A \exp(iNt)$. Here, if N is real the parcel oscillates about the initial, equilibrium position. If $N = 0$ there are no oscillations. If N is complex, the solution grows exponentially. Then the parcel keeps rising until it reaches a new equilibrium level or its energy is dissipated by friction.

The stability of the neutral atmosphere is related to the vertical temperature gradient or *lapse rate*. This can be seen by taking a logarithm of equation (1.11) and using equations (1.1) and (1.2) to simplify the result [Holton, 2004]:

$$\frac{T}{\theta_o}\frac{\partial \theta_o}{\partial z} = \Gamma_d - \Gamma \tag{1.13}$$

where $\Gamma = -\partial T/\partial z$ is the atmospheric lapse rate and $\Gamma_d = g/C_p$ is the dry adiabatic lapse rate, i.e. the lapse rate of an atmosphere where potential temperature is constant with height. If $\Gamma < \Gamma_d$, $d\theta/dz$ is positive, N is real and any displaced parcels oscillate about their initial positions. The atmosphere is said to be *statically stable* or stably *stratified*. If $\Gamma > \Gamma_d$ then $d\theta/dz$ is negative, N is complex and the atmosphere is unstable.

This explains the stratification of Earth's atmosphere. In the troposphere the environmental lapse rate is greater than the adiabatic lapse rate leading to large scale convection. In the stratosphere the temperature gradient is positive and thus the layer is stably stratified. In the mesosphere the temperature gradient is again negative enabling some convection. In the neutral thermosphere the temperature gradient is positive and thus the thermosphere is stably stratified. This argument can be extended to gas giants with some reservations. In particular, the stability of exoplanet thermospheres is affected by various other factors like the possibility of thermal or hydrodynamic escape, or tidal effects due to close proximity to the host star (see Chapter 5).

1.1.5 Pressure Coordinates

Equation (1.6) shows that pressure is a monotonically decreasing function of height. Thus it can be used as an alternative vertical coordinate. It turns out that this greatly simplifies the equations of motion in atmospheric dynamics. It is for this reason that most atmospheric models take advantage of the assumption of hydrostatic balance and use pressure coordinates. The conversion to pressure coordinates is based on a few relatively simple transformations. Consider, for instance, a scalar quantity s given by [Salby, 1996]:

$$s(x, y, z, t) = \hat{s}[x, y, p(x, y, z, t), t]$$

We define the horizontal gradient evaluated on surfaces of constant geopotential height in Cartesian coordinates as:

$$\nabla_z = \frac{\partial}{\partial x}\mathbf{\hat{e}}_x + \frac{\partial}{\partial y}\mathbf{\hat{e}}_y \tag{1.14}$$

By using the chain rule it can be readily shown that:

$$\nabla_z s = \nabla_p s + (\frac{\partial s}{\partial p})_{xyt}\nabla_z p \tag{1.15}$$

where ∇_p is the horizontal gradient evaluated on an isobaric surface. Also, the Lagrangian derivative (1.10) can be written in Cartesian pressure coordinates as:

$$\frac{Ds}{Dt} = (\frac{\partial s}{\partial t})_{xyp} + \mathbf{u}_h \cdot \nabla_p s + \frac{Dp}{Dt}(\frac{\partial s}{\partial p})_{xyt} \tag{1.16}$$

where $\mathbf{u}_h$ now denotes the horizontal velocity along an isobaric surface, and Dp/Dt is the Lagrangian derivative of pressure, evaluated in terms of ordinary coordinates. By using the equation of hydrostatic balance (1.2) together with equations (1.15) and (1.3), we obtain a fundamental relationship between the pressure gradient and the geopotential:

$$\nabla_z p = \rho \nabla_p \Phi \tag{1.17}$$

Also the equation of hydrostatic balance can be written as:

$$\frac{\partial \Phi}{\partial p} = -\alpha \tag{1.18}$$

These relations are sufficient to allow for conversion of all the relevant equations of atmospheric physics into pressure coordinates. In this investigation we use spherical pressure coordinates and this feature makes the conversions extremely cumbersome. The conversions of our equations are discussed in some detail in Appendix A.

1.2 The Dynamical Equations of Motion

The equations of motion used in atmospheric physics are based on the assumption that the neutral atmosphere can be treated as a fluid. This enables the use of formalism developed for fluid dynamics. Alternatively, one can approach the problem from the standpoint of gaskinetic theory. As far as the plasma in the ionosphere is concerned, this is the only acceptable approach, although the resulting equations often come close to fluid formalism. Both methods are valuable and to some degree complementary. Gaskinetic theory allows for a better qualitative understanding of some of the implicit assumptions in fluid mechanics while fluid mechanics was used to guide the development of gaskinetic theory. The following discussion is limited to the neutral atmosphere and for brevity the equations are described in terms of fluid mechanics.

1.2.1 The Equation of Continuity

The basic equation of continuity for a small volume τ of gas can be expressed as:

$$\int_\tau (\frac{\partial \rho}{\partial t} - \psi) dV = -\int_\sigma (\rho \mathbf{u}) \cdot d\mathbf{S}$$

where $\mathbf{u}$ is the bulk flow velocity of the gas and ψ is the net source density, i.e. the sum of the rates of production and loss of all species per unit volume of the gas. This equation simply states that the local time rate of change of density inside a small volume τ is equal to the sum of the net flux crossing the surface σ bounding this volume and the net source density. With the aid of Gauss's theorem (see Appendix A) and the Lagrangian derivative (1.10) it can be expressed as:

$$\frac{D\rho}{Dt} + \rho\nabla \cdot \mathbf{u} = \psi \tag{1.19}$$

Here $D\rho/Dt$ is the rate of change of density of a parcel of gas that moves with the bulk flow. For an incompressible fluid this quantity is invariant and thus $\nabla \cdot \mathbf{u} = 0$.

1.2.2 The Momentum Equation

The momentum equation is based on Cauchy's equation of motion, which is given by [O'Neill and Chorlton, 1989]:

$$\rho\frac{Du_i}{Dt} = \rho g_i + \frac{\partial T_{ij}}{\partial x_j} \tag{1.20}$$

where g_i is the acceleration due to gravity, T_{ij} is known as the stress tensor, and we have assumed the summation convention for tensor notation. The components of the stress tensor describe the surface stresses on a parcel of gas. The perpendicular components are due to pressure while the tangential components are due to shearing motions. Thus the stress tensor is given by:

$$T_{ij} = -p\delta_{ij} + d_{ij} \tag{1.21}$$

where p is scalar pressure given by the equation of state (1.1), δ_{ij} is the Kronecker delta, and d_{ij} is known as the deviatoric stress tensor. For a Newtonian fluid the deviatoric stress tensor is given by:

$$d_{ij} = \mu(\frac{\partial u_i}{\partial x_j} + \frac{\partial u_j}{\partial x_i}) + \lambda\delta_{ij}\frac{\partial u_k}{\partial x_k} \tag{1.22}$$

where μ is the coefficient of dynamic viscosity, and λ is the second coefficient of viscosity. If the flow velocity is uniform the stress tensor is diagonal and there is no dynamical friction. Then the diagonal elements are equal to scalar pressure. This is the case for a fluid in local thermodynamic equilibrium (LTE), in which the mean free path between collisions is much shorter than the distance over which macroscopic quantities like temperature or density vary significantly. If the fluid deviates from LTE, the off-diagonal elements become significant. It should be noted that large deviations are not permitted because equation (1.22) is not appropriate for large perturbations.

Equation (1.20) can be written in a vector form as follows [O'Neill and Chorlton, 1989]:

$$\rho\frac{D\mathbf{u}}{Dt} = \rho\mathbf{g} - \nabla p + \mathbf{F}_v \tag{1.23}$$

where $\mathbf{F}_v$ is the force due to friction, given by:

$$\mathbf{F}_v = \nabla(\lambda\nabla \cdot \mathbf{u}) + \mu[\nabla^2\mathbf{u} + \nabla(\nabla \cdot \mathbf{u})] + 2(\nabla\mu \cdot \nabla)\mathbf{u} + \nabla\mu \times (\nabla \times \mathbf{u}) \tag{1.24}$$

Equation (1.23) is valid in the inertial frame. In atmospheric physics the equations of motion are commonly expressed in the Eulerian or corotating frame. This is a frame of reference that corotates with the planet around its axis. Inertial acceleration can be transformed into Eulerian acceleration by using the following relation [Holton, 2004]:

$$(\frac{D\mathbf{u}}{Dt})_I = (\frac{D\mathbf{u}}{Dt})_E + 2\mathbf{\Omega} \times \mathbf{u}_E + \mathbf{\Omega} \times \mathbf{\Omega} \times \mathbf{R}$$

where Ω is the angular rotation rate of the planet, $\mathbf{u}_E$ is the flow velocity in the rotating frame, and $\mathbf{R}$ is the radial position vector, measured from the axis of rotation. The second term on the right hand side is due to the Coriolis force and the last term can be identified as centrifugal acceleration due to rotation. With this transformation, equation (1.23) can be written in the Eulerian corotating frame as:

$$\rho\frac{D\mathbf{u}}{Dt} = \rho\mathbf{g}' - \nabla p - 2\mathbf{\Omega} \times \mathbf{u} + \mathbf{F}_v$$

where $\mathbf{g}' = \mathbf{g} - \mathbf{\Omega} \times \mathbf{\Omega} \times \mathbf{R}$ is the effective gravity, i.e. the sum of gravity and centrifugal acceleration. The presence of the centrifugal acceleration means that effective gravity, the force felt by an observer standing on a surface of constant geopotential, does not point to the centre of the planet. Instead the effective gravity is approximately parallel to the local vertical on a planet that may have adopted an oblate shape.

1.2.3 The Energy Equation

The evolution of the internal energy content and hence temperature within a small volume τ can be described by [Keith, 2000]:

$$\dot{Q} - \dot{W} = \frac{D}{Dt}\int_\tau \rho E dV \tag{1.25}$$

where $\dot{Q}$ is the rate at which heat is added to the system, $\dot{W}$ is the rate at which the system does work on its surroundings, and $E = E_{kin} + U$ is the sum of kinetic energy and internal thermal energy per unit mass within the system. The rate at which heat is added to the system can be written as:

$$\dot{Q} = -\int_\sigma \mathbf{q} \cdot \hat{\mathbf{n}} d\sigma$$

where σ is the surface bounding the volume τ, $\hat{\mathbf{n}}$ is a unit vector normal to that surface, and $\mathbf{q}$ is the heat flow vector, i.e. the quantity of heat flowing through a unit area perpendicular to the flow. In most atmospheric applications an external heat source, such as radiation from a star, is assumed. If, in addition, the heat flow vector within the atmosphere is given by the Fourier heat conduction law $\mathbf{q} = -\kappa\nabla T$, where κ is the coefficient of heat conduction [Keith, 2000], we can use Gauss's theorem (A.1) to express the rate at which heat is added to the system as:

$$\dot{Q} = \int_\tau \nabla \cdot (\kappa\nabla T) dV + \int_\tau \rho Q_R dV \tag{1.26}$$

where Q_R is the net heating rate due to radiative processes (Wkg^{-1}).

The work done by the system is expressed as [Keith, 2000]:

$$\dot{W} = \int_\tau \rho \mathbf{g} \cdot \mathbf{u} dV - \int_\sigma \mathbf{u} \cdot (\mathsf{T}\hat{\mathbf{n}}) d\sigma$$

where the first integral is the work done against gravity, and the second integral is the work done against surface stresses that are given by the stress tensor T. An application of Gauss's theorem turns this into:

$$\dot{W} = \int_\tau \rho \mathbf{g} \cdot \mathbf{u} dV - \int_\tau \nabla \cdot (\mathbf{u}\mathsf{T}) dV \tag{1.27}$$

Substituting equations (1.26) and (1.27) into equation (1.25) and using the fact that mass is conserved along the flow, i.e. that $D(\rho d\tau)/Dt = 0$, we obtain the following differential equation for energy conservation:

$$\rho \frac{DE}{Dt} = \nabla \cdot (\kappa \nabla T) + \rho Q_R - \rho \mathbf{g} \cdot \mathbf{u} + \nabla \cdot (\mathbf{u}\mathsf{T}) \tag{1.28}$$

The definition of T for a Newtonian fluid (1.21) yields:

$$\nabla \cdot (\mathbf{u}\mathsf{T}) = -p \nabla \cdot \mathbf{u} - \mathbf{u} \cdot \nabla p + \nabla \cdot (\mathbf{u}\mathsf{d})$$

where d is the deviatoric stress tensor. If we assume that the horizontal velocity $\mathbf{u}_h$ is perpendicular to gravity, then $\rho \mathbf{g} \cdot \mathbf{u} = \rho g u_z$ where u_z is the vertical velocity, perpendicular to surfaces of constant geopotential. Together with the assumption of hydrostatic equilibrium (1.2), these modifications allow us to write equation (1.28) as:

$$\rho \frac{DE}{Dt} = \nabla \cdot (\kappa \nabla T) + \rho Q_R - p \nabla \cdot \mathbf{u} - \mathbf{u}_h \cdot \nabla_z p + \nabla \cdot (\mathbf{u}\mathsf{d}) \tag{1.29}$$

where ∇_z is the gradient operator at constant height, given in Cartesian coordinates by:

$$\nabla_z = \frac{\partial}{\partial x} \hat{\mathbf{e}}_x + \frac{\partial}{\partial y} \hat{\mathbf{e}}_y$$

Equation (1.29) can be developed further by using the equation of continuity (1.19) to show that:

$$p \nabla \cdot \mathbf{u} = \rho p \frac{D\alpha}{Dt}$$

Then, differentiating the equation of state (1.1) we obtain:

$$\rho p \frac{D\alpha}{Dt} = \rho R \frac{DT}{Dt} - \omega$$

where ω is the Lagrangian derivative of pressure. Noting that $U = C_v T$ and that $R = C_p - C_v$, we can use the above relations to write equation (1.29) as:

$$\frac{D\epsilon}{Dt} = Q_R - \alpha \mathbf{u} \cdot \nabla_z p + \alpha \omega + \alpha \nabla \cdot (\mathbf{u}\mathsf{d}) + \alpha \nabla \cdot (\kappa \nabla T) \tag{1.30}$$

where $\epsilon = C_pT + E_{kin}$ is the specific enthalpy. This equation is valid for Newtonian fluids and allows for frictional heating and heat conduction. Collectively equations (1.19), (1.23), (1.24) and (1.30) are known as the Navier-Stokes equations. In general they are valid for subsonic flow and allow for slight deviations from LTE. As such these equations are ideal for modelling the global circulation regime in the thermosphere. It should be noted that equations (1.9) and (1.30) are not contradictory. By using the momentum equation (1.20) it is possible to show that equation (1.30) reduces to equation (1.9). The form of the energy equation (1.30) is not very conventional. The derivation is included here as a justification for the energy equation used in this work and described in Chapter 3.

1.2.4 The Primitive Equations

The transformations presented in section 1.1.5 allow us to express the continuity equation (1.19) in pressure coordinates as follows [Jacobson, 1999]:

$$\nabla_p \cdot \mathbf{u}_h + \frac{\partial \omega}{\partial p} = 0 \tag{1.31}$$

where $\omega = Dp/Dt$, the Lagrangian derivative of pressure, and we have omitted the source term. Similarly, the pressure coordinate conversions allow us to write the momentum equation (1.23) as:

$$\frac{D\mathbf{u}}{Dt} = -\nabla_p \Phi - 2\mathbf{\Omega} \times \mathbf{u} + \alpha \mathbf{F}_v \tag{1.32}$$

where D/Dt is given by equation (1.16), and $\mathbf{F}_v$ is the general friction force. Together with the energy equation (1.9), equations (1.31) and (1.32) are known as the *primitive equations* and they are the starting point for any investigation of large scale global circulation.

It should be noted that in meteorology the friction force is often formally different to the one given by equation (1.24) earlier. The viscous force for a Newtonian fluid arises from molecular viscosity, i.e. the random motions of colliding particles and subsequent momentum transfer. In Earth's atmosphere molecular viscosity is negligible below 100 km, apart from a very thin layer near the planet's surface. Instead, momentum is transferred primarily by turbulent eddy motions. Turbulent eddies arise from shearing motion due to variable winds or as a result of convection. In general, they are much more effective in transferring heat and momentum than molecular processes.

Unfortunately turbulent eddies consist of irregular quasi-random motions and often contain small scale flows that cannot be resolved by spatial or temporal resolutions of most known models or observing networks. Thus modelling them reliably is a challenging task. In stably stratified atmospheric layers, it is often customary to assume that turbulent eddies behave in a manner similar to molecular viscosity. This approximation is sometimes referred to as *K theory* [Holton, 2004]. It simply means that equations similar to those describing molecular viscosity and heat conduction are used to describe turbulent transfer but the coefficients of viscosity and heat conduction are replaced by eddy coefficients. The values of the eddy coefficients are either crudely estimated or worked out from observations, if such are available.

In the neutral upper atmosphere, as we stated before, turbulent motions are overtaken by molecular diffusion. Thus the primary source of viscosity and heat conduction is molecular diffusion. Nevertheless, turbulence persists in the lower thermosphere and in some cases may be of significance even in the upper thermosphere. There is no agreement on how it should be modelled though, and throughout the course of this investigation, we have largely ignored it. Further details on our method with regard to turbulent transfer can be found in Chapter 3.

1.3 Jupiter's Atmosphere

Jupiter is the largest planet in our Solar System. With a radius at 1 bar level of 69911 km (corresponding to about 11 R_E) and mass of 1899×10^{24} kg (corresponding to about 318 M_E) it is more massive than all other planets and satellites put together. These figures yield a mean density of 1326 kg m^{-3}, which is only slighly higher than the density of water. Indeed Jupiter is a gaseous planet that is primarily composed of hydrogen and helium. Its bulk composition is similar to the Sun, although there are some notable differences, especially when it comes to heavy elements.

The visual appearance of Jupiter was first described in the 17th century. The most distinct features of its disc are the bright and dark bands, known as *zones* if they are bright and *belts* if they are dark. Imbedded in these bands are various other structures such as the Great Red Spot (GRS), brown spots, red spots, white ovals etc. Most of these visual features arise from moving clouds at pressures between 0.7 and 1.5 bar [Ingersoll et al., 2004].

By observing the motion of the clouds in the zones and belts one can estimate the zonal wind speed in the bands and the rotation rate of Jupiter around its axis. Such analysis has revealed that the zonal winds are strongest at the boundaries between zones and belts and that the circulation in the zones is anticyclonic, with an eastward jet on the poleward site and a westward jet on the equatorward site. In contrast the circulation in the belts is cyclonic. The rotation rate estimates based on cloud tracking vary depending on what part of the disk is observed. A better estimate is based on the analysis of decimetric radio emissions by relativistic particles trapped in Jupiter's rotating magnetic field (System III) and this returns a spin period of 9 h 55 min 30 s.

In general, Jupiter appears muted brown, with shades of yellow, white, and deep red. The white clouds in the upper troposphere have been identified as ammonia ice crystals along with some water ices. The major cloud components are ammonia, H_2S, and water that are all essentially colourless. The colours arise from impurities such as elemental sulphur, phosphorus and organic compounds. The faint yellow covering most of Jupiter's disk is probably due to hydrocarbon droplets produced by photochemistry in the stratosphere. The yellowish and brownish hues tainting the layer of clouds in the lower troposphere are thought to be traces of elemental sulphur. The red brick colour of the GRS may be due to elemental phosphorus, released by the action of solar radiation [Taylor et al., 2004].

Jupiter is surrounded by 63 natural satellites. The most important and largest out of these are

Io, Europa, Ganymede, and Callisto - known collectively as the *Galilean satellites* because they were discovered by Galileo in 1610. Jupiter also has a faint ring composed of fine, rocky particles [Hartmann, 1999]. The satellites are embedded in Jupiter's vast magnetosphere. Due to its rapid rotation, Jupiter has a strong internal magnetic field, which is thought to be generated by the motion of free electrons in the planet's deep interior. This field interacts with the solar wind and the interaction leads to the formation of the magnetosphere. One of the moons, Io, is volcanic and it spews out matter that becomes ionised and helps to form Jupiter's plasma torus. The plasma creates current systems in the magnetosphere that interact with the ionosphere in the polar auroral regions, feeding fast energetic particles into the atmosphere.

Modern instruments and space missions have greatly improved our understanding of Jupiter. The first spacecraft that flew to Jupiter was Pioneer 10 in 1973, followed by Pioneer 11 in 1974. These two probes had equipment on board to record images of the Jupiter system, detect charged particles of various kinds, and characterise the magnetosphere and the atmosphere. The next satellites to visit Jupiter were Voyager 1 and Voyager 2, both of which passed Jupiter in 1979. The Voyager mission produced spectacular images of Jupiter and its moons, characterised their atmospheres, and studied the magnetosphere. After their visit to the system the spacecrafts exploited Jupiter's gravity to continue their journey towards the outer planets and beyond.

The most comprehensive review of Jupiter's atmospheric properties was performed by the Galileo mission. The Galileo spacecraft arrived to the Jupiter system on December 7 1995 and stayed in orbit for nearly six years. It also included a probe that was detached and allowed to fall into the atmosphere, reaching a depth of 22 bar before connection was lost. After Galileo, the Jupiter system has been probed from a distance by the Cassini satellite, which also exploited Jupiter's gravity to get a boost to Saturn. Much of what is known about Jupiter's atmosphere is based on measurements performed by these missions.

1.3.1 Interior and Lower Atmosphere

The thermal structure of the Jovian atmosphere and other features are shown in Figure 1.3. The most abundant species in the atmosphere are H_2 and He. According to Voyager and Galileo data, the volume mixing ratios of these species are 0.86 and 0.136, respectively [Taylor et al., 2004]. The rest of the atmosphere consists of traces of methane (CH_4), ammonia (NH_3), water (H_2O), hydrogen sulphide (H_2S), neon (Ne), argon (Ar), hydrogen deuteride (HD), and other minor heavy elements.

A simple way to model the composition of gas giant planets is to assume that the elemental abundances are the same as in the Sun, and that chemical equilibrium is attained in the interior. Chemical equilibrium models allow common elements to combine with hydrogen to form methane, ammonia, water, and other species. The equilibrium concentrations depend on pressure and temperature, and thus the models can be used to predict vertical composition profiles. The models also allow for the measured composition to be used to deduce elemental abundance ratios that can be compared with those of the Sun. Such a

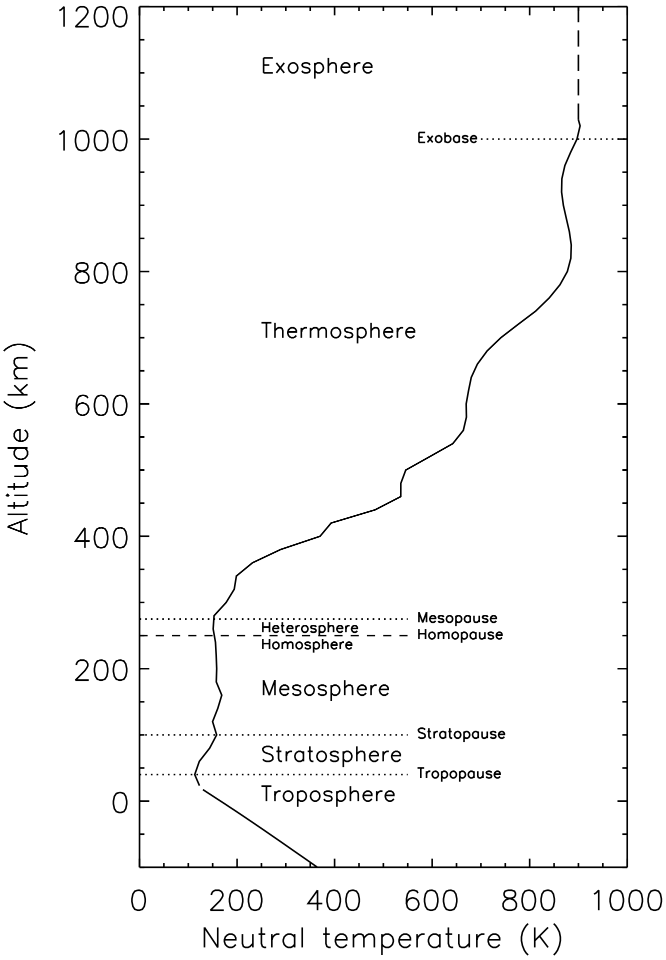

Figure 1.3: The thermal structure of Jupiter's atmosphere [Smith, 2006].

comparison yields valuable clues to the formation history of the planets as different formation scenarios produce different ratios.

The jovian ratio of helium to hydrogen (He/H) is roughly the same as in the Sun. This points at a common origin in the protosolar nebula. However, the ratio is primordial, which is problematic because the protosolar nebula should have been enriched in helium due to material from dead stars. In the Sun, the helium is in the core and thus the ratio cannot be determined reliably by surface measurements. It is possible that on Jupiter the extra helium has also condensed to the deep interior. The hydrogen in Jupiter's core is expected to be in a state of pressure ionisation. At $\sim$1.0 Mbar pressures the electron clouds of individual atoms are pushed together and the atomic structure breaks down. The electrons begin to move freely, as happens in metals, while the ions attempt to form a crystal lattice. In these conditions helium and neon form droplets that "rain out" deeper towards the core. This mechanism of depleting helium in the atmosphere is supported by the fact that the Jovian Ne/H ratio is depleted to 0.13 times solar.

One big breakthrough that has arisen from the analysis of atmospheric abundances is the realisation that Jupiter is enriched in heavy elements. The ratio of carbon to hydrogen (C/H) is enhanced by a factor of 2.9 compared to the solar value, the N/H and S/H ratios appear to be enhanced to 2 and 2.5 times solar, respectively, and values of 2.7–2.9 times solar are expected for the Ar/H, Kr/H, and Xe/H ratios [Taylor et al., 2004]. This enrichment in metallicity seems to solve some of the controversies related to Jupiter's formation.

The two leading theories of gas giant formation are direct collapse and core nucleation. According to direct collapse models Jupiter formed simply by condensing out of the solar nebula. The problem with this idea is that it produces solar metallicity. According to core nucleation theories, Jupiter formed around an icy planetesimal, around 12 M_E in mass, that was large enough to accrete the protosolar nebula and other planetesimals [Lunine et al., 2004]. Calculations based on this model produce a metallicity of 3 times solar, which agrees with the observed values. However, elemental abundance ratios are still somewhat uncertain. They are based on measurements in the atmosphere and often limited to specific regions. Converting these measurements into bulk elemental abundances is not an exact science. There are also problems with the theoretical details of core nucleation models. The lifetime of a gaseous disk is only 10 million years or less, and it is not clear whether a planetesimal of 12 M_E can form within that timescale. Also, if the icy planetesimal formed at Jupiter's orbit, it should have been depleted in nitrogen and argon as the temperatures are too high for them to be trapped on the planetesimals. The source of these elements remains unknown [Lunine et al., 2004]. Nevertheless, core nucleation must be the favoured theory for gas giant formation at present as it is the only theory that produces the observed metallicity enhancement.

The vertical temperature profile through Jupiter's atmosphere is shown in Figure 1.3. The temperature in the deep atmosphere is relatively high and it decreases with altitude following a dry adiabat near 1.0 bar. At pressures higher 300 mbar, in the troposphere, the atmosphere is convective. Methane is the most abundant minor species in the upper troposphere, although generally water vapour is expected to be the most abundant minor species overall in the troposphere. Methane does not condense in the atmosphere of Jupiter and it is chemically stable all the way to ∼1.0 mbar where it is dissociated by solar UV radiation and, at auroral regions, by precipitating energetic particles [Taylor et al., 2004].

According to chemical equilibrium models, ammonia should combine with hydrogen sulphide to produce ammonium hydrosulphide (NH_4SH). This species is expected to condense at around 2.2 bar to form clouds. The residual NH_3 condenses in the upper troposphere to form the white clouds of ammonia ice crystals observed at around 0.7 bar. Above the tropopause, ammonia is also depleted by solar UV radiation and energetic particle precipitation [Taylor et al., 2004].

The water vapour abundance in the troposphere is uncertain. Chemical equilibrium models that assume solar abundances produce a higher water vapour content than that observed. This could be due to observational bias. Earth-based measurements are biased towards the dark belts. These have been identified as downwelling regions of planetary scale convection cells and they should be depleted of volatiles or water vapour, which are expected to condense in the updrafts of the zones. There is some evidence of a deep, thick water cloud at pressures between 3.5 and 7 bars. Such a cloud layer is also predicted by chemical equilibrium models for the observed temperature profile. The humidity measurements performed by the Galileo probe also returned lower than expected values, but it is now believed that the entry site of the probe was anomalously dry [Taylor et al., 2004].

1.3.2 Upper Atmosphere and Magnetosphere

The atmosphere is statically stable above the 300 mbar level, with temperature increasing slightly with altitude. The tropopause is located at ∼100–300 mbar, and due to the temperature inversion, the layer above is called the stratosphere. Analogously to Earth, Jupiter's stratosphere is heated by absorption of solar UV and near-IR radiation. In addition, it is also heated to some degree by infrared radiation from deeper layers of the atmosphere. The absorbed energy is reradiated in the infrared wavelengths.

Methane is the most abundant minor species in the stratosphere and it plays a major role in controlling stratospheric chemistry and radiative transfer. It is dissociated by solar UV radiation and precipitating energetic particles in the polar auroral regions. The dissociation products form hydrocarbon species such as ethane (C_2H_6), acetylene (C_2H_2), propane (C_3H_4) and several others. The hydrocarbon photochemistry is immensely complicated and it proceeds through hundreds of different reactions, making any easy characterisation of Jupiter's stratosphere an impossible task. Some of the reactions are presented in Moses et al. [2004].

The volume mixing ratio of methane decreases with height and the methane homopause has been located at about 10^{-3} mbar. At this level molecular diffusion begins to dominate over turbulent mixing. It is thus usually considered as the upper boundary of the stratosphere. Water has also been detected in the stratosphere and in fact the mixing ratio of H_2O increases with altitude above the 10 mbar level. This is not possible unless the water is of some external origin. It is probably carried to Jupiter's upper atmosphere by interplanetary dust and/or satellite and cometary material.

The Neutral Thermosphere

Above the stratosphere, in Jupiter's thermosphere at pressures lower than 10^{-3} mbar, the temperature increases steeply with altitude reaching about 1000 K at the exobase. The dominant neutral species in the lower thermosphere are H_2 and He, but atomic hydrogen dominates at high altitudes and the exobase. The dominant transport mechanism in the thermosphere is molecular diffusion and thus the species are diffusively separated. We know that the scale heights of the individual species are inversely proportional to their mass. Thus heavier species fall off more rapidly with height and this explains the neutral density profiles in the thermosphere.

The thermosphere absorbs solar XUV radiation, which also dissociates and ionises the neutral species. Photochemistry involving hydrocarbons and absorption by methane is important near the lower boundary but due to diffusive separation, it is negligible at middle and high thermospheric altitudes. Thus photochemistry in the thermosphere is much simpler than in the stratosphere as it only involves reactions between H_2, He, H, and the ions H^+, He^+, HeH^+, H_2^+, and H_3^+ [Yelle and Miller, 2004].

Contrary to the thermosphere on Earth, there are several radiatively active species in Jupiter's thermosphere that re-emit some of the absorbed energy in the thermal infrared wavelengths. Enhanced hydrocarbon emissions in the mid-IR have been observed from the auroral zones, and these are naturally confined to the lower thermosphere or stratosphere. Faint emissions from H_2 have also been observed, but these tend to be rather insignificant from the thermal perspective. H_2 is a symmetric diatomic molecule that does not have a permanent or induced dipole moment, and thus the emission comes from quadrupole allowed ro-vibrational transitions [Yelle and Miller, 2004].

By far the most significant infrared-active species is the H_3^+ ion. It is an equilateral triangle structure, and as such it has no permanent dipole. Thus it has no allowed purely rotational spectrum. The symmetric stretching vibration, ν_1, is also forbidden as it maintains symmetry, leaving the asymmetric stretching vibration, ν_2, as the only allowed vibration. The fundamental band of this vibration, $\nu_2 = 1$, is centred at 4 μm and the overtone $\nu_2 = 2$ band is centred around 2 μm. The ro-vibrational transitions are much stronger than those from H_2, making H_3^+ an efficient radiator in the infrared. Apart from the lower boundary region, the thermosphere is optically thin and the emitted radiation escapes directly to space. Thus these emissions have a significant cooling effect on the thermosphere. Indeed H_3^+ emissions are very sensitive to temperature and they have been used to analyse temperatures and winds in the auroral and non-auroral ionosphere.

Several complementary methods have been employed to deduce the vertical temperature profile in Jupiter's thermosphere. The results are different for the auroral and non-auroral zones. In the auroral zones, precipitation of energetic particles, such as electrons or ions, from the magnetosphere leads to enhanced heating, impact ionisation and dissociation of neutral species. Drossart et al. [1993] used H_3^+ emission spectra to derive a translational temperature of 1150 K for the auroral ionosphere. Other studies of H_3^+ spectra reveal that ro-vibrational temperatures are enhanced in the auroral regions, but that they are also relatively high around the equator, between 750 K and 1000 K [Yelle and Miller, 2004].

Voyager 1 recorded the transmission of solar UV radiation through the upper atmosphere while passing behind the star. Such occultations measure the vertical profile of the horizontal column density that can be converted into a pressure-temperature (P-T) profile. Analysis of the Voyager data shows that the average temperature over several scale heights centred at 2×10^{-6} μbar is about 1000 ± 200 K [Yelle and Miller, 2004].

Voyager 2 measured a similar occultation by a star Alpha Leo in the UV, and this data was used to constrain the location of the methane homopause. H_2 in the upper atmosphere emits in the UV in the Lyman and Werner band systems, and occultations in these lines constrain the H_2 density and P-T profile. Further information on the temperatures and density in the upper atmosphere has been obtained from ground-based stellar occultations.

The Galileo probe, which plunged into Jupiter's atmosphere, provided the most definitive set of measurements to constrain the temperature and density properties of the thermosphere. The upper stratospheric temperature is about 200 K. This increases to about 1000 K near the exobase with a peak temperature gradient of 2.9 K km^{-1} at 357 km. The data also revealed periodic temperature variations now believed to be due to buoyancy waves [Yelle and Miller, 2004]. Similar temperature variations have been observed in the stratosphere [Ingersoll et al., 2004], indicating that wave motion is important in Jupiter's upper atmosphere.

No matter what measurements are preferred, one inconvenient feature arises from all of them. Jupiter's upper atmosphere is hotter than implied by simple modelling based on solar heating. If it was heated solely by solar XUV radiation, the exospheric temperature should not be more than a little over 200 K. Some other process is needed to heat the thermosphere to the observed temperatures. Suggestions for the additional heating mechanism include gravity wave breaking, low-latitude particle precipitation and redistribution of auroral energy. Modelling studies show that none of these mechanisms on their own solve the problem. There is considerable uncertainty over the role of wave breaking. The estimated energy deposited by low latitude precipitation is only of the same order of magnitude as solar XUV heating. The auroral zones receive enough energy, but the Coriolis force arising from Jupiter's fast rotation makes redistribution to equatorial regions unfeasible. In fact, a recent study by Smith et al. [2007] indicates that circulation driven by particle precipitation in the auroral zones may actually cool the equatorial thermosphere. The conclusion is that, to our embarrasment, we do not actually understand the thermal structure of Jupiter's thermosphere.

The Ionosphere

The dominant ion in Jupiter's ionosphere is H^+, while the minor ion species in the upper and middle thermosphere are H_3^+, H_2^+, He^+ and HeH^+. H_2^+ is extremely short-lived and turns almost immediately into H_3^+, which is also relatively short-lived and quickly recombines with free electrons. The He^+ ions are also short-lived. The resulting photochemistry between these ions and the neutral species appears relatively straightforward and with the exception of H^+, fast timescales seem to justify the assumption of photochemical equilibrium. As usual, reality escapes such simplistic ideas and models that utilise these assumptions fail to match the observed plasma density profiles.

The assumption of quasineutrality within the partly ionised plasma in the ionosphere allows for the determination of plasma densities from the electron density profile, which can be deduced from radio occultation measurements. Both Pioneer and Voyager missions included radio occultations, in which the spacecraft emits a radio signal as it passes behind the planet and the signal is then detected by Earth-based observers. The radio waves are refracted by free electrons in the ionosphere.

It turns out that the electron densities are highly variable. Most of the measured profiles have an electron density peak of 0.5–2 $\times 10^{11}$ m^{-3} at 1500–2000 km [Yelle and Miller, 2004]. However, some profiles exhibit a lower ionospheric peak below 1000 km, that is absent in other measurements. This could be due to the lower ionosphere diminishing during the night but the conclusion is not borne out by Galileo profiles in which the lower peak is absent at dusk.

Photochemical models fail to match both the measured plasma density and the peak altitude. They tend to exaggerate the electron density and place the peak altitude lower than observed. This brings up the question of plasma transport for the long-lived H^+ ion. Neutral winds can carry the ions along magnetic field lines, shifting the peak altitude upwards with upwelling and downwards with downwelling. In addition, H^+ can be lost through a reaction with vibrationally excited H_2, and this could reduce the high electron densities produced by the models [Yelle and Miller, 2004]. We will learn that both processes could also be significant in the ionospheres of giant exoplanets.

The Aurorae

The jovian polar aurorae have been observed in X-rays, UV and IR. The observed X-ray emission rate is 4×10^9 W [Metzger et al., 1983], with energies of 0.2 to 3.0 keV measured from both auroral zones. These emissions are thought to arise from energetic oxygen ions. The UV emissions are Lyα emissions from atomic hydrogen and Lyman and Werner band system emissions from H_2. Lyα emissions have also been detected from non-auroral regions, where they arise mainly from resonance scattering of the solar Lyα line. In the auroral zones, the emission is enhanced by electron impact excitation. The observed line profiles in the auroral ionosphere are highly asymmetric, suggesting ion winds of several km s^{-1} [Yelle and Miller, 2004]. The aurorae are extremely bright in the H_2 Werner and Lyman band systems, due to electron impact excitation. Observations of these bands constrain the energy spectrum of the precipitating particles and provide an estimate of ionospheric temperature through analysis of the ro-vibrational lines.

The infrared aurorae are a result of emissions from H_3^+, H_2 and hydrocarbons in the lower thermosphere, all enhanced by energetic charged particle precipitation. H_3^+ emissions are naturally much brighter in the aurorae than elsewhere on the disk. The Doppler shifted line profiles of H_3^+ emissions have revealed ion wind speeds of several km s^{-1}, confirming the conclusions based on Lyα emissions.

The precipitating particles originate in Jupiter's plasmasphere. This is a unique environment, which has a fundamental influence on Jupiter's ionosphere and neutral thermosphere. Embedded in Jupiter's magnetosphere is the moon Io, which is highly volcanic. Continuous eruptions feed matter into the surrounding space that is subsequently ionised. The result is a plasma torus centred on Io's orbit. Io's orbital rotation rate is slightly different from Jupiter's System III spin period, which leads the corotating magnetic field lines to sweep past the moon. This process creates a huge current system that closes in the ionosphere and allows for charged particle precipitation along the field lines into Jupiter's auroral zones. For a long time it was thought that the auroral oval would coincide with the footprint of the Io plasma torus. However, mapping of H_3^+ emissions has revealed that in fact the auroral oval coincides with the footprint of the magnetic field lines that connect to an equatorial plasma sheet in the magnetosphere [Yelle and Miller, 2004].

1.4 Exoplanet Thermospheres

Most of the currently known exoplanets are gaseous giant planets primarily composed of hydrogen and helium. Some similarities with Jupiter are thus to be expected, although the differences are also likely to be significant due to the fact that many of the EGPs orbit their host stars much closer than Jupiter orbits the Sun.

Unfortunately, there are only a handful of observations that constrain the nature of exoplanet thermospheres, and even those are ambiguous (see Chapter 2). Thus current modelling studies in this area are largely speculative. Jupiter is a convenient starting point for such speculations, as it is a gas giant planet, which has been studied and observed at least to some degree. Generalising Jupiter's properties to other gas giants too liberally is dangerous, but there are reasons to believe it may at least be more justifiable in the upper atmosphere than it is in the lower atmosphere.

Thermospheric pressures are low, lower than 1.0 μbar. At low pressures diffusive separation is probably a reasonable assumption, at least in relatively stable atmospheres. This means that heavy species can be neglected in much of the thermosphere, and consequently the composition and photochemistry are relatively simple. It is more than likely that in the molecular diffusion regime the neutral and ion species are the same as on Jupiter and that photochemistry proceeds along similar lines. While there is considerable uncertainty over the stratospheric properties of exoplanets, it appears feasibe to produce a first order study of EGP thermospheres simply by moving a thermospheric model of Jupiter closer to the Sun, by intensifying the XUV fluxes by increments.

Of course this approach has its weaknesses. The magnetic field and plasmasphere of Jupiter is unique and no generalisation to EGPs is possible or feasible without some kind of observational constraints on EGP magnetic fields or plasma environments. Interaction with the stellar wind is probably a general feature, but it depends on the nature of the internal magnetic field of EGPs. There are no definite observational confirmations of the existence of a magnetic field around any of the known EGPs at present.

In addition, existing thermospheric models of Jupiter do not actually work, and this may have significant implications for the kind of EGP models discussed in this thesis. Everything depends on the unknown heating mechanism on Jupiter. We do not know whether this mechanism can be generalised to other gas giants. If it depends on the properties of Jupiter's unique plasma environment and aurorae, it cannot be generalised. If it is an intrinsic property that is amplified by an increasing solar XUV flux, then it may significantly affect the results of this investigation.

Chapter 2

The Properties of Exoplanets

2.1 General Characteristics

Since the discovery of the first extrasolar planets around the millisecond pulsar PSR 1257+12 by Wolszczan and Frail [1992], more than 290 extrasolar planets have been found (by May 2008). Most of the known exoplanets orbit FGK stars, but a few have also been found around M stars [1]. The predominance of solar or nearly solar-type host stars is a selection effect as they have been prioritised for observing programs.

Most of the known exoplanets have been detected by using the Doppler or radial velocity method, which is based on deducing radial velocity variations induced by the planet in the spectrum of the host star. In addition, seven planets have been detected by gravitational microlensing, another five have been imaged directly in the infrared, and a number of planets have been uncovered by transit surveys.

Due to the limitations of the radial velocity technique, very little precise information of the known exoplanets is available at present. Kepler's laws of orbital motion and the observed stellar characteristics can be used to deduce the orbital semi-major axis, period, and eccentricity for the planet from the variations in the host star's spectrum. In principle, the mass of the planet can also be estimated from the data. However, in most cases the viewing angle to the orbital plane is unknown and the analysis only yields a value for the minimum mass $M_p \sin(i)$, where i is the inclination of the orbit. Accurate estimates of masses and radii only exist for transiting planets that are seen periodically transiting across the disk of their host star, producing an observable dip in the amplitude of the spectrum of the star. Over 40 transiting planets are known presently, and these planets have proven to be very useful in advancing our understanding of close-orbiting EGPs.

Present instruments can achieve a precision of $\sim$3 m s^{-1} for radial velocity surveys [Marcy et al., 2005], although only a few planets have been observed below the 10 m s^{-1} threshold [Lecavelier Des Etangs, 2007]. As a point of comparison, the radial velocity semi-amplitude produced by Earth around

---

[1] J.Schneider: The Extrasolar Planet Encyclopaedia (www.exoplanet.eu)

the Sun is ~0.1 m s^{-1}, whereas Saturn and Jupiter manage 2.7 m s^{-1} and 12.5 m s^{-1}, respectively. In the future, a precision of below 1 m s^{-1} is achievable but at such a precision it is difficult to distinguish the wobble due to an orbiting planet from noise caused by stellar surface turbulence, spots, and acoustic oscillations [Marcy et al., 2005].

As a result of these limitations the current distribution of exoplanets is biased to massive planets orbiting close to their host stars. The minimum mass of the known exoplanets varies from ~5 M_E to 19 M_J while the semi-major axis range from ~0.02 AU to 9 AU. About 55 % of the known exoplanets orbit within 1.0 AU of their host star, and roughly 25 % orbit as close as within 0.1 AU. Due to their high effective temperatures, gas giants orbiting within 0.1 AU are often called *Hot Jupiters*. The rest of the known planets orbit between 1.0 and 9 AU. Incidentally, only one gas giant has been found so far orbiting between 5-6 AU (55 Cnc d), corresponding to Jupiter's orbit around the Sun.

Marcy et al. [2005] performed a Doppler survey of 1330 FGKM stars. They found that ~ 6-7 % of stars harbour giant planets within 5 AU. The number of planets in their sample seems to increase towards the lower mass end of the distribution. This is interesting because of the observational bias towards higher masses. Even with this bias, lower mass planets are more common, indicating that giant planets with a mass comparable to that of Jupiter are common whereas really massive planets are rare.

Since the orbital periods decrease with decreasing orbital distance, many of the close-in exoplanets within 0.1 AU have very short periods, some of the order of one Earth day. The discovery of such planets is surprising and has lead to an extensive review of the leading theories of planet formation. Due to the extreme irradiation these planets receive from the host star, their stability, or instability, is still a subject of intense debate.

Figure 2.1 shows the orbital eccentricities of the known giant planets versus the semi-major axis of the orbit. Most of the close-in EGPs are found on circular or nearly circular orbits, although as the figure shows, there are some deviations. At close-in distances, tidal forces between the star and the planet tend to circularise the orbit and synchronise the spin of the planet to its orbital period so that the same side of the planet always faces the star [Trilling, 2000]. A close-in eccentric orbit may be a signature of another large planet in the system that perturbs the orbit of an inner planet.

The rough timescale for tidal spin-locking is given by [Guillot et al., 1996]:

$$\tau \sim Q(\frac{R_p^3}{GM_p})\omega_p(\frac{M_p}{M_*})^2(\frac{D}{R_p})^6 \tag{2.1}$$

where Q is the tidal dissipation factor, ω_p is the primordial rotation rate of the planet, G is the gravitational constant, R_p and M_p are the radius and mass of the planet, respectively, D is the semi-major axis of the planet's orbit, and M_* is the mass of the host star. For a Jupiter-type EGP with $Q \sim 10^5$ and $\omega_p \sim 1.7 \times 10^{-4}$ orbiting a solar-type star, the spin-locking time scale is $\sim 1.3 \times 10^8$ years at 0.1 AU and $\sim 2 \times 10^6$ years at 0.05 AU. The typical age of an EGP system varies from 3×10^9 to 10^{10} years, implying that within 0.1 AU the synchronisation timescale is much shorter than the age of the system. Thus it is commonly assumed that close-in EGPs are rotationally synchronised.

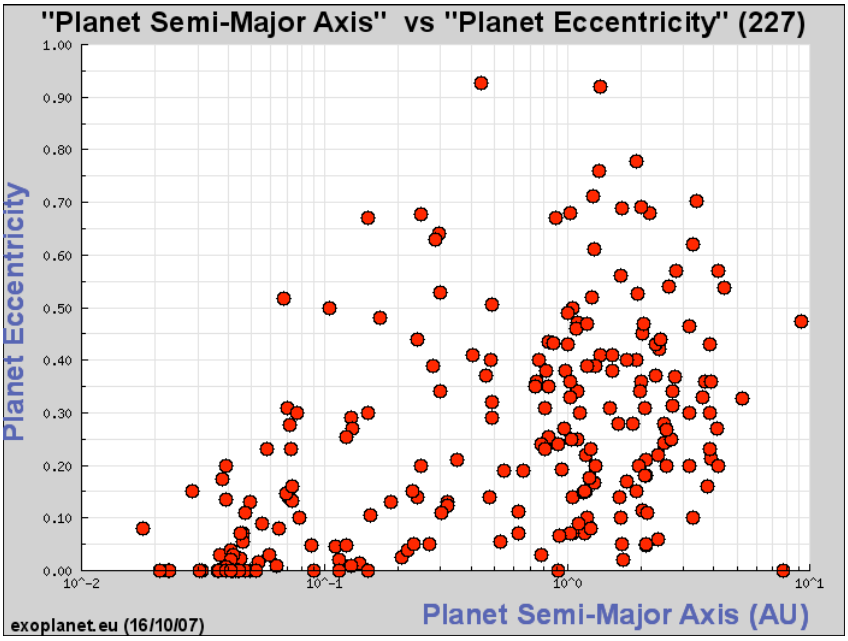

Figure 2.1: Eccentricity vs. the logarithm of semi-major axis for a sample of 227 exoplanets. The eccentricity of the orbit tends to decrease with decreasing orbital distance and close-in exoplanets are found on circular or nearly circular orbits. (Source: The Extrasolar Planets Encyclopaedia, www.exoplanet.eu)

The synchronisation timescale reaches values comparable to the age of the Sun ($\sim 4.5 \times 10^9$ years) between 0.18 AU and 0.19 AU. It is therefore likely that even at these distances the rotation rate of an EGP is considerably slower than that of Jupiter and that the deviation from synchronisation should be slight. It should be noted, though, that the synchronisation process is much more complicated than the above rather simplistic argument implies. For instance, atmospheric circulation can maintain a permanent and potentially significant offset from pure synchronisation even at very close orbital distances [Showman and Guillot, 2002]. However, in the absence of more accurate information, rotational synchronisation for close-in EGPs remains a good first approximation. In thermospheric modelling it is particularly appropriate because the radiative timescale in the upper atmosphere is relatively short. This implies that forcing is mainly due to the uneven stellar heating instead of circulation-related phenomena or turbulence. In these circumstances small asynchronous deviations should not have a significant impact on the general nature of the thermosphere.

Figure 2.2 points to an interesting correlation between planet occurrence and the metallicity of the host star. It appears that metal-rich stars are more likely to harbour giant planets. This correlation was noted early on when the first planets were discovered and it has become statistically stronger as the sample of planets has increased [Udry and Santos, 2007]. The fact that planet occurrence appears to correlate with metallicity supports the core accretion model of giant planet formation as this theory predicts that higher metallicity leads to enhanced planet formation due to the availability of small particle condensates that are the building blocks of planetesimals [Marcy et al., 2005, Udry and Santos, 2007].

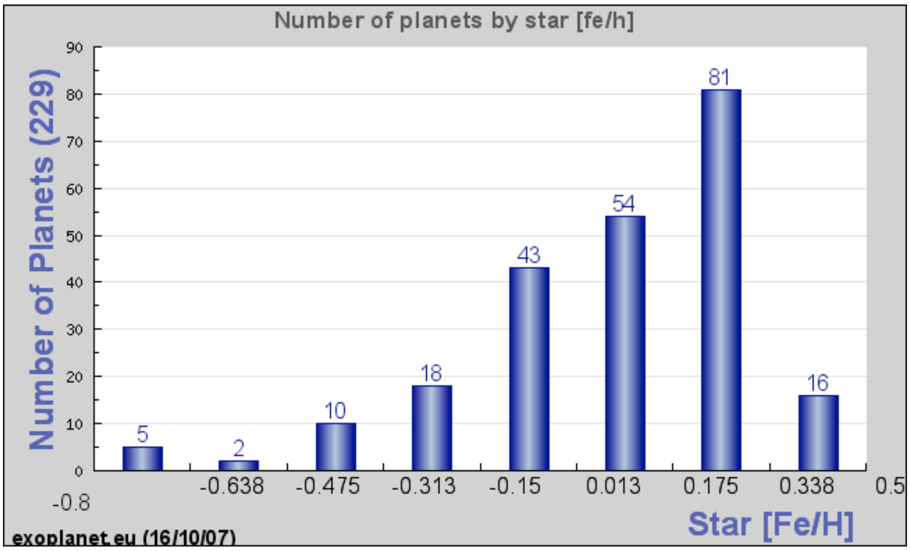

Figure 2.2: Planet occurence vs. the metallicity of the host star in units of Fe/H for a sample of 229 exoplanets. Note that Fe/H = 0 indicates solar metallicity. The figure illustrates that a higher than solar metallicity is favourable, although not a prerequisite, for planet formation. (Source: The Extrasolar Planets Encyclopaedia, www.exoplanet.eu)

One of the problems associated with the traditional core accretion models is that the predicted growth time of a gas giant (5-10 Myr) is longer than the observed lifetime of circumstellar (T Tauri) disks, estimated at $\sim$ 3 Myr. This problem may be solved by including migration and disk evolution in the models. As giant planet embryos migrate in towards the host star, they sweep through fresh gas-rich regions and this enhances the accretion of the gas onto the planet. New models that combine migration and core accretion predict formation timescales of $\sim$1 Myr, well within the constraints of disk lifetimes [Marcy et al., 2005, Udry and Santos, 2007].

Giant planets are expected to form beyond 3 AU from a solar-type host star where icy rock cores can form and accrete large amounts of cool gas. The embryos then migrate inwards at a rate of $\sim$10 AU Myr^{-1} (R.P.Nelson, *personal communication*). Two possible types of migration have been identified recently. Type I migration arises as a result of planets losing energy and angular momentum to the disk whereas Type II migration is driven by the gas in the disk accreting onto the host star and dragging any planets with it.

Some core accretion models predicted migration even before any exoplanets were found. In the past, giant planet migration could not be confirmed by observations of the solar system but now, it is firmly supported by exoplanet statistics. In the current sample of planets, most EGPs orbit much closer than 3 AU from their host stars. Icy rock-cores cannot form at these distances, and thus the planets must have migrated inwards from farther out orbits after they were formed. Further evidence comes from the fact that resonances indicative of migrational settling have been observed in some of the known multi-planet systems.

2.2 Transiting Planets

The first planet observed transiting its host star was HD209458b [Charbonneau et al., 2000]. As stated before, transiting planets play an important role in advancing our understanding of the rapidly growing sample of extrasolar planets. The detection of transits, first of all, confirmed that the observed radial velocity variations were indeed due to planets. Also, transit observations enable a more accurate characterisation of the planets than radial velocity data and they even allow us to probe the composition and thermal structure of the atmospheres of these planets.

The probability of detecting transits is highest for close-in EGPs. Thus most of the transiting planets orbit within 0.1 AU, and quite a few of them are found within 0.05 AU. Orbiting at such close-in distances, these planets typically have very short orbital periods. The stellar irradiation falling on these planets is far more intense than anything experienced on solar system planets, and they are also affected by the strong tidal forces between the star and the planet. Indeed, the proximity of the host star raises important questions about the stability of these exotic worlds.

As an illustration, Figure 2.3 displays the in-transit light curve of HD209458b measured through the red Johnson R filter [Charbonneau et al., 2000]. The transit is clearly visible, producing a 1.6 % flux decrement in the spectrum of the system. The shape and amplitude of the decrement depend on the radius of the planet, the radius and mass of the star, limb darkening on the star, and the orbital inclination. The stellar parameters can be deduced from theory and observations, and once these are known, best-fit values for the radius of the planet and the inclination of the orbit can be calculated. The mass of the planet can then be calculated by making use of the radial velocity data. Recent analysis of Hubble Space Telescope (HST) observations of HD209458b yields a radius of 1.32 R_J, an inclination of 86.677 degrees, and a mass of 0.69 M_J for the planet [Knutson et al., 2007b]. These values imply an average density of 372 kg m^{-3}, which confirms that HD209458b is a gas giant primarily composed of hydrogen and helium. It should be noted that before transit observations, there were no means of definitely confirming that close-orbiting giants were gaseous.

A multitude of new transit observations, including detailed spectroscopy, have allowed for considerable progress to be made recently in characterising close-in EGPs. Both transmission and occultation spectroscopy can be used to probe the atmospheres of transiting planets. The altitude at which the atmosphere first becomes opaque to tangential rays from the star depends on the wavelength of the incoming radiation. Thus the in-transit flux decrement is wavelength-dependent and spectroscopically active species in the atmosphere can significantly influence the transmission spectrum sampled at different wavelengths [Brown, 2001]. A deeper transit in some wavelength band compared to adjacent bands then implies absorption by some species in the atmosphere.

During secondary eclipse, as the planet passes behind the star, there is an observable dip in the infrared spectrum of the system. This is because the planet is heated by the absorption of stellar radiation, and some of the absorbed energy is reradiated in the thermal infrared. A comparison of the eclipse spectrum and the out-of-eclipse spectrum thus yields an estimate of the photospheric temperature

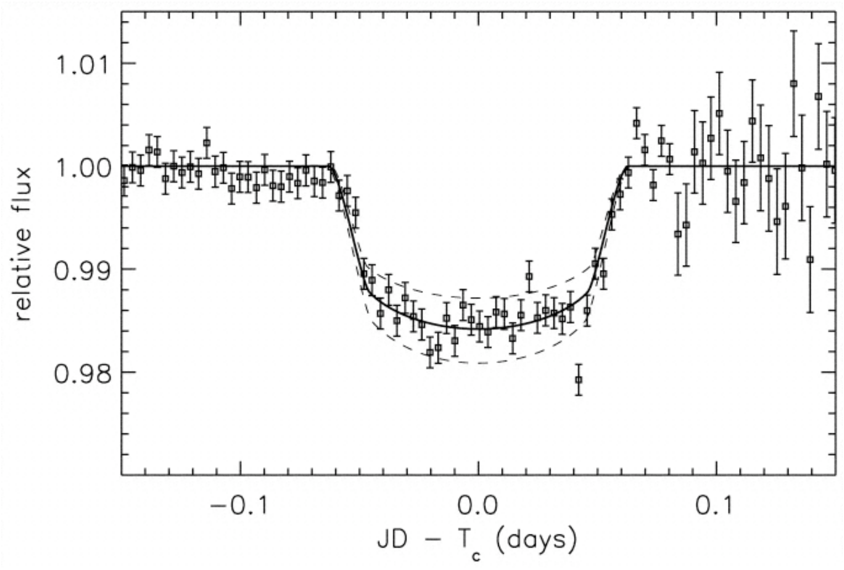

Figure 2.3: Transit light curve in the Johnson R band for HD209458b. The increased scatter after the transit is due to increasing air mass [Charbonneau et al., 2000].

of the planet and provides clues to the composition of the atmosphere. More recently, combined infrared observations at different phases of the orbit have produced estimates of horizontal temperature variations and the degree of redistribution of the absorbed energy by atmospheric circulation.

2.3 Exoplanet Atmospheres

As mentioned earlier, a remarkable surge of new observations has shed light on the previously evasive Hot Jupiters. The interplay of these observations and different models has ensured that the study of EGP atmospheres is now a very rapidly advancing field. Section 2.3.1 summarises some of these observations, while section 2.3.2 deals with some of the models of EGP atmospheres. The remainder of this chapter concentrates on the upper atmospheres of EGPs, the subject of my investigation.

2.3.1 Observations

Charbonneau et al. [2002] reported the first detection of an extrasolar planet atmosphere. They used the Space Telescope Imaging Spectrograph (STIS) onboard HST to observe four transits of HD209458b and detected an $\sim$0.02 % absorption in the region of the sodium resonance doublet near 589.3 nm. They concluded that this feature was due to absorption by sodium in the planet's atmosphere. They also found that the transit depth was shallower than the signature predicted by a standard solar composition, cloudless chemical equilibrium model of the atmosphere. They suggested that this discrepancy could be explained by a high cloud deck, situated at $\sim$0.37 mbar pressure, that would obscure part of the signal, or depleted sodium abundance (to $\sim$0.01 % of the solar value). Depletion of sodium occurs if atomic sodium combines into molecules that are then sequestered from the atmosphere as condensates or if much of the sodium is ionised by UV radiation from the star. It is also possible that the metallicity of the host star was much lower than solar at the time of planet formation, as this could lead to a depleted sodium abundance in the atmosphere of the planet.

The detection of sodium was followed by the detection of atomic hydrogen on HD209458b. Vidal-Madjar et al. [2003], also by using STIS, observed a 15 % in-transit absorption of the stellar Lyman α line (at 121.567 nm), produced by atomic hydrogen in the atmosphere of the planet. This absorption corresponds to an occultation by an object of 4.3 R_J (or 3.3 R_p), indicating that the planet is surrounded by an extended upper atmosphere composed mainly of atomic hydrogen. Most of the hydrogen should be ionised as the lifetime of atomic hydrogen against photoionisation by stellar XUV radiation is only of the order of few hours.

HD209458b is located only 9.5 R_{Sun} away from the (solar-type) host star and thus the extended atmosphere is affected by stellar gravity. The Roche lobe, which determines the sphere of influence of planetary gravity, is limited to 2.7 R_p. Filling up of the Roche lobe would only produce a 10 % absorption in the Lyman α line, implying that some hydrogen must be escaping the atmosphere. Also, the observed absorption is blueshifted, with Doppler velocities ranging from 0 to 130 km s^{-1}. The current explanation for this feature is that the escaping hydrogen is repelled away from the system by stellar radiation pressure, resulting in a cometary tail. However, this explanation has been questioned by Holstrom et al. [2008] and others who argue that radiation pressure is not sufficiently powerful to explain the high velocity tail of the absorption line (see Section 5.5).

Based on a simple model of the thermosphere, Vidal-Madjar et al. [2003] derived a minimum escape rate of 10^{10} g s^{-1} for HD209458b. Various other models indicate that such evaporation is possible in the upper atmosphere heated by stellar XUV radiation, as the intense heating will drive fast hydrodynamic escape from the planet [eg. Lammer et al., 2003, Yelle, 2004, Tian et al., 2005, García Muñoz, 2007, Koskinen et al., 2007a]. This behaviour is in marked contrast to solar system giants that have relatively thin, gravitationally bound and stable atmospheres.

Vidal-Madjar et al. [2004] also reported the detection of ionised carbon (C II) and neutral oxygen (O I) in the atmosphere of HD209458b. The absorption strengths imply that these species are present in the escaping, upper atmosphere. This is controversial, because under molecular diffusion conditions heavy species should fall off under gravity much faster than lighter species and thus they should not be present in the thermosphere in significant quantities. Turbulent mixing cannot explain their presence either because the Doppler velocity spread of the absorption is higher than that produced by oxygen and carbon brought up by eddy diffusion at the estimated upper atmospheric temperature of 10,000 K. If the observations are accurate, they are best explained by hydrodynamic escape, which allows the escaping hydrogen to drag heavier species up from the lower atmosphere with it and produces a velocity dispersion of at least 10 km s^{-1}.

The nature of the upper atmosphere on HD209458b has been further constrained by the detection of 0.03 % absorption by atomic hydrogen in the region of the Balmer jump and continuum (near 364.6 nm), reported by Ballester et al. [2007]. Modelling indicates that such absorption can be produced in a layer 1000 km thick, located at an altitude of 8500 km, and with a temperature of 5000 K. This layer is caught between the cooler lower atmosphere, composed mainly of H_2, and a hotter escaping part, composed mainly of H and H^+. Also, the evaporating nature of the atmosphere is supported by recent observations of two transits, performed with the HST Advanced Camera for Surveys (ACS), that imply deeper absorption in the Lyman α line compared to the visible range [Ehrenreich et al., 2008].

The above observations are based on transmission spectroscopy during the primary transit of the planet. Spectroscopy during the secondary eclipse can be used to probe the thermal characteristics of the atmosphere at the photospheric altitude, where most of the planetary thermal emission originates. The *Spitzer* space telescope has been instrumental in performing such spectroscopy on EGPs in the infrared. The first measurements of infrared light from an EGP were reported nearly simultaneously by Deming et al. [2005b] and Charbonneau et al. [2005]. Deming et al. [2005b] used the Multiband Imaging Photometer (MIPS) on *Spitzer* to observe the secondary eclipse of HD209458b through the 24 μm channel while Charbonneau et al. [2005] used the Infrared Array Camera (IRAC), also on *Spitzer*, to observe the secondary eclipse of another close-in EGP, TrES-1, through the 4.5 and 8.0 μm channels. Both groups used the timing of the secondary eclipses to determine the orbital eccentricities of the two planets and confirmed that both have circular orbits, as expected for close-in EGPs.

The observed 24 μm flux from HD209458b implies a brightness temperature of 1130 K. It should be noted that this value is not necessarily equivalent to the effective temperature of the planet at the photospheric level, given by [Marley et al., 2007]:

$$T_{eff} = T_\star(\frac{R_\star}{2a})^{\frac{1}{2}}[f(1-A)]^{\frac{1}{4}} + \frac{L_{int}}{4\pi R_p^2 \sigma} \tag{2.2}$$

where a is the orbital distance of the planet, A is the Bond albedo, i.e. the fraction of reflected radiation to total intercepted radiation, $R_\star$ and $T_\star$ are the radius and effective temperature of the star, L_{int} is the internal heat flux, σ is the Stefan-Boltzmann constant, R_p is the radius of the planet at the photospheric level, and the factor f parameterises the level of redistribution of heat by circulation. If $f = 1$ reradiation is isotropic, and if $f = 2$, reradiation is from the dayside only. The effective temperature can be quite different to the brightness temperature at 24 μm depending on the nature and composition of the atmosphere. Measurements at shorter wavelengths are required for a realistic estimate of the effective temperature. Once such estimates are available, a value for the Bond albedo can be calculated from the above equation and the internal heat flux can also be estimated.

TrES-1 is another transiting planet that orbits a K0V star at a distance of 0.039 AU with a period of ∼3 days. Its mass is 0.61 M_J and its radius is 1.08 R_J. For this planet, Charbonneau et al. [2005] derived brightness temperatures of 1010 K and 1230 K at 4.5 μm and 8.0 μm, respectively, and deduced an effective temperature of 1060 K from these two data points. By using equation (2.2) and assuming isotropic re-emission, they obtained a Bond albedo of ∼0.31. The discrepancy between the two brightness temperatures suggests a deviation from blackbody emission. Such deviations can be used to analyse the composition of the atmosphere. In particular, the emergent spectra of Hot Jupiters in the IRAC bandpasses is expected to be dominated by water and carbon monoxide features.

In addition to HD209458b and TrES-1, infrared flux estimates in the various *Spitzer* wavelength bands also exist for three other transiting planets: HD189733b, HD149026b and GJ436b. Also, phase-dependent infrared light curves have been obtained for HD209458b, HD189733b, HD179949b, 51 Peg b, and υ And b. Relative variations in these light curves depend on the horizontal temperature differences at the photospheric level and can thus be used to study the redistribution of heat and circulation on the planets.

Out of these planets, HD189733b has now become a well-known target, especially after water vapour was detected in its atmosphere [Tinetti et al., 2007]. It is a gas giant planet orbiting a K1-K2 star very close-in at 0.03 AU with a period of 2.22 days. Its mass is 1.15 M_J and its radius is 1.16 R_J. Deming et al. [2006] used the Infrared Spectrograph (IRS) onboard *Spitzer* to observe thermal emission from the planet in the 16 μm band. They reported a flux of ~660 μJy in this wavelength band, and deduced a brightness temperature of 1117 K, a value that is very similar to those derived for HD209458b and TrES-1.

HD149026b was observed by Harrington et al. [2007] with IRAC on *Spitzer* during secondary eclipse in the 8 μm band. HD149026 is a G0 star and the planet orbits it at 0.042 AU with a period of 2.88 days. The radius and mass of the planet are 0.73 R_J and 0.36 M_J, respectively. The eclipse depth at 8 μm is unexpectedly large, with a brightness temperature of ~2300 K. Harrington et al. [2007] point out that the strong infrared emission implied by this observation is matched by a zero-albedo, local blackbody model with a substellar temperature of 2500 K, and an effective temperature of 2200 K. This model assumes instantaneous re-emission, and thus implies negligible redistribution of heat by circulation. An alternative explanation for the deep eclipse is thermal emission from an inversion layer that resembles the stratosphere on Earth. Emission from water vapour at 8 μm, associated with the temperature inversion, could create a high dayside temperature while the effective temperature remained consistent with uniform redistribution of the absorbed stellar energy around the planet. The presence of an inversion layer would necessarily imply the presence of strong absorbers in the upper atmosphere (such as TiO or VO, for instance). In this context, it is interesting to note that evidence for stratospheric water emission from HD209458b was recently obtained by Knutson et al. [2008].

Orbiting an M-dwarf at 0.029 AU with a period 2.64 days, GJ436b is the most exotic of the known transiting planets. Deming et al. [2007] and Demory et al. [2007] recently reported *Spitzer* observations of the planet in the IRAC 8 μm band, taken during both the primary transit and secondary eclipse. The radius and mass of the planet are 4.33 R_E and 0.07 M_J. The radius is slightly larger than that expected for an ocean planet, and thus the planet is probably surrounded by a small hydrogen-helium envelope, placing it in the 'Hot Neptune' class of objects. The secondary eclipse data implies a brightness temperature of 712 K and, based on eclipse timing, Deming et al. [2007] derived an orbital eccentricity of $e = 0.15$. The large eccentricity does not agree with equation (2.1), and this implies that the planet is driven out of circularisation by an ongoing gravitational perturbation provided by another, unseen planet in the system.

Extended infrared spectra, as opposed to single band measurements, have been obtained for two exoplanets, HD209458b and HD189733b. Richardson et al. [2007] observed the secondary eclipse of HD209458b with *Spitzer* IRS and extracted the contrast spectrum (F_{planet} / F_{star}) between 7.5 and 13.2 μm. They conclude that the spectrum is essentially flat, apart from a broad emission feature centred at 9.65 μm and a sharp emission feature spanning only a few wavelength channels centred at 7.78 μm. They point to the possibility of a stratospheric temperature inversion, and note that the 9.65 μm feature could be due to stratospheric silicate clouds. In this context, it is interesting to note that the presence of such high altitude clouds is also suggested by the low sodium abundance observed by Charbonneau et al. [2002], an upper flux limit for CO bands [Deming et al., 2005a], and the absence of water vapour absorption near 2.2 μm [Richardson et al., 2003].

Swain et al. [2008a] analysed the same raw data as Richardson et al. [2007] by using a more sophisticated data reduction technique for the IRS instrument. In addition to the contrast spectrum, they also derived the absolute spectrum of HD209458b between 7.46 and 15.25 μm. This is the first determination of an absolute emission spectrum for any exoplanet. They derived a broad band eclipse depth of 0.315 % and argue that it implies significant redistribution of heat from the dayside to the night side. Overall, the analysis reveals a relatively smooth spectrum, dominated by thermal emission over most of the wavelength range. However, between 7.5 and 8.5 μm, there is evidence for one broad spectral feature centred at 8.1 μm, which could be due to absorption, and one narrow feature around 7.7 μm, which could be due to either absorption or emission, depending on wavelength and the baseline trend assumptions. Swain et al. [2008a] find no evidence for the 9.65 μm 'silicate' feature proposed by Richardson et al. [2007], and the evidence for the 7.78 μm feature is only tentative. The spectral modulation between 7.5 and 8.5 μm suggests that the dayside P-T profile of the atmosphere is not entirely isothermal. Also, it is interesting to note that neither the analysis of Richardson et al. [2007] or Swain et al. [2008a] was able to confirm the presence of water vapour absorption predicted by atmospheric modelling at wavelengths shortward of 10 μm.

Burrows et al. [2005] proposed that the *Spitzer* data points for HD209458b [Deming et al., 2005b] and TrES-1 [Charbonneau et al., 2005] are best interpreted with atmospheres containing water and carbon monoxide, but due to the limited data set such a conclusion could not be confirmed with adequate rigour. Knutson et al. [2007b] used HST STIS to observe primary transits of HD209458b between 290 nm and 1030 nm and used the data to refine the orbital parameters for the planet. Barman [2007] analysed this data and argued that the observed fluxes between 0.8 and 1 μm could be explained by water vapour absorption. The absorption features supposedly present in the spectrum were predicted by a model of the transmission spectrum that assumes a cloud-free atmosphere with solar elemental abundances, properly treats gravitational settling of grains in the atmosphere and includes full redistribution of heat by atmospheric circulation. Further, he argued that the inclusion of photoionisation of sodium and potassium in his model explains the low sodium abundance observed by Charbonneau et al. [2002]. Interestingly, these proposals do not include the presence of high altitude clouds. Such clouds are inconsistent with the upper limit for the albedo of the planet, which is relatively low [Rowe et al., 2006]. With significant cloud cover at high altitude the reflectivity should be higher.

The presence of water vapour signatures in the primary transit data, while they are absent in the secondary eclipse spectra, can be explained by strong circulation at the photospheric level. Circulation produces a nearly isothermal P-T profile in the dayside of the planet, masking out signatures from the infrared spectrum. The transmission spectrum is not affected, however, and thus the claims put forward by Barman [2007] are not in disagreement with the infrared spectra. However, Tinetti et al. [2007] disagree with his analysis on the basis that it is based on the lowest flux region of the spectrum, which suffers from the largest systematic error arising from edge effects on the STIS detector array. Tinetti et al. [2007] themselves claimed the first definite detection of water vapour in the atmosphere of another exoplanet, HD189733b.

Knutson et al. [2008] point to an altogether different explanation for the absence of water vapour absorption in the infrared spectrum of HD209458b. They observed thermal emission from the planet simultaneously in the IRAC 3.6, 4.5, 5.8 and 8.0 μm bands, which should be dominated by water vapour and carbon monoxide signatures. They pointed out a peak in flux centred around 5.8 μm and, intriguingly, significantly higher flux at 4.5 μm compared to the 3.6 μm channel. Models predict a trough between 3.6 μm and 8.0 μm arising from absorption by water vapour, and higher or comparable fluxes at 3.6 μm to the 4.5 μm bandpass. Knutson et al. [2008] argue that water vapour signatures are present in their data between 4 μm and 8 μm, but in emission. This emission, they propose, arises from a stratospheric inversion layer, which could also explain the (questionable) emission features observed by Richardson et al. [2007].

Cowan et al. [2007] have constrained the nature of photospheric circulation on HD209458b by observing the system at eight different orbital phases in the IRAC 3.6, 4.5 and 8.0 μm bandpasses. Their data was completely polluted by instrumental effects at 3.6 and 4.5 μm and the 8 μm data exhibited considerable scatter, but it still allowed them to derive a lower limit of 32 % for redistribution of heat by circulation. This limit was updated by Knutson et al. [2008] who note that together with their measurements at 8 μm, it implies that the night side flux is at least 60 % of the dayside flux. This in turn implies that the atmosphere of HD209458b is affected by strong circulation, which would support the idea that the infrared spectrum is washed out by an isothermal dayside P-T profile.

The spectrum of HD189733b between 7.5 and 14.7 μm was measured by Grillmair et al. [2007] with IRS onboard *Spitzer*. This spectrum is essentially flat, and consistent with blackbody emission. The absolute fluxes for several wavelength bands in the spectrum appear to be consistent with the 16 μm flux measured by Deming et al. [2006]. A comparison of the spectrum with a model of HD189733b by Burrows et al. [2006] implies that strong day/night differences in the atmosphere are unlikely, and that redistribution of heat by circulation is efficient. Also, absorption by water vapour blueward of 8.2 μm is absent in the data. As on HD209458b, this could be due to strong circulation and a nearly isothermal P-T profile in the dayside of the planet.

Knutson et al. [2007a] used IRAC to monitor the HD189733 system through the 8 μm bandpass for about half of the planet's orbit, covering both the primary transit and secondary eclipse. They deduced hemispheric minimum and maximum fluxes corresponding to 8 μm brightness temperatures of 973 K and 1212 K, respectively. The minimum occurred 6.7 hours after the primary transit while the maximum occurred 2.3 hours before the secondary eclipse. Thus the flux maximum is shifted 30 degrees longitude east from the substellar point, and the flux minimum is shifted 30 degrees longitude west from the anti-stellar point. The observations indicate that photospheric winds advect a significant fraction of the absorbed energy and that, intriguingly, the temperature minimum and maximum are located on the same hemisphere.

Fortney and Marley [2007] point out that the 8 μm flux measured by Knutson et al. [2007a] is not consistent with the short-wavelength part of the Grillmair et al. [2007] spectrum. Instead, it appears to be consistent with a downturn due to water vapour absorption predicted for this region. This dicrepancy between the two data sets could arise from instrumental differences between IRAC and IRS. Fortney and Marley [2007] suggest that the published IRS spectrum does not reflect the true spectrum shortward of 10 μm. By using a one-dimensional model of HD189733b that includes absorption by water vapour, they were able to match the 8 μm [Knutson et al., 2007a] and 16 μm [Deming et al., 2006] data points. Also, their models match the IRS spectrum of HD209458b [Richardson et al., 2007] reasonably well. Based on this, they claim that water vapour absorption is present in the atmospheres of both HD209458b and HD189733b.

As mentioned earlier, the presence of water vapour on HD189733b was also detected by Tinetti et al. [2007] who analysed the primary transit observations of Beaulieu et al. [2008] at 3.6 and 5.8 μm, and Knutson et al. [2007a] at 8 μm. Modelling indicates that this data is consistent with absorption by water vapour in the atmosphere. The authors acknowledge possible problems with the IRS instrument [Fortney and Marley, 2007] but ascribe the the lack of water absorption signals in the secondary eclipse observations to strong circulation.

The detection of water vapour by Tinetti et al. [2007] appears to be confirmed by recent observations of Swain et al. [2008b]. They used the NICMOS camera onboard the HST to measure the transmission spectrum of HD189733b between 1.4 and 2.5 μm during primary transit. The H_2O absorption band centred around 1.9 μm is evident in the spectrum, and the adjacent 1.5 μm band is probably also present. However, a steep change in absorption at 2.2 μm indicates that the observations cannot be explained by water absorption only. Modelling implies that the spectrum is consistent with the presence of methane in the atmosphere. The best fit to the data is achieved by a model, which has a mixing ratio of $\sim$5.0 $\times 10^{-4}$ for water, less than 5.0 $\times 10^{-5}$ for methane, and 1.0 $\times 10^{-5}$ for ammonium in the pressure range of a few mbar to 0.2 bar. The detection of methane is controversial because thermochemical models tend to indicate that the dominant carbon-bearing molecule in the atmospheres of Hot Jupiters should be carbon monoxide. It should be noted, though, that CO can still be included in the analysis of Swain et al. [2008b] up to the abundance of water without significantly worsening the best fit model.

Pont et al. [2008] observed HD189733b during three transits with the ACS camera onboard the HST, and derived the transmission spectrum of the planet between 550 and 1050 nm. Surprisingly, the spectrum is featureless and the predicted strong absorption lines due to sodium, potassium and water in this wavelength region are absent. The authors propose that the absence of these features is due to the absorption of the stellar flux by a haze of condensates at high altitude in the atmosphere of HD189733b. This is essentially the same explanation as has been put forward for the lower than expected sodium absorption in the atmosphere of HD209458b [Charbonneau et al., 2002]. Pont et al. [2008] also propose that high-altitude hazes or clouds inject heat at high altitudes by scattering stellar radiation, and could produce a temperature inversion in the upper atmosphere.

In contrast to Pont et al. [2008], Swain et al. [2008b] argue that their spectrum in the 1.4-2.5 μm region is haze-free. They point out that if aerosols are present, they must consist of small particles and only affect wavelengths shorter than 1.5 μm. Also, recent observations performed by Redfield et al. [2008] appear to contradict Pont et al. [2008] head-on. Redfield et al. [2008] measured the transmission spectrum of HD189733b between 500 and 900 nm. They observed the planet over the course of a year during 11 in-transit and 25 out-of-transit visits by using the High Resolution Spectrograph (HRS) on the 9.2 m Hobby-Eberly Telescope (HET) in Texas. The Na I doublet is fully resolved in the spectrum, and the authors claim that excess absorption is evident in the in-transit spectrum for both lines of the doublet. In the spectral region of 588.7-589.9 nm, which is the same as that defined by Charbonneau et al. [2002], they measure an excess absorption of ~0.067 % compared to the adjacent spectrum. This absorption is 3 times as large as that derived for HD209458b. Such strong absorption by sodium is consistent with an isothermal P-T profile in the atmosphere. The cores of the sodium lines extend to the altitude of about 1.06 R_p and they appear to be blueshifted from the stellar line centre by ~38 km s^{-1}. The authors point out that this may be due to a combination of planetary orbital motion and winds blowing from the dayside to the night side in the atmosphere of the planet.

Different observations of HD189733b appear confusing and, at times, contradictory. Some of this is no doubt due to instrumentation and the different data reduction and analysis methods adopted by different researchers. However, much of the confusion may arise from the nature of the HD189733 system itself. The star HD189733 is variable to the percent level and it has a strong magnetic field. There is also strong evidence for starspots on its surface [Pont et al., 2007], and these can influence both the transmission and secondary eclipse spectra, introducing features into the data that can be confused with planetary signals. It is important that any observations of HD189733b are treated with caution and that the data reduction and analysis are performed with rigour. Researchers should not add to the confusion by attempting to publish their results hastily as soon as possible in order to achieve the glory of exclusivity or first detections associated with their name. If not for anything else, the researchers should show restraint for the sake of ignorant PhD students.

In addition to HD209458b and HD189733b, attempts have been made to constrain the nature of photospheric circulation on 51 Peg b and HD179949b [Cowan et al., 2007], and υ And b [Harrington et al., 2006]. None of these planets transit their host stars, and thus their exact orbital parameters are not known. For these systems, only relative variations in the emitted infrared fluxes at different orbital phases can be analysed as absolute fluxes or star-planet contrasts cannot be determined. 51 Peg b orbits a Sun-like star at 0.052 AU, HD179949b orbits an F-type star at 0.045 AU, and υ And b orbits an F-type star at 0.059 AU. The observations of Cowan et al. [2007] were corrupted at 3.6 and 4.5 μm, but the 8.0 μm fluxes imply efficient redistribution of heat on 51 Peg b, while on HD179949b circulation appears to be less important. Harrington et al. [2006] measured the phase-dependent infrared light curve for υ And b centred at 24 μm. This light curve is consistent with a significant diurnal temperature contrast and implies very little horizontal advection of heat.

Judging by the observations, atmospheric dynamics and temperature profiles seem to vary significantly between different close-in EGPs despite the fact that the external circumstances of these planets appear quite similar. The observations of HD149026b, HD179949b, 51 Peg b, and υ And b imply that horizontal advection of heat is negligible. However, these observations are limited in scope, and affected by different uncertainties. In particular, light curve analysis for non-transiting planets is unlikely to be completely reliable. On the other hand, the majority of observations seem to suggest that horizontal advection is important on both HD209458b and HD189733b. Also, the flux measurement for HD149026b can be made consistent with efficient redistribution if there is a stratosphere-like temperature inversion in the upper atmosphere of the planet. Evidence for such an inversion has been obtained for HD209458b and the jury is still out on whether a similar inversion is possible on HD189733b. As HD209458b and HD189733b are both transiting planets, and they have been observed during several campaigns, they may indicate a general trend for Hot Jupiters despite contradictory evidence from more uncertain observations and interpretations.

2.3.2 Models

The previous section highlights the interplay between observations and their interpretation through model fitting. Atmospheric modelling, and thus the description of the expected signals, is of vital importance in interpreting the results of transmission or secondary eclipse spectroscopy. As the examples here show, uncertainties related to the models result in uncertainties in the interpretation of the observations. On the other hand, with the aid of models a simple transit or thermal emission signal can yield much more stringent constraints on the nature of the atmosphere than simply providing the identification of an absorbing or emitting species.

Reliable models of EGP atmospheres, and their composition, are a necessary prerequisite for accurate modelling of EGP spectra. At present, most of the synthetic spectra presented in the literature are based on chemical equilibrium models [Marley et al., 2007]. In general, these models assume solar elemental abundances [eg. Anders and Grevesse, 1989] and calculate the equilibrium composition by minimising the Gibbs free energy in the system by allowing common elements to combine into molecules [eg. Mandl, F., 1988]. Such models include thermochemical data for hundreds of different gas-phase and condensed-phase species.

The equilibrium composition depends on the pressure and temperature of the surrounding atmosphere. The pressure-temperature (P-T) profile, on the other hand, depends strongly on the transfer of radiation through the atmosphere. Thus chemical equilibrium models must be coupled to a radiative transfer scheme and a self-consistent solution must be sought iteratively. Most of the coupled models are one-dimensional and assume that the atmosphere is relatively thin, which justifies the use of planar geometry. A three-dimensional model, that would simultaneously account for chemistry, transfer of radiation and advection of matter and energy by circulation, would be very complex mathematically and computationally expensive. Some degree of simplification is thus necessary in present modelling efforts.

Early work on the synthetic spectra and atmospheres of EGPs was based on an analogy with brown dwarfs. P-T profiles generated for isolated brown dwarfs were used to calculate atmospheric compositions for various EGPs and the results were used to simulate the spectra of reflected starlight from these planets [eg. Marley et al., 1999]. This approach neglected irradiation by the host star and thermal emission from the planet itself [Sudarsky et al., 2003].

The photospheric region of brown dwarf atmospheres is relatively thin compared to the size of these objects, and as they are heated exclusively by internal luminosity, horizontal pressure and temperature variations should be negligible. Thus spherically symmetric, planar models are ideally suited for modelling the spectra of brown dwarfs. However, on close-in EGPs stellar irradiation is much more significant than internal luminosity, which arises from slow gravitational contraction. In addition, close-in EGPs are rotationally synchronised, and the resulting uneven heating should produce strong horizontal temperature and pressure variations between the day-and night sides. This should lead to vigorous global circulation that effectively redistributes energy around the planet and can result in non-equilibrium chemistry. Thus the analogy with brown dwarfs is of limited value.

Stellar irradiation and thermal emissions from the planet may have a drastic impact on the atmosphere and emergent spectra of EGPs. Radiative-convective models of irradiated planets, such as have been developed for solar system giants, are clearly more suitable than brown dwarf models for the task of modelling EGP atmospheres and increasingly, the new generation of EGP models are based on such models. However, even these models are still one-dimensional. In fact, the expansion to three dimensions seems to require additional simplifications that would be unacceptable for the purposes of coupled radiative transfer and chemical equilibrium simulations.

In order to facilitate studies of the significance of atmospheric circulation, models of meteorology on EGPs are required. Very recently, many groups have undertaken the task of developing three-dimensional dynamical atmospheric models for close-in EGPs such as HD209458b [eg. Showman and Guillot, 2002, Cho et al., 2003, Burkert et al., 2005, Cooper and Showman, 2005, Cho et al., 2008, Dobbs-Dixon and

Lin, 2008]. Apart from Burkert et al. [2005] and Dobbs-Dixon and Lin [2008], these models are based on a numerical solution of the primitive equations (see Section 1.2). Burkert et al. [2005] solve the Navier-Stokes equations in 2D for an axisymmetric, tidally locked atmosphere and Dobbs-Dixon and Lin [2008] solve the full Navier-Stokes equations in 3D without assuming hydrostatic equilibrium. All of these models assume a fixed composition and utilise simple approximations to the radiative transfer problem. In general, they simulate the photospheric level, where most of the thermal emission originates, which ranges from the surface level to ∼2 mbar pressure.

Lower atmosphere circulation varies wildly from one model to the other, and the results seem to depend strongly on the modelling approach and the level of approximation. However, it is possible to identify some broad characteristics of circulation that all models agree on. The differences to solar system giants are notable. For instance, on Jupiter and Saturn, due to their relatively large separation from the Sun, the intrinsic heat flux is comparable to the total heat flux and thus convection in the interior greatly affects the atmosphere. Indeed, the convective zone (troposphere) in their atmospheres extends to the visible cloud layer at 1.0 bar pressure. In contrast to this, the strong irradiation on the atmospheres of close-in EGPs should produce a stable radiative zone that extends down to 100–1000 bar [Showman et al., 2007].

Showman and Guillot [2002] point out that even if close-in EGPs are tidally locked, rotation plays a central role in controlling the nature of the circulation. The Coriolis force affecting the flow pattern arises from synchronous rotation of the planet around its axis and the magnitude of the force is determined by the orbital period. For instance, HD209458b has a period of ∼3.5 Earth days and this corresponds to an angular rotation rate of 2.1×10^{-5} s^{-1}, compared to ∼1.7×10^{-4} s^{-1} for Jupiter.

The Rossby number measures the importance of rotation for atmospheric dynamics, and it is given by [Holton, 2004]:

$$Ro = \frac{u}{fL} \tag{2.3}$$

where $f = 2\Omega \sin\phi$ is the Coriolis parameter with ϕ being the latitude (see equation 1.32), u is the mean horizontal wind speed, and L is the typical atmospheric length scale. The Rossby number is simply the ratio of nonlinear advective acceleration to the Coriolis acceleration. For planetary-scale winds ranging from 100–1000 m s^{-1}, which may or may not be realistic for planets like HD209458b, Showman and Guillot [2002] obtain Rossby numbers of 0.03–0.3. This implies that advective terms are small and that the pressure gradient terms in the momentum equation are primarily balanced by the Coriolis force (in meteorology this situation is commonly known as geostrophic balance).

On Jupiter, circulation is characterised by several, narrow zonal bands. Cho and Polvani [1996] point out that this circulation can be interpreted as a dynamical equilibrium state of a stably-stratified shallow layer of turbulent fluid constrained on a rotating sphere. In such a stratified, rotating fluid turbulent eddies merge and grow. This growth is restricted in the meridional direction by the Coriolis force that acts as a restoring force, while it is unrestricted in the zonal direction. Rhines length is a measure of the width of the resulting zonal bands, and it is given by:

$$k_\beta = (\frac{u}{\beta})^{1/2} \tag{2.4}$$

where $\beta = 2\Omega \cos\phi / R_p$. Another measure of the zonality of the flow is the Rossby deformation radius, which is given by:

$$L_D = \frac{NH}{f} \tag{2.5}$$

where N is the frequency of the buoyancy oscillations, H is the atmospheric scale height, and f is the Coriolis parameter. Turbulent eddies and vortices often have sizes comparable to this radius. Showman and Guillot [2002] point out that for wind speeds above 400 m s^{-1} the Rhines length scale for HD209458b exceeds the planetary radius and the deformation radius is ~40000 km. This allows eddies to grow on hemispheric scales, producing global scale circulation instead of several bands or local small-scale features.

Geostrophic balance allowed Showman and Guillot [2002] to use simple analytical expressions to estimate the magnitude of mid-latitude wind speeds on HD209458b near the 1.0 bar level. The geostrophic wind depends on the gradient of the geopotential on isobaric surfaces (ref. equation 1.32) and thus it is related to the horizontal temperature gradient by the thermal wind equation [Holton, 2004]:

$$f \frac{\partial \mathbf{v}_g}{\partial lnp} = -R\mathbf{k} \times \nabla_p T \tag{2.6}$$

where $\mathbf{v}_g$ is the horizontal wind. Showman and Guillot [2002] use the energy equation (1.9) to obtain a rough estimate of the horizontal temperature variation for two different scenarios, one in which radiative heating and cooling is balanced by horizontal advection and one in which is balanced by vertical advection. The heating and cooling rates themselves are obtained by allowing the radiative equilibrium temperature profile to be perturbed by dynamics. At the 1.0 bar level, they obtain diurnal temperature differences ranging from 500 K to 800 K and wind speeds of 2–3 km s^{-1}. The build-up of winds faster than ~3 km s^{-1} is suppressed by the onset of Kelvin-Helmholtz shear instabilities. It is possible that such instabilities play a role in the atmosphere of HD209458b. Shear instability arises from turbulence overtaking buoyancy and thus it threatens the stable stratification of the atmosphere.

By using the Explicit Planetary Isentropic Coordinate (EPIC) model, Showman and Guillot [2002] also produced three-dimensional, time-dependent numerical simulations of HD209458b. The EPIC model is a GCM based on solving the primitive equations (ref. Section 1.2.4). These simulations allow for the study of 3D circulation in detail around the planet, but unfortunately they often include a number of rough approximations. For instance, computational constraints prevent GCMs from being coupled to accurate radiative transfer and chemical models and thus approximate heating and cooling schemes must be adopted. In addition, global models often rely on coarse grids that cannot properly account for various atmospheric wave motions and small-scale turbulence that can have a significant impact on the resulting circulation and these processes must therefore be parameterised very roughly.

Showman and Guillot [2002] parameterise the heating and cooling rates by adopting the Newtonian thermal relaxation scheme. This scheme assumes that the solution to the radiative transfer equation is dominated by the cooling-to-space terms, while interaction between different layers and the surface level is negligible. In radiative equilibrium, the net heating rate within a layer in the atmosphere vanishes. If the layer is displaced from its position by circulation, it will experience net heating or cooling that attempts to bring it into radiative equilibrium with its new surroundings [Salby, 1996]. The Newtonian scheme accounts for dynamics by relaxing the temperature at a given position towards a prescribed equilibrium temperature profile. This approximation is only valid if the temperature perturbation at a given point is small compared to the equilibrium temperature at that point. Also, the timescale for advection must be much shorter than the radiative timescale or the method becomes equivalent to simply imposing an assumed equilibrium temperature profile on the simulations. The validity of the Newtonian scheme for HD209458b and other similar planets is certainly questionable as large diurnal temperature differences may result from strong uneven heating. Also, as Showman and Guillot [2002] point out, the timescale for advection becomes comparable or longer than the radiative timescale between 1.0–0.1 bar.

The circulation resulting from Newtonian forcing depends on the assumed radiative-equilibrium temperatures. Showman and Guillot [2002] assume a diurnal radiative-equlibrium temperature difference of 100 K. Under advection, this results in an eventual day-night temperature difference of 50 K. Due to the unrealistically shallow diurnal temperature gradient, the quantitative results they obtain are likely to be unreliable, but they may still provide some hints to the qualitative behaviour of the circulation. The authors note that, as expected, jets and vortices grow on the global scale and the circulation is dominated by an eastward circumplanetary jet along the equator and two global-scale vortices. The eastward winds are expected to shift the highest temperature 'hot spot' away from the substellar point by about 60 degrees longitude, an effect that could potentially be verified by phase-dependent observations in the infrared.

An alternative approach is offered by Cho et al. [2003, 2008]. They model the atmosphere of HD209458b as a hydrostatically balanced, frictionless gas under the influence of the Coriolis force and gravity by using the adiabatic shallow-water equations [Salby, 1996]. This approach assumes equivalent barotropy, which implies that surfaces of constant pressure, density and potential temperature can be taken to share a common horizontal structure [Salby, 1989]. In this case the 3D primitive equations can be integrated vertically and reduced to a set of 2D equations for a shallow layer of turbulent fluid that can be solved numerically. The reduced computation time allows for a substantially finer horizontal grid and as a result the model captures turbulent phenomena from large to small spatial scales, well below full 3D models. Similar models have been used succesfully to reproduce the basic features of circulation on solar system giants, where turbulence and convection play a dominant role in driving circulation patterns.

The primary motivation for using the equivalent barotropic formulation is to demonstrate the influence of turbulent eddies and waves on the large-scale flow rather than an accurate representation of the day-night heating contrast. The simulations seem to confirm the general observation that eddies and vortices grow on the global scale, simply producing a few broad jets. Otherwise the results are very different to those presented by Showman and Guillot [2002]. The equatorial jet tends to flow westward instead of eastward and the simulations produce time-variable polar vortices, with maximum and minimum temperature spots revolving around the poles. Unfortunately these simulations do not provide an independent estimate for the day-night temperature variation or wind speeds as the characteristic wind speed and the amplitude of hemispheric thermal forcing are free parameters.

It is questionable if the use of shallow-water, adiabatic equivalent-barotropic formulation is appropriate for close-in EGPs, where circulation is likely to be strongly affected by uneven stellar heating and 3D features such as vertical acceleration or shear instabilities. Instead of including diabatic heating in their present model, Cho et al. [2008] parameterise the effect of radiative heating by varying the elevation of the lower bounding surface of the modelled layer and the layer thickness so that initially mass flows away from the substellar point. The rather exotic nature of the predicted circulation from these models may well be an artefact of the rather strict set of assumptions that lead to the shallow-water equations and the adiabatic setting. It should be noted that diabatic versions of the equivalent barotropic equations exist [eg. Salby, 1989], but in those the included diabatic heating must be such that it preserves the equivalent barotropic stratification in the atmosphere.

Yet another approach to the circulation problem was developed by Burkert et al. [2005]. Their work concentrates on isolating the influence of atmospheric opacity to radiation on the mean flow and diurnal temperature differences. They assume that circulation on tidally locked planets is axisymmetric, and solve the Euler equations for continuity, momentum and energy on a 2D grid involving the vertical and zonal directions. While this approach ignores the Coriolis forces, it does not assume hydrostatic equilibrium.

Burkert et al. [2005] use a more realisitic radiative transfer scheme by calculating the radiative flux at each layer according to flux-limited radiative diffusion, which depends on the Rosseland mean opacity. However, in order to simulate stellar heating they impose an equilibrium temperature profile at the upper boundary of the grid, and assume a diurnal temperature difference of ~1100 K for HD209458b. This is much more realistic than 100–200 K adopted by Showman and Guillot [2002] and Cho et al. [2003, 2008] for their circulation models, but the radiative transfer scheme is still not self-consistent.

The main opacity sources in gas giant atmospheres are likely to include ice-coated silicate grains at temperatures below the ice evaporation limit at ~170 K and grains composed of silicates, amorphous carbon and iron at higher temperatures. For their standard model Burkert et al. [2005] calculate Rosseland mean opacities assuming the interstellar grain size distribution and solar metallicity and these values are then varied in other simulations.

At the photospheric level, where the optical depth $\tau = 2/3$, the resulting diurnal temperature difference is ~700 K and there is a steep drop in temperature accross the terminator. The winds flow from the dayside to the night side, converging at the anti-stellar point, with a maximum speed of ~3.5 km s^{-1}.

At deeper depth a return flow to the dayside develops, producing a simple circulation cell. This picture, however, is likely to be oversimplistic as rotation is ignored.

Enhanced metallicity with respect to solar values results in higher opacity. Multiplying the standard opacity by 100 shifts the photosphere to a higher altitude and produces a steeper horizontal temperature gradient with lower night side temperatures. Correspondingly the winds are faster, and supersonic winds of $\sim$5 km s^{-1} are produced.

Opacities can also be reduced with respect to the standard case by settling, coagulation and evaporation. Reduced opacity shifts the photosphere to lower altitudes, where pressure and density are higher. As a result the diurnal temperature difference is less pronounced and wind speeds are lower. If the opacity is reduced by a factor of 1000, the photosphere shifts to the region of the westward return flow and the maximum wind speed is reduced to less than 1 km s^{-1}. Burkert et al. [2005] note that the work of Showman and Guillot [2002] assumes an opacity even lower than this, and still their results seem to be quite different from the low opacity case. Burkert et al. [2005] ascribe the discrepancy to the errors arising from adopting the Newtonian cooling approximation.

Cooper and Showman [2005] developed their circulation model based on the work of Showman and Guillot [2002] and thus it is also based on numerical integration of the three-dimensional primitive equations and uses the Newtonian relaxation scheme. In order to model stellar insolation, they adopted a simple angular distribution of equilibrium temperatures based on the radiative-equilibrium model of Iro et al. [2005]. They treat the diurnal temperature difference as a free parameter, and assume values ranging from 1000 K at the top of the atmosphere (at 0.01 mbar) to $\sim$500 K at 10 bar.

At pressures near 2 mbar, they find that the circulation has strong zonal and meridional components and that the winds tend to flow from the dayside to the night side. Curiously the wind speed exceeds 9 km s^{-1} at high latitudes, which implies a highly supersonic circulation regime. The primitive equations may not be suitable for modelling such a regime. Also, Showman and Guillot [2002] have shown that shear instabilities arise from such strong winds. In addition, due to the short radiative timescale in the upper layers, the Newtonian relaxation scheme is unlikely to be valid at such low pressures.

Deeper down, near the photospheric altitude at 220 mbar, the results are likely to be more accurate, although radiative timescales are still relatively short. The simulations exhibit a broad equatorial eastward, super-rotating jet with maximum wind speed reaching $\sim$4 km s^{-1}. The hot spot is swept 60 degrees downstream from the substellar point. This shift, predicted by both Showman and Guillot [2002] and Cooper and Showman [2005], has not been observed on the known transiting planets so far. The 8 μm light curves of HD209458b [Cowan et al., 2007, Knutson et al., 2008] imply strong circulation, but details are yet unknown. For HD189733b, the corresponding light curve [Knutson et al., 2007a] indicates that the 'hot spot' is shifted downstream by $\sim$ 30 degrees longitude, but the flux minimum is also shifted westward from the anti-stellar point and the models cannot account for this feature. In addition, the light curve for υ And b [Harrington et al., 2006] does not support strong circulation at all.

Dobbs-Dixon and Lin [2008] developed the approach of Burkert et al. [2005] further by extending the

2D axisymmetric calculations to three dimensions, without the assumption of hydrostatic equilibrium. In many ways their simulations of HD209458b are very interesting, as they do not constrain the stratification of the atmosphere. They indicate that a sharp drop in temperature between the dayside and the night side persist along the terminator. This is despite the Coriolis force now included in the model. The steep gradient produces fast winds reaching $\sim$4 km s^{-1} near the terminators. At the surface altitude the winds retain a day-night tendency, although the eastward-flowing material seems to be directed from mid-latitude regions into an eastward equatorial jet that faces westward flow from the dayside near the dawn terminator. At high latitudes on the night side, westward flow dominates, and this flow is pushed towards the poles by the Coriolis force. The authors confirm the variations due to changing opacities that were introduced by Burkert et al. [2005]. They also note that reducing the opacity significantly from solar-based values allows circulation to start shifting the 'hot spot' away from the substellar point, as suggested by Cooper and Showman [2005].

The above discussion shows that circulation models for EGPs produce different results, even qualitatively. To make things worse, available observations of transiting planets are not yet accurate enough to discriminate between different models. Thus there is considerable uncertainty over the nature of circulation on EGPs and even its driving mechanism. This is unfortunate as circulation can have a significant impact on the spectrum of EGPs.

Compared to brown dwarfs at similar temperatures, the P-T profiles of EGP atmospheres are expected to be more isothermal. In particular, the dayside P-T profile near the photospheric altitude can become isothermal as a result of strong circulation [eg. Cooper and Showman, 2006, Fortney et al., 2006a, Dobbs-Dixon and Lin, 2008]. As we have already learned, such isothermality would effectively suppress emergent spectral features in the infrared and produce a blackbody-type thermal spectrum.

In general, the nature of the emergent spectrum depends on the composition of the atmosphere at different altitudes, and the composition depends strongly on temperature and moderately on pressure [Sudarsky et al., 2003]. The most important minor species in EGP atmospheres are expected to be methane (CH_4), water (H_2O), ammonia (NH_3), carbon monoxide and molecular nitrogen (N_2). Many of these species have been observed in Jupiter's atmosphere (see Section 1.3). At high temperatures chemical equilibrium models favour CO over CH_4 as the main carbon repository. If the temperature is constant and the pressure varies, CH_4 is favoured over CO at high pressure. N_2 is expected to be the main nitrogen carrier at high temperatures. At constant temperature, NH_3 is favoured at high pressure.

Most chemical equilibrium models predict that CO should be the main carbon carrier in the visible atmosphere of close-in EGPs [eg. Sudarsky et al., 2003, Cooper and Showman, 2006, Fortney et al., 2006a]. It is thus interesting that attempts to detect it on HD209458b have failed, despite the fact that the resolution and the predicted fluxes should make it possible [Richardson et al., 2003, Fortney et al., 2006a, Deming et al., 2005a]. There are a number of possible reasons for the non-detection. First, CO may not be abundant in the atmosphere, although this would be surprising. The planet would have to be much cooler than previously thought, and that is not supported by the infrared flux measurements.

Second, the spectral signature of CO may be flattened by an isothermal P-T profile on the dayside [Fortney et al., 2006a] or by clouds and hazes [Deming et al., 2005a, Cooper and Showman, 2006]. In this context the detection of methane and possibly of ammonia on HD189733b is surprising [Swain et al., 2008b]. It indicates that we may not yet properly understand the chemistry of EGP atmospheres.

Other molecular species expected to be present in EGP atmospheres include TiO and VO that form at temperatures greater than 2000 K and have been observed in M dwarf stars and brown dwarfs. TiO and VO could be responsible for stratospheric heating on HD209458b and other EGPs, although it is not clear how they would survive at high altitudes where they should condense and fall to deeper layers [Fortney et al., 2006b].

Alkali metals like sodium and potassium are important for brown dwarfs and modelling implies that they are significant absorbers in close-in EGP atmospheres. This has been confirmed by the detection of sodium in the atmosphere of HD209458b [Charbonneau et al., 2002] and the possible detection on HD189733b [Redfield et al., 2008]. Lithium, rubidium and cesium should also be present, but in much lower quantities. Sulphur is expected appear in the form of H_2S and phosphorus should be present as PH_3.

Contrary to stellar atmospheres, where gaseous species dominate, condensation and gravitational settling alter the equilibrium composition significantly. Heavier components such as silicon, magnesium, calcium, aluminium and iron tend to condense into compounds that 'rain out' from the outer layers of the atmosphere. Condensate species expected to be present in EGP atmospheres include methane and water clouds, NH_4SH clouds (see Section 1.3), silicates like forsterite (Mg_2SiO_4) and enstatite ($MgSiO_3$), iron or other iron-rich compounds, and aluminium and calcium compounds. Also, photochemical processes can produce stratospheric hazes composed of polyacetylene and other aerosols.

Sudarsky et al. [2003] calculated equilibrium compositions and resulting infrared spectra for EGPs under different irradiation conditions and used their results to classify EGPs based on their composition. They calculated P-T profiles by using a one-dimensional, planar radiative transfer model assuming minimum redistribution of heat by circulation. In order to calculate the absorption and scattering of radiation through the atmosphere, they included absorption by gaseous atoms and molecules, Rayleigh scattering, and absorption and scattering by condensates and clouds. They identified five distinct classes of EGPs, and their P-T profiles together with the condensation curves for the principal condensates are shown in Figure 2.4.

Their results indicate that EGPs with orbital distances of at least a few AU should be similar to Jupiter. The dominant gaseous species, after hydrogen and helium, should be methane and ammonia. As noted in Section 1.3, ammonia ices condense in the upper atmosphere and water clouds should settle in the deep atmosphere. The spectrum is dominated by reflected stellar light as temperatures are too low for significant infrared emissions. Planets found orbiting between 1.0 and 2.0 AU are characterised by tropospheric water clouds. Their effective temperatures remain below 250 K. Absorption features due to water, methane and ammonia are expected, and the water clouds reflect light in the visible and

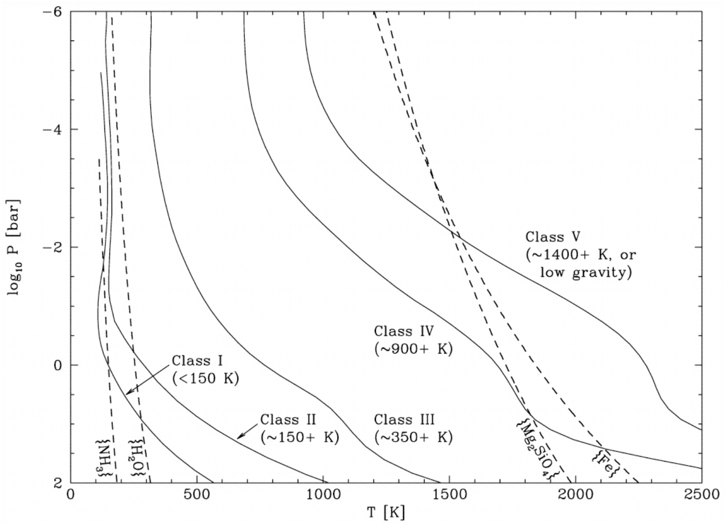

Figure 2.4: Temperature-pressure (P-T) profiles for five classes of EGPs and condensation curves for ammonia, water, silicates and iron. The cloud bases are expected to be found at the intersection of the P-T profile and the condensation curves. EGPs have been classified according to their effective temperatures, assuming dayside re-emission only [Sudarsky et al., 2003].

near-IR wavelengths.

Between 0.2 AU and 1.0 AU, EGP atmospheres should be almost purely gaseous. The equilibrium temperatures range from 350 to 800 K, and thus the planets are too warm for water to condense in the atmosphere while they are still too cool to produce silicate and iron condensates. The infrared spectrum should be dominated by water and methane absorption, while ammonia absorption is becoming less significant. Sodium and potassium lines should appear, albeit with modest intensities. Due to lack of cloud cover, one should expect very low albedos.

Between 0.1 and 0.2 AU atmospheric temperatures are around 1000 K, with a decreasing trend towards the upper atmosphere. CO takes up much of the carbon in the atmosphere and the alkali metal abundance is significantly higher than on further-out planets. Both CO and methane absorption are present in the spectrum and water absorption remains strong. Silicate and iron clouds form at pressures higher than 10 bar without having an influence on the visible atmosphere.

Hot Jupiters orbiting around 0.05 AU are under extreme stellar irradiation and their equilibrium temperatures can be over 1400 K. CO is expected to be the main carbon repository, as mentioned earlier, and both CO and water absorption should feature strongly in the infrared spectrum, unless features are washed out by some other effects. Interestingly, models indicate that iron and silicate clouds could form at high altitudes (5–10 mbar pressure).

Observations indicate that the presence of high-altitude clouds is certainly possible in the atmospheres of close-in EGPs, as has been pointed out in this section. However, the low geometric albedo measured for HD209458b [Rowe et al., 2006] seems to rule out silicate clouds composed of forsterite and enstatite

[Burrows et al., 2007]. It is interesting that HD209458b seems to fall more naturally in the gaseous class of EGPs with low albedo and modest sodium absorption rather than in the Hot Jupiter class.

Disequilibrium chemistry may be important on a number of EGPs. This can arise as a result of circulation, which affects composition not only through its influence on the temperature profile but also directly. If the typical timescale for dynamical mixing is shorter than the chemical equilibration timescale, chemical reactions do not happen fast enough to maintain equilibrium. In this case disequilibrium effects become important. For instance, horizontal and vertical winds can transfer gas that has reached equilibrium in one part of the atmosphere to regions where the equilibration timescale is much longer than the advection timescale, and this produces deviations from local equilibrium conditions. The enhanced CO abundance in Jupiter's lower troposphere is thought to be due to a similar effect, with CO being transported upwards by convection from deeper, hotter layers [Cooper and Showman, 2006]. Disequilibrium can also arise from photodissociation and photochemistry, which is important in the Jovian stratosphere and thermosphere and is likely to play a significant role in the atmospheres of close-in EGPs [eg. Liang et al., 2003, 2004, Yelle, 2004, García Muñoz, 2007]. In addition, impacts by meteorites and comets, and other inbound external matter can also affect the composition of giant planets.

In summary, the main sources of opacity in giant planet atmospheres are scattering and absorption by atoms, molecules and ionised species, Rayleigh scattering by atoms and molecules, and absorption and scattering by clouds, condensates and hazes resulting from photochemistry. Scattering and absorption by atoms and molecules in gaseous form is relatively easy to model, but the radiative properties of clouds and condensates are poorly understood. Modelling their influence on the P-T profiles and the emergent spectra is not straightforward and it usually involves some degree of parametrisation. Clouds and hazes are an old problem for climate models, where they usually act as the most prominent source of uncertainty. It is perhaps not suprising then that the current observations of close-in EGPs are not sufficient to conclusively establish or rule out the presence of clouds on these planets. This is precisely due to the difficulty of including them reliably in the models that are used to interpret the data.

2.3.3 The Upper Atmosphere

Reliable observations probing the upper atmosphere of a giant exoplanet only exist for HD209458b [Vidal-Madjar et al., 2003, 2004, 2008, Ehrenreich et al., 2008, Ballester et al., 2007]. As mentioned earlier, these observations indicate that the planet is surrounded by a large envelope of atomic hydrogen, which extends farther than ∼3 R_p, and escapes hydrodynamically with a minimum mass loss rate of 10 g s^{-1}. For this to be possible, the temperature in the upper atmosphere must be extraordinarily high, certainly in excess of 10,000 K. Lammer et al. [2003] investigated whether such high temperatures could be produced by the absorption of XUV radiation in the thermosphere. They estimated exospheric temperatures of EGPs by scaling calculated temperatures at Jupiter's exobase to different orbital distances around solar-type stars of different ages. These stars have variable XUV emissions with younger stars emitting more XUV radiation. Analogously to Earth, they assumed that the thermosphere is heated by stellar XUV radiation and that the absorbed energy is conducted downwards to the lower atmosphere where it is eventually reradiated. This approach neglects photochemistry, infrared cooling and thermospheric circulation, but it yields a handy scaling law for the temperature of the exobase:

$$\frac{(T_\infty - T_0)_p}{(T_\infty - T_0)_{Jup}} \approx \frac{I_{XUV}^{p} g_{Jup}}{I_{XUV}^{Jup} g_p} \tag{2.7}$$

where T_∞ is the exobase temperature, T_0 is the lower boundary temperature, I_{XUV} is the XUV intensity at the given orbital distance, and g is the gravitational acceleration, which depends on the radius and mass of the planet.

The resulting exospheric temperatures are shown in Figure 2.5. Within 1.0 AU from the host star these temperatures are significantly higher than the corresponding effective temperatures. For current solar XUV fluxes the simplified analysis yields temperatures well over 10,000 K within 0.3 AU from the star. Within this range evaporation is significant. The degree to which the upper atmosphere is liable to thermal escape is measured by the thermal escape parameter, given by [Hunten, 1973]:

$$\lambda = \frac{GM_p m}{kT_\infty r} \tag{2.8}$$

where k is the Boltzmann constant. This is simply the square of the ratio of the escape velocity to the most probable thermal velocity at the altitude of the exobase and as such it is an indicator of the proportion of particles that have sufficient thermal kinetic energy to escape the atmosphere. If $\lambda >1.5$, Jeans escape dominates. In this regime, the upwards-propagating high velocity tail of the locally Maxwellian velocity distribution escapes at the top of the thermosphere, and the escape flux is maintained by diffusion from below. Jeans escape is significant for $\lambda \leq 30$ and becomes negligible for values greater than that.

If $\lambda \leq 1.5$, the thermal kinetic energy becomes comparable to the gravitational potential energy at the exobase level. Most particles are then able to escape the atmosphere and the outer layers begin to drift out in bulk, generating fast hydrodynamic escape and vertical acceleration, which causes a breakdown in hydrostatic equilibrium. Such outflow can be modelled by using the vertical part of the Navier-Stokes equations for continuity, momentum and energy. In contrast, fluid modelling is not appropriate for Jeans escape. For stable atmospheres, the particle density in the exosphere is so low that the velocity distribution deviates significantly from a local Maxwellian. In this case higher order moments of the Boltzmann equations, derived from kinetic theory, must be adopted instead.

Lammer et al. [2003] point out that, indeed, the stellar XUV flux alone drives hydrodynamic escape from a planet such as HD209458b orbiting within ~0.3 AU from the host star. They used the energy-limited theory of Watson et al. [1981] to model the the expansion radius and evaporation rate of HD209458b and found that the upper atmosphere expands to ~3 R_p and loses mass at a rate of 5×10^{12} g s^{-1}. These results agree roughly with the observations presented by Vidal-Madjar et al. [2003].

The XUV fluxes of solar-type stars decrease over time as the star evolves along the main sequence. The *Sun in Time* program [Ribas et al., 2005] uses solar proxies and theoretical models to characterise

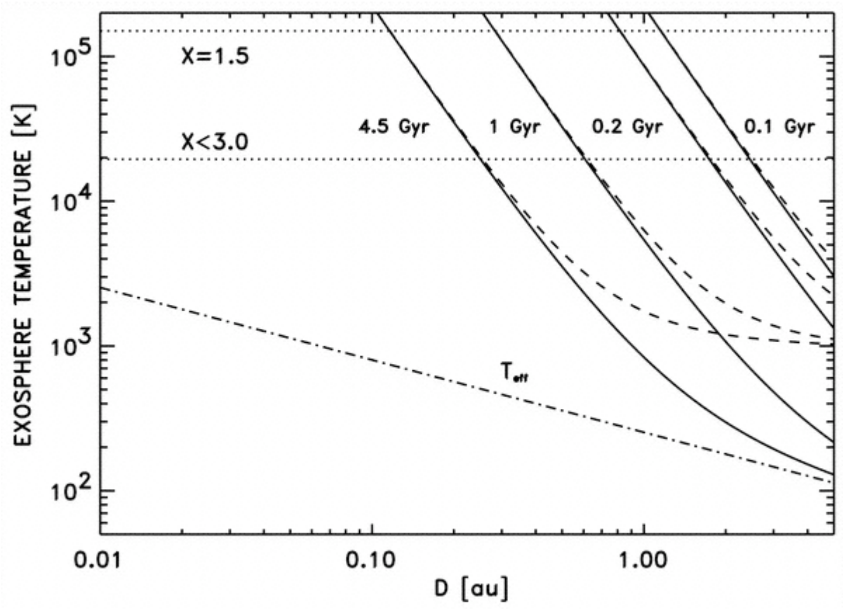

Figure 2.5: Scaled exobase temperatures for Jupiter-type EGPs at different orbital distances around solar-type stars of different ages. The dashed lines show temperatures from models that include XUV heating and an additional, constant heating source. The solid lines show temperatures from models that include XUV heating only. The dashed-dotted line shows the effective temperature. The parameter X is the thermal escape parameter (see text). [Lammer et al., 2003]

the evolution of the XUV fluxes emitted by the Sun between 0.1 and 170 nm. The results imply that the XUV fluxes from young solar-type stars are ∼112 times higher than the current solar fluxes during the first 100 Myr of evolution, and then steadily decreasing. This may have interesting consequences for giant planet evolution. Gas giants are thought to form between 5 AU and 20 AU from the host star, and they are then expected to migrate inwards at a rate of ∼10 AU Myr^{-1} (R.P.Nelson, *personal communication*). Figure 2.5 shows the exospheric temperatures for EGPs orbiting stars of different ages, based on the XUV fluxes from the *Sun in Time* program. The results indicate that close-in EGPs undergo hydrodynamic escape throughout their evolution as the limit for such escape moves in from ∼2.5 AU after the first 100 Myr of evolution.

The work of Lammer et al. [2003] is based on simple scaling, and it ignores photochemistry, possible infrared cooling, detailed energetics and circulation in the upper atmosphere. Yelle [2004] introduced a more sophisticated, one-dimensional model for the aeronomy of close-in EGPs. This model solves the one-dimensional equations of motion for planetary wind iteratively. It includes photoionisation and subsequent photochemistry, assuming reactions similar to those that take place in Jupiter's thermosphere. Vertical diffusion of both ions and neutrals is also included in the calculations. The model is particularly useful for studying ion chemistry and it accounts for infrared cooling from H_3^+ ions that may enhance the stability of EGP atmospheres.

The results from the model confirm that the absorption of stellar XUV radiation in the upper atmosphere of HD209458b is enough to drive hydrodynamic escape and inflate the outer layers of the envelope beyond 3 R_p. Due to thermal dissociation of H_2, the outer thermosphere is composed primarily of H and H^+, whereas the lower thermosphere is dominated by H_2. Consequently H_3^+ cooling is important in the lower thermosphere, but negligible in the hot outer layers. The temperature near the lower boundary of the model stays below 5000 K, but the temperature increases dramatically with altitude between 1.1 R_p and 1.25 R_p, reaching over 10,000 K in the upper thermosphere. These results were used to interpret the hydrogen Balmer continuum observations of Ballester et al. [2007], which is why they agree so well with the interpretation of the observations. The mass loss rate from the model is 4.7×10^{10} g s^{-1} [Yelle, 2004, 2006]. This agrees well with the lower bound of Vidal-Madjar et al. [2003] but, due to the inclusion of photochemistry, infrared cooling and a more sophisticated modelling approach, it is lower than the value calculated by Lammer et al. [2003].

Both Lammer et al. [2003] and Yelle [2004] ignore the tidal forces between the planet and the star. These arise from the difference between stellar gravity and the centrifugal force in the frame of reference of the orbiting planet. Near the Roche lobe the tidal forces alter the shape of gravity equipotentials of the planet from purely spherical to asymmetric elongated shapes. Lecavelier des Etangs et al. [2004] have shown that this leads to a new escape mechanism at intermediate temperatures between the Jeans escape regime and hydrodynamic escape, known as *geometrical blow-off.* It arises as the tidal forces pull material up from the thermosphere and fill the Roche lobe. Lecavelier des Etangs et al. [2004] used simple scaling laws to estimate the influence of both the tidal forces and XUV heating and concluded that the lifetime of HD209458b against evaporation should be between 10^{10} and 10^{11} years. Their calculations imply that the planet has lost 1-7 % of its mass during a lifetime of ~5 Gyr.

Tian et al. [2005] and García Muñoz [2007] have recently developed time-dependent, one-dimensional models of HD209458b and other close-in EGPs by solving the outflow equations with varying degree of assumptions and simplifications. Tian et al. [2005] obtain an escape rate of 1-10 × 10^{10} g s^{-1} for HD209458b, which agrees with the minimum mass loss constraint presented by Vidal-Madjar et al. [2003]. They simulated the Lyman α transit absorption explicitly and claim that the observations can be fully explained by a hydrodynamically escaping envelope of atomic hydrogen. They also point out that the atmosphere is stable under hydrodynamic escape as the planet loses only ~1 % of its mass in 6 Gyr and its lifetime against evaporation is ~10^{11} years. It should be noted, though, that their approach does not account for photochemistry or tidal forces.

García Muñoz [2007] developed a very comprehensive planetary outflow model that accounts for radiative cooling, photochemistry and various chemistry schemes including hydrocarbons, carbon and oxygen, and nitrogen and deuterium that may be important in the lower thermosphere. By considering the simple helium-hydrogen chemistry similar to that adopted by Yelle [2004, 2006], he obtains a mass loss rate of 6×10^{10} g s^{-1} for HD209458b, which agrees roughly with earlier studies and the observations. In terms of neutral and ion composition, his results are nearly identical to those of Yelle [2004].

Other studies have not considered the possibility that CII and OI are present in the upper atmosphere in significant quantities [Vidal-Madjar et al., 2004]. In order to explore the significance of carbon and oxygen chemistry, García Muñoz [2007] varied the heavy element abundances in the upper atmosphere and included a range of photochemical pathways from previous work on solar system giants. He noted that enhanced heavy element abundances (comparable to solar metallicity) lead to the dissociation of H_2 by reactions with oxygen, and this makes H the dominant species even in the lower thermosphere. Thus the formation of H_3^+ is prevented, and any H_3^+ that does form, is depleted in reactions with water and CO. The result is a hotter thermosphere and a higher mass loss rate of $\sim 5 \times 10^{11}$ g s^{-1}.

Hovever, these results may not be particularly realistic. García Muñoz [2007] adopted initial and lower boundary mixing ratios for CO, CH_4, H_2O, N_2 and HD from a chemical equilibrium model of Burrows and Sharp [1999]. They are based on solar elemental abundances and appropriate for the 1.0 bar level with a temperature of 1200 K. In the thermosphere, due to molecular diffusion, only trace amounts of heavy species are expected unless eddy diffusion is particularly effective in mixing the atmosphere. García Muñoz [2007] notes that if the initial mixing ratios are divided by 100 or 1000 to produce more realistic heavy element abundances, the basic hydrogen-helium chemistry is unaffected by the addition of heavier molecules. On the other hand, he also notes that only the enhanced abundances can explain the observed absorption strengths of carbon and oxygen. This leaves open the possibility that the hydrodynamically escaping hydrogen is bringing heavy elements up from the lower atmosphere, producing the required mixing ratios.

The study also accounts for tidal forces and, in contrast to Lecavelier des Etangs et al. [2004], the results imply that for a planet like HD209458b, tidal forces would be significant only at orbital distances less than 0.03 AU. In line with other studies, these results imply that HD209458b is stable against evaporation despite hydrodynamic escape.

It is not enough, however, to simply calculate mass loss rates to estimate the lifetime of a planet. Evaporation must be coupled to basic evolutionary models for a realistic description. This was done by Baraffe et al. [2004] who used escape rates similar to those of Lammer et al. [2003] to study the long-term response of the radius and mass evolution to evaporation in the atmosphere. They found that planets with an initial mass of formation lower than a certain critical mass, which depends on the timescale for gravitational contraction and the rate of mass loss, would evaporate entirely within 5 Gyr. Their calculations imply that HD209458b should be entering a critical stage of runaway evaporation now, although statistically this is extremely unlikely. The result is, however, based on a mass loss rate that is almost two order of magnitudes higher than those published by Yelle [2006], Tian et al. [2005], or García Muñoz [2007] and thus it should be taken with more than a pinch of salt.

Lecavelier Des Etangs [2007] recently published a diagram of the evaporation status of all EGPs known at the time. He assumed that all the XUV energy absorbed in the upper atmosphere powers vertical escape, and contrasted the heating rates with the total gravitational potential energy of the planets in order to estimate their lifetimes. He found no planets in the evaporation-forbidden region, in which their lifetimes would be less than 5 Gyr. This is despite the fact that his escape rates are almost certainly too high, as it is unlikely that all the absorbed XUV energy powers evaporation.

All of the models reviewed above are one-dimensional and many of them are subject to gross simplifications. For this thesis work, a need was identified to develop a three-dimensional model of the thermosphere and ionosphere for EGPs that would be capable of modelling radiative transfer, photochemistry and ion densities, neutral composition and thermospheric circulation in a self-consistent manner. The details of this model are presented in Chapter 3.

Simulations by this model show that infrared cooling from H_3^+ plays a significant role in the thermospheres of EGPs orbiting their host stars between 0.2 AU and 1.0 AU [Koskinen et al., 2007b]. The exospheric temperature for such planets ranges from 3000 K to 1500 K, respectively, and the thermal escape parameter attains values more than 70. This implies that evaporation even by Jeans escape is negligible. In this range of orbital distances, almost none of the absorbed energy is available to power escape, pointing to a potential flaw in the diagram published by Lecavelier Des Etangs [2007]. The stability of the thermosphere is determined by the coupling between the ionosphere and the neutral thermosphere, as the ion densities and thus radiative cooling and other mechanisms are sensitive to photochemistry, dynamics-driven composition and distribution of heat by circulation. Much of the detail involved in these processes is missed out by one-dimensional models.

Within 0.2 AU, thermal dissociation of H_2 becomes significant as the temperature in the upper thermosphere grows beyond 3000 K. At high temperatures, most of the upper thermosphere is rapidly converted into atomic hydrogen, much of which is quickly ionised, and this process leads to the loss of infrared cooling from H_3^+. Modelling led to the identification of a sharp stability limit for Jupiter-type EGPs orbiting a solar-type star between 0.14 AU and 0.16 AU [Koskinen et al., 2007a]. Within this limit the planet is surrounded by an inflated envelope of H and H^+, that extends to several planetary radii, and escapes hydrodynamically. This behaviour is in agreement with the predictions of Yelle [2004] and seems to agree at least qualitatively with the implications of the observations by Vidal-Madjar et al. [2003] and Ballester et al. [2007]. Outside the stability limit the atmosphere is relatively thin, cool and stable. Evaporation by Jeans escape in this region is negligible and has no impact on the radius or mass evolution. It should be noted that instability here refers to hydrodynamic escape from the upper atmosphere. Mass loss rates based on the model, that are presented in Chapter 5 of this thesis, are in line with other models [Yelle, 2004, 2006, Tian et al., 2005, García Muñoz, 2007], and they indicate that the planet loses only a small fraction of its mass during the main sequence lifetime of a typical host star.

Recently, the model was employed to simulate the upper atmosphere and ionosphere of HD17156b, which is a newly found transiting planet orbiting its G-type host star in a highly eccentric orbit (e $\sim$0.67) with an orbital semi-major axis of 0.16 AU. The planet moves from 0.26 AU at apastron to periastron at 0.052 AU during one 21.2 day orbit, undergoing a 27-fold variation in the incoming stellar flux. Despite the close-in periastron passage, modelling indicates that the atmosphere of the planet remains stable and, contrary to HD209458b, does not undergo hydrodynamic escape [Koskinen et al., 2008]. In the following chapters, these and other results will be discussed in much greater detail.

Chapter 3

The Model

3.1 Basic Equations

The model is based on a thermospheric GCM (TGCM) for Saturn [Smith et al., 2005, Müller-Wodarg et al., 2006] that has been modified to work for EGPs at different orbital distances. The original 'no frills' Saturn TGCM basically consists of a dynamical core for the neutral thermosphere and as such it can easily be generalised to any gas giant planet. However, it does not include any neutral or ion chemistry, it does not contain a magnetosphere and has no capability for modelling current systems or electric fields expected in the partly ionised region of the upper atmosphere. Some of these essential features have been incorporated into the model, which has then been used to simulate EGP thermospheres with the aid of some crude approximations. In the absence of detailed observations of upper atmospheric conditions on EGPs, this work is intended to provide a first-order understanding of some basic physical processes. This understanding can then be improved and extended by adding more relevant processes to the model and thus making it more physical. The results can then be compared to detailed observations that will hopefully be available in the future.

The model solves the 3D Navier-Stokes equations of continuity, momentum and energy by explicit time integration, assuming that the thermosphere is composed of H_2, H and He and that it is in hydrostatic equilibrium throughout. The basic equations of motion are solved on a non-inertial Eulerian, corotating spherical grid, using spherical pressure coordinates. The conversion of the Navier-Stokes equations into spherical pressure coordinates is performed by using the transformations presented in Section 1.1.5 and this conversion produces the primitive equations introduced in Section 1.2.4. The difference to lower atmosphere meteorology is that the thermospheric GCM includes transport of momentum and energy by molecular diffusion, which is important in the upper atmosphere. In general, the basic equations have been reviewed extensively and corrected in the model where necessary. Particular attention has been paid to the terms involving molecular viscosity and diffusion.

The pressure levels in the model are defined by

$$p_n = p_0 \exp[-\gamma(n-1)] \tag{3.1}$$

where p_0 is the lower boundary pressure, γ is the pressure level spacing (in units of one pressure scale height), and n is the pressure level index.

As stated before in Section 1.2.4, the continuity equation in the pressure coordinate system is

$$\frac{\partial \omega}{\partial p} + \nabla_p \cdot \mathbf{u} = 0$$

where $\omega = Dp/Dt$, the material derivative of pressure, and $\nabla_p \cdot \mathbf{u}$ is the divergence of the velocity vector evaluated on a constant-pressure surface.

The neutral horizontal momentum equation is given by

$$\frac{\partial \mathbf{u}}{\partial t} + (\mathbf{u} \cdot \nabla)\mathbf{u} = -\nabla_p \Phi - 2\Omega \times \mathbf{u} + \mathbf{F_v}$$

where Ω is the angular rotation rate of the planet, Φ is the gravitational potential energy, and all vector operations are converted into spherical pressure coordinates. The conversions and some of the momentum equation terms are presented in Appendix A. Following Achilleos et al. [1998], the frictional force due to viscosity, $\mathbf{F_v}$, is estimated as

$$(\mathbf{F_v})_i \approx \frac{\mu_m}{\rho} \nabla_P^2 u_i + \frac{g}{a^2} \frac{\partial}{\partial P}(a^2 \mu_m \rho g \frac{\partial u_i}{\partial P}) \tag{3.2}$$

where μ_m is the coefficient of molecular viscosity, ρ is the density of the neutral atmosphere, and a is the altitude of the pressure level. This approximation implies that horizontal variations of vertical velocity and any viscosity terms involving the divergence of the velocity vector are considered negligible. This is justified because these terms are much smaller than the other terms in the expression. The coefficients of molecular viscosity for H_2 and He are identical to those used in the Jovian ionospheric model (JIM) by Achilleos et al. [1998]. These values arise from parameter fits to experimental data. For H a fit presented in Banks and Kockarts [1973] that is based on analytical calculations was used. The values for H are technically not appropriate for temperatures higher than 1000–2000 K, but in comparison to other uncertainties, the error arising from their variations with temperature is unlikely to be significant even at higher temperatures.

The thermal state of the model is described by the following energy equation, which is an approximation to the pressure coordinate version of equation (1.30):

$$\frac{\partial \epsilon}{\partial t} + \mathbf{u} \cdot \nabla_p(\epsilon + \Phi) + \omega \frac{\partial(\epsilon + \Phi)}{\partial p} \approx \dot{Q}_{XUV} + \dot{Q}_{IR} + \frac{1}{\rho} K_m \nabla_p^2 T$$

$$+ \frac{g}{a^2} \frac{\partial}{\partial p}(a^2 K_m \rho g \frac{\partial T}{\partial p}) + \frac{g}{a^2} \frac{\partial}{\partial p}(a^2 u_\theta \mu_m \frac{\partial u_\theta}{\partial p} + a^2 u_\phi \mu_m \frac{\partial u_\phi}{\partial p}) \tag{3.3}$$

where $\epsilon = C_p T + E_{kin}$ is the specific enthalpy, Φ is the gravitational potential energy (per unit mass), $\dot{Q}_{XUV}$ is the heating rate (per unit mass) due to absorption of the stellar XUV radiation between 0.1

nm and 105 nm, $\dot{Q}_{IR}$ is the cooling rate due to IR emissions from H_3^+ ions, and K_m is the coefficient of molecular conductivity. The coefficients of molecular conductivity for H_2 and He are taken from Achilleos et al. [1998], while the coefficient for H is taken from Banks and Kockarts [1973]. The last term on the right-hand side describes the energy changes due to viscosity. In calculating the viscous heating term, the vertical velocity terms and any terms that arise from horizontal variations of velocity were ignored.

Eddy viscosity and eddy heat conduction were ignored in all simulations. There are currently no observations to constrain turbulent eddies on EGPs. The conventional picture is that eddy conduction leads to cooling of the upper thermosphere. However, eddy motion is driven by dynamical processes such as wind shear or dissipation of wave energy that act as a heat source. Hunten [1974] points out that the heating effect may be equal or even dominant compared to cooling by eddy conduction. As the model does not include heating due to dissipation of eddy and wave energy, it would not be consistent to include eddy conduction either. To the first approximation, it was assumed that eddy heating and cooling rates are comparable and balance each other [Smith, 2006].

3.2 Neutral Composition

As noted before, the model assumes that the thermosphere is simply composed of H_2, He, and H that are diffusively separated. In order to avoid complications and speculation, the complex photochemistry involving heavier molecules (eg. hydrocarbons) and radiative transfer in molecular vibrational bands that are, for instance, significant below and around Jupiter's homopause, were ignored. It should be noted that, as Chapter 2 implies, there is considerable uncertainty over the composition of EGP upper atmospheres near thermospheric altitudes, and the composition seems to depend on the orbital distance in a complex fashion. A detailed study of all possible lower boundary chemistry variations would be out of the scope of this thesis, and as a first-order approximation it does not seem appropriate to favour any particular scenario systematically in these simulations. Thus the calculations are most appropriate for the region above the homopause where it is safe to assume negligible mixing ratios for heavier molecules. The problem with this approach is, of course, that there is no data to constrain the location of the homopause on EGPs, and in some cases where the planets are affected by hydrodynamic escape, the whole concept of a homopause may be misplaced. On Jupiter, the homopause is situated roughly at the pressure of 1 μbar. In the absence of any other constraints, 2 μbar was adopted as the lower boundary pressure for most of the simulations, although this choice is largely arbitrary and one should keep in mind that the results near the lower boundary are likely to be affected by more complicated chemistry and energetics.

The basic equations of motion presented in Section 3.1 are coupled to species continuity equations that can be used to calculate the mass mixing ratios of individual neutral species. The continuity equation accounts for horizontal advection, convection, molecular and eddy diffusion, and neutral chemistry. For species i, the equation is given by [Müller-Wodarg et al., 2006]:

Table 3.1: Chemical reactions used by the model

Reaction	**Rate**[a]	**Reference**
1a. $H_2 + h\nu \rightarrow H_2^+ + e$	-	Yan et al. [1998]
1b. $H_2 + h\nu \rightarrow H^+ + H + e$	-	Chung et al. [1993], Dujardin et al. [1987]
1c. $H_2 + h\nu \rightarrow 2H^+ + e$	-	Dujardin et al. [1987]
2. $H + h\nu \rightarrow H^+ + e$	-	Hummer and Seaton [1963]
3. $He + h\nu \rightarrow He^+ + e$	-	Yan et al. [1998]
4. $H_2 + M \rightarrow 2H + M$	$1.5 \times 10^{-9} exp(-4.8e4/T)$	Baulch et al. [1992]
5. $2H + M \rightarrow H_2 + M$	$8.0 \times 10^{-33}(300/T)^{0.6}$	Ham et al. [1970]
6. $H^+ + H_2(\nu \geq 4) \rightarrow H_2^+ + H$	$1.0 \times 10^{-9} exp(-2.19e4/T)$	Yelle [2004]
7. $H_2^+ + H_2 \rightarrow H_3^+ + H$	2.0×10^{-9}	Thread and Huntress [1974]
8. $H^+ + H_2 + M \rightarrow H_3^+ + M$	3.2×10^{-29}	Kim and Fox [1994]
9. $He^+ + H_2 \rightarrow H^+ + H + He$	$1.0 \times 10^{-9} exp(-5700/T)$	Moses and Bass [2000]
10. $He^+ + H_2 \rightarrow H_2^+ + He$	9.35×10^{-15}	Anicich [1993]
11. $H_3^+ + H \rightarrow H_2^+ + H_2$	2.0×10^{-9}	Yelle [2004]
12. $H_2^+ + H \rightarrow H^+ + H_2$	6.4×10^{-10}	Kapras et al. [1979]
13. $H^+ + e \rightarrow H + h\nu$	$4.0 \times 10^{-12}(300/T_e)^{0.64}$	Storey and Hummer [1995]
14. $H_2^+ + e \rightarrow H + H$	$2.3 \times 10^{-8}(300/T_e)^{0.4}$	Auerbach et al. [1977]
15. $He^+ + e \rightarrow He + h\nu$	$4.6 \times 10^{-12}(300/T_e)^{0.64}$	Storey and Hummer [1995]
16a. $H_3^+ + e \rightarrow H_2 + H$	$2.9 \times 10^{-8}(300/T_e)^{0.65}$	Sundstrom et al. [1994]
16b. $H_3^+ + e \rightarrow H + H + H$	$8.6 \times 10^{-8}(300/T_e)^{0.65}$	Datz et al. [1995]

---

[a] Photoionisation rates are calculated explicitly by using the photoionisation cross sections given in the references. Two-body rates are given in cm^3s^{-1} and three-body rates are given in cm^6s^{-1}. The electron temperatures are assumed to be the same as neutral temperatures.

$$\frac{\partial Y_i}{\partial t} + \frac{u_\theta}{a}\frac{\partial Y_i}{\partial \theta} + \frac{u_\phi}{asin\theta}\frac{\partial Y_i}{\partial \phi} + \omega\frac{\partial Y_i}{\partial p} = \frac{g}{a^2}\frac{\partial}{\partial p}[a^2 \rho Y_i (w_i^D + w_i^K)] + J_i \tag{3.4}$$

where $Y_i = \rho_i/\rho$ is the mass mixing ratio, u_θ, u_ϕ and ω represent the mean velocity of the atmosphere, w_i^D is the molecular diffusion velocity, w_i^K is the eddy diffusion velocity, and J_i is the net chemical source rate. The only chemical reactions that affect neutral densities *directly* are thermal dissociation of H_2 and the reverse reaction, collisional recombination of two H atoms (see Table 3.1).

The molecular diffusion velocities are given by [Chapman and Cowling, 1970, Müller-Wodarg et al., 2006]:

$$d_i = \frac{\partial Y_i}{\partial z} - (1 - \frac{m_i}{m} - \frac{H}{m}\frac{\partial m}{\partial z})\frac{Y_i}{H} = -\sum_{i \neq j} \frac{m Y_i Y_j}{m_j D_{ij}}(w_i^D - w_j^D) \tag{3.5}$$

where m_i is the molecular mass of the ith constituent, m is the mean molecular mass of the atmosphere, and D_{ij} is the binary diffusion coefficient. Self-diffusion ($i = j$) is neglected and the binary diffusion coefficients for the pairs H_2-H, H_2-He and He-H are the same as those used by Müller-Wodarg et al. [2006]. For N species, equation (3.5) only results in $N - 1$ independent equations. Thus an additional constraint is required to solve the diffusion velocities for all N species. This constraint is the requirement that the net flow across horizontal surfaces due to molecular diffusion vanishes:

$$\sum_{i=1}^{N} Y_i w_i^D = 0 \tag{3.6}$$

These equations have been rearranged into a matrix equation for two species and solved consistently by using Cramer's rule.

The turbulent eddy diffusion velocity for species i is given by:

$$w_i^K = -K_\tau \frac{\partial \ln(Y_i)}{\partial z} \tag{3.7}$$

where K_τ is the eddy diffusion coefficient. The magnitude of K_τ determines the altitude of the homopause and depends on turbulent small scale motions. The nature of such motions on EGPs is highly uncertain and the value of K_τ is not well defined. In most of the simulations, $K_\tau = 0$ was used for consistency, but occasionally $K_\tau = 1.0 \times 10^3$ $m^2 s^{-1}$ was also adopted. The latter value is in line with the values deduced for solar system giants such as Jupiter and Saturn. A discussion of the effects of eddy diffusion is included in Section 4.6.5.

Similarly to molecular diffusion velocities, mass fractions are also solved only for $N - 1$ species from equation (3.4). The mass mixing ratio of the remaining (preferably, although not necessarily the dominant) species is then given simply by:

$$Y_N = 1 - \sum_{i=1}^{N-1} Y_i \tag{3.8}$$

3.3 XUV Heating

The primary heating mechanism is the absorption of stellar XUV radiation. The original model included the wavelength range of 5.0-105 nm. This has been extended to 0.1–105 nm, including the full energetic X ray spectrum. The photoabsorption, and ionisation cross sections of the neutral species for the whole range have also been updated. The total photoionisation cross sections for H_2 and He were calculated by using the formulae of Yan et al. [1998]. In order to work out the branching ratios for reactions 1a, 1b and 1c (see Table 3.1), fits to experimental data published by Chung et al. [1993] and Dujardin et al. [1987] were calculated, and the resulting formulae were used to calculate the appropriate cross sections. For H, an analytical result published by Hummer and Seaton [1963] was used. Also, at wavelengths longer than the ionisation limit for each species, photoabsorption cross sections presented by Moore et al. [2004] were adopted. The cross sections are listed in Appendix B. It should be noted that radiation longward of 105 nm was not taken into account. Thus, for instance, the Lyman α absorption within the thermosphere has been neglected. However, such radiation is not energetic enough to ionise H, H_2 or He, and absorption is of limited importance. Hence this omission is not likely to be significant, given that the heating is dominated by the energetic short-wavelength spectrum.

The model calculates the neutral mass heating rate by using a numerical approximation of

$$\dot{Q}_{XUV} = \frac{f_s}{\rho} \sum_{i=1}^{N} n_i(z) \int_{\lambda} F_{\infty} \exp[-\tau(z,\lambda,\chi)] \sigma_i(\lambda) d\lambda \tag{3.9}$$

where f_s is the efficiency factor, n_i is the number density of species i, σ_i is the photoabsorption cross section of species i, F_{∞} is the XUV flux at the top of the atmosphere, and $\tau(z,\lambda,\chi)$ is the optical depth at the altitude z with stellar zenith angle χ. In general, following Achilleos et al. [1998], it was assumed that 50 % of the absorbed energy is thermalised. This is consistent with calculations performed by Waite et al. [1983] for Jupiter's upper atmosphere, if cooling due to H_3^+ is ignored. Yelle [2004] noted that in the atomic hydrogen envelope of HD209458b, the heating efficiency is likely to be lower at ∼10 %. This is because in the outer layers of the atmosphere much of the stellar energy goes into ionising H, and this energy is lost either due to the recombination of H^+ or through the escape of H^+. Thus in some simulations, a heating efficiency of 10 % has been adopted for radiation absorbed by atomic hydrogen.

In most cases, a solar-type source has been assumed as most known EGPs orbit solar-type stars. For consistency, solar maximum fluxes from the SOLAR2000 model have been used [Tobiska et al., 2000] in most solar-type simulations. Both solar maximum and minimum fluxes used in modelling are listed in Appendix B.

3.4 The Ionosphere

The photoionisation rate for species i ($m^{-3}s^{-1}$) is equal to the number of photons (with energy more than or equal to the ionisation threshold) absorbed by this species. A formula from Schunk and Nagy [2000] has been adopted:

$$P_i^{ion}(z,\chi) = \frac{n_i(z)}{hc} \int_0^{\lambda_{th}} I_{\infty}(\lambda) exp[-\tau(z,\lambda,\chi)] \lambda \sigma_i^{ion}(\lambda) d\lambda \tag{3.10}$$

where σ_i^{ion} is the photoionisation cross section of species i, $I_{\infty}(\lambda)$ is the intensity of the XUV radiation hitting the top of the atmosphere, and $E_{ph} = hc/\lambda$ is the photon energy. Photoionisation rates are updated self-consistently every few time steps as the simulation proceeds. The rates are based on neutral densities along ray paths, but the neutral mass mixing ratios themselves are unaffected by ionisation. This approximation is valid as long as neutral source densities are much higher than the resulting ion densities.

Photoionisation is followed by complex photochemistry, in which ions react with the neutrals to form new ions or recombine with electrons. The reactions that have been included in this model are listed in Table 3.1 and they resemble those that take place in Jupiter's upper atmosphere. The only exceptions are that hydrocarbons are ignored and pathways involving the HeH^+ ion are skipped because HeH^+ densities are considered negligible. Thus the ion species included in the model are H^+, H_2^+, H_3^+ and He^+. Ion densities are calculated for two distinct scenarios: tidally locked exoplanets and planets that rotate asynchronously. In both cases, it has been assumed that photochemical equilibrium holds. This implies that transport of ions by neutral winds or diffusion is considered negligible. This, of course, may not be a realistic assumption, especially if the planet is magnetised. However, there are some good reasons for using it as a starting point, which helps to avoid complications and speculation.

First, as Yelle [2004] points out, thermospheric temperatures of EGPs are likely to be higher than on Jupiter, which means that photochemical timescales are shorter. This reduces the importance of ion transport. Second, on magnetised planets ions diffuse along magnetic field lines. There are no detailed observations of magnetic fields around EGPs, and as close-in EGPs rotate slowly their magnetic fields could be very weak. Weakly magnetised plasmas are dominated by collisions with the neutrals, and thus ions are carried by the neutral atmosphere. This, however, may be an oversimplification. Ionospheric plasma is also affected by electric fields in the atmosphere. On solar system planets the electric fields for magnetised planets arise mainly from complex interactions between the magnetic field, the solar wind, and the ionised species in the plasmasphere and the atmosphere. On non-magnetised planets they are induced by the impinging solar wind and its interactions with the plasmas. There are no observations to constrain these electric fields on EGPs and this makes the ion transport problem very difficult to solve. In these circumstances it is better to adopt a simple order of magnitude approach rather than to attempt to model the ionosphere in detail.

This approach is supported by the work of Williams [2004] who used a version of JIM [Achilleos et al., 1998] to model ion densities in the thermospheres of both magnetised and non-magnetised EGPs, including ion transport by diffusion and winds. For unmagnetised, rotationally synchronised models he obtained dayside ion densities that are of the same order of magnitude as those generated by this model. For models with a centered, aligned dipole magnetic field of roughly the strength of the magnetic field of Jupiter, he found that while the ion profiles were more complicated than on an unmagnetised planet, the column densities were nearly identical.

In general, ion densities were calculated from:

$$\frac{dn_i}{dt} = P_i - \Psi_i n_i \tag{3.11}$$

where P_i and Ψ_i are the production and loss rates, respectively, for species i. The reaction rate coefficients are given in Table 3.1. For photochemical equilibrium we have:

$$P_i - \Psi_i n_i = 0 \tag{3.12}$$

If the planet rotates asynchronously around its axis the position of the star in the planet's sky varies and for a point in the Eulerian corotating frame, equation (3.12) does not hold. Explicit time-integration must be used to solve equation (3.11) in this case. This is difficult numerically as the photochemical timescales are so short that only very short timesteps allow for stable integration and this is computationally expensive and time-consuming. In order to alleviate this problem, it was noted that equation (3.11) can be integrated analytically by using integrating factors. The integration yields:

$$n_i(t + \delta t) = \frac{P_i}{\Psi}[1 - \exp(-\Psi\delta t)] + n(t)\exp(-\Psi\delta t) \tag{3.13}$$

This equation allows for smooth progress in time and does not produce bothersome negative ion densities that result from short reaction timescales and the use of simple forward time-stepping.

For rotationally synchronised planets the radiation field on the dayside is constant and equation (3.12) holds. This is very convenient because the equation can then be solved iteratively and thus instabilities arising from numerical time-stepping can be avoided. Equation (3.12) expands to a series of simultaneous equations of the form:

$$F_i(n_1, n_2, ..., n_N) = 0, i = 1, 2, ..., N \tag{3.14}$$

where N is the number of variable species involved in the calculation. Note that in these calculations only the ion species are variable, while neutral densities are considered constant. The resulting non-linear simultaneous equations can be solved by using Newton-Raphson iteration. First the functions are expanded as a Taylor series. This produces, in matrix notation [Press et al., 1992]:

$$\mathbf{F}(\mathbf{n} + \delta\mathbf{n}) \approx \mathbf{F}(\mathbf{n}) + \mathbf{J} \cdot \delta\mathbf{n} \tag{3.15}$$

where $\mathbf{J} = J_{ij} \equiv \partial F_i / \partial n_j$ is the Jacobian matrix. Setting $\mathbf{F}(\mathbf{n} + \delta\mathbf{n}) = 0$ yields the corrections $\delta\mathbf{n}$ that move each function closer to zero simultaneously:

$$\mathbf{J} \cdot \delta\mathbf{n} = -\mathbf{F} \tag{3.16}$$

The above equation is solved by inverting the Jacobian matrix numerically. The iteration continues in the same manner until the new values for $\mathbf{n}$ begin to satisfy equation (3.14). The ion densities are updated in this fashion every few time steps while the model approaches steady state. The benefit of this method is that it is stable and produces steady state ion densities immediately, given the temperature and number densities in the background atmosphere. This is obviously not the case for semi-analytic time-stepping (equation 3.13), which approaches steady state over time.

3.5 Infrared Cooling

The atmosphere absorbs stellar short-wave radiation and reradiates the absorbed energy back to space at infrared wavelengths. One of the most significant radiatively active species in gas giant thermospheres is H_3^+ that acts as an important coolant on Jupiter and Saturn. It is important to include infrared cooling in the energy equation as it may have a significant influence on the thermal profile. H_3^+ forms mainly through reactions 1a, 6, and 7 listed in Table 3.1. In Jupiter's auroral regions H_3^+ is also formed as a result of collision-induced ionisation of H_2, which is driven by precipitating energetic electrons. However, particle precipitation also dissociates some H_2 and may act to prevent the formation of some H_3^+. The model does not include particle precipitation. In Jupiter's auroral regions the overall effect of particle precipitation is to increase the H_3^+ densities on one hand but to increase the temperature on the other. Neglecting it may underestimate H_3^+ densities, but as H_2 dissociates thermally at high temperatures and under particle bombardment, it may also overestimate the H_3^+ content.

The H_3^+ infrared emission rate is based on a complete line list published by Neale et al. [1996]. They calculated emission rates for different temperatures. For this model, the data was parameterised by curve fitting for two temperature ranges and the following per molecule emission rates (erg^{-1} s^{-1} sr^{-1}) were obtained:

$$\dot{Q} = -2.6884596 \times 10^{-15} + 1.5581041 \times 10^{-16}T - 7.0948211 \times 10^{-19}T^2$$

$$+9.3850444 \times 10^{-22}T^3 - 1.6178412 \times 10^{-25}T^4$$

for

$$T \leq 2750K \tag{3.17}$$

$$\dot{Q} = -2.5786238 \times 10^{-11} + 1.9735301 \times 10^{-14}T - 3.8078930 \times 10^{-18}T^2$$

$$+2.877954 \times 10^{-22}T^3 - 7.2083644 \times 10^{-27}T^4$$

for

$$T > 2750K \tag{3.18}$$

These fits are strictly valid for temperatures ranging from 500 K to 8000 K only but the same fits were nevertheless used for lower and higher temperatures in many of the simulations. In some cases, the emission rates were calculated by using the line list of Dinelli et al. [1992] for temperatures less than 500 K. Figure 3.1 illustrates the excellent quality of the fit in the 500–8000 K temperature range.

As noted before, the frequency of intermolecular collisions in the upper atmospheres of gas giants is not high enough to ensure that LTE conditions hold. Thus the emission rates calculated by Neale et al. [1996] are not appropriate for gas giant thermospheres as they are derived for LTE environments. The emission rates must be corrected for non-LTE effects. The correction factor was estimated by using detailed balance calculations based on the method of Oka and Epp [2004] (S. Miller, *personal communication*), which is valid for a H_2 background atmosphere. It would be computationally impossible to perform detailed balance calculations for over three million line transitions included in the line list of Neale et al. [1996], at every grid point in the model, during each time step. Instead, the non-LTE emission rates were calculated for 17 vibrational transitions included in the line list of Dinelli et al. [1992] that account for most of the LTE infrared emissions. The non-LTE emission rates were evaluated for a simple table of temperatures and densities that encompasses the likely values within the model. As the model proceeds,

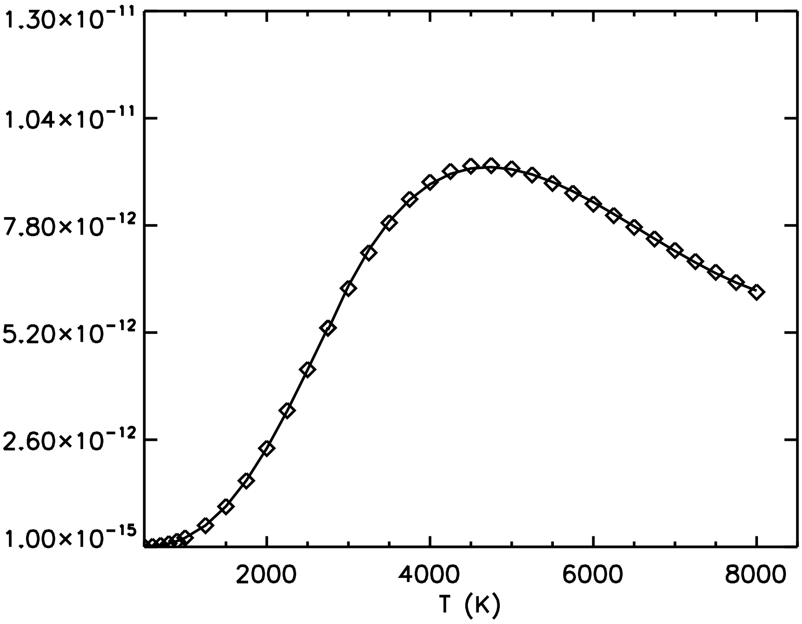

Figure 3.1: Infrared emission rate vs. temperature. The open diamonds show the data points calculated by Neale et al. [1996] and the solid line is the fit based on equations (3.17) and (3.18).

it interpolates bilinearly from this table, calculates the LTE emission rate for the 17 vibrational lines, and thus evaluates the ratio of the non-LTE to LTE emission rates at each grid point. The actual emission rate is then worked out by multiplying the total LTE emission rate, obtained from equations (3.17) and (3.18), by this ratio.

In some simulations, an experimental correction factor given by [Williams, 2004] was also used:

$$f = \exp[-0.1(n-9)] - \exp(-2.1) \tag{3.19}$$

where n is the pressure level index. This correction is applied to pressures less than ~50 nbar. It is based on Galileo observations of H_3^+ in the jovian thermosphere. Surprisingly, the non-LTE rates that are based on proper detailed balance calculations agree rather well with this correction (see Chapter 4, Section 4.6.4). Despite this, the detailed balance calculations were preferred and that is recommended for other users as well. The correction factor (3.19) is only valid in the pressure range of this model and follows the specific pressure level spacing that it uses. Note also that it becomes negative at $n > 30$, implying that above this level emissions should vanish if this correction is used.

It has also been assumed that the upper thermosphere is optically thin in the infrared and that radiation emitted into a solid angle of 4π is radiated directly into space or to the lower atmosphere and thus contributes to the cooling of the thermosphere.

3.6 H_3^+ Spectrum

For potential observations validating the results presented in this thesis, the total radiated output power and two line fluxes for the Q(3,0-) [2509.0803 cm^{-1}] and the R(6,6+) [4777.3583 cm^{-1}] transitions are calculated for each simulation. Naturally, other lines can also be included, if requested. The energy emitted in a specific transition (erg^{-1} s^{-1} sr^{-1}) is given by:

$$\dot{Q} = \frac{1}{4\pi Z(T)} hc\omega_{if} A_{if} g_f (2J_f + 1) \exp(-E_f/kT) \tag{3.20}$$

where ω_{if} is the frequency of the transition (cm^{-1}), A_{if} is the Einstein A coefficient, g_f is the nuclear spin degeneracy factor, J_f is the rotational quantum number of the final state (f), E_f is the energy of the final state (cm^{-1}), and Z(T) is the temperature dependent partition function of H_3^+. The values for A_{if}, g_f, and J_f were calculated by Neale et al. [1996] and the partition functions for different temperatures were taken from Neale and Tennyson [1995]. The total fluxes are calculated based on the ion densities and temperatures through the atmosphere, which is optically thin in the infrared and radiation emitted into the solid angle of 2π is assumed to leave the planet.

3.7 Numerical Methods

The equations of motion form a set of non-linear partial differential equations in seven dimensions. These equations cannot be solved analytically, and instead a numerical solution must be sought. This solution is based on approximating partial derivatives with finite difference analogues in terms of finite grid intervals and utilising a time-stepping procedure to integrate the equations numerically.

The calculations are performed on a grid of 36 evenly spaced longitude points, 31 latitude points and a varying number of pressure levels, usually ranging from 28 to 34. The pressure level spacing is 0.4 scale heights in all simulations. This is a rather coarse grid and as such ideally suited for global simulations producing first-order accuracy. It should not be used for detailed, local modelling. The calculations do not extend to the polar latitude circles (31,30,1,2), and instead the field variable values are interpolated over to the poles.

The calculation proceeds so that during each time step horizontal wind velocities and temperatures are solved from equations (1.32) and (3.3), respectively. Given temperature and pressure, density is solved from the ideal gas law. Mass mixing ratios of the individual neutral species are then solved separately from equation (3.4). Ion densities, unless indicated otherwise, are solved simultaneously with the energy and momentum equations for fixed neutral densities. Vertical velocities are solved from equation (1.31). This equation ensures that matter is conserved by insisting that vertical flows feed into the horizontal winds, while actual vertical accelerations are absent.

This work does not concentrate on predictive modelling and normally the solution was allowed to proceed until some kind of steady state is achieved. Predictive modelling is concerned with short-timescale, and possibly local, processes driven by some external or internal influences and the results depend heavily on the the start-up atmosphere. Instead of such detailed simulations, this work concentrates on the global steady-state simulations of EGP thermospheres at different orbital distances from the host star.

The finite difference analogues used in the model are mostly centred-space, which means that first and second derivatives with respect to any arbitrary variable x are approximated as follows:

$$\frac{\partial f}{\partial x} \approx \frac{f^{i+1} - f^{i-1}}{2\delta x} \tag{3.21}$$

$$\frac{\partial^2 f}{\partial x^2} \approx \frac{f^{i+1} - 2f^i + f^{i-1}}{\delta x^2} \tag{3.22}$$

where i is any arbitrary grid point index, and δx is the grid interval.

Time integration of the momentum and neutral continuity equations is based on the simple forward-time technique:

$$f(t + \delta t) \approx f(t) + [\frac{\partial f}{\partial t}]_{approx} \delta t$$

whereas the energy equation is integrated by using the following Taylor expansion:

$$\begin{aligned} \epsilon(t + \delta t) &\approx \epsilon(t) + \frac{\partial \epsilon}{\partial t}\delta t + \frac{1}{2}\frac{\partial^2 \epsilon}{\partial t^2}\delta t^2 \\ &\approx \epsilon(t) + (C_p \frac{\partial T}{\partial t} + \mathbf{u} \cdot \frac{\partial \mathbf{u}}{\partial t})\delta t + \frac{1}{2}(\frac{\partial \mathbf{u}}{\partial t})^2 \delta t^2 \end{aligned}$$

where ϵ is the specific enthalpy and second derivatives of temperature and velocity with respect to time are ignored.

3.7.1 Numerical Smoothing

The equations of motion presented above cannot be integrated numerically by using finite difference analogues and the forward-time centred-space (FTCS) technique without the addition of smoothing and filtering terms that control numerical instabilities. All GCMs require numerical smoothing to work, but the simple formulation and the FTCS method is particularly sensitive to instabilities. The horizontal solution of the equations (i.e. temperatures and winds) form wave-like patterns of a 2D surface. These patterns can be described as a series of Fourier components [eg. Phillips, 1959, Arakawa, 1966, Shapiro, 1970]. The shortest wavelength that can be resolved by the grid is two grid intervals. In a process known as ‘aliasing’, the grid interprets unresolved waves with wavelengths shorter than this as longer wavelength patterns. Thus the numerical solution does not conserve energy, and the energy in these unresolved waves, transferred to longer wavelengths, grows disproportionally and the solution blows up [Arakawa, 1966]. The instability arises primarily from the advective part of the equations and it is removed by introducing a smoothing element that is applied periodically to filter out the short-wave components and to stabilise the model.

This model uses a two-step smoothing procedure described by Shapiro [1970]. For a scalar variable Z on a 2D Cartesian surface the smoothing element is given by:

$$\overline{Z}_{ij}^{ij} = Z_{ij} + \frac{S}{4}(Z_{i-1,j} + Z_{i+1,j} + Z_{i,j-1} + Z_{i,j+1} - 4Z_{ij}) \tag{3.23}$$

where i and j are grid point indices. This element has a resemblance to the scalar Laplacian and thus it is often referred to as 'numerical diffusion'. During each application it is used twice, once with $S = 1$ and then immediately after with $S = -1$ [Shapiro, 1970]. For the purposes of a spherical model, the smoothing element has been adapted for spherical geometry and vector algebra by utilising the analogy with the scalar and vector Laplacians. The resulting terms resemble the 'hyperviscosity' term used by Dowling et al. [1998].

Unfortunately, the smoothing element is not perfect and in addition to controlling instabilities, it also stamps out real features and reduces the amplitude of the long-wave solution unphysically. Thus the physicality of the solution should act as a guide to smoothing applications. In general, the smoothing element should be used as rarely and as conservatively as possible simply to maintain stability and to do little else. A discussion and some illustrations of the effects of the smoothing filter are included in Chapter 4, Section 4.6.6.

3.8 Boundary Conditions

In most cases, the lower boundary is placed at 2 μbar, while the upper boundary varies from 0.04 nbar to 3.7 pbar. In most simulations, the upper boundary was placed near the exobase. The initial composition is taken from a one-dimensional model of the Jovian auroral thermosphere by Grodent et al. [2001]. Effectively this fixes the mixing ratios of the neutral species at the lower boundary. As we will learn, varying the lower boundary composition can affect the results, so this is an important point.

The temperature at the lower boundary was usually held constant and equal to the equilibrium temperature of a gas giant with a Bond albedo equal to 0.3 under solar irradiation. Thus the lower boundary temperatures are roughly consistent with the P-T profiles presented by Sudarsky et al. [2003] (see Chapter 2). In line with this boundary condition, zero winds at the lower boundary have also been assumed in most of the simulations. This assumption may not be realistic, and considerable winds are possible at the $\sim \mu$bar level.

Lower atmosphere circulation and composition of EGPs are extensively discussed in Chapter 2. We learned that for a planet like HD209458b, winds of 1–10 km s^{-1} are feasible in the lower atmosphere, although there is little agreement on the nature of the circulation and possible wind speeds. Also, all of the existing models concentrate on 'Hot Jupiters' and none of them extend to $\sim \mu$bar pressures, where circulation could be very different compared to the circulation at photospheric pressure levels. As a result, lower boundary winds were examined as a parameter variation, but for a systematic study, vanishing lower boundary winds were adopted.

At the upper boundary, the model assumes that the vertical temperature gradient vanishes between the two uppermost levels. This is an appropriate condition if the upper boundary is located near the exobase where the P-T profile tends to become isothermal. Further, the model assumes that there is no vertical outflow at the upper boundary apart from adiabatic expansion and that the neutral species are in diffusive equilibrium between the three uppermost levels.

The planetary and orbital parameters can be varied depending on the system, although for the systematic and general stability studies presented in this thesis, a solar-type source and a Jupiter-type planet were used. For these studies, lower boundary gravity is the same as on Jupiter, $R_p \sim R_J$ (the whole lower atmosphere being contained within this radius) and $M_p \sim M_J$. All simulations assume equinox conditions, and most also assume zero obliquity.

Chapter 4

Thermospheres of Extrasolar Giant Planets at Different Orbital Distances

4.1 A Jupiter-type Planet at 5.2 AU

It makes sense to try to use the model to simulate a Jupiter-type planet orbiting a Sun-like star at 5.2 AU. Such a simulation can be used to identify the basic features of the model and the results can be contrasted to actual observations of Jupiter. We have already hinted, in section 1.3, that the simulations are unlikely to match observations of temperature and ion densities in Jupiter's upper atmosphere. Thus the simulations will reveal potential weaknesses and uncertainties associated with the model. On the other hand, they will also unmask specific features of Jupiter that cannot be assumed in a more generic study of EGP upper atmospheres.

In the current sample of known EGPs (May 2008), there is only one planet with an orbital semi-major axis between 5 and 6 AU. This planet is 55 Cnc d, which orbits a G-type host star at 5.77 AU. However, the projected mass of the planet is $\sim$3.8 M_J, and thus its atmosphere is likely to be radically different to that of Jupiter. There are four planets orbiting between 4 and 5 AU, namely HD217107c, HD160691c, HD72659b, and HD89307b. All of these planets orbit G-type stars of roughly solar mass, but their projected masses are $\sim$2–3 M_J. Jupiter-mass planets between 5 and 6 AU are yet to be found, but there is no doubt that they exist and that many will be discovered with more sophisticated technologies in the future.

Figure 4.1 shows the equatorial P-T profiles for a simulated thermosphere of Jupiter orbiting the Sun at 5.2 AU. The planetary and orbital parameters used in the simulations match those of Jupiter and they are listed in Table 4.1, which also shows the parameters for models of Jupiter orbiting at 1.0 AU

Table 4.1: Jupiter Simulations

Common parameters			
Radius	69911 km	Season	Equinox
Pressure[a] (p_o)	4 μbar	Runtime[b]	200
Temperature (T_o)	180 K	Time Step	1-3 s
Altitude (z_o)	350 km	Heating Efficiency	50 %
Gravity (g_o)	24.5 ms^{-2}	Solar Activity	Max
Spin period	9.9259 hr	K_τ[c]	10^7 cm^{2}s^{-1}
Obliquity	3.13 degrees		

Simulations			
Identifier	Distance (AU)	Ionosphere	X-ray heating
Jup01	5.2	Off	Off
Jup02	5.2	Off	On
Jup03	5.2	On	On
Jup04	1.0	On	On
Jup05	5.2	On	On (Solar min)
Jup06	1.0	On	On (Solar min)

---

[a] Pressure at the lower boundary of the model

[b] Running time in simulated rotations (local days)

[c] Coefficient of eddy diffusion used in calculating neutral mixing ratios

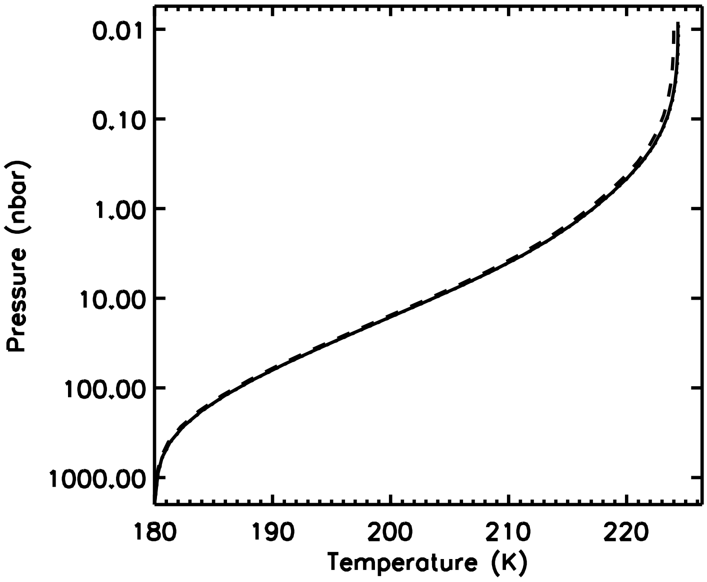

Figure 4.1: Subsolar, simulated P-T profiles for Jupiter. Three different profiles are shown: one for a simulation that excludes X-ray heating and radiative cooling (solid line), one for a simulation that includes X-ray heating but excludes radiative cooling (dotted line), and one for a simulation that includes both X-ray heating and radiative cooling (dashed line). The results indicate that neither X-ray heating or H_3^+ cooling has much influence on the temperatures, and the three P-T profiles can hardly be told apart.

that are discussed later in Section 4.2. The results apply to equinox conditions under solar maximum fluxes. In all simulations, the only external heating source is solar XUV flux. Figure 4.1 includes P-T profiles for three different models, one where the solar X-ray spectrum is excluded, one that includes both X-ray and EUV heating and one where infrared cooling from H_3^+ ions is included together with full XUV heating. For comparison, Figure 4.2 shows the equatorial temperature profiles measured by the Galileo probe and Voyager remote sensing equipment (ref. Section 1.3).

The Galileo profile shows that the temperature increases sharply with altitude at pressures lower than 2 μbar and around 1.0 nbar it is about 900 K. The profile also displays vertical temperature oscillations that suggest the presence of gravity waves in the thermosphere. The simulated P-T profiles also show temperature increasing with altitude at sub-μbar pressures, but much less steeply, and the temperature at 1.0 nbar is only $\sim$219 K. Also, the simulated profiles are smooth and show no evidence for gravity waves because such waves are not included in the model formulation. Clearly the solar heating input is not enough to explain the high temperatures in Jupiter's thermosphere, not even if the energetic solar X-ray spectrum is included. Indeed, as Figure 4.1 demonstrates, the inclusion of the X-ray heating has a negligible impact on the P-T profile, as X rays tend to penetrate deep into the thermosphere where density is relatively high. Also, it appears that H_3^+ cooling does not affect the P-T profile significantly. This

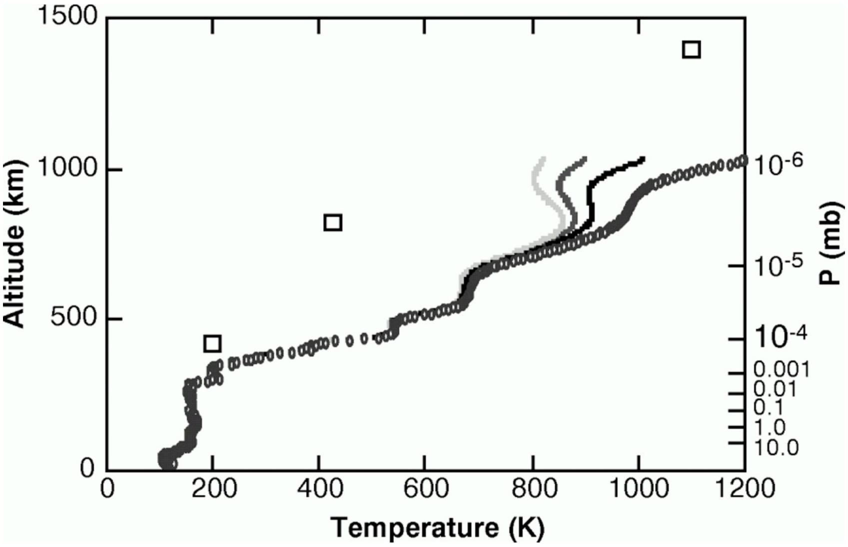

Figure 4.2: Temperatures in Jupiter's atmosphere derived from Galileo deceleration data (circles) and Vogager solar and stellar occultation results (squares). The four Galileo profiles assume upper boundary temperatures from 800 K to 1200 K, but the profiles converge at an altitude of 700 km. Vertical oscillations in the temperature profile imply the presence of gravity waves [Seiff et al., 1997]

does not apply to the real Jupiter, however, because the model severely underestimates thermospheric temperatures and thus the H_3^+ emissions.

The conclusion that solar heating is not enough to explain the high temperatures in Jupiter's upper atmosphere can also be reached by using a much simpler method. If radiative cooling is neglected and we assume that the solar XUV radiation is absorbed in the thermosphere, conducted downwards by molecular diffusion and reradiated at longer wavelengths from layers below the homopause, the exospheric temperature can be estimated by using the following formula:

$$T^s = T_o^s + \frac{F_\infty H_o s}{A T_o} \ln(\frac{p_o}{p}) \tag{4.1}$$

where T_o, H_o, and p_o are the temperature, scale height and pressure at the base of the thermosphere, p is the top boundary pressure, F_∞ is the total XUV flux hitting the top of the atmosphere, and A and s are constants. If we adopt values typical for Jupiter, i.e. $s = 0.751$, $A = 252 \times 10^{-5}$ $\mathrm{Wm^{-1}K^{-(s+1)}}$, $T_o = 160$ K, $H_o = 25.5$ km, $F_\infty = 7.4 \times 10^5$ $\mathrm{Wm^{-2}}$, and $\ln(p_o/p) \approx 9$ [Yelle and Miller, 2004], we obtain an exospheric temperature of 240 K at the 1 nbar level. The slight discrepancy between this and the simulated temperature arises from the fact that the simulations are not in exact steady-state. If the simulations are continued indefinitely, the upper boundary temperature reaches 230–240 K and is thus in line with the simple calculation. Nevertheless, both estimates are much lower than the observed temperatures.

It is interesting that the measured temperatures are higher than the model temperatures consistently at all levels above the lower boundary. We pointed out in Section 1.3 that possible heating mechanisms

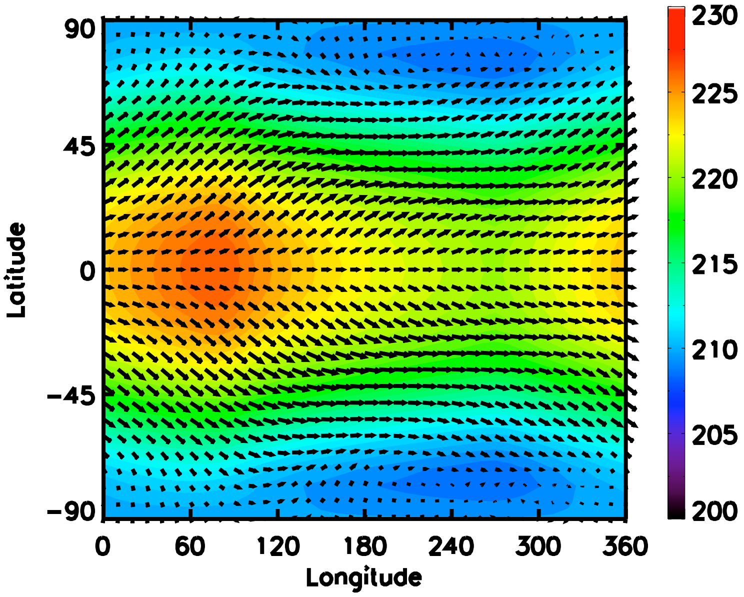

Figure 4.3: Temperatures and winds for the Jupiter-simulation Jup03 at 0.016 nbar. The maximum temperature is 226 K, and the maximum wind speed is 22 m s^{-1}. The subsolar point is at zero longitude.

in Jupiter's thermosphere include gravity wave breaking, low-latitude particle precipitation, and redistribution of auroral energy from the polar regions towards the equator. Whichever mechanism is generating the required heat, somehow it must penetrate all the way to the lower thermosphere and mesospheric boundary.

Figure 4.3 shows the temperatures and winds at the upper boundary (0.016 nbar) of the Jupiter reference model, Jup03, which includes full XUV heating and H_3^+ cooling. At the upper boundary the average temperature is 219 K, and the altitude is about 770 km above the 1.0 bar level. This altitude is lower than would be expected from the Galileo measurements as the temperature is also lower in the simulation. The equator is warmer than its surroundings and forms a warm belt around the planet, although overall the horizontal temperature differences in general are not particularly notable. The maximum temperature is 226 K, and this 'hot spot' is shifted eastward from the subsolar point by about 60–80 degrees longitude. The temperature minima are located in the night side near the poles, where the temperature drops to 209 K. The winds blow eastward around the planet in one broad jet centred on the equator. The dayside meridional flows originating from the equator are turned eastward by the Coriolis force that arises from the relatively fast rotation of Jupiter around its axis. The equatorial wind speed is around 10–15 m s^{-1}. The maximum zonal wind speed is just over 20 m s^{-1}, blowing over the terminator at mid-latitudes. Deeper in the thermosphere, the temperature is close to uniform and wind speeds are lower. The broad eastward jet wind persists at all levels.

This circulation regime is characteristic of Coriolis-driven neutral dynamics in the upper atmosphere.

It should be noted that the model is based on severe and simplistic approximations and thus it is unlikely to be a realistic depiction of Jupiter's thermosphere. The model ignores particle precipitation in the auroral and low-latitude regions, it cannot resolve small-scale wave motion or turbulence, it ignores ion transport, interaction of the atmosphere with the solar wind, and does not account for the presence of Jupiter's magnetosphere. Simplistically it could be argued that the model represents the average behaviour of the neutral atmosphere, averaging out any small-scale fluctuations, but even this would be misleading. Small-scale turbulent motions and friction result in large-scale circulation patterns that can completely distort this simplistic picture. At any rate, auroral particle precipitation drives a very different circulation pattern in Jupiter's thermosphere. The circulation pattern presented in Figure 4.3 is thus only appropriate for a 'bare bones' gas giant where all of Jupiter's peculiar characteristics have been removed.

In order to explore ionisation and electron density profiles, we generated a version of the Jupiter model (Jup05) that used solar minimum XUV fluxes from December 1996 instead of solar maximum fluxes that were adopted for most of our simulations. This is because we wanted to compare our electron density profiles with the Galileo radio occultation measurements that took place between December 1995 and December 1996. Figure 4.4 shows the subsolar P-T profile for this model. The average temperature at the upper boundary is about 12 K cooler than under solar maximum conditions, and at the subsolar point the temperatures are cooler by 1–14 K at pressures lower than 0.1 μbar (above 462 km altitude). The horizontal temperature distribution and circulation are qualitatively similar to the solar maximum simulation.

Figure 4.5 shows the Galileo electron density profiles for ingress and egress at 24^o and 43^o southern planetocentric latitude, respectively. At ingress, the electron density peaks at an altitude of 900 km with a density of $\sim 10^{11}$ m^{-3}. At egress, the electron density peak is located at 2000 km altitude with a peak density of 2.0 $\times 10^{10}$ m^{-3}. The profiles show some evidence for the presence of gravity waves, especially in the lower regions of the ingress profile. The ingress took place in the evening side, while the egress took place in the dawn side of the planet. Our simulated electron densities are not fully comparable with these measurements, because the temperatures do not agree with the observed conditions in the Jovian thermosphere. Higher temperatures imply longer scale heights, and thus the pressure level altitudes are lower in the simulations compared to the Galileo profiles. In addition, the recombination rates of the ions and the overall density both depend on temperature. Nevertheless, it is interesting to assess the ionisation impact of solar XUV radiation by comparing the model profiles to the observations.

Figure 4.6 shows the simulated solar minimum dusk and dawn electron density profiles at 24^o and 42^o southern latitude, respectively. At dusk the electron density peak is located around 4 nbar, with a peak density of 6.3 $\times 10^{11}$ m^{-3}. In general, models tend to underestimate the altitude of the electron peak and overestimate the peak electron density. It is thus interesting that, judging from Figure 4.2, the 900 km altitude is located between 10 and 1.0 nbar. In other words, the simulated electron density peak appears to be around the right pressure level. Also, the peak density agrees roughly with the dashed-line

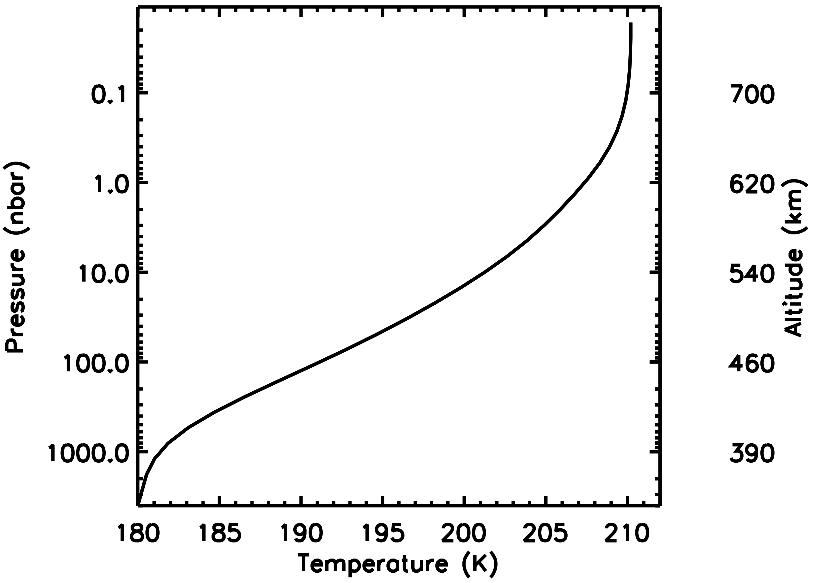

Figure 4.4: Subsolar P-T profile for a model of Jupiter's thermosphere generated with solar minimum XUV fluxes (Jup05). The altitude is given in km above the 1.0 bar pressure level.

profile in Figure 4.5. However, at higher altitudes the model exaggerates the electron densities.

At dawn the situation is very different. In the model, the electron density decreases near the lower boundary compared to the dusk profile, but the peak density and location are virtually unchanged. The Galileo measurements indicate that the density of electrons in the 1.0–10 nbar region should decrease significantly at night. The model does not agree with this. Instead, the electron density is horizontally nearly uniform in the middle-and upper thermosphere. The electron density reflects the ion densities in the thermosphere. The model indicates that at pressures lower than 0.1 μbar, H^+ is by far the dominant ion. The lifetime of H^+ around the altitude of the electron density peak is $\sim$69 hours, whereas the rotation timescale is about 5.0 hours. If the ions rotate with the planet, a significant portion of them are carried to the night side, and this explains the uniform electron densities.

The corresponding lifetimes for H_3^+ and He^+ are 3.4 s and 11 min, respectively. This means that while photochemical equilibrium is a wildly unrealistic approximation for modelling H^+ densities, it works to some degree for the minor ions. At pressures higher than 0.1 μbar,the density of H^+ decreases steeply, and H_3^+ is the dominant ion. The densities of He^+ and H_2^+ are tiny in comparison. The density of He^+ is higher than the density of H_2^+ at pressures higher than about 0.4 nbar. The subsolar column densities of H^+ and H_3^+ are 1.0 $\times 10^{17}$ m^{-2} and 1.0 $\times 10^{15}$ m^{-2}, respectively. The total H_3^+ emission rate is 1.4 $\times 10^{6}$ W. This is obviously underestimated because the model temperatures are lower by 800-1000 K than the observed values.

It has been suggested that transport of H^+ along magnetic field lines, and the reaction of H^+ with

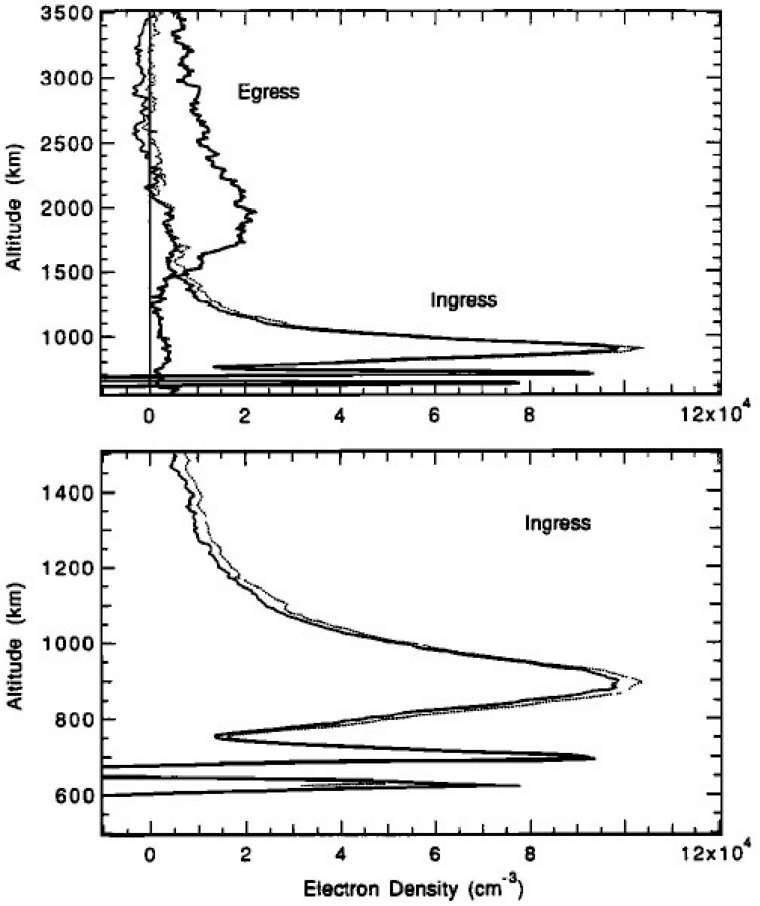

Figure 4.5: Electron density profiles in the Jovian ionosphere, derived from Galileo radio occultation measurements [Hinson et al., 1997]. The upper panel shows both ingress and egress profiles and the lower panel shows the ingress profile in the vicinity of the electron density peak near 900 km altitude. The solid line shows the data that was reduced by using standard analysis of the radio emissions. For the dashed-line profile multipath, defocusing, and diffraction effects were removed from the data (see Hinson et al. [1997] for details). The two thin layers in the ingress profile could be forced by upwards propagating gravity waves.

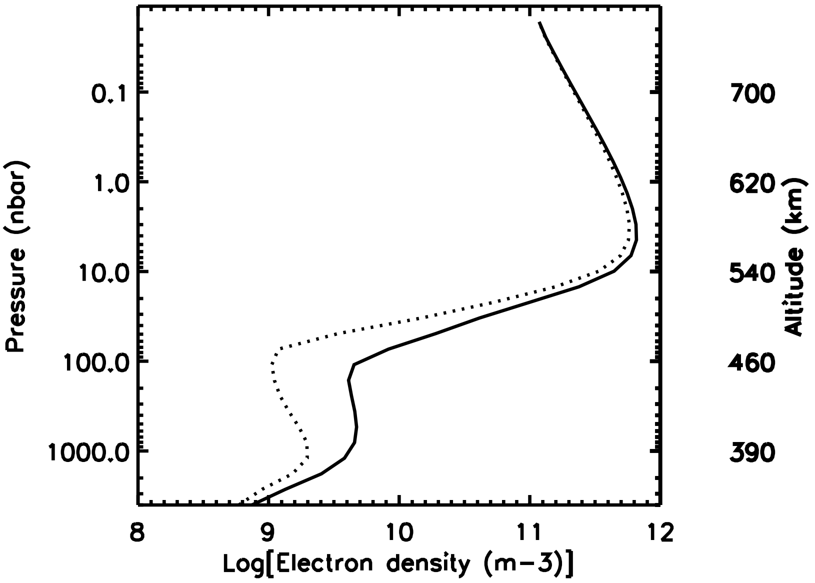

Figure 4.6: Simulated electron densities for Jupiter under solar minimum conditions at dusk at 24^o southern latitude (solid line) and dawn at 42^o southern latitude (dotted line).

vibrationally excited H_2 could be responsible for the discrepancies between photochemical models and observations [Yelle and Miller, 2004]. The latter reaction is included in the model, and maybe this explains the rough agreement between the measured and simulated peak electron densities. The long lifetime of H^+ certainly indicates that ion transport is an important factor, and if taken into account, it would shift the plasma density peak to higher altitudes and reduce the ion densities in the upper thermosphere. It would certainly be interesting to include some of the plasma transport effects in the model in the future, as this would allow for realistic modelling of Jupiter's ionosphere in a 3D setting.

The interpretation, based on some of the observed profiles, that the low-altitude electron density peak is a feature of the dayside ionosphere that is depleted at night due to recombination is very tempting. The low-altitude peak appears in the Voyager 2 data and the data from the *first* Galileo occultation at ingress, which in both cases took place at dusk. In the same measurements, the low-altitude peak is absent at dawn, in the egress data. However, the later Galileo occultation measurements do not exhibit such behaviour [Yelle and Miller, 2004]. Also, the modelling presented in this section suggests that the ion density peak is primarily made of the long-lived H^+ ions. If this is the case, the electron densities in the peak region should not be significantly depleted during the short Jovian night. It appears that the Jovian ionosphere is variable in ways that are difficult to understand.

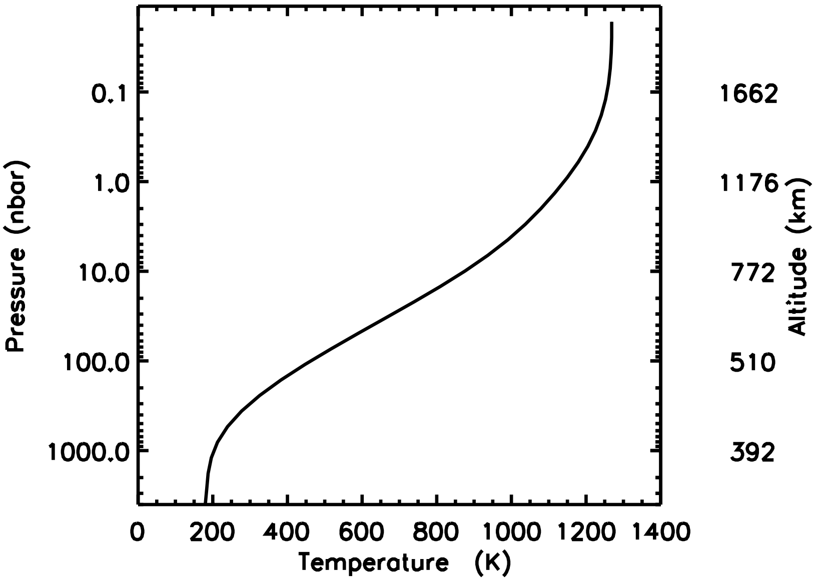

Figure 4.7: Subsolar, simulated P-T profile for a Jupiter-type planet orbiting at 1.0 AU. The altitude scale shows the altitude (in km) above the 1 bar level.

4.2 A Jupiter-type Planet at 1.0 AU

It is interesting to explore what would happen to Jupiter's upper atmosphere if the planet was moved from its current position to Earth's orbital distance. In order to do so, a model (Jup04) was generated that is identical to the Jupiter simulations in every other respect apart from its orbital distance and thus the intensity of the solar XUV flux. Moving the planet from 5.2 AU to 1.0 AU corresponds to multiplying the impinging solar flux by a factor of about 27. The subsolar P-T profile for this simulation is shown in Figure 4.7. The temperature increases with altitude between 0.7 μbar and 1.0 nbar (altitudes of 400 and 1200 km). Above the altitude of 1200 km the profile is shallower, and finally isothermal at pressures lower than 0.1 nbar (above 1650 km). The temperature at 1 nbar is 1150 K, and the upper boundary temperature is 1270 K. What is intriguing about these results is the fact that the temperatures throughout the thermosphere are much closer to the Galileo measurements for Jupiter than those from the actual Jupiter simulations.

The total integrated XUV heating rate in the Jupiter reference model (Jup03) is 2.37 $\times 10^{12}$ W, and the volume heating rate peaks in mid-thermosphere around 10 nbar (550 km). For the 1.0 AU model (Jup04), the total heating rate is 6.5 $\times 10^{13}$ W, and the volume heating rate peaks in the lower thermosphere near 1 μbar (400 km). This implies that an extra heat input of 6.0 $\times 10^{13}$ W is required to bring the simulated Jupiter P-T profiles roughly in line with observations. This estimate agrees in order of magnitude with a previously proposed extra heat input of 4.0 $\times 10^{13}$ W [Yelle and Miller, 2004].

The excess heat input required to explain the elevated temperatures in the upper atmosphere of

Jupiter is much greater than the solar XUV heating rate at 5.2 AU, implying that solar heating is almost negligible in Jupiter's thermosphere. It is not certain, however, if this will also be the case for close-in EGPs orbiting within, say, 1.0 AU from their host stars. At such close distances it may be reasonable to assume that the stellar XUV input dominates over other heat sources. We have seen that the solar XUV input overtakes the unknown heating mechanism at 1.0 AU, and we cannot be certain that this unknown heating mechanism would be similarly enhanced at shorter orbital distances. The Jupiter system is peculiar in many ways, and it would be dangerous to generalise its properties to all other EGPs. We do not know if other EGPs have volcanic moons that create plasma toruses around the planets. In most cases, we do not know what the stellar wind regime is like in the vicinity of the planets, and we do not even know how strong their magnetic fields are. As a results of these uncertainties, it appeared safer to exclude other heating sources than stellar XUV radiation in our exoplanet modelling at this stage.

Figure 4.8 shows the upper boundary temperatures and winds for Jup04. The average temperature at the upper boundary is 1180 K, and the altitude is 1975 km above the 1 bar level. Qualitatively, the circulation regime is fairly similar to the reference model at 5.2 AU. The temperature maxima and minima along the equator are located 60–80 degrees downstream from the subsolar and antisolar points, respectively, and the temperatures are 1320 and 1150 K. Thus the diurnal temperature difference is slightly more pronounced than in Jup03. The temperature minima are again located near the poles, with temperatures of around 1000 K. The equatorial wind flows eastward around the planet, with wind speed ranging from 50 to 180 m s^{-1}. The fastest zonal wind blows across the terminator at mid-latitudes, with a speed of 350 m s^{-1}. Contrary to Jup03, in the night side the wind converges around the equator, and this tendency is driven by the more pronounced diurnal temperature gradient. At greater depth the temperature is again uniform, and the eastward wind blows around the planet.

For comparison with the ion densities in the Jup05 simulation, another Jupiter-type simulation (Jup06) was set up at 1.0 AU that uses the December 1996 solar minimum XUV fluxes. Compared to solar maximum conditions at 1.0 AU, the average upper boundary temperature for Jup06 is about 280 K cooler. Figure 4.9 shows the subsolar P-T profile for this simulation. Compared to Jup04, the temperatures are cooler by 1–300 K at pressures lower than 0.1 μbar (above 520 km). Hovewer, the horizontal temperature variations and circulation are similar to the solar maximum simulation.

Figure 4.10 shows the simulated solar minimum electron density profiles at dusk and dawn around 24^o and 42^o southern latitude at 1.0 AU. At dusk, the electron density peak is located around 7.0 nbar, which is slightly deeper than at 5.2 AU. In contrast to the peak density of 6.3 $\times 10^{11}$ m^{-3} at 5.2 AU, the peak density at 1.0 AU is 3.1 $\times 10^{12}$ m^{-3}. At dawn, the peak is located at the same pressure level, and the peak density is only slightly lower than at dusk, at 2.75 $\times 10^{12}$ m^{-3}. H^+ is the dominant ion, although the density of H_3^+ is higher at the bottom of the thermosphere below 520 km. Compared to H^+ and H_3^+, the densities of He^+ and H_2^+ are small. The density of He^+ is higher than that of H_2^+ between 520 and 1065 km (100 and 1 nbar, respectively), but at other levels the density of H_2^+ is higher. The density of H_2^+ approaches that of H_3^+ in the outermost layers of the model.

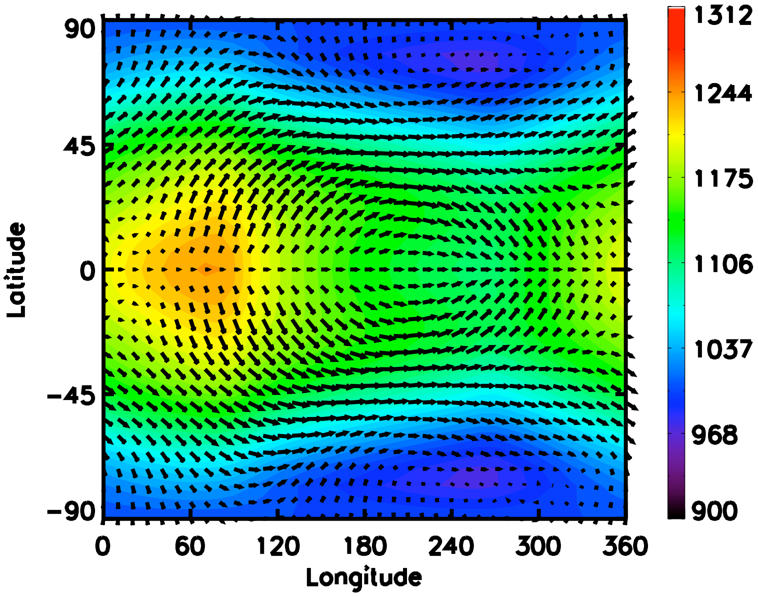

Figure 4.8: Upper boundary temperatures and winds for a Jupiter-type planet orbiting at 1.0 AU. The maximum temperature is 1320 K, and the maximum wind speed is 350 m s^{-1}.

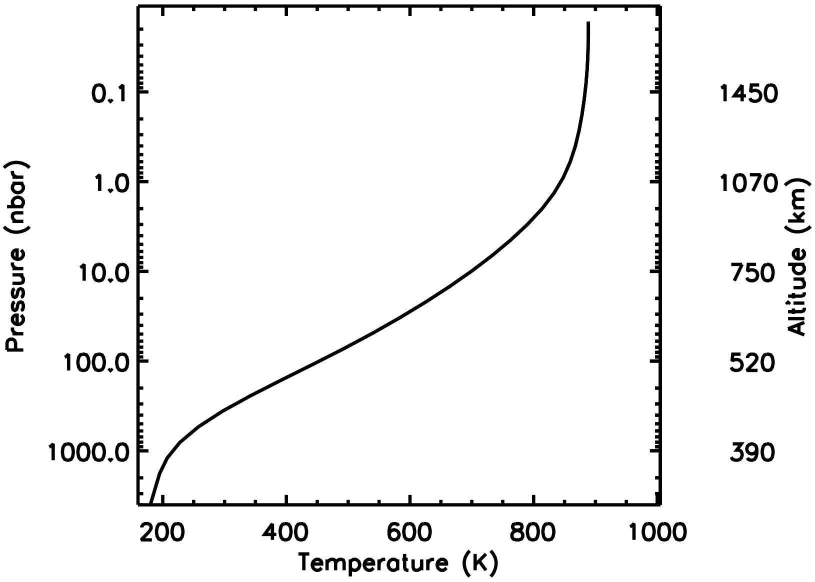

Figure 4.9: Subsolar P-T profile for a model of a Jupiter-type planet at 1.0 AU generated with solar minimum XUV fluxes. The altitude is given in km above the 1.0 bar pressure level.

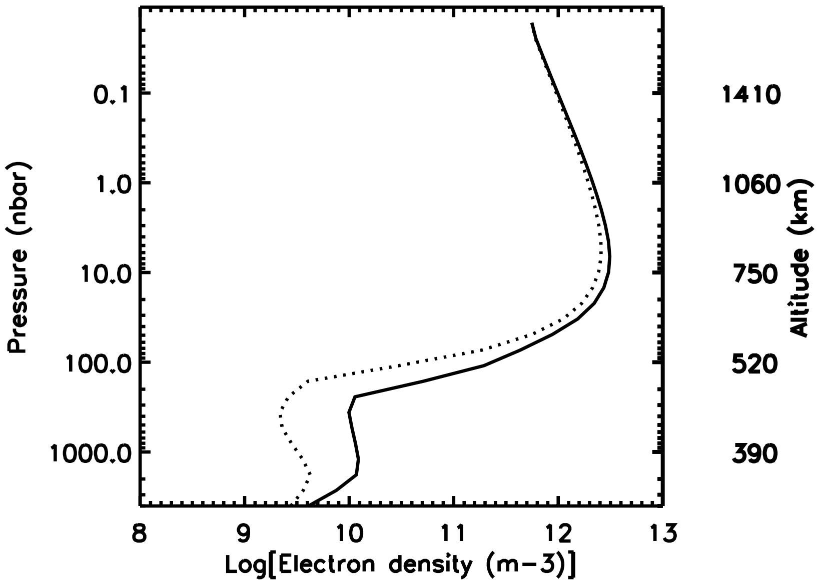

Figure 4.10: Simulated electron densities for a Jupiter-type planet at 1.0 AU under solar minimum conditions at dusk at 24^o southern latitude (solid line) and dawn at 42^o southern latitude (dotted line).

The lifetime of H^+ around the electron density peak is around 39 hours, whereas the lifetimes of H_3^+ and He^+ are 2.5 s and 33 s, respectively. In other words, the assumption of photochemical equilibrium is not likely to be appropriate for H^+, for which transport effects should be considered. However, the ion lifetimes are clearly shorter than at 5.2 AU, and within 1.0 AU they are shorter still. This justifies the assumption of photochemical equilibrium for close-in EGP models at least to some degree (see following sections in this chapter). The subsolar column densities of H^+ and H_3^+ are 2.0 $\times 10^{18}$ m^{-2} and 6.9 $\times 10^{15}$ m^{-2}, respectively. The total H_3^+ emission rate is 3.0 $\times 10^{12}$ W. Between 5.2 AU and 1.0 AU, the XUV flux increases 27-fold. Consequently, the column density of H^+ is 20 times higher and the column density of H_3^+ is 7 times higher compared to 5.2 AU. Despite the relatively modest increase in the column density of H_3^+, the H_3^+ emission rate is six orders of magnitude higher at 1.0 AU. This reflects the temperature-sensitivity of the emissions.

As a point of interest, known exoplanets that orbit their host stars at a distance of about 1.0 AU include HD142b, HD156846b, HD177830b, ChaHa8b, HD74156b, and HD122430b. Out of these, HD142b, HD156846b, and HD74156b orbit G-type stars. HD156846 is a young G type star with an estimated age of 2 Gyr, while the ages of HD142 and HD74156 are 6 Gyr and 7.4 Gyr, respectively. HD74156b has a projected mass of 0.4 M_J and it is a part of a multi-planet system together with two other more massive gas giants. HD142b, on the other hand, has a projected mass of 1 M_J. Thus it is most like our simulated planet, although the eccentricity of its orbit is relatively high at $e = 0.38$.

4.3 Temperature Trends within 1.0 AU

This section examines how the thermospheric temperatures of a Jupiter-type EGP change when the planet is moved closer to a solar-type host star. Figure 4.11 is a plot of globally averaged thermospheric temperatures near the exobase level (3.7 pbar) versus the orbital distance. The prototype model used to generate this data resembles Jupiter with zero obliquity and no magnetic field. The common planetary parameters used in the simulations are listed in Table 4.2. The run parameters for specific simulations together with their identifiers are given in Table C.1 of Appendix C. The rotation rates adopted for the simulations depend on the orbital distance so that rotation is asynchronous outside 0.2 AU and synchronous from there on in. Temperatures are displayed for two distinct scenarios, one where radiative cooling is excluded and one where cooling due to H_3^+ is properly included. All simulations use solar maximum fluxes from the SOLAR2000 model. The results were produced by using a version of EXOTIM that has been updated considerably since the publication of Koskinen et al. [2007b] (as described in Chapter 3). The cross sections have been improved, the pressure range has been extended from 0.04 nbar to 3.7 pbar, X-ray heating has been added and the non-LTE calculations are now based on detailed balance analysis. Despite these changes, the results are still essentially similar to those published earlier in the paper.

Table 4.2: Common Parameters for Jupiter-type EGP Simulations

Radius	70000 km	Season	Equinox
Pressure[a] (p_o)	2 μbar	Solar Activity	Max
Obliquity	0 degrees	Time Step	1–5 s
Altitude (z_o)	0 km[b]	Heating Efficiency	50 %
Gravity (g_o)	20 m s^{-2}	Full Heating Spectrum	On

---

[a] Pressure at the lower boundary of the model

[b] Lower atmosphere contained within the radius of the planet

If radiative cooling is excluded, stellar heating is primarily balanced by downward heat conduction. In this case the topside thermosphere reaches a temperature of 10,000 K roughly between 0.6 and 0.5 AU. Also, between 1.0 and 0.8 AU the upper thermosphere, at pressures lower than ∼16 nbar, is converted into atomic hydrogen by thermal dissociation of H_2. It should be noted that the results from the models where radiative cooling is not included are somewhat arbitrary as the models that they are based on did not run to steady state. Molecular diffusion is a very slow process and thus it is not always possible to run the 3D thermosphere model to steady state within reasonable time constraints if radiative cooling is ignored. In contrast, those models that include H_3^+ cooling approach steady state relatively quickly. This is because the XUV heating in these models is primarily balanced by H_3^+ cooling and the overall radiative timescales are relatively short in the upper atmosphere.

In the absence of radiative cooling the thermosphere reaches a temperature of over 20,000 K at 0.4

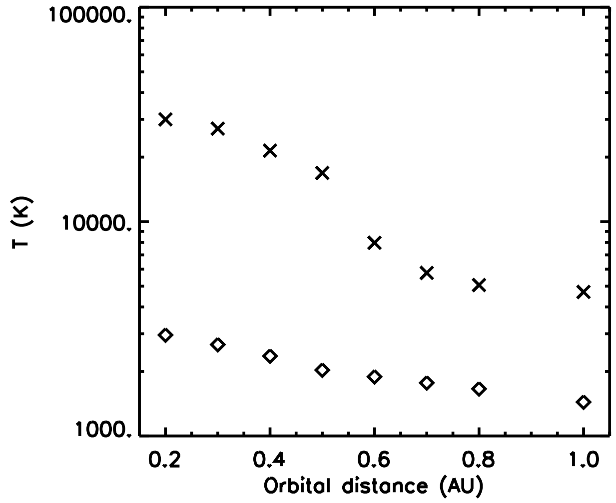

Figure 4.11: Globally averaged temperatures at the 3.7 pbar pressure level (exobase) for a Jupiter-type giant planet orbiting a Sun-like star at different orbital distances. The crosses show temperatures from models that exclude radiative cooling and the diamonds show temperatures from models that properly include H_3^+ cooling.

AU, and the upper boundary altitude expands beyond 3 R_p. At this point the upper thermosphere is entirely composed of atomic hydrogen due to thermal dissociation of H_2 and much of this hydrogen is subsequently ionised to form H^+. In the lower thermosphere the mixing ratio of H is controlled to some degree by the fixed lower boundary condition, which sets the mixing ratio of H to $\sim 2 \times 10^{-4}$ at 2 μbar. This figure is taken from the Grodent et al. [2001] model of Jupiter's auroral ionosphere. A higher ratio is possible for close-in EGPs (ref. Section 4.6.1).

If radiative cooling is not included, the exospheric thermal escape parameter in the simulated thermospheres decreases toward 1.5 within 0.4 AU, indicating that the atmosphere begins to undergo fast hydrodynamic escape. According to equation (4.1) the temperature reaches 20,000 K within 0.6 AU from the host star. Thus in the absence of H_3^+ cooling hydrodynamic escape takes hold at least within 0.5 AU. This distance represents a compromise between the crude scaling law and the simulations. Vertical bulk flow is excluded by EXOTIM because the model assumes hydrostatic equilibrium throughout. This bars the transition from a stable atmosphere into a rapidly escaping envelope. As a result, the temperatures calculated by the model are much too high inside 0.4 AU. Rapid evaporation would result in adiabatic cooling that in reality would produce lower temperatures along the outflow [Yelle, 2004].

The results presented above are roughly similar to those of Lammer et al. [2003] who argued that gas giants undergo hydrodynamic escape within 0.3 AU from a solar-type host star. Their work is based on a 1D scaling model that excludes radiative cooling. However, as Figure 4.11 suggests, the exospheric conditions are strikingly different if H_3^+ cooling is properly included. In this case the XUV heating is efficiently balanced by radiative cooling. Exospheric temperatures then range from 1440 K at 1.0 AU to 2960 K at 0.2 AU, and the whole upper atmosphere remains dominated by H_2 all the way down to 0.2 AU. At 0.4 AU, in contrast to over 20,000 K, the temperature at the exobase is only 2400 K and the thermal escape parameter is over 80, indicating that the atmosphere is stable and not escaping hydrodynamically. Indeed, the atmosphere remains stable against hydrodynamic escape in the whole range between 0.2 AU and 1.0 AU. The results clearly indicate that H_3^+ cooling is something that cannot be ignored in realistic models of EGP thermospheres. Together with thermospheric circulation it ensures that the upper atmosphere is stable much further in toward the host star than previous modelling implies.

The contrast between the two types of models, those including radiative cooling and those excluding it, has interesting observational consequences that could be exploited to verify some of these results. If, for some reason, H_3^+ cannot form in EGP atmospheres, we should see them surrounded by an extended envelope of H within 1.0 AU from the host star. Further, within 0.5 AU we should see evidence for hydrodynamic escape and planetary wind. If, however, these features are absent or only seen for Hot Jupiters orbiting within 0.1 AU, then the observations could provide indirect evidence for H_3^+ cooling even if the infrared emissions themselves are too faint for reliable detection.

In this context, it should be emphasised that the above results only apply to a Jupiter-type EGP orbiting a solar-type star with an age similar to the Sun. The XUV flux of solar-type stars depends on the age of the star so that younger stars tend to emit much stronger fluxes [Ribas et al., 2005]. This has obvious implications for the stability of EGPs, and it will be discussed in more detail in Chapter 5.

4.4 A Jupiter-Type Planet at 0.2 AU

In order to illuminate the general features of the simulations, such as energy balance and global scale circulation, this section discusses an elementary model of a hypothetical EGP orbiting a solar-type host star at 0.2 AU. This model is not intended to be a representation of any specific known EGP, but rather it allows us to explore the crude, generic features of EGP thermospheres and estimate the conditions that are likely for similar planets orbiting at this distance. Of course, it will also allow us to develop an order-of-magnitude estimate of the H_3^+ emissions that are likely to be observable in the future, if they exist.

Currently known exoplanets orbiting solar-type or nearly solar-type stars between 0.15 AU and 0.25 AU include, for example, HD6434b, HD102117b, HD17156b, HD33283b, ρ CrB b, HD11964b, HD224693b, 55 Cnc c and HD43691b. Out of the host stars, HD33283, HD224693 and HD4391 are relatively young, while the rest have ages comparable to the Sun or are older than the Sun (5–10 Gyr). The projected masses of HD6434b, HD102117b, HD11964b and 55 Cnc c are relatively low (less than 0.5 M_J), whereas the mass of HD17156b is $\sim$3 M_J. The orbit of HD17156b is highly eccentric (e $\sim$ 0.67), which makes it an interesting target for 3D atmospheric modelling. Detailed simulations of the planet are discussed in Chapter 6. For the purposes of this chapter, however, ρ CrB b is a particularly

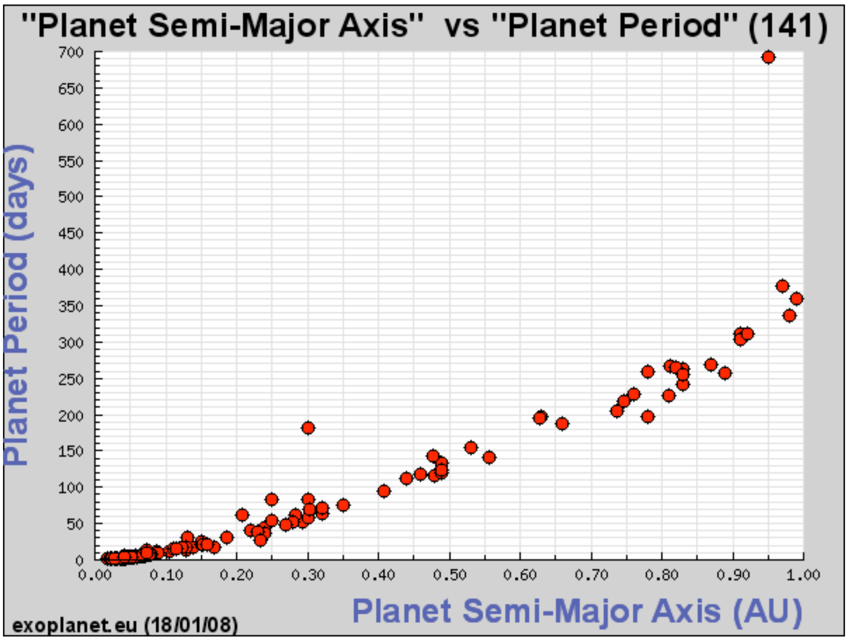

Figure 4.12: Orbital period (Earth days) of exoplanets orbiting within 1.0 AU versus the semi-major axis of the orbit. (Source: The Extrasolar Planet Encylopaedia, www.exoplanet.eu)

interesting target. Its projected mass is ∼1 M_J and its orbit is circular, with a radius of 0.22 AU. ρ CrB is a mature star with an age of 9 Gyr. The rough timescale for tidal synchronisation of the planet, calculated from equation (2.1), is 14 Gyr. This may appear rather long compared to the estimated age of the system, but the circularity of the orbit means that tidal forces may have been effective enough to bring the planet at least close to synchronisation. Although the aim was not to simulate ρ CrB b, the reference model for 0.2 AU presented here may still hint at the actual conditions on the planet.

The common planetary parameters for the reference model, labelled EX02r, are the same as for all the simulations discussed in Section 4.3 and they are listed in Table 4.2. The specific run parameters for different variations are listed in Table C.1 of Appendix C. The orbital period is set at 35 Earth days. This choice is based on Figure 4.12, which is a plot of orbital period versus distance for a sample of the known exoplanets orbiting within 1.0 AU from the host stars. The period decreases with decreasing orbital distance, ranging from 350 days to only a few days at close-in orbits, with 35 days appearing to be a typical period for planets orbiting near 0.2 AU.

Figure 2.1 indicates that orbital eccentricities vary between 0 and 0.7 near 0.2 AU. Together with the rather long timescale for rotational synchronisation (∼8 Gyr at 0.2 AU), the spread in eccentricities implies that EGPs orbiting at 0.2 AU are unlikely to be rotationally synchronised. However, it is also true that due to tidal forces, fast rotation is unlikely. Tidal synchronisation may thus be a good approximation, especially in modelling the upper atmosphere, which is why a rotationally synchronised reference model was chosen.

With an orbital period of 35 days, the angular rotation rate of the planet around its axis is $\Omega_p \sim 2.1$

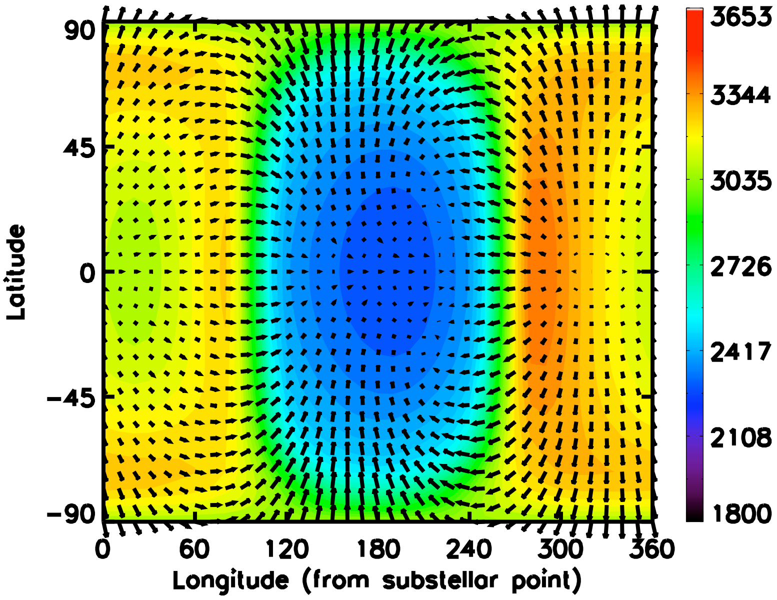

Figure 4.13: Temperatures and winds from EX02r (0.2 AU) at 3.7 pbar. The substellar temperature is 3300 K while the night side temperature is 2200 K. The maximum zonal wind speed is 2 km s^{-1}.

$\times 10^{-6}$ s^{-1} (contrast to $\Omega_p \sim 1.7 \times 10^{-4}$ s^{-1} for Jupiter). In order to expand the validity of the results, models were also generated with rotation rates corresponding to local day lengths of 48 Earth hours, with $\Omega_p \sim 3.8 \times 10^{-5}$ s^{-1}, and 24 Earth hours, with $\Omega_p \sim 7.5 \times 10^{-5}$ s^{-1} (ref. simulations EX02rf1 and EX02rf2, respectively). These simulations are discussed in Section 4.4.4.

4.4.1 Temperatures and Winds

Figure 4.13 displays the horizontal temperature map and winds at the upper boundary of the reference model EX02r. The globally averaged temperature at this level is 2960 K and the thermal escape parameter is ~122 (calculated for a mixture of H and H_2). The number of collisions that an escaping hydrogen atom suffers within one scale height is ~2.4, indicating that the 3.7 pbar level is indeed very close to the exobase. Thus it can be said that the atmosphere is stable, and only negligible Jeans escape erodes the top layers.

The substellar temperature is 3300 K, and the temperature drops across the terminator by ~1200 K, reaching down to 2200 K near the night side anti-stellar point. Using terms like ‘dawn’ and ‘dusk’ for a rotationally synchronised model makes little sense, but they are nevertheless adopted in the following discussion for convenience. The temperature increases towards the ‘dusk’ terminator, rising to 3500 K before falling in the night side. It is curious that the substellar point is not the hottest region on the dayside. Instead, it appears to be surrounded by a ‘hot ring’ displaced by about 60^o off-centre. This ring is ~200 K warmer than the substellar point. Along the ring, the temperature peaks in the dayside, near the ‘dawn’ terminator, reaching 3700 K there. In the night side the temperature minimum is shifted very slightly eastward from the anti-stellar point.

The winds emerge on the dayside, bringing material up from deeper thermosphere, and blow to the night side reaching maximum speeds of 1.6–2.0 km s^{-1} at high latitudes. The speed of sound in the outer layers is between 4.0 and 5.0 km s^{-1}, so the wind speeds remain subsonic. Along the equator, the zonal wind flows eastward across the anti-stellar point until it faces the opposing westward flow from the dayside near 220 degrees longitude. At this longitude the eastward flow flips underneath the strong westward flow. Having passed the ‘dawn’ terminator, the westward wind at high latitudes twists around into the equatorial eastward flow, enhancing it and creating a significant downwelling region along 220 degrees longitude. In general, downwelling is prominent along the terminator in the night side, in the region of the dramatic drop in temperature. Vertical divergence winds reach 30 m s^{-1}, but remain slow enough to justify the assumption of hydrostatic equilibrium.

Exploration of the model indicates that the enhanced temperatures in the ‘hot ring’ arise from the complex interaction between the composition and dynamics and the way these affect the energy balance. The winds slow down drastically at the terminator leading to advective heating in the region of the ‘hot ring’. This means that vertical downward winds develop around the terminator while upwelling is seen around the substellar point. Due to molecular diffusion, the mixing ratio of heavier molecules decreases more steeply with altitude than the mixing ratio of lighter species. Thus in upwelling regions, where vertical advection brings up material from deeper in the atmosphere, the local mixing ratio of H_2 increases whereas the opposite is true for downwelling regions. The H_2 mixing ratio peaks on the dayside and decreases towards the terminators. The mixing ratio of H correspondingly peaks in the night side and on the dayside it increases towards the terminators. The decreasing mixing ratio of H_2 and the increasing prevalence of H^+ (due to increasing mixing ratio of H) ensures that the formation of H_3^+ is dampened toward the terminator, and consequently the IR cooling rate drops off more steeply toward the terminator than the XUV heating rate or the ionising flux. The imbalance between heating and cooling keeps the ring warmer than the substellar point.

The slight temperature asymmetry between the ‘dawn’ and ‘dusk’ sides along the ‘hot ring’, evident in Figure 4.13, arises from the influence of the Coriolis force. In order to conserve angular momentum in a rotating system, the Coriolis force turns northward flow eastward, eastward flow toward the equator, westward flow toward the pole and southward flow westward in the northern hemisphere. In the southern hemisphere, southward flow is directed eastward, easward flow again toward the equator, westward flow toward the pole and northward flow westward (see equation 1.32).

From a steady state model like EX02r it is not immediately clear what is driving the circulation and causing the temperature variations. Instead the simulation should be monitored as it develops from the initial set-up. The start-up atmosphere for EX02r has a uniform temperature and zero winds everywhere, the composition is horizontally uniform and the vertical composition profile is akin to Jupiter’s neutral thermosphere. As the planet is exposed to uneven, strong insolation, the dayside quickly heats up while the night side stays cool. Initially the hottest region is around the substellar point. Strong winds develop between the two hemispheres, and the night side is then heated efficiently by horizontal advection, contraction and downwelling until rough energy balance is established and the winds slow down. Due to the Coriolis force eastward winds tend to be initially stronger than westward winds around the equator and the winds push the 'hot spot' eastward off the substellar point. Upwelling in the 'dusk' side then leads to an enhanced H_2 mixing ratio there compared to the 'dawn' side. This means that IR cooling peaks in the 'dusk' side and in steady state, the 'dawn' side is eventually warmer

There is one possible caveat to these arguments. The temperature on the dayside only varies by 200–400 K (6-13 % of the substellar temperature) and the peaks are located near the dramatic horizontal drop across the terminator. Any features near the region of the steep diurnal temperature drop can also arise from numerical irregularities because finite difference methods cannot easily deal with steep gradients. The 'hot ring' feature is not particularly significant in terms of the overall picture, so any interpretation of it should perhaps be offered with a pinch of salt.

In general, significant diurnal temperature differences only persist at pressures lower than $\sim$1 nbar. Deeper than this, the temperature is horizontally nearly uniform. This is due to the efficient distribution of energy by circulation. Figure 4.14 shows the temperature and winds at $\sim$55 nbar. At this level the temperature is uniform at 1500 K. There is a circumplanetary jet flowing around the equator and two vortices remain at high latitudes near the 'dawn' terminator. The wind reaches a maximum speed of $\sim$80 m s^{-1} in the night side. Deeper down the two high-latitude vortices shift from 'dawn' to 'dusk' and the wind slows down around the anti-stellar point.

4.4.2 Energy Balance

Figure 4.15 shows the steady-state substellar and anti-stellar P-T profiles for EX02r. The temperature increases with altitude rather steeply near the lower boundary. Between 500-2500 km (above the lower boundary) the gradient is slightly shallower. Above 2500 km in the night side the P-T profile is isothermal, but on the dayside the temperature increases from 2000 K to over 3000 K in the upper thermosphere, although near the upper boundary the profile becomes isothermal. It should be noted that the upper boundary condition imposes isothermality at the two uppermost pressure levels. This condition is appropriate because overall the model produces an isothermal P-T profile naturally in the outer layers below the upper boundary. This P-T profile reflects the balance of the energy equation terms. Figure 4.16 shows the volume heating and cooling rates (W m^{-3}) plotted with pressure and altitude for both the day-and night hemispheres.

On the dayside the stellar heating rate shows two peaks, one centred around 7 nbar and one near the lower boundary. For wavelengths between 30 and 105 nm, the region where the optical depth becomes unity is between 12 and 0.7 nbar, i.e. near the upper peak. In this region the radiation is primarily absorbed by H_2 and H. The high energy X-rays and EUV radiation (with wavelengths less than 30 nm) penetrate deep into the lower boundary region. At wavelengths less than 5.0 nm the optical depth of

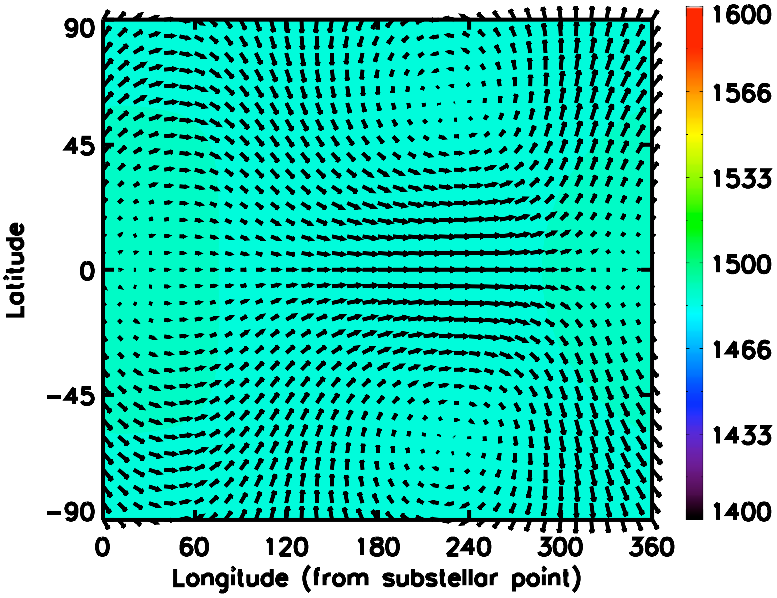

Figure 4.14: Temperatures and winds from EX02r (0.2 AU) at 55 nbar. The temperature is nearly uniform at 1500 K. The maximum zonal wind speed is 80 m s^{-1}.

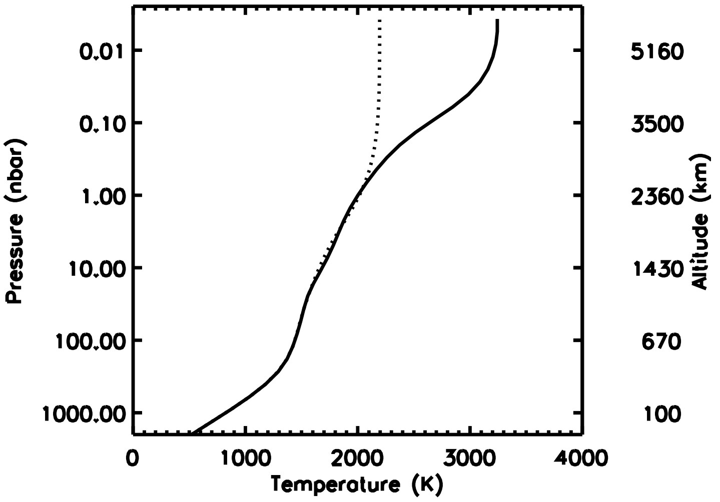

Figure 4.15: Substellar and antistellar temperature profiles for EX02r at 0.2 AU. The solid line is the substellar profile and the dotted line is the antistellar profile. Altitudes are given in km above the lower boundary (2 μbar) and they apply to the dayside profile although only the highest altitude point on the dayside differs from the night side.

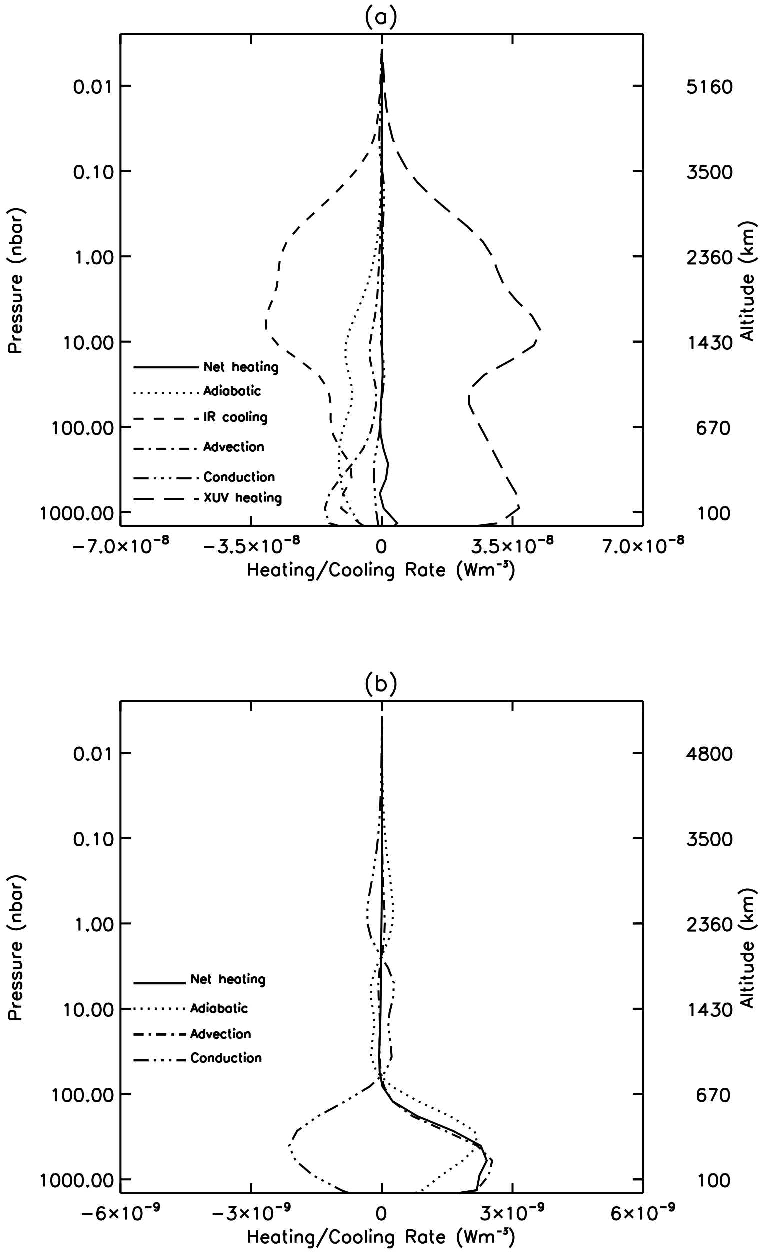

Figure 4.16: Dominant heating and cooling terms in the energy equation (3.3) for EX02r (a) at the substellar point and (b) at midnight. Altitudes are given in kilometres above the lower boundary (2 μbar) for both profiles.

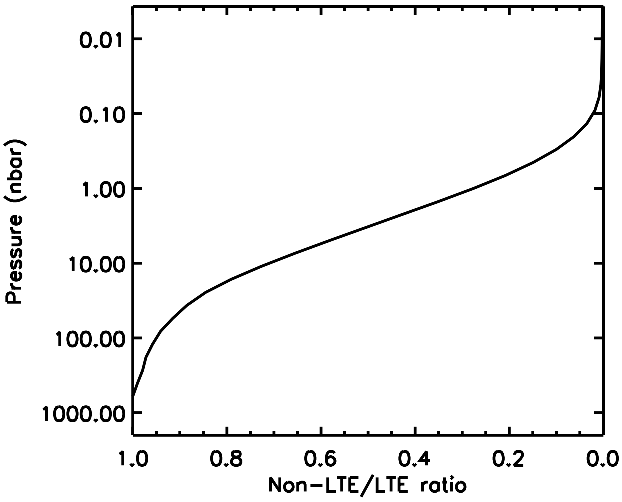

Figure 4.17: The ratio of the H_3^+ total non-LTE cooling rate to the total LTE cooling rate as a function of pressure at the substellar point of EX02r, orbiting at 0.2 AU. The ratio reduces to less than one part in thousand at high altitudes near the exobase.

unity is reached near or below the lower boundary. The mixing ratio of helium exceeds that of H at pressures higher than ~100 nbar. The photoabsorption cross section of helium at high energies is roughly an order of magnitude higher than those of H_2 or H. This together with the increasing concentration of helium in the lower thermosphere gives rise to the lower heating peak. Figure 4.16 indicates that the dayside is near steady state throughout, and certainly so in the upper thermosphere. Between 55 and 0.1 nbar the XUV heating is efficiently balanced by H_3^+ cooling. In the deeper thermosphere the balance is between XUV heating and cooling due to expansion of the atmosphere, upward convection and H_3^+ emissions. Near the exobase, the departure from LTE conditions stamps out H_3^+ cooling. Indeed, as Figure 4.17 shows, the actual cooling rate reduces to less than 1 % of the expected LTE cooling rate at the exobase level. Thus, in the upper thermosphere the energy balance is between XUV heating and downward conduction.

On the night side the upper thermosphere is heated by contraction and downward advection, and this heating is balanced by cooling due to downward conduction. Between 55 nbar and 3 nbar the atmosphere is cooled slightly by expansion and vertical advection that drive a weak westward return flow near the 'dusk' terminator. Deeper down the thermosphere is again heated by contraction and downwelling, and the heating is balanced by downward conduction. Figure 4.16 indicates that the lower thermosphere in general is not in exact steady state. This, however, is not very significant as the temperatures have stabilised, and the remaining heating rates are relatively small. In steady state, transport of energy by advection does not play a notable role, but in balancing the temperatures between the two hemispheres during the early evolution of the run it is crucial.

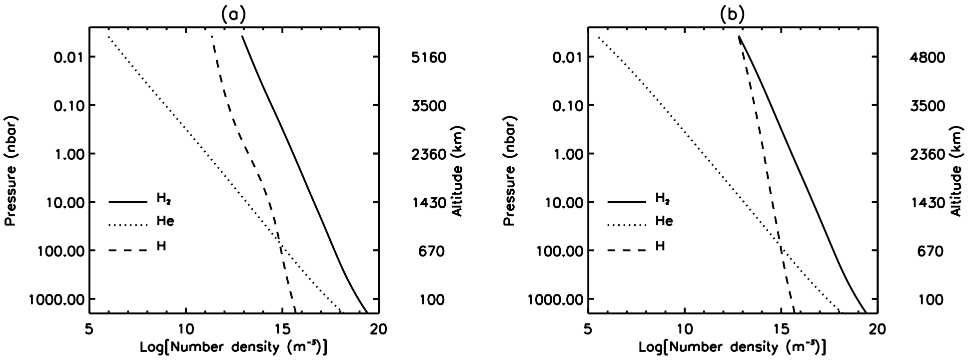

Figure 4.18: Number densities of H_2 (solid line), He (dotted line), and H (dashed line) at (a) the substellar point and (b) the antistellar point of EX02r.

4.4.3 The Composition

Figure 4.18 shows the number densities of the neutral species H, H_2 and He with pressure and altitude at the substellar and anti-stellar points. Figure 4.19 is an equatorial plot of the mixing ratio of H at 8.2 pbar, which is the uppermost pressure level for which the mixing ratios are solved from the equation of continuity (3.4). Above this level the mixing ratios are based on the boundary condition that imposes diffusive equilibrium in the outer two layers. The mixing ratio of He decreases from 5.5 % at the lower boundary to virtually zero at 7 nbar. This makes helium chemistry irrelevant in the upper thermosphere. On the dayside, the mixing ratio of H_2 is over 90 % at all levels, but in the night side it drops to 50 % between 1 nbar and 3.7 pbar. At the 8.2 pbar level the mixing ratio of H varies from 2–3 % on the dayside to 40 % in the night side. This distribution arises from upwelling and downwelling on the dayside and in the night side, respectively, as explained in section 4.4.1. Overall, it is clear that H_2 is the dominant species in the thermosphere and that thermal dissociation is insignificant. At pressures higher than 7 nbar the mixing ratios become horizontally nearly uniform, indicating that the neutral species are efficiently mixed by advection.

Figure 4.20 shows the substellar ion density profiles. H^+ is the dominant ion, with a peak density of $\sim 10^{13}$ m^{-3} centred at 7 nbar. It is formed by photodissociation of H_2 (see Table 3.1, reactions 1b and 1c), photoionisation of H_2 followed by reaction 12, and direct photoionisation of H. H_3^+ is the second most abundant ion, with a peak density of $\sim 10^{11}$ m^{-3} near the lower boundary. The vertical profile shows an upper peak with a density of $\sim 5 \times 10^{10}$ m^{-3} near the 0.06 nbar level. The substellar column densities of H^+ and H_3^+ are 2.5×10^{19} m^{-2} and 1.8×10^{17} m^{-2}. Overall, H_2^+ is effectively converted into H_3^+ by reaction 7, although H_2^+ begins to catch up with H_3^+ near the exobase. He^+ appears rather insignificant throughout the thermosphere. This justifies the partial omission of helium photochemistry (pathways including HeH^+).

There is an element of anticorrelation in the H^+ and H_3^+ profiles. This is due to the varying electron content of the thermosphere. The lifetime of H^+ at 1 nbar is $\sim$4 hours whereas at the same level the

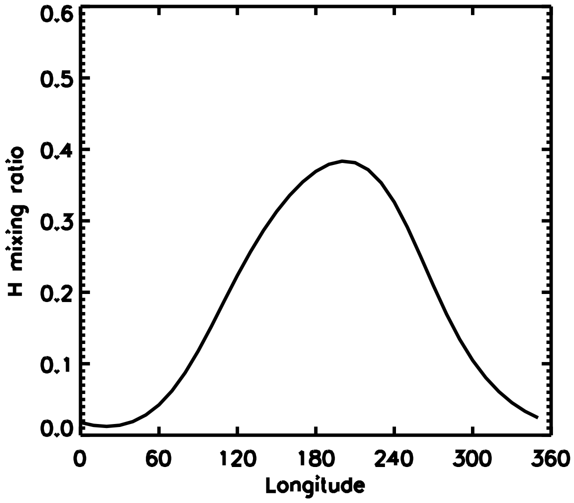

Figure 4.19: The volume mixing ratio of atomic hydrogen plotted along the equator of EX02r at the 8.2 pbar pressure level. The mixing ratio has a maximum in the night side that arises from downward advection carrying heavier hydrogen molecules toward deeper layers.

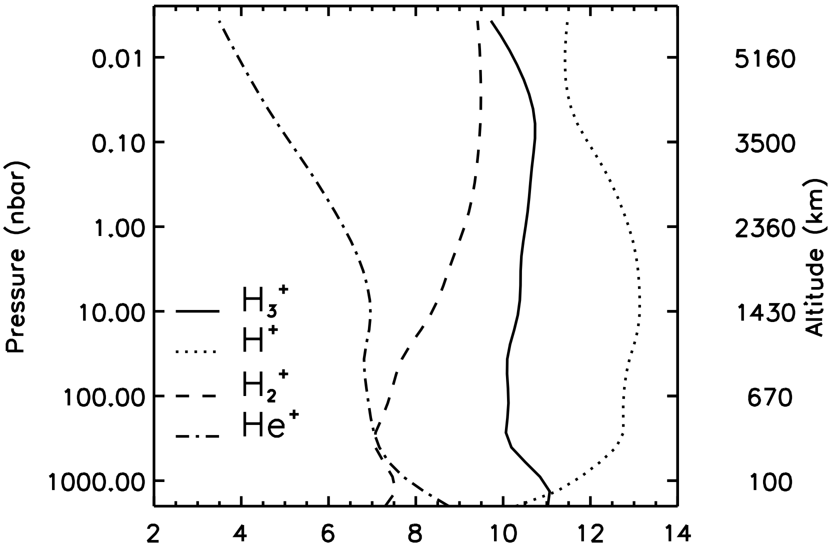

Figure 4.20: Number densities of H^+, H_2^+, H_3^+ and He^+ at the substellar point of EX02r.

lifetime of H_3^+ is ~ 4 s. At 1 nbar most of the electrons arise from photoionisation of H and H_2. Increasing density of H^+ leads to increasing electron densities, and this leads to enhanced recombination of H_3^+ while the relatively long-lived H^+ remains stable in the background.

In general, the lifetime of H_3^+ is very short throughout the thermosphere, ranging from a few seconds to a few minutes at most. The same applies to H_2^+ and He^+. The lifetime of H^+, on the other hand, varies from a few minutes in the lower thermosphere to ~40 hours near the exobase. In other words, the assumption of photochemical equilibrium is likely to be valid throughout the lower thermosphere, but with H^+ it becomes questionable in the upper thermosphere where transport of H^+ along magnetic field lines or otherwise is likely to be significant. It is interesting that the same situation appears to hold in Jupiter's ionosphere where H^+ is also the only ion with a relatively long lifetime.

Figures 4.18 and 4.20 indicate that the density of H^+ becomes comparable to the density of H in the upper thermosphere, but that all ion densities are negligible compared to the overall neutral density on all levels. The assumption that photochemistry has negligible direct impact on neutral densities that are constrained by the ideal gas law and distributed horizontally and vertically by advection and diffusion, may appear questionable because the densities of H and H^+ are expected to be comparable in the upper thermosphere. This need not worry us too much, though, because H^+ is also formed by photodissociation and ionisation of H_2, and the number density of H_2 is everywhere much greater than the number density of any of the ions.

4.4.4 Fast Rotators at 0.2 AU

We turn now to the effects of asynchronous rotation on the thermosphere. This could be significant because EGPs orbiting near 0.2 AU, such as ρ CrB b, are not likely to be rotationally synchronised. Intuition tells us that faster rotation should lead to stronger Coriolis forces and thus more effective redistribution of heat around the atmosphere. Diurnal temperature difference should be smoother and the temperatures on the dayside should be lower. Curiously, this intuition turns out to be wrong. In fact, stronger Coriolis forces and more vigourous circulation result in more effective redistribution of atomic hydrogen around the thermosphere and thus higher mixing ratio of H on the dayside. If rotation is fast enough, this affects the formation of H_3^+ and once the cooling function is lost, the thermosphere heats up and expands.

Figure 4.21 displays the temperatures and winds at the 3.7 pbar and 55 nbar pressure levels for EX02rf1, a model of a planet that rotates around its axis in 48 Earth hours. Compared to EX02r, the globally averaged exospheric temperature in this model is ~160 K higher, and the dayside is warmer by over 400 K. The P-T profiles of the two models diverge only at pressures lower than 0.3 nbar. Overall, then, the temperature difference is not that significant, especially if other possible sources of error and uncertainties are taken into account.

The horizontal temperature map and circulation in EX02rf1 are qualitatively similar to EX02r. Overall, as Figure 4.21 indicates, the wind blows from the dayside to the night side at the upper boundary.

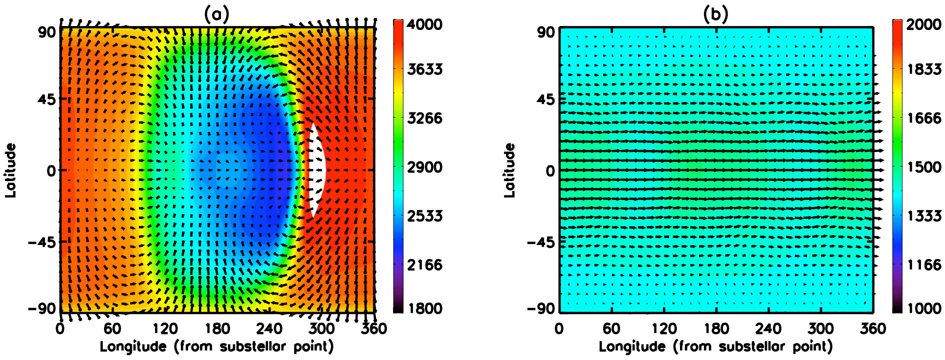

Figure 4.21: Temperatures and winds from EX02rf1 (0.2 AU) at (a) 3.7 pbar and (b) 55 nbar. At the 3.7 pbar pressure level the dayside temperature is about 3700 K. The white spot shows the 'dawn' temperature maximum. The feature is slightly exaggerated by the temperature colour scaling that was chosen to highlight the day-night contrast and the night side temperature distribution. Nevertheless it is still ∼500 K warmer than its surroundings. The maximum zonal wind speed is ∼4 km s^{-1}. At the 55 nbar level the temperature is nearly uniform at 1500 K. The maximum zonal wind speed is 450 m s^{-1} along the equator.

In the dusk side the Coriolis force directs the flow into a downwelling region located along the equator at about 120 degrees longitude. Consequently the eastward zonal wind slows down considerably at the dusk terminator. However, in the night side the zonal wind blows eastward along the equator until it faces the westward wind at dawn. This westerly night wind draws gas from the high-latitude eastward wind that is directed into it by pressure gradients and the Coriolis force, the high-latitude westward wind that is twisted around into it, and slight upwelling in the pre-midnight section. Circulation makes the pre-midnight side in the night side slightly warmer compared to the dawn side. In general, circulation is stronger than in EX02r, and zonal wind reaches maxima of 3.0–4.5 km s^{-1} at high latitudes.

On the dayside the dawn temperature enhancement is sharper than in EX02r and in the meridional direction the 'hot ring' feature is absent, leaving the equator as the warmest latitude band. Presumably, the mechanism for creating the temperature enhancement is the same as in EX02r. Initially, westerly winds force the 'hot spot' eastward from the substellar point. Thus on the dusk side the upwelling of H_2 leads to enhanced H_3^+ densities compared to the rest of the day hemisphere and hence more effective cooling.

At 55 nbar the temperature is nearly uniform around 1500 K. There is a broad, circumplanetary eastward zonal jet flowing around the planet. It is faster and more uniform than the corresponding jet in EX02r, with equatorial wind speed ranging from 400 to 500 m s^{-1}.

The globally averaged mixing ratios of atomic hydrogen in EX02r and EX02rf1 are 22 % and 23 %, respectively. These values are very similar but the horizontal distributions of atomic hydrogen are very different. Figure 4.22 contrasts the equatorial mixing ratios of H at the 8.2 pbar pressure levels between

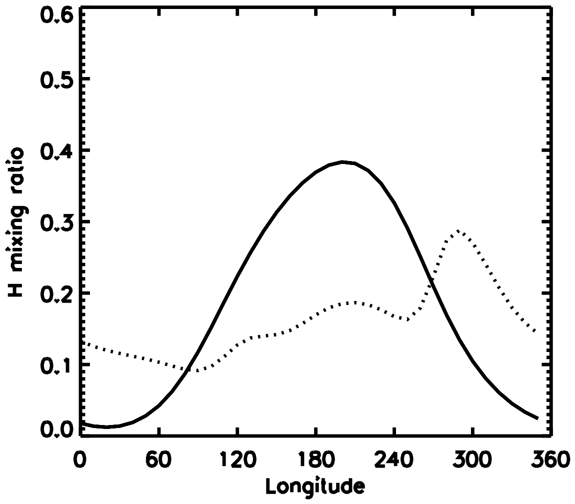

Figure 4.22: The volume mixing ratio of atomic hydrogen at the 8.2 pbar pressure level plotted along the equator of EX02r (solid line) and EX02rf1 (dotted line). EX02r is tidally locked and EX02rf1 rotates around its axis in 48 Earth hours. The latter simulation distributes H more evenly around the thermosphere because faster rotation breaks the simple symmetry of dayside upwelling and night side downwelling.

the two models. On the dayside, the mixing ratio of H in EX02rf1 is 13 %, compared to 2-3 % in EX02r. The mixing ratio of H peaks in the night side of EX02r, and there it is generally higher than the night side mixing ratio of H in EX02rf1. In contrast, the concentration of H peaks near the dawn temperature enhancement in EX02rf1. In both cases the mixing ratio appears to anticorrelate with the equatorial temperature profile. The horizontal distribution of H_3^+ mirrors these features. The upper thermosphere of EX02rf1 is slightly warmer than that of EX02r because there is less H_3^+ in it.

Overall, it does not appear to make much difference if the model is tidally locked or rotating asynchronously in 48 Earth hours. However, the situation changes dramatically if the rotation rate is doubled so that it corresponds to 24 Earth hours. In this case the dynamic redistribution of atomic hydrogen to the dayside is so effective that the H_3^+ cooling rate is significantly lowered. Consequently the temperature rises rapidly and becomes high enough to dissociate H_2. As H_2 is removed, H_3^+ cannot form, and the subsequent further loss of infrared cooling launches a runaway process in which the whole upper thermosphere is converted into atomic hydrogen. The exospheric temperature rises to ~20,000 K and the outer envelope expands beyond 2 R_p. As the thermal escape parameter approaches 1.5 at the upper boundary, the atmosphere begins to undergo fast hydrodynamic escape.

Figure 4.23 contrasts the substellar P-T profiles from EX02rf1 and EX02rf2. At pressures higher than about 7 nbar, which in both models corresponds to an altitude below 1800 km, the P-T profiles are nearly identical. Figure 4.24, which shows the infrared cooling rates from both models, indicates

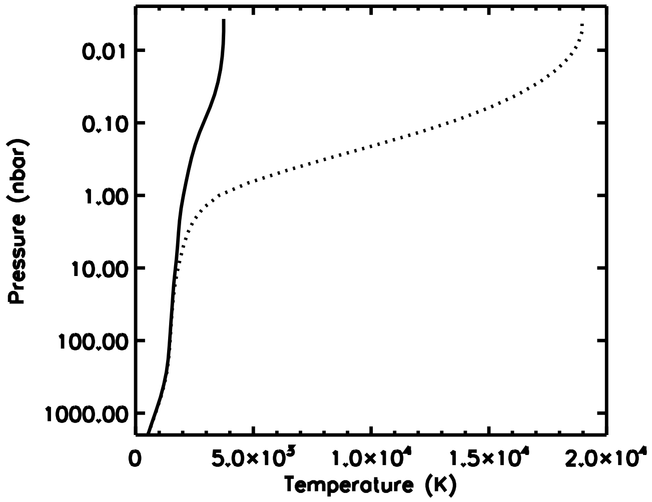

Figure 4.23: Substellar temperature profiles for EX02rf1 (solid line) and EX02rf2 (dotted line) at 0.2 AU. EX02rf1 rotates around its axis in 48 Earth hours while EX02rf2 rotates in 24 Earth hours. The difference between the two models is dramatic, with the faster rotating model being much hotter due to effective horizontal mixing of atomic hydrogen in the thermosphere.

that the lower thermosphere is effectively cooled by H_3^+ emissions in both simulations. In EX02rf2 the temperature increases rapidly with altitude at pressures lower than 7 nbar, and rises to ∼19,000 K near the upper boundary. In EX02rf1, the altitude of the upper boundary is only 5000 km, while in EX02rf2 it is over 60,000 km. The difference in temperature is reflected by the cooling rates is shown in Figure 4.24. The reader should note that the data plotted for EX02rf2 applies at the onset of hydrodynamic escape, at which point the model is stopped. EXOTIM cannot be used for realistic simulations of hydrodynamic escape because the bulk outflow, or planetary wind, that this condition implies violates the assumption of hydrostatic equilibrium (see Chapters 5 and 7 for further discussion).

Figure 4.25 shows the dayside mixing ratios of H from the two models. Again, the mixing ratios are similar in the lower thermosphere, but differ drastically in the upper thermosphere. For EX02rf2, atomic hydrogen is the dominant species at pressures lower than 2 nbar (above 2000 km) and the thermosphere is entirely composed of atomic hydrogen at pressures lower than 0.7 nbar (above ∼3000 km). Much of the hydrogen is ionised at high altitudes and thus near the upper boundary the dominant species is H^+. In other words the planet is surrounded by a huge shell of first partly and then nearly fully ionised plasma.

Figure 4.26 shows the temperatures and winds at the upper boundary of EX02rf2 at the onset of hydrodynamic escape. The results should be treated with caution as the simulation did not reach steady state. Bulk outflow through the upper boundary is likely to alter the P-T profiles in the atmosphere significantly, and as ionisation is significant in the outer envelope, the assumption of negligible ion

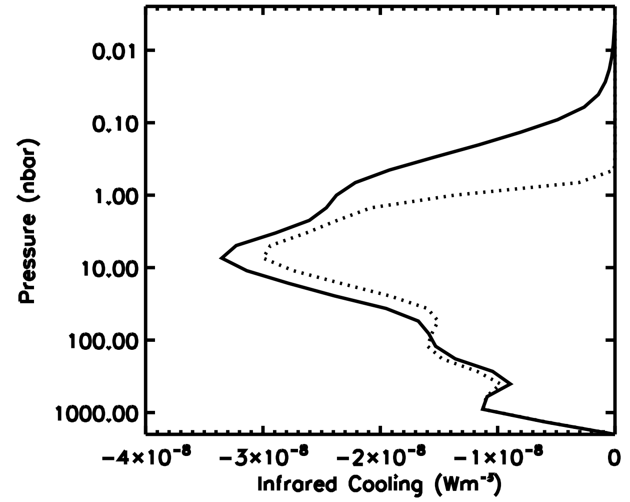

Figure 4.24: Substellar H_3^+ cooling rate profiles for EX02rf1 (solid line) and EX02rf2 (dotted line) at 0.2 AU. EX02rf1 rotates around its axis in 48 Earth hours while EX02rf2 rotates in 24 Earth hours. The infrared cooling rates are similar in the lower thermosphere but at pressures lower than 7 nbar infrared cooling is much less significant for faster rotation.

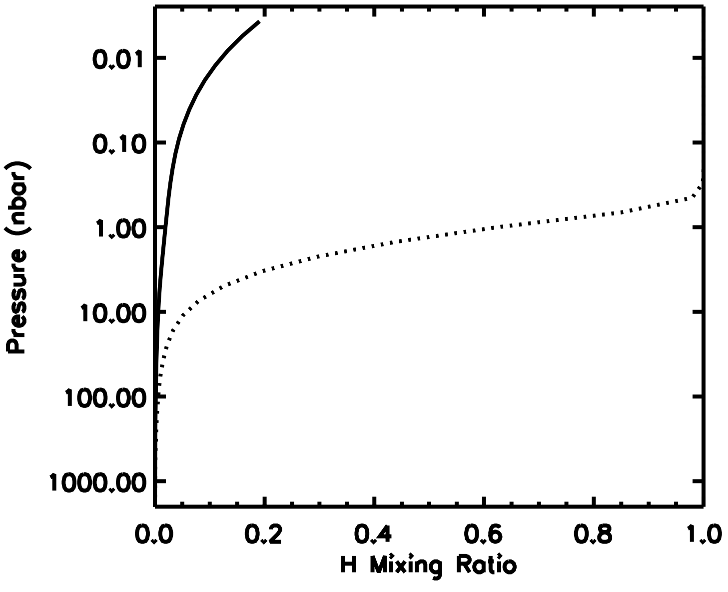

Figure 4.25: Substellar mixing ratios of atomic hydrogen for EX02rf1 (solid line) and EX02rf2 (dotted line) at 0.2 AU. EX02rf2 is surrounded by a huge shell of H and H^+ plasma.

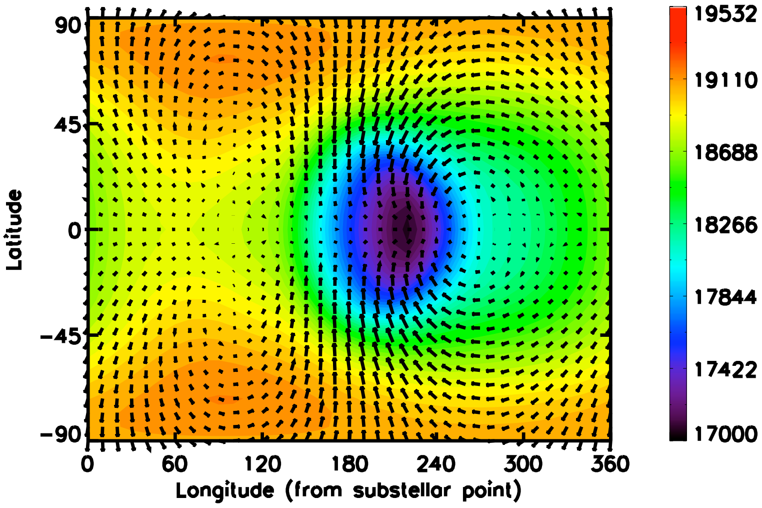

Figure 4.26: Temperatures and winds from EX02rf2 (0.2 AU) at 3.7 pbar. The temperature ranges between 19,000 and 19,500 K on the dayside and drops to 17,000 K in the night side ‘cool spot’. The highest temperatures are found near the poles. The maximum wind speed is ∼3 km s^{-1}.

fractions is not valid (see Section 3.4). However, some crude characteristics can be identified with some confidence from Figure 4.26. First, the temperature is fairly uniform horizontally, showing only about 10 % diurnal variation and less than 500 K meridional variation on the dayside. This is partly due to effective redistribution of heat by circulation, but it is also due to fact that in the low-density outer envelope radiation penetrates past the terminator deep into the night side. Second, despite the extreme temperatures in the envelope, the wind speeds are relatively low, with maxima of only 1.0–3.0 km s^{-1}. The equatorial upwelling region is shifted eastward by about 60 degrees along the equator, and it feeds the winds that blow toward the downwelling region around the night side ‘cool spot’. Curiously the highest temperatures are found near the poles.

What is clear from this analysis is that the evaporation rate of the atmosphere depends on the rotation rate of the planet around its axis. Chapter 5 shows that the stability limit (against hydrodynamic escape) for a tidally locked Jupiter orbiting the Sun lies between 0.1 and 0.2 AU. This tidally locked limit also applies to a planet rotating asynchronously in 48 Earth hours. However, if the planet rotates faster, the limit is shifted further out from the star. Note that the upper boundary temperature of EX03r, which orbits at 0.3 AU and rotates around its axis in 24 hours, is only 2670 K (see Figure 4.11 and Table C.1). Thus the thermosphere is relatively thin and stable at 0.3 AU, and this implies that for a Jupiter-type EGP rotating in 24 hours the stability limit lies between 0.2 and 0.3 AU.

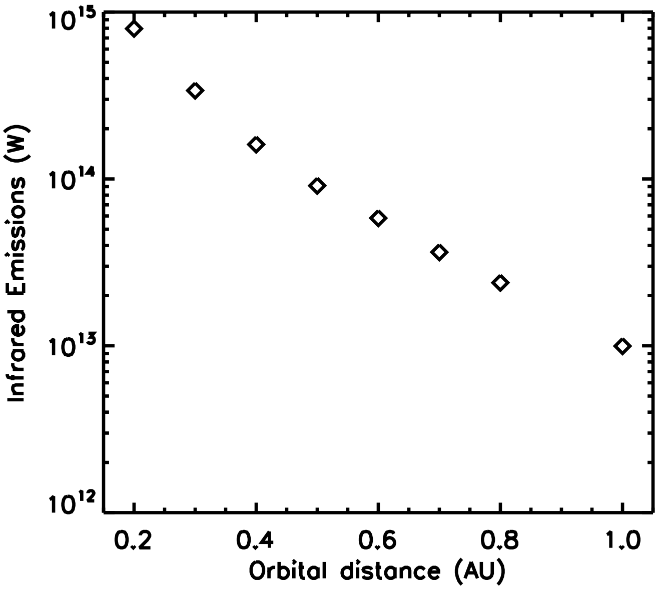

Figure 4.27: Total observable output power from H_3^+ infrared emissions (W) versus orbital distance.

4.5 H_3^+ Emissions

Figure 4.27 is a plot of the total observable output power from H_3^+ infrared emissions versus the orbital distance. The emission rates (per steradian) were multiplied by 2π because radiation lost into the lower atmosphere does not contribute to observable fluxes. It is not radiated to space unless the thermosphere is inflated compared to the radius of the planet. In all cases it was assumed that the thermosphere is optically thin in the infrared and that any outgoing radiation escapes directly to space. The total output power varies from 1.0×10^{13} W at 1.0 AU to 8.0×10^{14} W for the tidally locked model at 0.2 AU. Table 4.3 shows the individual line emissions, that may be observable in the future. The results were calculated for the same simulations that were used to compile Figure 4.11.

The emission rates for EX02rf1 and EX02rf2 are 8.0×10^{14} W and 7.0×10^{14} W, respectively. Overall, asynchronous rotation does not appear to alter the observable fluxes significantly. Even for EX02rf2, which is surrounded by a hot atomic hydrogen envelope, the total emission rate is not much lower compared to the tidally locked or slowly rotating case. This is due to the fact that H_3^+ survives in the lower thermosphere (at least initially) and the increased emission rate there compensates for the loss of H_3^+ in the outer envelope.

Observations of H_3^+ can be used to constrain the properties of the thermosphere. If emissions are not observed at predicted levels, the thermosphere is likely to be composed of H and H^+ and it should be relatively hot and inflated. The outer envelope should also begin to undergo hydrodynamic escape further out from the host star compared to the case where H_3^+ is regulating the thermospheric temperatures. If emissions are detected, the observations will help to characterise the thermosphere, and possibly imply

Table 4.3: H_3^+ emissions for specific spectral lines

Distance (AU)	Q(3,0-) (W)	R(6,6+) (W)[a]
0.2	7.39×10^{12}	1.06×10^{13}
0.3	4.15×10^{12}	5.63×10^{12}
0.4	2.04×10^{12}	2.76×10^{12}
0.5	1.28×10^{12}	1.70×10^{12}
0.6	9.08×10^{11}	1.18×10^{12}
0.7	7.56×10^{11}	9.49×10^{11}
0.8	5.53×10^{11}	6.80×10^{11}
1.0	3.23×10^{11}	3.79×10^{11}

---

[a] Total integrated emission rate in W

that the atmospheres of EGPs are stable further in toward the star than previously believed. The difficulty here is that the predicted signals are too weak for current observing techniques. Shkolnik et al. [2006] point out that the lower limit for a detection from an EGP orbiting at 0.24 AU around a Sun-like star (such as 55 Cnc c, for example) with the best ground-based telescopes is 1.2×10^{18} W in terms of the total observable output power. The fluxes predicted here are four orders of magnitude lower than this limit, and thus a detection in the near future is unlikely.

4.6 Caveats and Parameter Variations

4.6.1 Composition

A diligent reader will have noticed that the model assumes fixed composition at the lower boundary, and that the neutral mixing ratios there have been taken from a 1D model of the Jovian auroral ionosphere by Grodent et al. [2001] (see Section 3.8). This means that the lower boundary mixing ratios of H_2, H and He are 0.944, 0.056 and 1.8×10^{-4}, respectively. There is no reason to believe that these Jovian values apply to EGPs in general, and in fact it is very unlikely that they do.

Unfortunately, as was pointed out in Chapter 2, lower atmosphere chemical models are not in agreement on what the composition of different EGPs should be and current observations are too limited to discriminate between different models. Also, existing work tends to concentrate on photospheric pressure levels (between 1.0 bar and a few mbar). At our lower boundary of 2.0 μbar, the composition could be very different compared to the photosphere. Given these uncertainties, it appears reasonable to assume Jovian conditions at the lower boundary, although this is not necessarily realistic.

The most important factor affecting these simulations is the mixing ratio of atomic hydrogen because it has a profound effect on the photochemistry in the thermosphere. If the mixing ratio is high, there will be less H_3^+ and the thermosphere will be hotter. Liang et al. [2003] studied the production of atomic hydrogen in the atmosphere of HD209458b by using a one-dimensional, photochemical diffusive, diurnally averaged model including hydrocarbon and oxygen chemistry. This model extends to μbar and even nbar levels.

The photochemistry of oxygen and hydrocarbons is based on the parent molecules H_2O, CO, and CH_4, and it is driven by the stellar UV radiation. The abundances of the parent molecules are determined by thermodynamic equilibrium chemistry in the deep atmosphere. Liang et al. [2003] used P-T profiles and chemical abundances calculated by Seager et al. [2000]. The hydrocarbon photochemical scheme in the model is based on Jovian hydrocarbon chemistry, where photodissociation of CH_4 and subsequent reactions produce all the hydrocarbons present in the atmosphere. Oxygen photochemistry was added as photochemistry involving CO and H_2 is likely to be significant in EGP atmospheres. In this setting, the main sources of atomic hydrogen are from photodissociation of H_2, CH_4 and H_2O.

Liang et al. [2003] point out that the mixing ratio of atomic hydrogen is not very sensitive to exact abundances of the parent molecules. Their results indicate that an order of magnitude change in any of parent molecule abundances changes the amount of atomic hydrogen only by a factor of 1-2. Thus the production of atomic hydrogen is simply limited by the available UV flux. For HD209458b the mixing ratio increases with altitude and reaches ~1 % at the μbar level and several percent higher in the thermosphere. However, the results are not likely to be very accurate, especially at thermospheric altitudes, because the model does not include XUV heating. The temperature profile adopted from Seager et al. [2000] decreases with altitude and the temperature is below 1000 K throughout the upper atmosphere and this is clearly incorrect. Higher temperature favours CO and H_2 over CH_4 and H_2O. In addition, heavier molecules tend to fall off from the thermosphere under molecular diffusion. Also, our simulations indicate that the density of H^+ decreases with increasing pressure toward the lower boundary, indicating that photodissociation of H_2 does not appear to be an important source of atomic hydrogen near the lower boundary.

It remains to be seen what the mixing ratio of atomic hydrogen at the μbar level should be, and how it compares to Jupiter. As it could have an impact on our results, we have explored the effects of changing the lower boundary mixing ratio as a simple parameter variation. In order to do this, two additional models of EGPs orbiting at 0.2 AU were generated: one in which the lower boundary mixing ratio is fixed at 0.1 % and one where it is 1 %. These models are otherwise similar to EX02r, and they are labelled EX02rh1 and EX02rh2, respectively.

The XUV flux hitting the planet scales as $F_{XUV} \alpha a^{-2}$, where a is the orbital distance, and hence the flux on HD209458b is 13,400 times that on Jupiter (the orbital distances are 0.045 AU and 5.2 AU, respectively). The XUV flux hitting an EGP orbiting at 0.2 AU, however, is only 676 times that on Jupiter and 20 times less than the flux hitting HD209458b. As the lower boundary mixing ratio of atomic hydrogen depends on the flux of UV photons, it should be more than the Jovian value but still less than 1% for an EGP orbiting at 0.2 AU.

Figure 4.28 shows the substellar and equatorial mixing ratios of atomic hydrogen from EX02r,

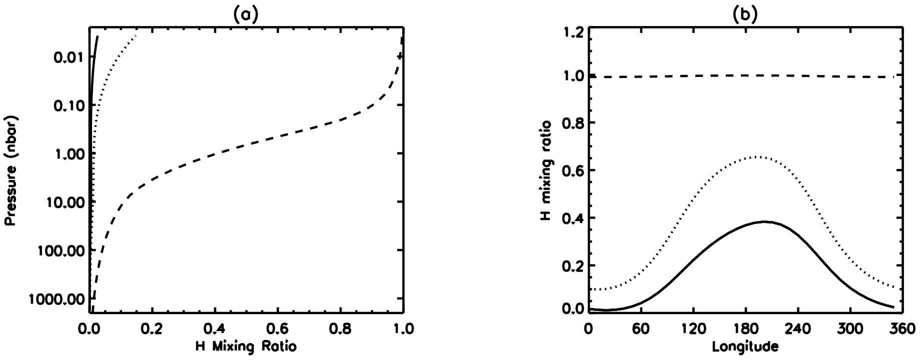

Figure 4.28: Volume mixing ratios of atomic hydrogen (a) at the substellar point and (b) along the equator at the 8.2 pbar level from EX02r (solid line), EX02rh1 (dotted line) and EX02rh2 (dashed line). The lower boundary mixing ratios are 0.0002, 0.001 and 0.01, respectively. Due to molecular diffusion atomic hydrogen is the dominant species in EX02rh2 at pressures lower than 1 nbar.

EX02rh1, and EX02rh2. Figure 4.29 compares the substellar P-T profiles in these models. Increasing the lower boundary mixing ratio by an order of magnitude from 0.01 % to 0.1 % does not significantly alter the general outcome, although it results in more atomic hydrogen in the thermosphere. On the dayside, near the upper boundary, the mixing ratio of H is ∼10 % compared to 2-3 % in EX02r. In the nightside, it increases from about 40 % in EX02r to over 60 % in EX02h1. Naturally, this means that there is slightly more H^+ in the upper layers of EX02rh1 and less H_3^+, but the difference is not significant and it does not affect the region where most of the XUV radiation is absorbed. Thus cooling rates are not affected and as a result the substellar P-T profiles are very similar in these models, although the upper boundary temperature is about 400-500 K warmer in EX02rh1. The exospheric thermal escape parameters (based on globally averaged field variables and composition) in EX02r and EX02rh1 are 120 and 96, respectively, and the exobase altitudes are nearly identical. Both models are stable and the prominent form of evaporation is Jeans escape of negligible magnitude.

The situation is very different for EX02rh2. Atomic hydrogen overtakes H_2 at pressures lower than 1 nbar, or above 3000 km, and consequently H_3^+ disappears from the upper thermosphere. The atmosphere heats up and expands, because it is not cooled adequately by infrared emissions from H_3^+. The P-T profile shown in Figure 4.29 for EX02rh2 does not depict steady state conditions, and in fact the model heats up further and becomes unstable once the simulation continues.

In general, we have now identified two major caveats that might affect the results presented in this chapter (and possibly in Chapter 5). First, if the planet rotates asynchronously and reasonably fast, with $\Omega_p \sim 7.5 \times 10^{-5}$ s^{-1} or faster, the limiting distance for hydrodynamic escape is somewhere between 0.2 AU and 0.3 AU. Otherwise the thermosphere is stable down to 0.2 AU and effectively cooled by H_3^+ emissions from the dayside. Second, the thermosphere is sensitive to the composition of the lower atmosphere and in particular, the mixing ratio of atomic hydrogen at the lower boundary altitude. The

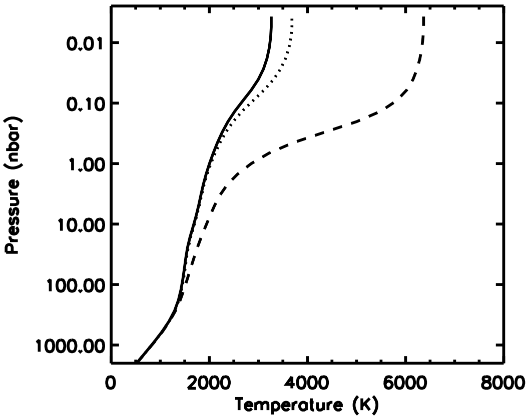

Figure 4.29: Substellar P-T profiles from EX02r (solid line), EX02rh1 (dotted line), and EX02rh2 (dashed line). As atomic hydrogen takes over in the upper thermosphere of EX02rh2, H_3^+ is removed and infrared cooling is greatly diminished. As a result the thermosphere heats up and expands. The P-T profile for EX02rh2 is not a steady state profile, and eventually the model becomes unstable and the atmosphere undergoes hydrodynamic escape.

results are unaffected if this mixing ratio is raised from 0.01 % to 0.1 %. In this case the model remains stable at 0.2 AU. However, if the mixing ratio is increased to 1 % at the lower boundary, atomic hydrogen overtakes H_2 as the dominant species in the upper thermosphere. Consequently, the balance between infrared cooling and XUV heating is lost and the thermosphere escapes hydrodynamically at least within 0.3 AU, as suggested by Lammer et al. [2003]. Note, however, that the dominance of atomic hydrogen in this case is not initially due to thermal dissociation of H_2. Instead it is a result of molecular diffusion, which requires the heavier H_2 molecule to fall off with altitude more steeply than lighter H. Molecular diffusion can be disturbed by vertical outflows or turbulence, which bring more H_2 up from deeper layers. Such outflows, if strong enough, can alter the H mixing ratio profiles presented here and even enhance the abundance of heavier molecules such as CH_4 or CO in the thermosphere.

The potential significance of the presence of heavier molecules has been ignored in this study. There is no agreement if the dominant trace species near the lower boundary is CO or CH_4 so both chemistries would have to be included. Hydrocarbon and oxygen photochemistry together with radiative transfer driven by the parent molecules and their reaction products would constitute an enormous complication to the model, which is beyond the reach of this PhD thesis. Also, their inclusion may not be necessary for a first order stability study like this. Even if hydrocarbon or oxygen species are present, due to molecular diffusion their mixing ratios are likely to be orders of magnitude less than the mixing ratios of H_2, He and H, at least in stable thermospheres. A comparison between the models of Yelle [2004] and García Muñoz [2007] shows that for realistic mixing ratios of the parent molecules CO, CH_4 and N_2, the inclusion of oxygen, nitrogen or hydrocarbon photochemistry does not affect the basic results obtained for simple H_2-He-H chemistry.

It is interesting that in their H_2-He-H simulations both Yelle [2004] and García Muñoz [2007] have assumed a lower boundary mixing ratio for atomic hydrogen, which is of the same order of magnitude as the one we have used. This is despite the fact that their models purport to simulate HD209458b, where the H mixing ratio could be as high as 1 % at μbar pressures. The escape rates they have derived for simple chemistry may be too low because an underestimated H mixing ratio at the lower boundary produces exaggerated H_3^+ cooling rates.

4.6.2 Lower Boundary Circulation

The assumption of zero winds at the lower boundary is unlikely to be accurate. It was pointed out in Chapter 2 that existing models disagree on the nature of circulation at the photospheric level, and that circulation regimes could be very different on different EGPs. Also, there are no estimates of the nature of circulation or wind speeds at the 2 μbar level. At first glance the zero winds assumption seems wildly unrealistic, but it turns out that in the orbital range where the effective temperature is below 1000 K neither that nor the fixed lower boundary temperature have a significant effect on the results. This is due to the strength of the XUV forcing in the thermosphere. Most of the XUV flux is absorbed above the lower boundary and the uneven forcing then dominates the temperature and circulation patterns instead of the fixed boundary conditions.

Two models of tidally locked, Jupiter-type EGPs orbiting a Sun-like host at 0.24 AU, EX024r and EX024rw, were generated to demonstrate the insignificance of the lower boundary conditions. The reference model EX024r assumes zero winds at the lower boundary, but in EX024rw winds and horizontal temperature gradients have been added to the lower boundary. The simulations are purely hypothetical and they are meant for comparison purposes only. The choice of orbital distance is arbitrary, based on a series of models published in Koskinen et al. [2007b], and the simulations do not differ greatly from those located at 0.2 AU.

As no reliable models of upper atmosphere circulations or observations exist, EX024r itself was used to generate the alternative lower boundary conditions. As circulation is driven by pressure gradients (or, on isobaric surfaces, geopotential gradients that are linked to temperature gradients) rather than the absolute values of pressure (or temperature), a horizontal temperature distribution was lifted from the outer layers of the model and shifted to higher pressures. The temperatures we scaled down so that the average temperature at the lower boundary remained near 520 K. Superposed on this temperature distribution, winds from the upper thermosphere were imposed. The lower boundary altitudes were also fitted to reflect the new circulation pattern. The resulting lower boundary temperature and wind map is shown in Figure 4.30. The maximum zonal wind speed is $\sim$1 km s^{-1}. With wind speeds of 1–10 km s^{-1} predicted for HD209458b at 0.045 AU, this may well be appropriate for a planet further away at 0.24 AU. Qualitatively the conditions at the lower boundary are somewhat similar to the circulation presented by Cooper and Showman [2005] for HD209458b at 2.5 mbar, although of course the wind speeds are much

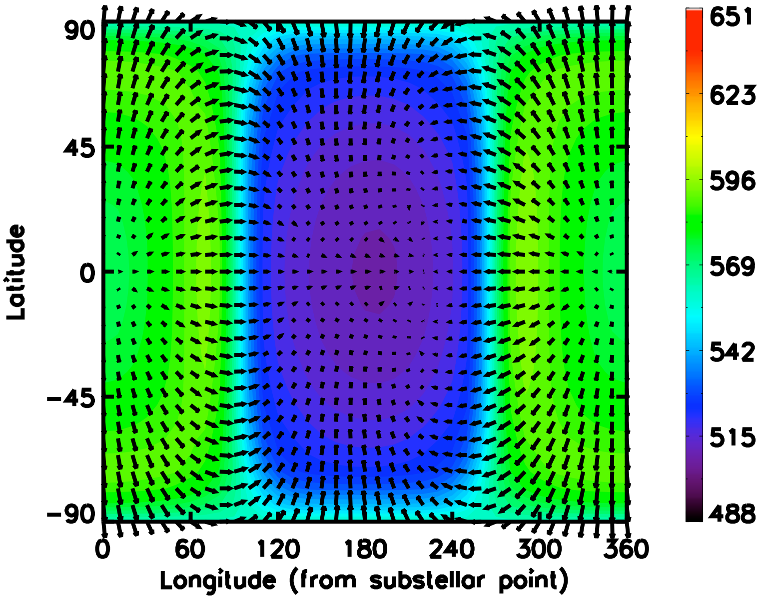

Figure 4.30: Lower boundary temperatures and winds for EX024rw (0.24 AU). The substellar temperature is 580 K, while the night side minimum temperature is 490 K. The global average is about 550 K. The maximum zonal wind speed is ~1 km s^{-1}.

lower here.

Figure 4.31 contrasts the temperatures and winds from EX024r and EX024rw in the upper thermosphere near the 0.04 nbar pressure level. The dayside temperatures and circulation are nearly identical in the two models. Some differences occur in the night side where heating of the anti-stellar point due to vertical advection and adiabatic contraction is slightly more efficient in EX024rw. Thus it appears that the influence arising from lower boundary circulation is felt by the dynamics of the night side thermosphere, although the effect is not particularly significant. Overall, the circulation in EX024rw is very similar to the circulation in EX024r.

Figure 4.32 shows the eastward (positive) zonal wind versus pressure at the equator, near the terminator where the winds are fastest, from EX024r and EX024rw. Remarkably, as the figure illustrates, even moderately strong lower boundary winds make little difference in the upper thermosphere. The lower boundary wind dies out by the third pressure level upward (2-0.9 μbar), and at pressures lower than 0.9 μbar the wind speeds in the two models are roughly identical.

The lower boundary condition on EX024rw is somewhat inconsistent. The rigid lower boundary does not allow for the interaction with the lower atmosphere and there is no feedback between the thermosphere and deeper layers of the atmosphere. In addition, the mixing ratios of the neutral species are held fixed and horizontally uniform at the lower boundary and thus the composition is not consistent with the imposed, fixed circulation. Due to these uncertainties, any small scale features of the model in

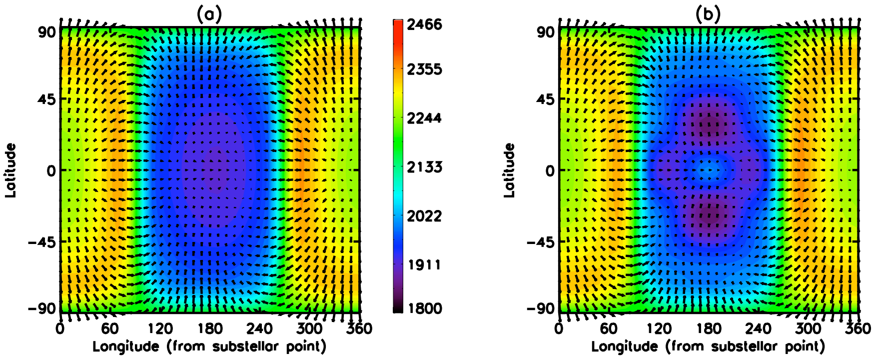

Figure 4.31: Temperatures and winds at the 0.04 nbar pressure level from (a) EX024r and (b) EX024rw. For EX024r the substellar temperature is 2340 K and the night side minimum temperature is 1950 K. The maximum zonal wind speed is 1 km s^{-1}. For EX024rw, which has circulation imposed at the lower boundary, the substellar temperature is also 2340 K and the night side minimum temperature is 1900 K. The temperature at the antistellar point is 2070 K. The two models are remarkably similar despite the differences at the lower boundary.

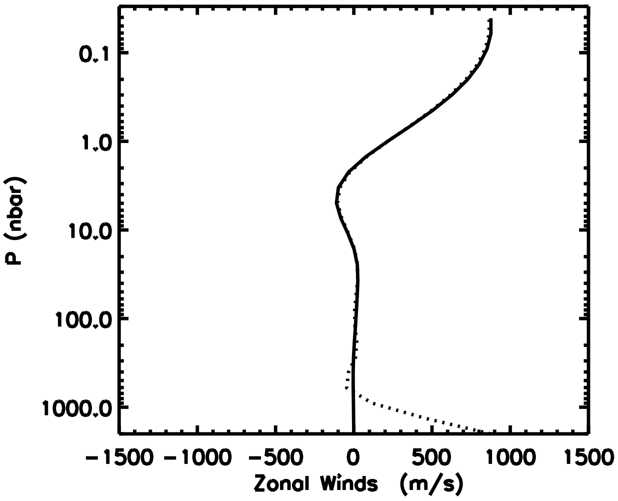

Figure 4.32: Zonal wind speed profiles on the equator at 80 degrees longitude from the substellar point from EX024r (solid line) and EX024rw (dotted line). The snapshot is from the terminator where zonal wind speeds reach their maximum values.

the lower thermosphere (and otherwise in the night side) should be viewed with suspicion.

The simulations indicate that lower boundary temperature and circulation do not affect the stability of the thermosphere or even the conditions in the upper thermosphere. Of course this conclusion may not be valid for fast winds of several km s^{-1}, lower boundary temperatures that are comparable to exospheric temperatures, or steep temperature gradients at the lower boundary. If such circumstances occur, the lower boundary conditions for the models should be re-evaluated.

4.6.3 Solar Variability and Heating Efficiency

Solar XUV fluxes vary significantly during the eleven-year solar cycle. One might ask if the simulations are different under solar maximum and minimum conditions. So far, all simulations discussed in this chapter have been generated by using solar maximum fluxes for November 1980 from the SOLAR2000 model [Tobiska et al., 2000]. In order to explore the effect of solar variability, simulations were created for solar minimum conditions of January 1996. Under the solar maximum conditions, the total XUV flux received at 1.0 AU between 0.1 and 105 nm is 8.7×10^{-3} W m^{-2}, while under solar minimum conditions, the flux is 3.7×10^{-3} W m^{-2}. These figures should be compared to the flux of 4.64×10^{-3} W m^{-2} for the wavelength range of 0.1-118nm, constructed by Ribas et al. [2005] for the average Sun in midcycle 1993, that has been adopted in many EGP studies to date.

The total XUV heating rate for EX02r is 1.7×10^{15} W, while for a simulation using the solar minimum fluxes (EX02smin) it is 7.5×10^{14} W. Thus adopting solar minimum fluxes corresponds to lowering the heating efficiency from 50 % to about 22 % for solar maximum fluxes. The resulting temperature differences are not particularly significant. Figure 4.33 contrasts the substellar P-T profiles of the reference model EX02r with EX02smin. The average temperatures at the upper boundary for the two simulations are 2962 K and 2727 K, respectively. This makes EX02smin about 235 K cooler near the exobase, and in general, about 0–230 K cooler in deeper thermosphere. Horizontal temperature variations and circulation are qualitatively similar in both models throughout the thermosphere, although the wind speeds are slightly slower in EX02smin.

The reduced XUV flux is also reflected in photoionisation rates, and here the differences between the two simulations are more notable. Figure 4.34 shows the logarithm of substellar electron densities for EX02r and EX02smin. For EX02smin, the density of H^+ is higher near the exobase, but lower at all other levels. These trends are reflected in the electron density profiles. The higher density of H^+ near the upper boundary of EX02smin is due to a higher dayside mixing ratio of H under solar minimum conditions. The density of H_3^+, on the other hand, is lower at all levels under solar minimum conditions. The substellar column densities of H_3^+ for EX02r and EX02smin are 2.0×10^{17} m^{-2} and 1.0×10^{17} m^{-2}, respectively. This, together with the lower temperatures, means that the total H_3^+ cooling rate under solar minimum conditions is 7.3×10^{14} W, which is less than half of the cooling rate of 1.6×10^{15} W for the reference model. In conclusion, reducing the external XUV flux to the solar minimum values does not significantly alter the temperatures in the model, but it does have a significant impact on photoionisation

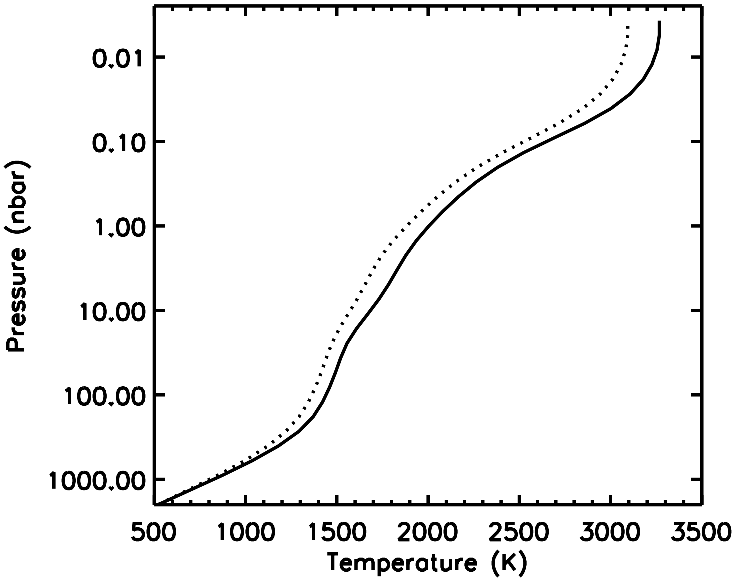

Figure 4.33: Substellar P-T profiles for the reference model EX02r (solid line) and EX02smin (dotted line), a model that uses solar minimum XUV fluxes as an external energy source.

and infrared cooling rates.

Instead of analysing detailed energetics to determine what proportion of the absorbed energy goes into the heating of the neutral thermosphere, the model generally assumes a uniform heating efficiency of 50 %. Excluding H_3^+ cooling, this heating efficiency has been found to be appropriate for the Jovian thermosphere [Waite et al., 1983]. The adopted heating efficiency is an important parameter that may affect the stability of the thermosphere. Assuming that the XUV flux is distributed evenly between 0.1 and 105 nm, lowering the heating efficiency to 10 % corresponds to moving the reference model from 0.2 AU to ~0.45 AU, where its upper boundary temperature would be around 2200 K, compared to 2960 K at 0.2 AU. Increasing the heating efficiency to 100 % corresponds to moving the model from 0.2 AU to ~0.14 AU. In Chapter 5 we will learn that the atmosphere becomes unstable at this orbital distance as it begins to escape hydrodynamically. We note, however, that a heating efficiency of 100 % is highly unlikely, and it is actually more likely that the heating efficiency is lower rather than higher than 50 % [Yelle, 2004].

4.6.4 Detailed Balance versus Exponential Cooling

Most simulations presented in this thesis were corrected for non-LTE effects in the upper atmosphere by using detailed balance calculations for the level populations of H_3^+ ions. However, their predecessors, and in particular, all the simulations published in Koskinen et al. [2007b] utilised the exponential correction factor given by equation (3.19). It is very interesting to explore the differences between the two

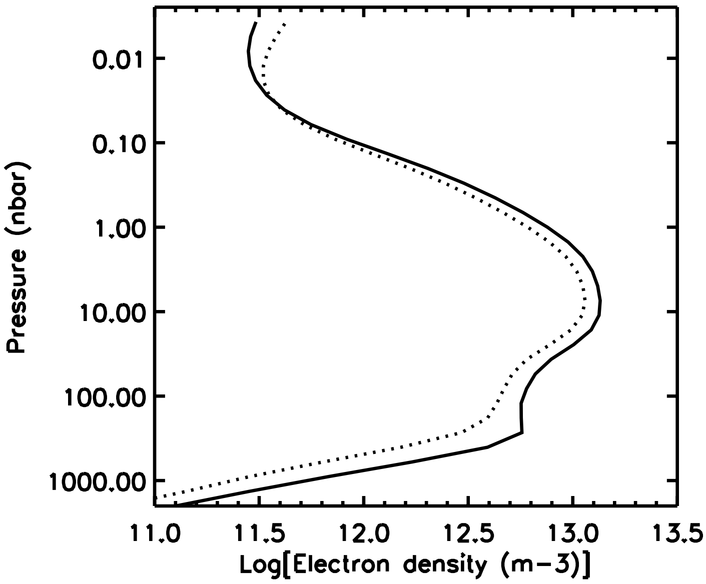

Figure 4.34: Substellar electron densities for the reference model EX02r (solid line) and EX02smin (dotted line), a model that uses solar minimum XUV fluxes as an external energy source.

approaches and thus, for comparison, a model otherwise identical to EX02r was generated by using the exponential correction. This model is labelled EX02exp.

Figure 4.35 shows the substellar P-T profiles for both EX02r and EX02exp. At pressures higher than 55 nbar, the P-T profiles are identical. Between 55 and 0.7 nbar EX02exp is warmer by about 10–100 K. In the outer layers, EX02exp is cooler by a few hundred degrees, but towards the exobase the temperature increases steeply with altitude so that at the upper boundary, the temperatures in the two simulations are roughly identical. The average upper boundary temperatures for EX02r and EX02exp are 2962 K and 2843 K, respectively. The upper boundary altitude is about 140 km lower in EX02exp. At all levels, circulation in the two simulations is qualitatively identical.

Figure 4.36 contrasts the volume infrared cooling rates at the substellar point of EX02r and EX02exp. Between 55 and 0.7 nbar, the cooling rate is slightly higher in EX02r, whereas between 0.7 and 0.03 nbar it is higher in EX02exp. The correction factor given by equation (3.19) goes to zero at pressure level 30 (0.02 nbar), and thus detailed balance calculations yield higher cooling rates near the upper boundary. In the lower boundary region, the cooling rates are practically identical. Despite differences in the cooling rate profiles, the total H_3^+ emission rates from the simulations are the same, i.e. 1.59×10^{15} W.

Overall, the differences between the two simulations are not particularly significant, and even the experimental non-LTE correction works remarkably well. This fact is further illustrated by Table 4.4, which lists the correction factors calculated from equation (3.19) and with the detailed balance method for different pressure levels in the simulations.

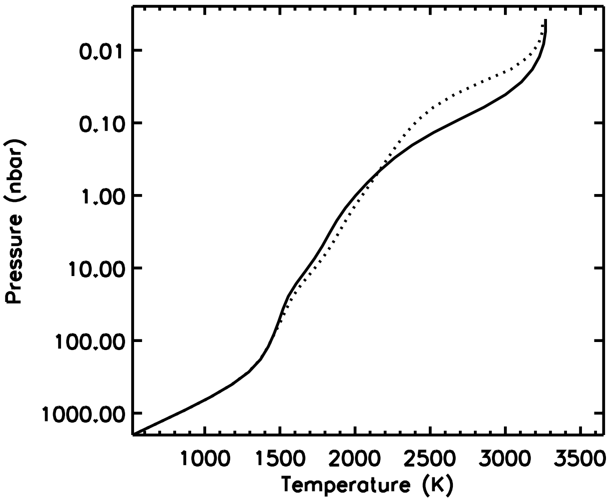

Figure 4.35: Substellar P-T profiles for EX02r (solid line) and EX02exp (dotted line). The orbital distance is 0.2 AU. EX02exp uses the experimental correction factor given by equation (3.19) to correct the H_3^+ emission rates in non-LTE conditions.

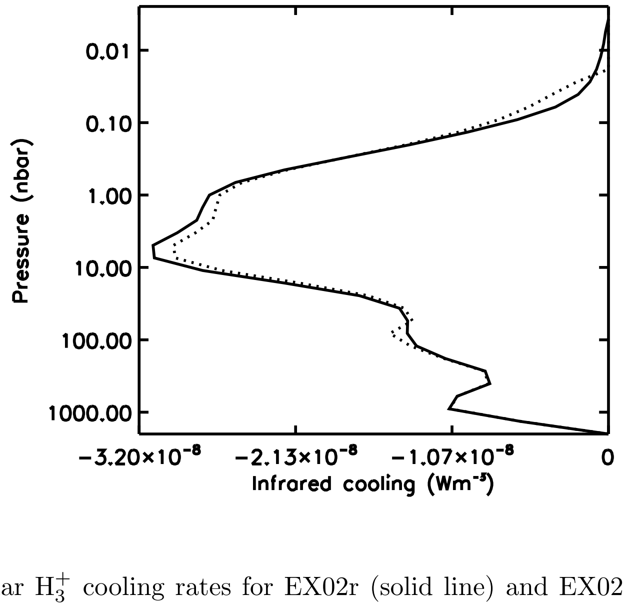

Figure 4.36: Substellar H_3^+ cooling rates for EX02r (solid line) and EX02exp (dotted line) at 0.2 AU. EX02exp uses the experimental correction factor given by equation (3.19) to correct the H_3^+ emission rates in non-LTE conditions.

Table 4.4: Non-LTE correction factors for the 0.2 AU simulations (based on the reference model EX02r)

Pressure (nbar)	Temperature (K)	Detailed balance	Experimental[a]
2000	520	1.00	1.00
1340	696	1.00	1.00
899	872	1.00	1.00
602	1036	1.00	1.00
404	1179	0.990	1.00
271	1293	0.979	1.00
181	1371	0.972	1.00
121	1422	0.958	1.00
82	1460	0.941	1.00
55	1492	0.915	0.878
36	1521	0.885	0.782
25	1556	0.845	0.696
16	1608	0.791	0.618
11	1670	0.727	0.548
7.4	1730	0.656	0.484
5.0	1783	0.581	0.426
3.3	1830	0.504	0.374
2.2	1878	0.427	0.327
1.5	1936	0.350	0.284
1.0	2004	0.276	0.245
0.67	2081	0.208	0.210
0.45	2167	0.149	0.179
0.30	2264	0.100	0.150
0.20	2381	0.0622	0.124
0.14	2523	0.0350	0.101
0.09	2689	0.0181	0.0794
0.06	2858	0.0093	0.0602
0.04	3001	0.0054	0.0428
0.03	3107	0.0038	0.0129
0.02	3179	0.0031	0.00
0.01	3226	0.0028	0.00
0.0084	3254	0.0026	0.00
0.0055	3267	0.0024	0.00
0.0037	3267	0.0023	0.00

---

[a] Given by equation (3.19)

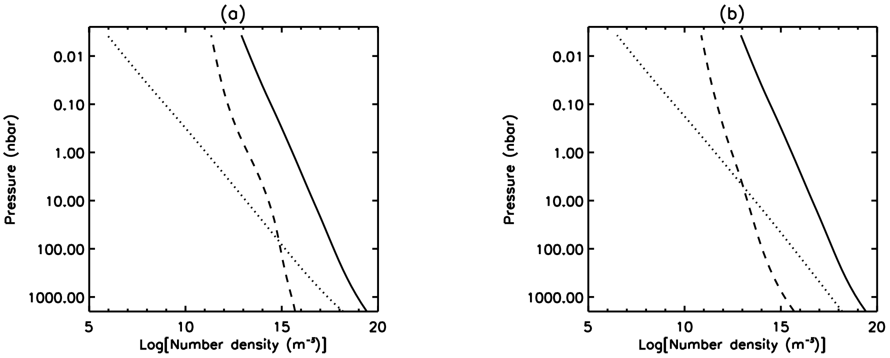

Figure 4.37: Number densities of the neutral species H_2 (solid line), He (dotted line), and H (dashed line) for (a) EX02r and (b) EX02re2 at the substellar point. The former assumes zero eddy diffusion, while in the latter model the eddy diffusion coefficient is $\kappa_\mathcal{T} = 10^9$ cm^{2}s^{-1}. Note that for EX02re2, the densities of different species decrease with altitude more uniformly at the bottom of the thermosphere.

4.6.5 Eddy Diffusion

Eddy diffusion processes are largely ignored in these simulations. Their nature on EGPs is uncertain, and in absence of accurate representation, it is more consistent to omit them than to include something in all simulations that may turn out to be wrong in the end. Turbulent conduction has also been consistently omitted due to theoretical difficulties and controversy related to it (see Section 1.2.4). Here we explore simulations with different eddy diffusion coefficients in order to investigate the effect of turbulent diffusion on the transport of neutral species. Two new models were generated for this purpose: EX02re1 and EX02re2. In the former we adopted the eddy diffusion coefficient typical for Jupiter ($\kappa_\mathcal{T} = 10^7$ cm^{2}s^{-1}), and in the latter we increased the Jovian value by two orders of magnitude ($\kappa_\mathcal{T} = 10^9$ cm^{2}s^{-1}).

Using the Jovian value does not significantly affect the results, so here we concentrate on the model with a higher rate of eddy diffusion only. In general, a higher rate of eddy diffusion shifts the homopause to higher altitudes (lower pressure). Below the homopause the mixing ratios of various species are constant with altitude. Above it the concentrations of heavier molecules or atoms decrease more steeply with altitude. Overall the upward shift of the homopause has the effect of increasing the concentrations of heavier molecules in the thermosphere. Figure 4.37 illustrates this tendency. It shows the substellar number densities of the neutral species in the EX02r and EX02re2 simulations. Strong eddy diffusion is potentially significant, because increasing mixing ratios of H_2 and He imply lower mixing ratios of H, and this affects the H_3^+ cooling function in the model. Figure 4.38 shows the mixing ratios of H along the equator at 8.2 pbar for EX02r and EX02re2. It shows that the dayside mixing ratio of H in EX02re2 is negligible, and in the night side the mixing ratio of H is about 35 percentage points lower than in EX02r. The average mixing ratio of H near the exobase is about 20 percentage points lower in EX02re2 than it is in the reference model. Thus eddy diffusion can have a significant influence on the mixing ratios of the neutral species in the upper thermosphere.

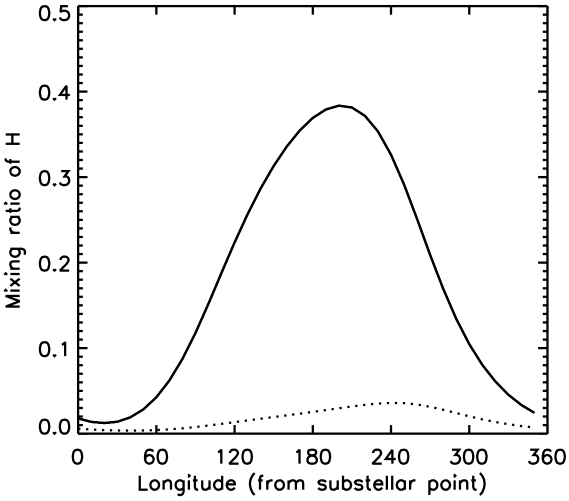

Figure 4.38: The mixing ratio of H for EX02r (solid line) and EX02re2 (dotted line) along the equator at 8.2 pbar. The former model assumes zero eddy diffusion, while in the latter model the eddy diffusion coefficient is $\kappa_{\mathcal{T}} = 10^9$ cm^{2}s^{-1}.

Figure 4.39 shows the substellar temperature profiles for EX02r and EX02re2. The temperature differences are not very significant despite the difference in composition. The average temperature in EX02re2 is only about 200 K cooler at the upper boundary. The temperature difference becomes apparent at pressures lower than 0.09 nbar, i.e. rather high in the thermosphere. This is because the dayside mixing ratio of H in EX02r is low to begin with, and reducing it further does not affect the radiative balance significantly. This situation is likely to be different in atmospheres where the horizontal mixing of atomic hydrogen is more uniform. In general, eddy diffusion counteracts the effects of a higher mixing ratio of H at the lower boundary (see Section 4.6.1) or fast asynchronous rotation (see Section 4.4.4).

4.6.6 Smoothing and Time Integration

It is an unfortunate fact of life that the equations of atmospheric dynamics cannot be solved analytically without severe approximations and omissions, and that they cannot even be integrated numerically without applying artificial smoothing filters. Perfect filters do not exist, and in addition to stamping out instability, numerical smoothing algorithms affect the physical solution. Aggressive smoothing of the horizontal wind pattern, for instance, will reduce the maximum wind speeds on the grid and make minima shallower [Shapiro, 1970]. In the light of these observations it is prudent to inquire about the degree to which the simulations are changed by numerical smoothing.

Figure 4.40 illustrates the effect of horizontal temperature smoothing on the simulations. It shows temperatures at the upper boundary along the equator for four 0.2 AU simulations with different temperature and wind smoothing frequencies. The simulations are labelled EX02st1, EX02st2, EX02st3, and

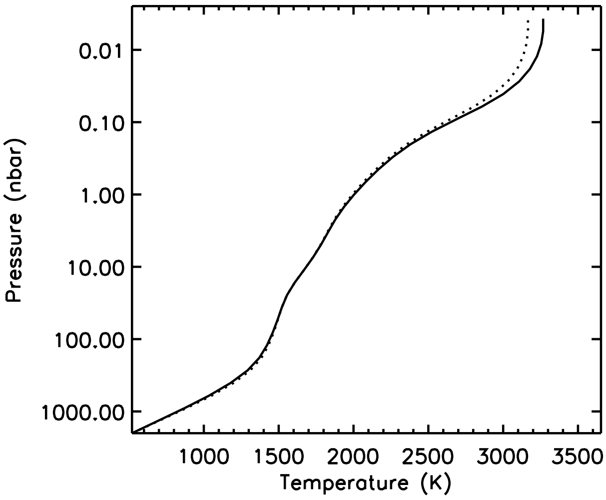

Figure 4.39: Substellar P-T profiles for EX02r (solid line) and EX02re2 (dotted line). The former model assumes zero eddy diffusion, while in the latter model the eddy diffusion coefficient is $\kappa_\tau = 10^9$ cm^{2}s^{-1}.

EX02st4. EX02st1 is a limited run, for which smoothing was switched off. Such a run eventually becomes numerically unstable. For EX02st2, EX02st3, and EX02st4, the smoothing filter was used every 720, 7.2 and 1.44 s (of simulated time), respectively. EX02st2 is identical to the reference model at 0.2 AU, EX02r. There is not much difference between EX02st2 and EX02st1, although some of the sharp edges of the temperature pattern are rounded off in EX02st2 by smoothing. As EX02st2 is stable, and does not differ much from the no-smoothing case, the smoothing frequency adopted for the reference model is appropriate. If this frequency is multiplied by a factor of 100, as was done for EX02st3, smoothing begins to affect the qualitative nature of the results. The maximum temperature drops, and the 'dawn' peak is brought in line with the temperature at 'dusk'. In the night side, the temperatures are generally higher, apart from the antistellar point, where the temperature minimum is deeper than in EX02st2. If the smoothing frequency is multiplied by a factor of 500, as was done for EX02st4, the night side temperature becomes considerably higher than in the reference model. Also, the dayside temperature is over 500 K higher, and the hot ring surrounding the substellar point in EX02r is smoothed out. Instead, the night side gradients associated with the 'dawn' and 'dusk' temperature peaks are interpreted as ascending slopes of a temperature 'wave', which peaks at the substellar point, and this causes the dayside temperature to increase.

Figure 4.41 shows the zonal wind speeds at the upper boundary along the equator for the same simulations. The plot shows the tendency of the smoothing filter to remove sharp peaks in the wind pattern, and also the tendency to reduce the amplitude of the wave-like solution. The maximum wind speed drops from over 2.0 km s^{-1} to 500 m s^{-1} between EX02st1 to EX02st4. Also, qualitatively the circulation in EX02st4 is characterised by winds blowing from the dayside to the night side, and

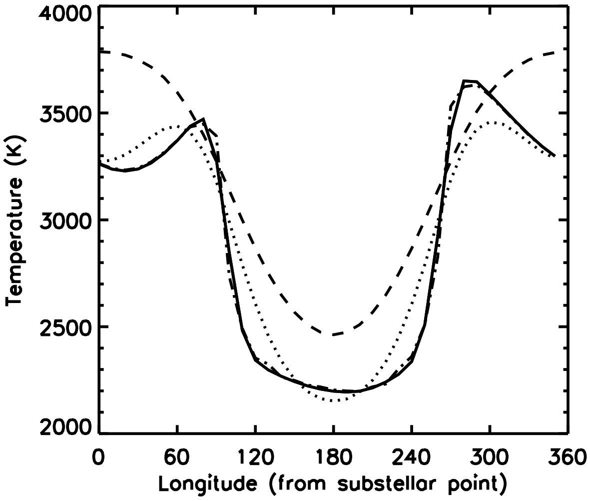

Figure 4.40: Temperature vs. equatorial longitude at 3.7 pbar for four 0.2 AU simulations with different horizontal temperature smoothing frequencies: no smoothing (dash-dotted line), smoothing every 12 min (solid line), 7.2 s (dotted line) and 1.44 s (dashed line).

converging at the antistellar point instead of the 'dawn' terminator. Contrary to other simulations, which develop eastward equatorial jets in the lower thermosphere, circulation in EX02st4 is axisymmetric about an axis joining the substellar and antistellar points at every level. Thus aggressive smoothing removes the influence of the Coriolis force from the simulations, and this is a very dangerous feature. In order to avoid such unphysical outcomes, it is important to keep the smoothing frequency as low as possible to secure the numerical stability of the model. We note that applying smoothing every 12 min leads to an outcome that is not very different from the no-smoothing case. However, if this smoothing frequency is multiplied by a factor of 100, so that smoothing is applied every 7 s, the results begin to divert significantly from the expected outcome.

In addition to the smoothing of temperature and horizontal winds, the neutral mass mixing ratios are also subjected to the filter, because the species continuity equations have advective parts. Figure 4.42 shows the mass mixing ratio of atomic hydrogen along the equator at the 8.2 pbar level for five 0.2 AU simulations with different smoothing frequencies of the composition terms. These simulations are labelled EX02sc1, EX02sc2, EX02sc3, EX02sc4, and EX02sc5. The basis for all these simulations is the reference model EX02r, and for EX02sc3 the smoothing frequency is the same as in EX02r. For EX02sc2, EX02sc4, and EX02sc5 smoothing of the mass mixing ratios takes place every 72 s, 7.2 s, and 3.6 s, respectively. For EX02sc1, smoothing of the composition terms is switched off. Without smoothing the model crashes fairly quickly due to numerical instabilities. The output for EX02sc1 is displayed just before the crash. Identically to EX02r, the smoothing of temperature and winds takes place every 12 min in all of these simulations.

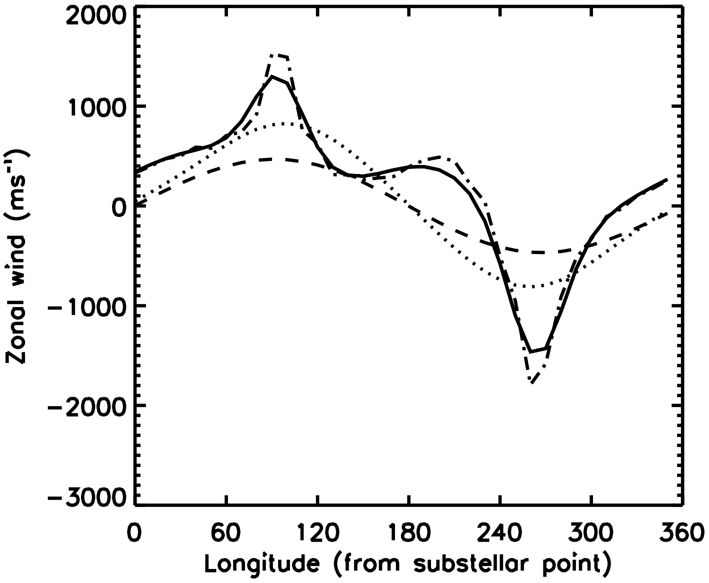

Figure 4.41: Zonal wind speed vs. equatorial longitude at 3.7 pbar for four 0.2 AU simulations with different horizontal wind smoothing frequencies: no smoothing (dash-dotted line), smoothing every 12 min (solid line), 7.2 s (dotted line) and 1.44 s (dashed line).

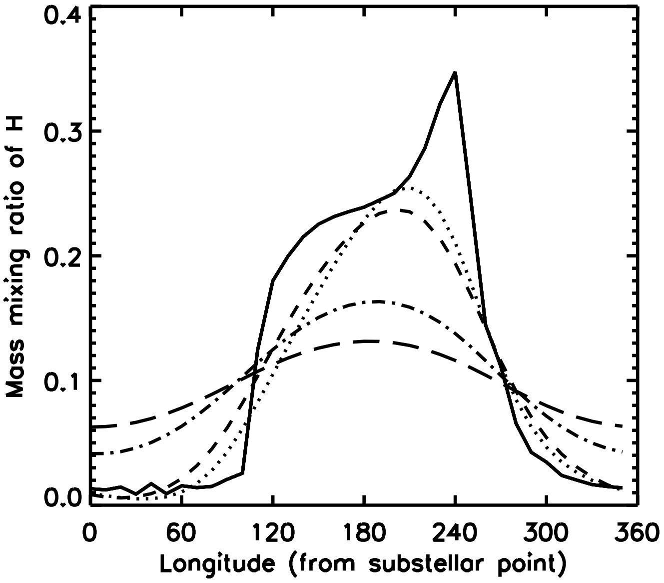

Figure 4.42: Mass mixing ratio of atomic hydrogen vs. equatorial longitude at 8.2 pbar for five 0.2 AU simulations with different composition smoothing frequencies: no smoothing (solid line), smoothing every 72 s (dotted line), 36 s (dashed line), 7.2 s (dash-dotted line) and 3.6 s (long dashes).

Compared to the solution of the momentum and energy equations, the solution of the species continuity equations is much more prone to numerical instability. Thus the smoothing frequency required to keep the solution stable is significantly higher. We find that smoothing has to take place at least every 36–72 s. Otherwise sharp spikes appear in the distribution of mass mixing ratios, and these eventually grow unphysically to produce negative densities. Figure 4.42 displays several such features for the unsmoothed simulation. It also displays how frequent applications of the smoothing filter remove sharp features and reduce the amplitude of the wave-like solution, thus reducing the concentration of atomic hydrogen in the night side and increasing it in the dayside. This confirms the conclusions drawn by Shapiro [1970], who pointed out that the filter would remove noise caused by the unresolved Fourier components in the grid, but that it would also reduce the amplitude of the long-wave solution (this is dangerous, because in doing so the filter interferes with the physical solution). In the extreme case of overzealous smoothing, the filter reduces the solution to a global average, and this trend is clearly visible in Figure 4.42. In general, it is prudent to choose the smoothing frequency so that it is just about sufficient to keep the solution stable (this philosophy is also advocated by Cooper and Showman [2006], based on Polvani et al. [2004]).

Helium concentrations are negligible in the upper thermosphere, and in the lower thermosphere helium mass mixing ratios are fairly uniform horizontally. Thus they are not affected by smoothing. H_2 concentrations are calculated by deducting all the other mass mixing ratios from one. Thus the mass fractions of H_2 mirror those of H. The mixing ratio of H, as we have learned, affects the H_3^+ cooling rate. Increasing the smoothing frequency thus leads to higher temperatures in the dayside, as the density of H_3^+ falls. This trend is illustrated by Figure 4.43.

Directly related to numerical smoothing is the impact of different grid sizes, their resolution and the frequency of time stepping. In addition to the potential of causing numerical instabilities, different grid sizes can alter the physical solution. Because EXOTIM is a *global* model, the horizontal and vertical grids are extremely coarse. The model is thus ideally suited for the study of simple, large-scale circulation, temperature variations and photochemistry. One should not get bogged down with spurious detail, unless they affect the global features, but look for the bigger picture.

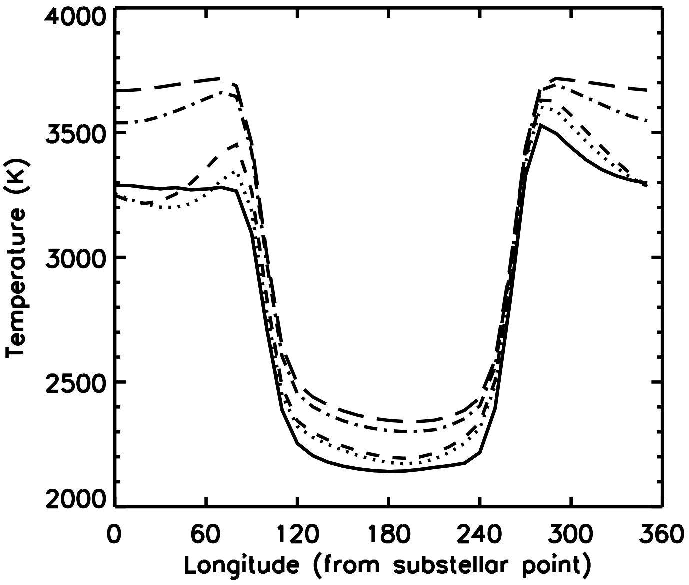

Figure 4.43: Temperature vs. equatorial longitude at 8.2 pbar for five 0.2 AU simulations with different smoothing frequencies of the composition terms: no smoothing (solid line), smoothing every 72 s (dotted line), 36 s (dashed line), 7.2 s (dash-dotted line) and 3.6 s (long dashes).

Chapter 5

Stability Limit

5.1 The Onset of Hydrodynamic Escape

After some distraction, we now return to our quest of bringing a simulated Jupiter inward towards the Sun. As we know, HD209458b is a close-in EGP orbiting a G-type host star at 0.045 AU, and observations indicate that it is surrounded by an expanded atmosphere of atomic hydrogen that is escaping hydrodynamically (see Section 2.3). Models of the upper atmosphere indicate that such escape is possible at least inside an orbit of 0.1 AU. On the other hand, we know that Jupiter, which orbits the Sun at 5.2 AU, has a thin and stable atmosphere. The implication is that somewhere between 0.1 AU and 5.2 AU there should be a crossover between relative stability and instability. The purpose of our quest is to quantify this stability limit for Jupiter and identify the mechanism responsible for driving the breakdown in atmospheric stability. It is important to note that instability here refers to hydrodynamic escape at the top of the atmosphere instead of convective instability that was discussed in Chapter 1. The thermosphere is stable against convective instability because the vertical temperature gradient is positive. Although both produce vertical flows, the mechanisms responsible for hydrodynamic escape and convection are completely different.

In Chapter 4 we found that the atmosphere of a Jupiter-type planet orbiting a Sun-like star can be stable, in that it is not escaping hydrodynamically, down to a distance of 0.2 AU from the host star, although this result depends on the mixing ratio of atomic hydrogen in the lower atmosphere and the rate of rotation. If the planet is tidally locked or slowly rotating and the mixing ratio of atomic hydrogen in the lower atmosphere is not anomalously high (less than ~ 0.5 %), the stability limit is located somewhere between 0.1 and 0.2 AU. For this special case, it is possible to identify the mechanism responsible for destabilising the atmosphere and quantify the limit. The exact location of this limit depends on the parameters of the model, and the physical processes included, but the mechanism driving the instability is more generic in nature and thus the qualitative results can easily be adapted to different planets orbiting different types of stars.

Figure 5.1 shows the globally averaged temperature and column densities of the dominant ions in the upper atmosphere between 0.1 AU and 0.2 AU. For consistency, the common planetary parameters of the simulations that were used to generate the data are the same as those given in Table 4.2. Parameters for the individual simulations are given in Table C.1 of Appendix C. Between 0.16 and 0.2 AU the average exospheric temperature is about 3000 K, and the exobase is located roughly 6000 km above the lower boundary - that is, the extent of the thermosphere is less than 10 % of the planetary radius. The average thermal escape parameter at the upper boundary ranges from 65 to 71, implying that the atmosphere is stable, in hydrostatic equilibrium, and thermal evaporation is due to Jeans escape, which is almost negligible. In these conditions, H_3^+ infrared cooling almost exactly balances the XUV heating, with downward conduction and other effects making up the difference. The thermal balance of the model is thus largely determined by the XUV heating and the infrared cooling that regulate the energies available for circulation and heating. Figure 5.2 shows the total XUV heating and infrared cooling rates, that are in rough balance between 0.16 AU and 0.2 AU, but begin to divert near 0.15 AU.

As the model is moved inwards from 0.16 AU, the character of the upper atmosphere changes within a surprisingly narrow range of orbital distances. As the temperature increases gradually, H_2 begins to dissociate, owing to collisions with other molecules. Once thermal dissociation becomes significant, transport effects on the dayside bringing more H_2 from below are not sufficient to compensate for it. This impedes the formation of H_3^+ and the subsequent loss of infrared cooling, leading to rapidly increasing temperatures, causes further breakdown of the H_2 atmosphere. This is not a subtle change. Once the model reaches a high enough temperature for significant dissociation to take place, a runaway breakdown occurs and the whole upper thermosphere converts into atomic hydrogen, much of which is quickly ionised.

As a result of the runaway dissociation of H_2 the thermosphere heats up and expands dramatically, producing an inflated upper atmosphere, with an extent comparable to or larger than the radius of the planet, where temperature exceeds 20,000 K. The simulations heat up until the thermal escape parameter at the upper boundary reduces to 1.5. At this stage the thermal kinetic energy becomes comparable to the gravitational potential energy at the upper boundary, and the atmosphere begins to escape hydrodynamically. This means that the atmosphere escapes at the upper boundary in bulk, instead of slow diffusion, and generates a continuous ‘planetary wind’. At the onset of hydrodynamic escape at 0.14 AU, roughly 25 % of the absorbed energy is available to power the outflow. The imbalance of heating and cooling rates in the model allows for crude estimates of mass loss to be calculated for the unstable atmosphere. Such estimates for different EGPs are presented in Section 5.2.

Under the conditions described above, the limiting distance for hydrodynamic escape is between 0.14 and 0.16 AU from the parent star. Figure 5.3 shows the expansion and horizontal temperature distributions at two different pressure levels for two simulations on either side of the stability limit, at 0.16 AU (EX016r) and 0.14 AU (EX014r). Outside the stability limit, at 0.16 AU, the model atmosphere is stable and relatively cool but inside the stability limit, at 0.14 AU, the thermosphere, which is on the

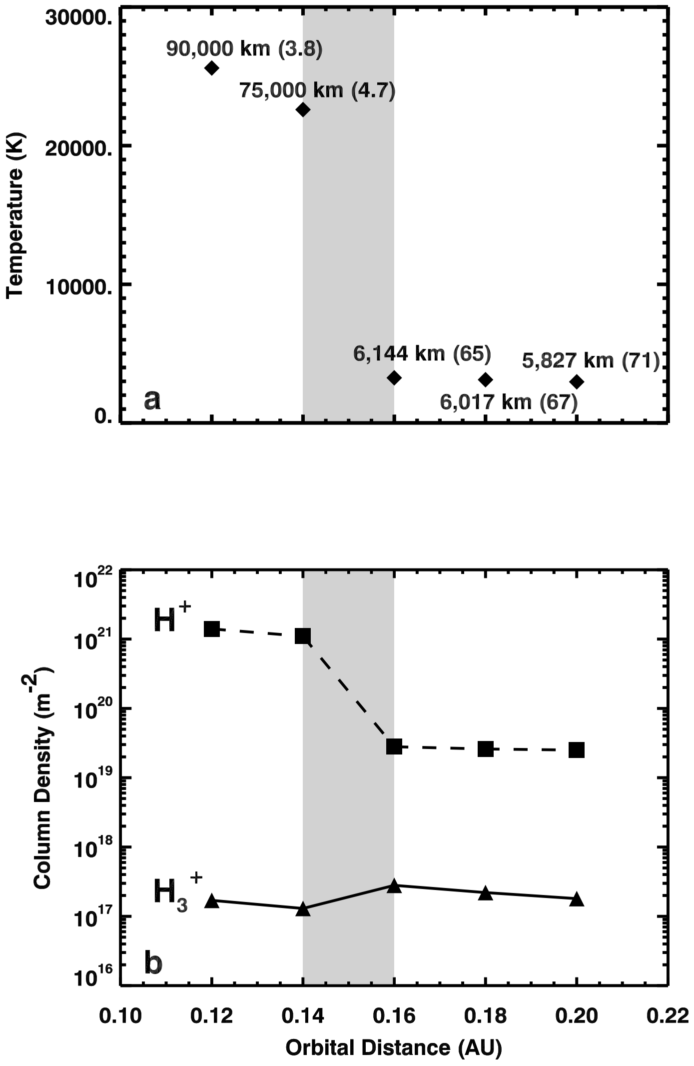

Figure 5.1: (a) Globally averaged temperatures at the 3.7 pbar level and (b) column densities of the dominant ion species versus orbital distance for a Jupiter-type EGP orbiting the Sun. In (a) the altitude of the upper boundary (in km above the lower boundary) is shown next to the data points, and the figure in brackets is the average thermal escape parameter. The grey-shaded area marks the crossover distance between atmospheric stability and hydrodynamic escape. The data points at 0.12 and 0.14 AU reflect the conditions at the onset of hydrodynamic escape, while the rest of the models are in approximate steady state. Within the stability limit the upper thermosphere converts into atomic hydrogen, significantly increasing the content of H^+ in the outer layers. At the same time the column density of H_3^+ decreases, although at least initially much of it survives in the lower thermosphere. [Koskinen et al., 2007a]

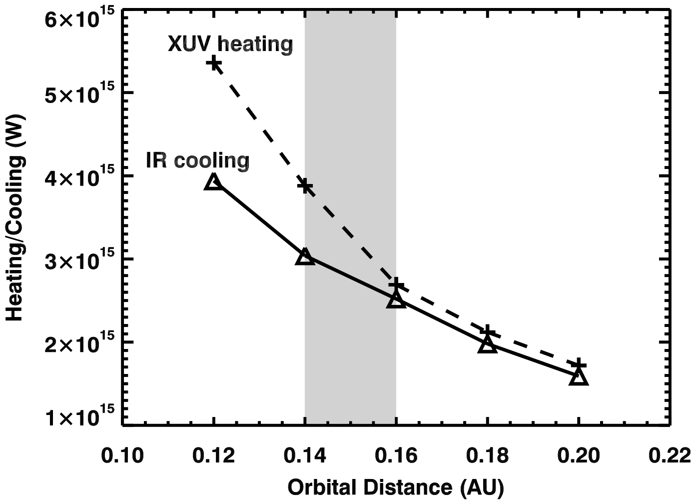

Figure 5.2: Total XUV heating and IR cooling rates at different orbital distances integrated over all pressure levels and both hemispheres. The gray-shaded area shows the crossover region between atmospheric stability and hydrodynamic escape. The data points at 0.14 and 0.12 AU depict conditions at the onset of hydrodynamic escape. Inside the stability limit the balance of radiative heating and cooling is disturbed and excess energy is available to power hydrodynamic escape. [Koskinen et al., 2007a]

verge of hydrodynamic escape, is inflated and hot. The differences between the two simulations are most dramatic at low pressures in the outer layers of the atmosphere. By contrast, in the lower thermosphere (near the 122 nbar level) the temperatures in the simulations are fairly similar, although the horizontal temperature distributions and circulation are different.

At 0.16 AU, the temperature at the 122 nbar level varies horizontally within a 20 K interval between 1410 and 1430 K. The circulation is characterised by an equatorial eastward jet, which shifts the ‘hot spot’ downstream along the equator to the ‘dusk’ terminator. The equator is slightly warmer than its surroundings everywhere around the planet. In the night side the wind flows in high-latitude vortices that circle around the temperature minima near the poles. The maximum equatorial wind speed is 100–120 m s^{-1}. Near the same pressure level at 0.14 AU, the temperature varies horizontally within a 60 K interval between 1450 and 1510 K. The temperature distribution is nearly axisymmetric about an axis joining the substellar point to the antistellar point, exhibiting a clear diurnal difference. The dayside ‘hot spot’ is shifted slightly westward towards ‘dawn’. Qualitatively, the circulation is similar to the circulation in EX016r, but the maximum zonal wind speed is higher, reaching 200 m s^{-1}, and the equatorial jet slows down considerably on the dayside. Overall, diurnal temperature differences persist to higher pressures in the inflated atmosphere.

The lower thermospheres are similar in these simulations because of the prevalence of H_3^+ cooling at low altitude. By contrast, the upper thermospheres are dramatically different. At 0.16 AU, the upper boundary resembles the outer layers of the 0.2 AU reference model EX02r (see Section 4.4), although

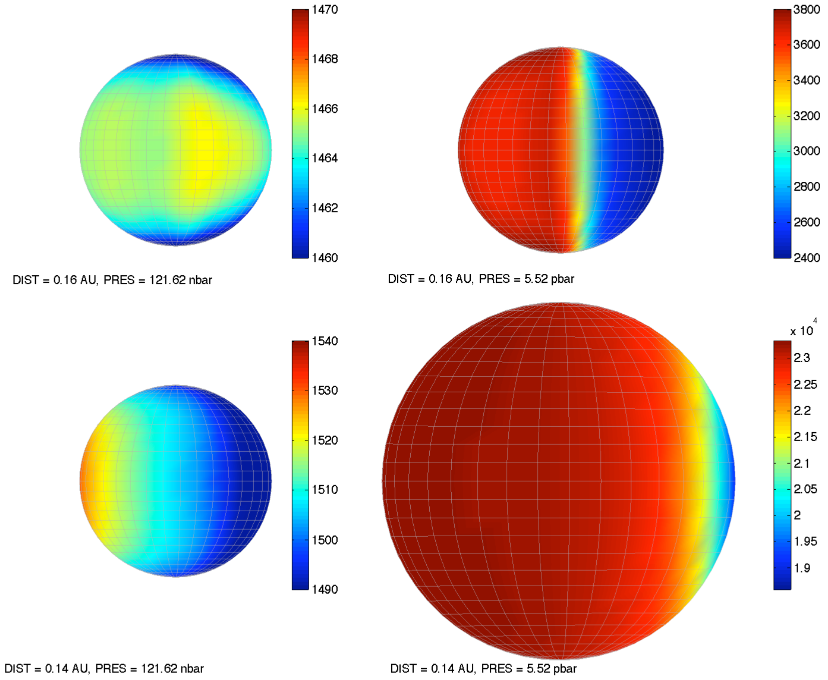

DIST = 0.16 AU, PRES = 121.62 nbar

DIST = 0.16 AU, PRES = 5.52 pbar

DIST = 0.14 AU, PRES = 121.62 nbar

DIST = 0.14 AU, PRES = 5.52 pbar

Figure 5.3: Hemispheric temperature maps centred at the 'dusk' terminator on both sides of the stability limit at 0.16 AU (top) and 0.14 AU (bottom) for two different pressure levels. The pressure levels of 122 nbar (left) and 5.52 pbar (right) correspond to the bottom and top of the thermosphere, respectively. The size of the globes is scaled to the relative planetary radius at the pressure levels shown. At 0.16 AU, the temperature is nearly uniform at 122 nbar, varying between 1410 and 1430 K. The altitude of the pressure level is 650 km above the lower boundary. At 5.5 pbar the substellar temperature is roughly 3750 K while the antistellar temperature is 2350 K, and the altitude is about 7000 km above the lower boundary. At 0.14 AU, the temperature varies between 1450 and 1510 K at 122 nbar and the altitude of the pressure level is about 650 km. At 5.5 pbar, on the other hand, the substellar temperature is over 23,000 K and the altitude is more than 75,000 km above the lower boundary. The temperature is fairly uniform horizontally, apart from the small region around the antistellar point where it drops to ~17,000 K [Koskinen et al., 2007a].

the temperatures are slightly higher. The dayside temperatures vary between 3500 and 4100 K, with a maximum along the equator on the ‘dawn’ side. The night side temperatures vary between 2300 and 2500 K, with a minimum on the equator toward the ‘dawn’ terminator. The maximum zonal wind speed is between 2–3 km s^{-1} and, measured from the lower boundary, the upper boundary altitude is 6800 km. At 0.14 AU, on the other hand, the temperature at the 3.7 pbar level varies between a minimum of 18,500 K, located a few degrees east from the antistellar point, and a maximum of 23,300 K, located at the substellar point. The steep diurnal temperature gradient, which normally occurs across the terminator, is shifted farther to the night side. Horizontally, the temperature is fairly uniform, apart from a cool circle, which is centred at the antistellar point and has a radius of about 40 degrees. These features are due to radiation penetrating farther to the night side through the tenuous, extended envelope and redistribution of heat by strong circulation. The winds blow from the dayside to the nightside, across the terminator, and the hot gas plunges downward from all directions into the antistellar cool spot. The horizontal flow reaches maximum speeds of 4–5 km s^{-1}. At the onset of hydrodynamic escape, the upper boundary altitude is 75,000 km - that is, more than the radius of the planet itself.

Figure 5.4 shows the substellar mixing ratios of atomic hydrogen for EX02r, a stable model at 0.2 AU, and EX012r, an inflated, hot model at the onset of hydrodynamic escape at 0.12 AU. These simulations were chosen, because they are sufficiently far from the stability limit to be considered reliably stable (at 0.2 AU) and unstable (at 0.12 AU). In the unstable model, atomic hydrogen dominates at pressures lower than 0.7 nbar (corresponding to altitudes higher than 3000 km) and is virtually the only neutral species at pressures lower than 0.3 nbar (corresponding to altitudes higher than 5000 km). By contrast, at 0.2 AU molecular hydrogen dominates at all altitudes.

Figure 5.5 contrasts the substellar P-T profiles from EX02r and EX012r. At pressures higher than $\sim$3 nbar, the temperatures increase only 100-300 K between 0.2 and 0.12 AU despite the nearly 3-fold increase in the incoming XUV flux. In the lower thermosphere the altitudes are also very similar, with the 3 nbar level corresponding roughly to the altitude of 2000 km. Above this level, the P-T profiles diverge considerably, and at 0.12 AU the top boundary temperature and altitude are $\sim$25,000 K and 94,000 km, respectively. The point where the profiles begin to diverge coincides with the region where atomic hydrogen takes over in EX012r. The variation in the P-T profiles can be understood in terms of the radiative heating and cooling terms displayed in Figure 5.6. The added heating in the lower thermosphere does not lead to greatly increased temperatures because the heating is efficiently offset by the enhanced infrared cooling. However, as the upper thermosphere is taken over by atomic hydrogen in EX012r, the cooling function approaches zero at pressures lower than 0.7 nbar. Due to the removal of H_2, the XUV heating also diminishes in the outer layers of the model but the excess energy is still enough to drive the atmosphere out of stability. It is worth noting here that the lack of cooling is *not* due to non-LTE effects in the outer layers. The fundamental finding of this thesis is that the efficiency of the cooling function depends on the availability of H_2.

Figure 5.7 shows the number densities of atomic hydrogen, H^+ and H_3^+ at the substellar point of

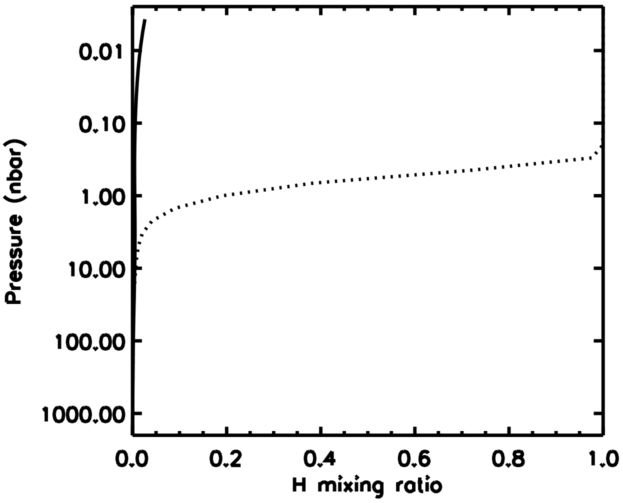

Figure 5.4: Pressure versus the mixing ratio of atomic hydrogen from EX02r (at 0.2 AU, solid line) and EX012r (at 0.12 AU, dotted line). The mixing ratio of atomic hydrogen is 1.0 for EX012 at pressures lower than about 0.3 nbar due to thermal dissociation of H_2.

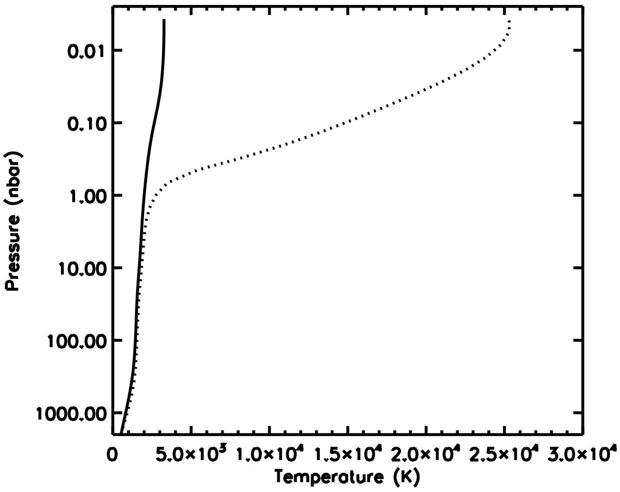

Figure 5.5: Substellar P-T profiles from EX02r (at 0.2 AU, solid line) and EX012r (at 0.12 AU, dotted line). The temperatures are comparable in the lower thermosphere but differ significantly at pressures lower than 1.0 nbar.

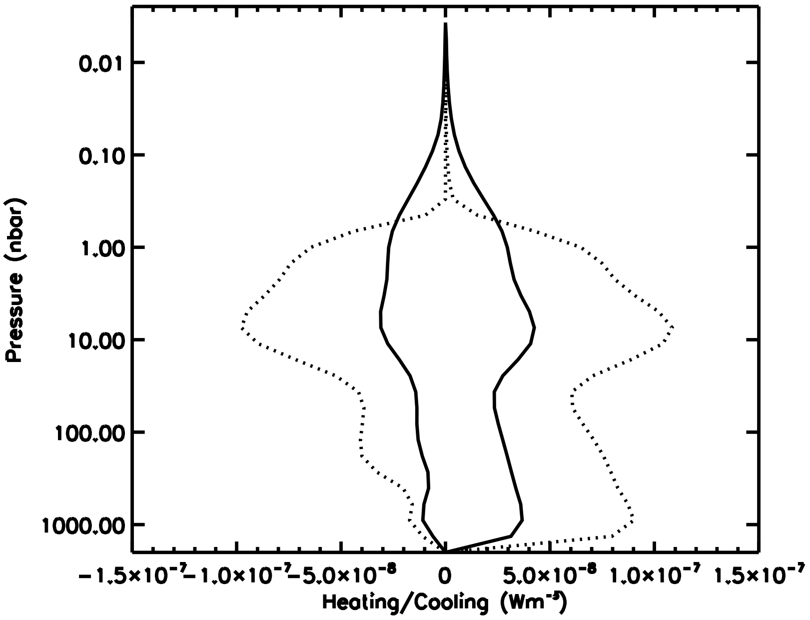

Figure 5.6: Volume infrared cooling and XUV heating rates beneath the substellar point from EX02r (at 0.2 AU, solid lines) and EX012r (at 0.12 AU, dotted lines). At 0.12 AU the cooling function approaches zero at pressures lower than 0.7 nbar, whereas this is not the case for EX02r. The XUV volume heating rate also drops steeply with altitude in the atomic hydrogen envelope, but the slight imbalance between the heating and cooling (barely visible in this plot) still drives hydrodynamic escape.

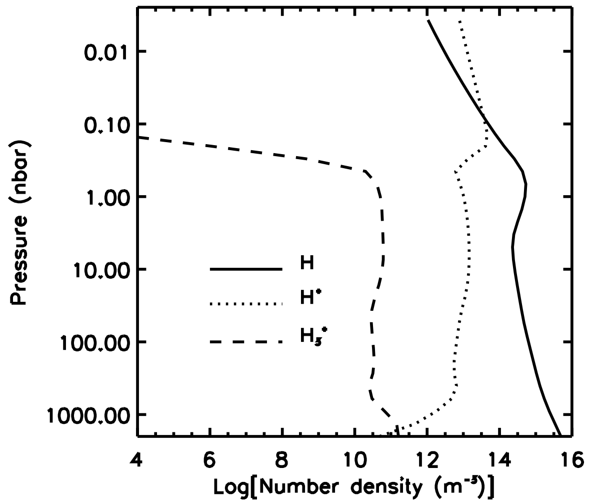

Figure 5.7: Pressure versus the logarithm of the number densities of atomic hydrogen (solid line), H^+ (dotted line) and H_3^+ (dashed line) in EX012r, orbiting at 0.12 AU, and at the onset of hydrodynamic escape. H^+ is the dominant species in the outer, escaping layer. The density of H_3^+ falls to zero by 0.1 nbar in the upper thermosphere due to thermal dissociation of H_2.

EX012r. The plot shows how the number density of H_3^+ drops with decreasing pressure in the layers where atomic hydrogen dominates. Also, the density of H^+ in the outer layer becomes comparable to the density of neutral hydrogen and H^+ dominates at pressures lower than 0.06 nbar (corresponding to an altitude of 17,000 km). In this regime the assumption that photochemistry does not impact the neutral density directly is clearly inadequate, and the number densities displayed in Figure 5.7 are thus suspect. The low pressure thermosphere-ionosphere system below the upper boundary should be modelled as a plasma, taking into account the partial pressures of electrons, ions and neutrals. For this system the ideal gas law is not an appropriate equation of state and instead a different equation of state should be derived for the plasma (see Chapter 7). However, from these results we can draw the qualitative conclusion that once hydrodynamic escape takes place, the escaping atmosphere is composed mainly of atomic hydrogen, with H^+ dominating at high altitudes.

A word of warning is appropriate here. A narrow stability limit is a dramatic result, as one might expect the transition from Jeans escape to hydrodynamic outflow to build up more gradually with decreasing orbital distance. We have already seen that the limit shifts farther out for EGPs that spin fast around their axis (see Section 4.4.4) and that a high mixing ratio of atomic hydrogen at the lower boundary leads to a reduced abundance of H_3^+ throughout the thermosphere and thus hydrodynamic escape farther out from the host star. The results and conclusions presented in this chapter are solid for lower boundary mixing ratios roughly less than 0.5 % for atomic hydrogen. For a higher mixing ratio than this, molecular diffusion leads to reduced density of H_2 in the upper atmosphere. In this case the thermosphere behaves more like a pure atomic hydrogen envelope and escapes hydrodynamically at least within 0.3 AU, as suggested by Lammer et al. [2003]. It is also possible that the lower boundary mixing ratio is under ~0.5 % at 0.2 AU, but increases above this value between 0.1 and 0.2 AU. In this case the stability limit is still between 0.1 and 0.2 AU, likely very near 0.15 AU, but the mechanism causing the instability is a combination of molecular diffusion and thermal dissociation of H_2. In this way the UV flux in general as well as X rays and the EUV flux would contribute to driving the rapid escape.

As a conclusion, the validity of these results can be confirmed only by suitable observations. Observations indicating hydrodynamic escape for HD209458b, orbiting well within the stability limit, already exist. What is needed now are observations of suitable planets orbiting outside or in the immediate vicinity of the stability limit. What is intriguing about such observations is that they can shed light not only on the stability and character of the upper atmosphere, but also on the composition of the lower atmosphere and perhaps even the rotation and day lengths of the planets. In this respect it is interesting that the recent observations of hot atomic hydrogen in the atmosphere of HD209458b [Ballester et al., 2007] suggest that the transition region between the cool lower atmosphere, composed mainly of H_2, and the hot upper atmosphere, dominated by H, is at the altitude of 8500 km. In this region the temperature is about 5000 K, and the pressure is between 1 and 10 nbar. These results are actually quite close to the corresponding values obtained for the EX012r simulation, and thus the observations seem to support a relatively low mixing ratio of H at the $\sim \mu$bar level.

5.2 Hydrostatic Equilibrium and Mass Loss

It has not been possible to model the inflated EGP atmospheres reliably after hydrodynamic escape sets in, because some of the basic assumptions in the model become suspect in this regime. Central to this problem is the breakdown of hydrostatic equilibrium. In hydrostatic equilibrium, the vertical part of the momentum equation can be dismissed because the pressure gradient term in the equation is exactly balanced by gravity and the rest of the terms are negligible. The assumption is valid in a regime where horizontal velocities do not vary dramatically with altitude (so as not to cause shear instability), the vertical velocities are generally slow and vertical acceleration can be considered negligible. As we have seen, hydrostatic equilibrium is the basis of the pressure coordinate system and although full 3D solvers do exist nowadays [eg. Ridley et al., 2006, Dobbs-Dixon and Lin, 2008], it is the central assumption in most general circulation models.

Yelle [2004] has shown for HD209458b that even if hydrodynamic escape is taking place, the atmosphere should be close to hydrostatic equilibrium. This opens up the possibility of simply inserting vertical escape as a boundary condition for EXOTIM. The model usually assumes that the vertical velocity vanishes at the outer boundary. It is relatively easy to replace this assumption by inserting a uniform escape velocity at the upper boundary that is based on the energy imbalance between the heating and cooling terms. However, experiments with the new boundary conditions are not very promising, in that they produce absurdly fast vertical outflows and either too low or too high temperatures.

In other words, even if the steady state results of Yelle [2004] are close to hydrostatic equilibrium, the model may evolve toward steady state in a fashion that implies the presence of vertical accelerations and thus any time-dependent model must allow for them. This shortcoming of the model is highly frustrating because it means that a comparison with actual observations is not possible. At present observations only exist for short-period EGPs orbiting within the stability limit. Otherwise it would have, for instance, been very interesting to model the Lyman α absorption for a planet like HD209458b and compare the results to the observed absorption signatures. This kind of modelling is only possible with a 3D model that solves the full set of Navier-Stokes equations with altitude as the vertical coordinate. The requirements and setting for such a model are discussed in Chapter 7.

Nevertheless, it is possible to use the existing results to calculate crude mass loss estimates, which can be compared to other such estimates presented in the literature. This gives an indication of the degree to which other models may be suffering from the neglect of 3D dynamics or, in some cases, the neglect of radiative cooling. The mass loss estimates presented in this section were calculated by assuming that, at the onset of hydrodynamic escape, the excess energy (not balanced by any cooling effects) available for a given simulation drives vertical mass flow.

The energy-limited escape flux from the atmosphere, S_{esc}, (particles per steradian per second) is given by [eg. Watson et al., 1981, Lammer et al., 2003]:

$$S_{esc} = \frac{F_{XUV} r_{XUV}^2 R_p}{G M_p m} \tag{5.1}$$

where F_{XUV} is the flux of XUV radiation absorbed by the atmosphere, r_{XUV} is the altitude where most of this radiation is absorbed (close to the altitude where the optical depth $\tau_{XUV} = 1$), $GM_p/R_p = \Phi_o$ is the gravitational potential of the planet, and m is the mass of the average atmospheric constituent in the escaping layer. This equation takes into account evaporation driven by the stellar XUV flux but it does not include the effect of the potentially strong tidal forces arising from the close proximity of the host star to short-period EGPs. Erkaev et al. [2007] modified equation (5.1) to allow for the influence of tidal forces by introducing a non-linear tidal enhancement factor $1/K(r_{RL}/R_p)$:

$$S_{esc} = \frac{F_{XUV} r_{XUV}^2}{m \Phi_o K(r_{RL}/R_p)} \tag{5.2}$$

where K is a function of r_{RL} and R$_p$, and r_{RL} is the altitude of the Roche lobe of the planet. Roche lobe is the the sphere of influence of planetary gravity beyond which the atmosphere is free to escape. Its size depends on the tidal forces between the planet and the star. On a line joining the star and the planet, there are two locations where the net gravitational potential is zero. These are the Lagrangian points L1 and L2, and for a small ratio of masses, M_p/M_*, these are roughly at the same distance from the planet. In this case, the Roche lobe distance is given by:

$$r_{RL} \approx (\frac{1}{3}\frac{M_p}{M_*})^{1/3} a \tag{5.3}$$

where M_* is the mass of the host star, and a is the orbital distance of the planet. If $\xi = r_{RL}/R_p$, the tidal enhancement factor, $1/K$, is [Erkaev et al., 2007]:

$$K(\xi) = 1 - \frac{3}{2\xi} + \frac{1}{2\xi^3} < 1 \tag{5.4}$$

For $F_{XUV} = Q_{XUV}/4\pi r_{XUV}^2$ at $r = r_{XUV}$, where Q_{XUV} is the total energy absorbed by the atmosphere (per second), the mass loss rate is simply given by:

$$\Gamma = \frac{Q_{XUV}}{\Phi_o K(\xi)} \tag{5.5}$$

Figure 5.8 shows the total XUV heating and the net infrared cooling rates versus orbital distance within 1.0 AU from the host star for the standard simulations discussed in this and the previous chapter. It also shows the net heating rate, which is the sum of all the terms in the energy equation integrated over the volume of the atmosphere, versus orbital distance. At 1.0 AU the total XUV heating rate is 6.6 $\times 10^{13}$ W. Assuming a heating efficiency of 50 %, the total energy absorbed by the thermosphere is 1.32 $\times 10^{14}$ W. This corresponds to a flux of $\sim$2 $\times 10^{-3}$ W m^{-2} through the upper boundary of the model (where $p \approx$3.7 pbar and the altitude is $\sim$3040 km). Scaling this flux to the distance of Jupiter at 5.2 AU, we obtain an effective flux of 7.4 $\times 10^{-5}$ W m^{-2}. Remarkably this flux is identical to the one given by Yelle and Miller [2004] for Jupiter, and thus it confirms that the radiative transfer scheme in the model is reasonably accurate. The effective flux is the flux of energy that is actually absorbed by the thermosphere. About 50 % of this energy is expended heating the neutral thermosphere. The XUV heating rates shown in Figure 5.8 depend only on the composition of the thermosphere and as such they can be used as guidelines for energy-limited scaling studies that often assume (erroneously) that all of the stellar XUV flux between $\sim$0.1 and 120 nm contributes to the heating of the thermosphere.

The total XUV flux received at 1.0 AU between 0.1 and 105 nm under the solar maximum conditions assumed in these simulations is 8.7 $\times 10^{-3}$ W m^{-2}. This flux is quite a bit higher than the flux of 4.64 $\times 10^{-3}$ W m^{-2}, which was constructed by Ribas et al. [2005] for the ‘average’ Sun in midcycle 1993 for the wavelength range of 0.1-118 nm. We note that the flux of 2 $\times 10^{-3}$ W m^{-2} flowing through our upper boundary is the average flux, distributed evenly around the planet, which is obtained by dividing the incoming flux by a factor of four. As this average flux is about 23 % of the total incoming flux received at 1.0 AU, we can conclude that 92 % of the total flux passes through the upper boundary while 8 % is absorbed in the exosphere.

Let us now turn our attention to the balance between heating and cooling. We have already noted that for Jovian thermospheric temperatures derived under the assumption that solar XUV radiation is the only source of heating, H_3^+ cooling is not at all significant. In fact H_3^+ begins to really have an impact on the results only within 1.0 AU from the Sun, and even at 1.0 AU the total cooling rate is only 40 % of the XUV heating rate. The ratio of cooling to heating increases with decreasing orbital distance until it reaches over 90 % between 0.3 and 0.16 AU. Then the ratio drops sharply at the stability limit as the cooling function is lost in the upper thermosphere.

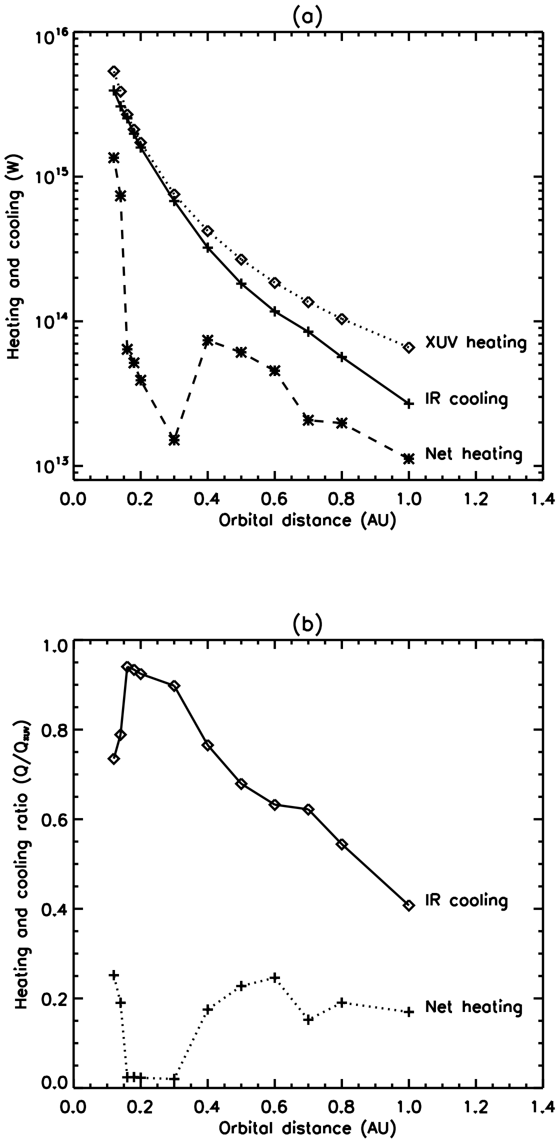

Figure 5.8: (a) The total heating and cooling rates (in W) obtained by integrating the volume heating and cooling rates over the whole volume of the atmosphere. The XUV heating rate is given by the fraction of absorbed stellar energy that heats the neutral thermosphere. The net heating rate is the sum of all the terms in the energy equation. (b) The ratios of the total infrared cooling rate and the net heating rate to the XUV heating rate. For perfect steady-state models, the latter ratio should approach zero.

As mentioned earlier, Figure 5.8 also shows the net energy input (in W) to the model. It is intriguing, and perhaps worrying, that the net heating rate is not always close to zero. At 1.0 AU, for instance, the net heating rate is about 17 % of the total heating rate. Between 1.0 and 0.4 AU it is around 20 %, and finally at 0.3 AU, it approaches zero. There are a number of reasons for the positive net heating. Firstly, the numerical volume integration of the energy terms is not entirely reliable, although this is not likely to explain the relatively large excess heating. Second, the models may not be in steady state after all, even if the temperatures in the atmosphere are clearly approaching steady state values and the values are not changing rapidly as the simulation proceeds. At 1.0 AU the cooling function is only 40 % of the heating function. Vertical conduction of heat, vertical and horizontal advection, and adiabatic expansion and contraction thus play a greater role in balancing the heating of the atmosphere. Compared to radiative cooling, these processes are slow and as a result, reaching steady state takes much longer than for radiation-dominated simulations. This is especially true if the primary cooling mechanism is downward conduction of heat, which is due to diffusion. It makes sense, then, that as the significance of radiative cooling increases with decreasing orbital distance, the simulations are closer to steady state and the net heating rate also decreases.

The policy we adopted was to run the simulations until the temperatures in the upper thermosphere stabilised, unless they became unstable, in which case they were stopped when the thermal escape parameter at the upper boundary had reduced near 1.5. Thus the excess heating should mainly affect the lower part of the stable thermosphere, where the response of temperatures to added heat is sluggish because the overall density is relatively high. It is therefore likely that the steady state temperatures would not be significantly different from the results presented here. Also, the models that orbit beyond 0.3 AU and rotate at the same rate should be cooler than the 0.3 AU simulation that is clearly in steady state.

A third potential reason for at least some of the excess heating is the fact that the numerical integration of the equations of motion does not conserve energy. At any time, the model is either leaking or gaining energy artificially due to a combination of numerical integration techniques and successive smoothing applications. Given that this inaccuracy exists, the balance of the energy terms at 0.3 AU is rather remarkable, although it is perhaps not that surprising because at this distance, the balance is mostly between radiative heating and cooling. Energy conservation is naturally easier to maintain when radiative balance dominates over advection and diffusion.

It is important to note that in a *stable* atmosphere the excess heating cannot drive atmospheric escape because thermal evaporation is limited to Jeans escape by the stability conditions at the exobase. Jeans escape is negligible in magnitude, and its impact on the energy balance is insignificant. However, in the *unstable* atmosphere the reason for the excess heating is well established, and the excess energy goes into driving hydrodynamic escape. Thus, within the stability limit, we can assume that the excess heating, measured at the onset of hydrodynamic escape, is balanced by the expansion and evaporation of the atmosphere. This allows us to calculate mass loss estimates for hydrodynamically escaping atmospheres.

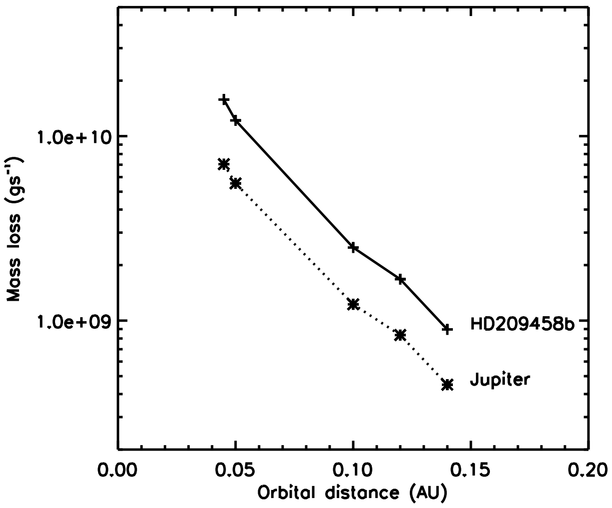

Figure 5.9: Mass loss rates for a planet like HD209458b and a Jupiter-type planet orbiting within 0.15 AU from a Sun-like host star. The values were calculated by assuming that the net heating, calculated by integrating the sum of all the terms in the energy equation over the volume of the atmosphere, goes into driving hydrodynamic escape.

Figure 5.9 shows the mass loss rates versus orbital distance for the standard Jupiter-type planet and a planet like HD209458b, both orbiting between 0.045 and 0.15 AU from the Sun. The rates were calculated by inserting the net heating rate given in Figure 5.8 into equation (5.5). The Roche lobe distance, given by equation (5.3), for a Jupiter-type planet orbiting the Sun varies from about 6.4 R_J at 0.045 AU to about 21 R_J at 0.15 AU. Correspondingly, the tidal enhancement factor, $1/K$, varies from 1.3 at 0.045 AU to 1.07 at 0.15 AU. For a planet like HD209458b, with a radius of R_p =1.32 R_J and mass of M_p = 0.69 M_J [Knutson et al., 2007b], the Roche lobe distances at 0.045 and 0.15 AU are 4.3 R_p and 14 R_p, respectively. The corresponding tidal enhancement factors are 1.5 at 0.045 AU and 1.12 at 0.15 AU. The specific planetary parameters enter equation (5.5) directly through the gravitational potential, which depends on the radius and mass of the planet. The net heating rate, on the other hand, depends largely on the composition of the upper atmosphere, which is influenced by the properties of the individual planets. In order to calculate the mass loss rates, we used identical energy inputs for HD209458b and the Jupiter-type planet we modelled, and thus the differences in energy deposition rates between the two planets were ignored. Given that the gravitational potential is then the only parameter affected by the specific properties of the planet, it is perhaps not surprising that the mass loss estimates from our calculations for HD209458b and the Jupiter-type planet do not differ significantly.

For a Jupiter-type planet, the mass loss rate varies from $\sim 4.5 \times 10^8$ g s^{-1} at 0.14 AU to 7.1 $\times 10^9$ g s^{-1} at 0.045 AU while for HD209458b, it ranges from 9.0 $\times 10^8$ g s^{-1} at 0.14 AU to 1.6 $\times 10^{10}$ g s^{-1} at 0.045 AU. Outside the stability limit Jeans escape is the prominent form of thermal evaporation and the escape rates are tiny compared to hydrodynamic escape. It is interesting that the mass loss rate of 1.6 $\times 10^{10}$ g s^{-1} is among the lowest quoted in the literature for HD209458b [eg. Lammer et al., 2003, Yelle, 2006, Lecavelier des Etangs et al., 2004, García Muñoz, 2007, Lecavelier Des Etangs, 2007, Erkaev et al., 2007, Penz et al., 2008], although it still complies with the minimum mass loss limit of 10^{10} g s^{-1} [Vidal-Madjar et al., 2003]. It is intriguing that Tian et al. [2005] who calculated mass loss rates for HD209458b by carrying out a time-dependent numerical integration of the vertical component of the equations of motion, obtained values very similar to our estimates. Assuming that radiative cooling can be ignored, they obtained a maximum mass loss rate of 6 $\times 10^{10}$ g s^{-1}. Then, by assuming that the total cooling function is about 80 % of the heating function, they reduced this rate to 2 $\times 10^{10}$ g s^{-1}, which is only marginally higher than our estimate. Also, our simulations imply a cooling function of about 75 % of the heating function, and this comes very close to their cooling function of 80 %.

In particular, these mass loss estimates are lower than those obtained by assuming that escape is simply energy-limited [eg. Lammer et al., 2003, Lecavelier Des Etangs, 2007]. Energy-limited escape is based on the idea that all of the available XUV energy goes into driving hydrodynamic escape. This approach often produces unrealistically high mass loss rates, although recent re-evaluations of the adopted scaling laws have brought mass loss estimates back in line with other, more sophisticated models [eg. Erkaev et al., 2007, Penz et al., 2008]. Mass loss rates of the order of 10^{10}-10^{11} g s^{-1} are produced by the majority of the existing models. Also, a recent 3D simulations of Lyman α absorption in the exosphere of HD209458b, based on the planet's interaction with the stellar wind, suggests that the mass loss rate should be around $(1.1 \pm 0.3) \times 10^{10}$ g s^{-1} [Schneiter et al., 2007]. A higher or lower rate would produce absorption that is inconsistent with the observations.

It is interesting to speculate on the possible reasons for the relatively low mass loss rate that is calculated here. One obvious factor is radiative cooling that depends on the availability of H_2 molecules in the thermosphere. Increasing the abundance of atomic hydrogen at the lower boundary would produce a higher mass loss rate, but the enhancement would not be consistent with the constraints evaluated by Schneiter et al. [2007]. Their work indicates that the mass loss rate is even lower than our results. This lends credibility to our approach, and highlights the need for more detailed observations characterising the upper atmosphere. The models of Yelle [2004] and García Muñoz [2007] include H_3^+ cooling but their mass loss estimates are still higher than ours, although the differences are modest. In fact, given the extremely crude nature of our calculations, they may not be significant at all. However, the key difference between EXOTIM and their models is that EXOTIM is three-dimensional. Horizontal dynamics distributes energy around the atmosphere and causes unforeseen variations in the composition of the thermosphere-ionosphere system. One of the most intriguing of such variations is the tendency of vertical upwelling to replenish H_2 concentrations on the dayside of slowly rotating EGPs that enhances the cooling function. The exact role of the different factors can only be properly understood in the context of a fully 3D model that does not assume hydrostatic equilibrium.

We have also calculated model-independent mass loss rates that account for XUV heating, different levels of radiative cooling and tidal forces. The results are shown in Figure 5.10 together with exospheric temperatures for a planet like HD209458b at different orbital distances within 0.3 AU from its host. The mass loss rates were calculated by assuming that the atmosphere escapes hydrodynamically within 0.3 AU and by adopting the average solar XUV flux (0.1-118 nm) of 4.64 $\times 10^{-3}$ W m^{-2} (at 1.0 AU, Ribas et al. [2005]). The incoming flux was averaged over the surface of the whole planet, and the temperatures were calculated from equation (4.1) by assuming a 50 % heating efficiency and adopting $\ln(p_o/p) \approx 10$ (placing the upper boundary at 0.09 nbar) and $T_o = 750$ K. The mass loss rates were calculated from equation (5.2), by assuming that most of the XUV energy is absorbed near $r = 1.1$ R$_p$ [Yelle, 2004, Erkaev et al., 2007]. Radiative cooling was crudely parameterised by allowing for different fractions of the heating rate to contribute to the heating of the thermosphere and atmospheric escape. The heating function was varied from 20 % to 200 %, where percentages between 20 %–100 % correspond to different levels of cooling and percentages over 100 % correspond to more than 50 % of the absorbed energy heating the thermosphere.

Assuming that the cooling function is 80 % (corresponding to only about 10 % of the total absorbed XUV energy heating the atmosphere), the exospheric temperature ranges from 3660 K at 0.3 AU to well over 300,000 K at 0.045 AU. It is intriguing that the simple scaling law (4.1) places the stability limit for the atmosphere between 0.1 AU and 0.2 AU, in fact very close to 0.15 AU. Inside 0.16 AU, the temperatures are very close to those derived from the full 3D calculation. Note that the cooling function in EXOTIM is more than 80 % outside 0.15 AU, but it decreases to about 75 % inside the limit. Correspondingly the mass loss rates for the 20 % heating efficiency are also very similar to those shown in Figure 5.9.

Heating efficiency of 100 % corresponds to the no-cooling case. In this case a planet like HD209458b undergoes hydrodynamic escape even farther out than 0.3 AU from the host star. The scaling law used to calculate the temperatures implies that the no-cooling case should be equivalent to the work of Lammer et al. [2003]. Using XUV fluxes of the current Sun, they obtained temperatures that are lower than those in Figure 5.10. This is because their calculations apply to a Jupiter-type exoplanet. Using Jupiter's parameters in equation (4.1) and assuming no radiative cooling yields exospheric temperatures that rise above 20,000 K between 0.2 and 0.3 AU, and above 100,000 K near 0.1 AU. The corresponding temperatures for HD209458b are higher than this due to the enhanced scale height in the atmosphere. Thus there is a crude agreement between the no-cooling case and the calculations of Lammer et al. [2003]. However, the mass loss rates here are lower because, as suggested by Penz et al. [2008] and our own radiative transfer calculations, we assumed that the XUV radiation is absorbed mainly at 1.1 R$_p$ instead of 3 R$_p$, as assumed by Lammer et al. [2003].

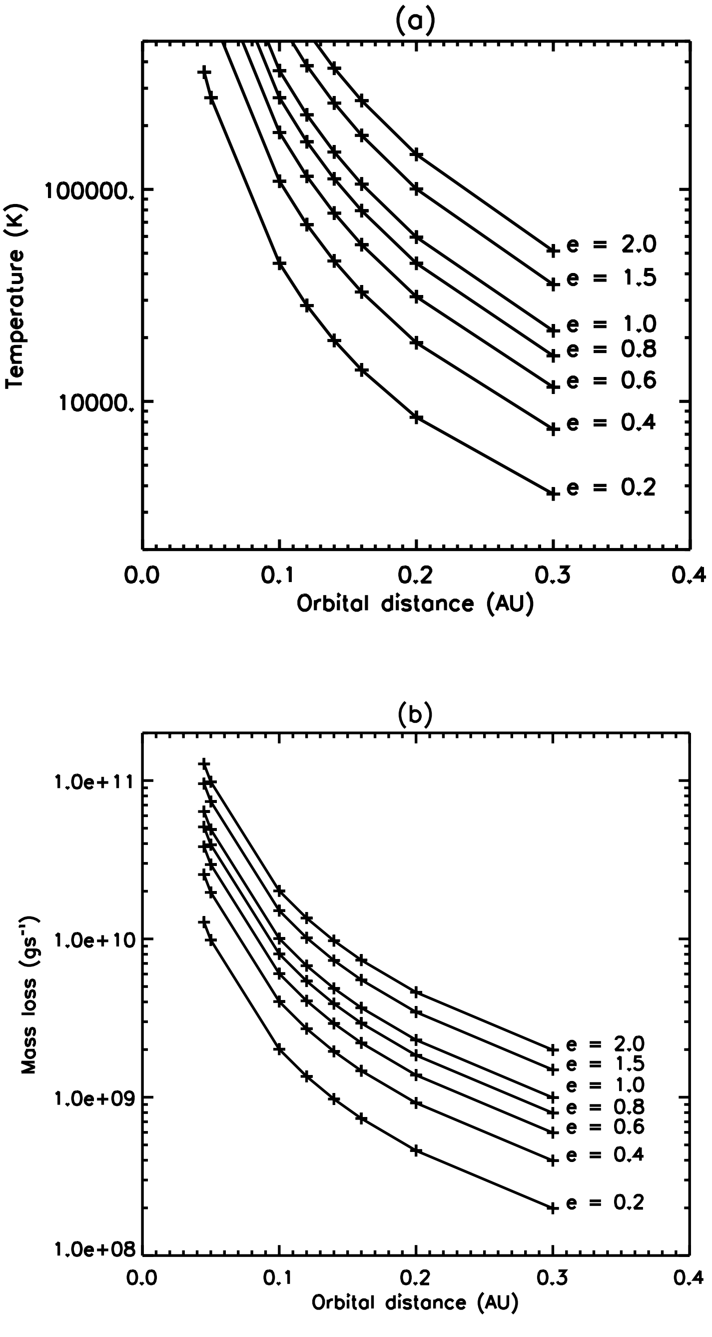

Figure 5.10: (a) Exospheric temperatures for a planet like HD209458b versus orbital distance inside 0.3 AU from the host star. Temperatures are shown for seven different heating functions, corresponding to different levels of thermalisation of the absorbed energy. The values were calculated by using equation (4.1). The lower boundary temperature was assumed to be 750 K. (b) Mass loss rates for the same heating functions.

5.3 XUV Fluxes of Different Stars

Obviously the 'H_2-breakdown limit' to thermospheric stability depends on the stellar XUV flux. So far we have only considered fluxes from a Sun-like star. The high-energy XUV emissions of the Sun originate in the solar chromosphere, transition region and the corona, and in general are due to the release of magnetic dynamo-generated energy. The strength of the dynamo is determined by the rotation rate of the star. Current observational evidence indicates that the Sun loses angular momentum with time due to magnetized winds [Ribas et al., 2005]. Also, zero-age main sequence solar-type stars tend to rotate over ten times faster than the Sun. The indication is that the rotation rates decrease during the evolution of these stars in the main sequence. Consequently the XUV emissions from young solar-type stars can be much higher than those used in this study.

In order to study the response of the model to XUV emissions from different host stars six stars were chosen from the '*Sun in Time*' sample, which uses observations of solar-type stars of different ages to characterise the evolution of the Sun's XUV emissions [Ribas et al., 2005, Lammer et al., 2003]. Also, XUV flux estimates calculated by Lecavelier Des Etangs [2007] for F6–F7, F8–F9, K, and M stars were adopted. The location of the stability limit around these stars was estimated by calculating the distance from them where the atmosphere would receive the same total XUV flux (0.1–118 nm) as it does at 0.16 AU around the Sun. The flux estimates and the stability limits obtained in this way are shown in Table 5.1.

Unfortunately, due to interstellar absorption, the stellar XUV fluxes are difficult to observe. In particular, there is a gap in the available observations between 36 and 92 nm, which is a region of very strong interstellar absorption in the H I Lyman α continuum. In the X ray wavelengths, the observations for the *Sun in Time* program were performed by the Advanced Satellite for Cosmology and Astrophysics (ASCA) and the Rontgen Satellite (ROSAT) (0.1–2.0 nm and 2.0–10 nm, respectively). These observations had to be calibrated by using a physical plasma emission model [Ribas et al., 2005]. The EUV and FUV fluxes were measured by the Extreme Ultraviolet Explorer (EUVE) and the Far Ultraviolet Spectroscopic Explorer (FUSE) (10–36 nm and 92–118 nm, respectively). These flux measurements are model-independent in that they were calibrated during data reduction and there was no need for assuming a plasma emission model beforehand. The fluxes for the H I Lyman α gap were estimated by using measurements of current solar fluxes in the missing interval and assuming that the power laws derived for time-evolution in the other wavelength intervals hold in the H I Lyman α gap as well.

It is even more difficult to estimate XUV fluxes from stars of different spectral type. Lecavelier Des Etangs [2007] used ROSAT observations between 11 and 20 nm and scaled the fluxes in this interval to the total solar EUV flux of 4.6×10^{-3} W m^{-2} given by Ribas et al. [2005]. He argued that this is justified because both the 10–20 nm and the XUV fluxes between 0.1 and 118 nm are emitted in the same region of the solar atmosphere. Despite this obvious defence, the approach appears oversimplified because it cannot be guaranteed that the limited 10 nm window (in which less than one quarter of the total XUV luminosity is emitted) can be used as a proxy for the whole range of XUV wavelengths. Also,

Table 5.1: XUV fluxes from different stars and thermospheric stability limits. The total XUV flux is given for the 0.1–118 nm wavelength interval and is normalised to a distance of 1.0 AU from the star. The *Sun in Time* fluxes were taken from Ribas et al. [2005] and the fluxes for other spectral types from Lecavelier Des Etangs [2007].

Sun in Time targets

Name	HD	Spectral type	Age (Gyr)	F ($\times 10^{-3}$ Wm^{-2})	Stability limit (AU)
EK Dra	129333	G1.5 V	0.1	513.5	1.68
π^1 UMa	72905	G1.5 V	0.3	129.3	0.84
κ^1 Cet	20630	G5 V	0.65	51.1	0.53
β Com	114710	G0 V	1.6	16.0	0.3
The Sun	...	G2 V	4.6	4.64	0.16
β Hyi	2151	G2 IV	6.7	2.9	0.13

Stars of other spectral type

Spectral type	F ($\times 10^{-3}$ Wm^{-2})	Stability limit (AU)
F6-F7	14.7	0.28
F8-F9	4.64	0.16
K	14.7	0.28
M	2.9	0.13

the method does not adequately account for the different ages and rotational states of the stars.

To conclude, the limits proposed in Table 5.1 suffer from a number of uncertainties, in *addition* to model-dependent uncertainties such as the lower atmosphere composition or the rate of planetary rotation. Firstly, uncertainties are associated with the reported XUV fluxes. Secondly, the simple scaling law used to calculate the stability limits does not take into account the fact that fluxes in different wavelength intervals contribute to the heating of the thermosphere in different proportions or that the evolution of the flux intervals is not uniform. For instance, according to Table 5.1, during solar evolution the total XUV flux (0.1–118 nm) reduces by a factor of ∼111, whereas the X ray flux reduces by a factor of ∼1201 and the total flux in the range of 0.1–36 nm reduces by a factor of ∼155. For the current Sun the X ray flux amounts to about 18 % of the total XUV emission, while the interval 0.1–36 nm amounts to 62.5 % of the total flux. During early evolution before the 100 Myr benchmark the corresponding percentages were 51 % and 88 %, respectively. As the high-energy XUV photons contribute more to the heating of the thermosphere, the stability limits for the early solar-type stars may well be underestimated in Table 5.1.

5.4 Implications on the Evolution of Close-In Gas Giants

It is thought that close-in EGPs form between 5 and 20 AU from the host star, in the region where the formation of icy planetesimals is possible, and then migrate inward to their final position close to the star. Figure 5.11 shows the orbital distance versus time for a typical migration of a 0.5 M_J planet if migration is driven by gas in the circumstellar disk accreting onto the host star and dragging the planet with it (Type II). The results are based on a photoevaporating disk model (R.P.Nelson, M.Fogg, *personal communication*). The plot indicates that the planet migrates from 5.0 AU to 0.1 AU in ∼500,000 years. This implies a migration rate of 10 AU Myr^{-1}.

The fast migration rate implies that close-in EGPs that orbit solar-type stars reach the relevant stability limit of 1.7 AU easily during the first 100 Myr of stellar evolution. This in turn means that their atmospheres undergo hydrodynamic escape throughout almost their entire lifetime, and this may significantly influence their evolution and the composition of their atmospheres. The escape rate is likely to be much higher during the early evolution and then gradually decreasing as the host star matures. In addition to close-in EGPs, even those EGPs that orbit their parent stars further out are likely to have undergone a period of hydrodynamic escape that may have altered the evolution of their atmospheres and interior.

Of course the important question is whether close-in EGPs survive evaporation or not, and if so, for how long? A Jupiter-mass exoplanet undergoing hydrodynamic escape at a rate of $dM/dt \approx 2 \times 10^{10}$ g s^{-1} would lose all its mass in about 3.0×10^{12} years. For a planet like HD209458b with a corresponding mass loss rate, the timescale for total mass loss is about 2.0×10^{12} years. The expected main sequence lifetime of HD209458 is $\sim 10^{10}$ years and the current age of the star is estimated as ∼4 Gyr. In other

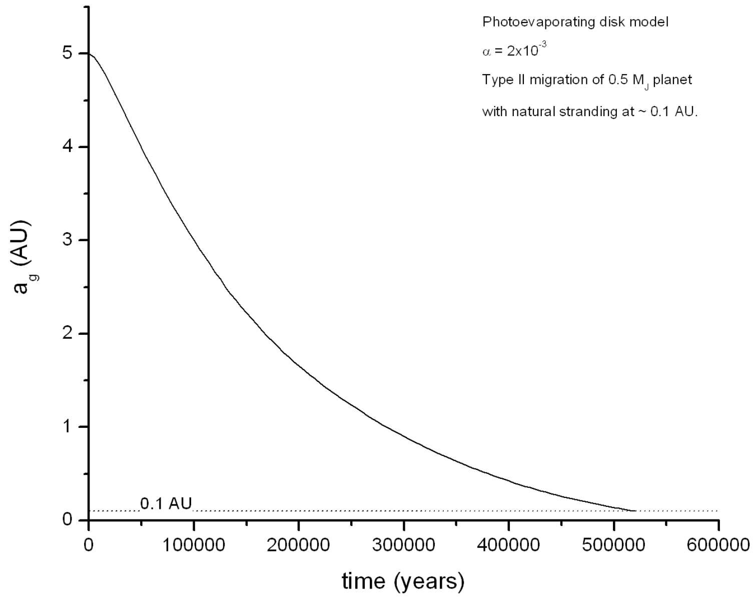

Figure 5.11: Semi-major axis versus time for a migrating giant planet.(R.P.Nelson and M.Fogg)

words, during the remaining 6 Gyr of main sequence evolution the planet will loose only 0.03 % of its current mass. Using the energy-limited mass loss formula, and assuming that the only variable is the available stellar XUV energy, the mass loss rate is likely to have been two orders of magnitude higher during the early evolution of the system. If one uses the an average value of 2 $\times 10^{11}$ g s^{-1} for the first 4 Gyr, the planet has lost the equivalent of 2 % of its current mass since its formation.

Lecavelier Des Etangs [2007] estimated mass loss rates and lifetimes for the whole sample of exoplanets known on June 15th, 2006. He used an extremely simplified procedure, assuming that the lifetime of the exoplanets against evaporation can be estimated by a ratio of the total gravitational potential energy to the mean EUV energy deposition rate into the atmosphere during the evolution of the planet. Correspondingly the mass loss rate is given by the ratio of the EUV energy deposition rate to the gravitational potential energy per unit mass. This calculation accounts, with crude parametrisations, for tidal forces, varying EUV fluxes from stars of different spectral types, the evolution of the EUV fluxes in time and the changing radius of the planet while it evolves. However, it makes a few crucially misleading assumptions. Firstly, it assumes that 100 % of the incoming energy flux that is converted into heat is used in escaping the gravity of the planet, i.e. to compensate for the negative potential energy. This implies that the atmosphere must always escape hydrodynamically. Such an assumption is almost certainly incorrect for most of the known giant planets orbiting farther than about 0.3 AU from their host stars, and consequently the escape rates in this range are likely to be hugely overestimated. Secondly, the simplistic method excludes any possibility of radiative cooling or effects arising from complex thermosphere-ionosphere dynamics. Our simulations indicate that outside the stability limit almost none

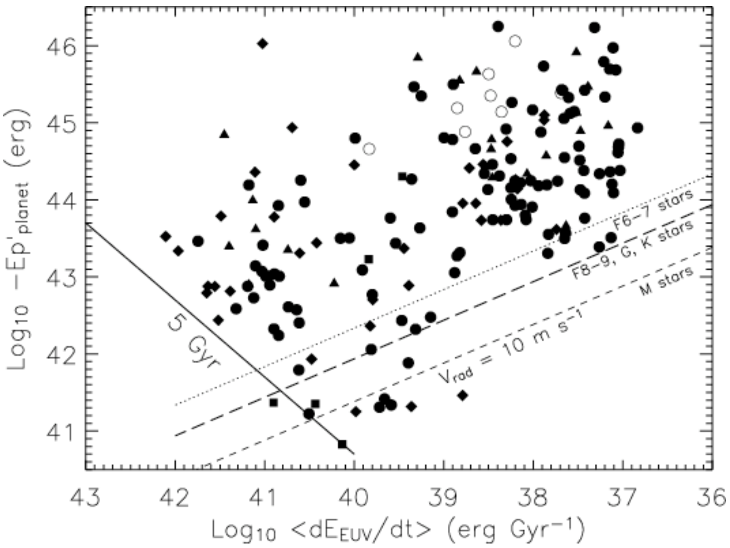

Figure 5.12: Potential energy of extrasolar planets known on June 15th, 2006 as a function of the mean EUV energy received per billion years. The 5 Gyr line marks the boundary of the evaporation-forbidden region in the lower left corner of the plot, where the lifetimes of any planets would be less than 5 Gyr. The dotted and dashed lines show the 10 m s^{-1} radial velocity isocurves for different types of host stars [Lecavelier Des Etangs, 2007].

of the absorbed energy is available to drive escape, and thermal evaporation is due to Jeans escape. Thus the assumption made by Lecavelier Des Etangs [2007] and some other modellers [eg. Lammer et al., 2003, Erkaev et al., 2007, Penz et al., 2008] that all of the available XUV energy powers escape is only likely to be valid for planets orbiting inside the stability limit. However, it may not always be accurate even if the atmosphere is escaping hydrodynamically because initially our modelling indicates that at the onset of hydrodynamic outflow, only ∼30 % of the heating rate is available to drive escape. All this implies that the results of Lecavelier Des Etangs [2007] correspond to the maximum possible evaporation, provided that his parameterisation of the different EUV fluxes is accurate.

Figure 5.12 shows the gravitational potential energies of the exoplanets included in the sample used by Lecavelier Des Etangs [2007] as a function of the mean EUV energy received per billion years. The plot indicates that only three planets are found to the left of the 5 Gyr limit, which indicates that their lifetimes against thermal evaporation are less than 5 Gyr. These planets are all Neptune-mass planets, while all of the Jupiter-class planets are firmly outside the so-called ‘evaporation-forbidden’ region. This indicates that most extrasolar gas giants survive mass loss throughout the main sequence lifetime of their hosts stars even under maximum evaporation conditions. The impact of hydrodynamic escape is thus limited to the details of the evolution and the coupling of the atmosphere to the interior. In this sense, the planets are stable against thermal evaporation throughout their lifetime, and the concept of instability that we have discussed in this chapter simply refers to fast hydrodynamic escape at the top of the atmosphere.

Scaling laws can only go so far when it comes to investigating the evolution of the planetary atmosphere under strong stellar irradiation. A more realistic picture requires a coupling of atmospheric models, including hydrodynamic escape, to evolution models for the interior. One such model was developed by Baraffe et al. [2004] who coupled energy-limited mass loss estimates to an evolutionary model for irradiated exogiants. They point out that the planet's response to mass loss over long timescales depends on the Kelvin-Helmholtz timescale (KH) for contraction of the interior and the evaporation timescale. If the evaporation timescale is shorter than the KH timescale, the mass of the planet decreases faster than its radius contracts. As a consequence, the ratio of the evaporation timescale to the KH timescale decreases further, eventually leading to a runaway expansion that spells a catastrophic fate for the planet's hydrogen-rich envelope. This observation led Baraffe et al. [2004] to introduce the concept of a critical mass, which is the initial mass of formation for exogiants below which the runaway evaporation regime is reached in less than 5 Gyr.

Baraffe et al. [2004] could not identify an evolutionary sequence that fits the properties of HD209458b. An old problem for this planet is, and their results again confirmed this, that in the absence of evaporation the predicted radius for the system turns out to be about 25 % larger than that observed. None of their models including evaporation can explain the properties of the planet either, but simulations do indicate that with an initial mass of 1.1–1.2 M_J, HD209458b should be reaching the runaway evaporation regime right now. To catch a planet at the right time for this is statistically extremely unlikely. It should be noted that Baraffe et al. [2004] used energy-limited evaporation rates calculated with a formula similar to that presented by Lammer et al. [2003] and thus their evaporation rate for HD209458b is likely to be too high, possibly as much as by two orders of magnitude. A lower evaporation rate pre-empts the potentially awkward conclusion that HD209458b is currently beginning to disintegrate. Nevertheless, the coupled evaporation-evolutionary model demonstrates that evaporation described in terms of simple scaling laws may not be adequate as more complex interactions arise from the coupling of the escaping atmosphere to the interior.

5.5 Non-Thermal Escape

For completeness, we must mention the prospect of non-thermal escape. This is usually related to the interaction between the stellar wind plasma, the atmosphere and the planetary magnetosphere. Many aspects of such interactions for exoplanets are currently poorly understood. Stellar wind properties of the host stars are difficult to constrain and the searches for planetary magnetic fields through the detection of radio emissions have not yet been successful.

Non-thermal escape arises from a number of different processes. For instance, charge exchange with the impinging stellar wind can produce hot neutral atoms that have enough kinetic energy to escape the atmosphere. The reverse, i.e. the formation of energetic neutral atoms (ENAs) in the stellar wind due to charge exchange with the atmosphere, was recently modelled by Holstrom et al. [2008] for HD209458b.

They argue that only ENAs can explain the high-velocity tail of the Lyman α absorption signature and used their simulations to constrain the properties of the stellar wind in the vicinity of the planet, estimating its velocity and temperature to be 50 km s^{-1} and 10^6 K, respectively. This interesting and somewhat provocative suggestion goes against the (by now) conventional idea that the cometary wake around the planet is due to escaping hydrogen atoms being accelerated by radiation pressure [Vidal-Madjar et al., 2003]. It also implies that observations of EGP upper atmospheres can potentially be used to probe stellar wind conditions around the host stars, which in itself is a useful goal.

Other triggers for non-thermal escape include dissociative recombination, photodissociation, escape of ions along open magnetic field lines, sputtering of neutral particles and pick-up of ions by the stellar wind, or impact ionisation and dissociation by the protons and electrons in the stellar wind. If molecular ions and electrons recombine dissociatively, the fragments may gain enough kinetic energy to escape the atmosphere. Also, ionising radiation that dissociates molecules may impart enough kinetic energy on the fragments to enable them to escape. Sputtering refers to collisions between the neutral particles in the atmosphere and the stellar wind plasma, in which enough kinetic energy may be exchanged to enable the atmospheric species to escape. Ions that are located high enough in the atmosphere can be picked up by the electromagnetic fields in the stellar wind plasma and thus escape. In general, ion escape is inhibited by the magnetic field, but fast ions can escape in regions of open field lines, where they can even be accelerated by atmospheric electric fields.

Yelle [2004, 2006] estimated the impact of a potential global magnetic field on thermal escape from HD209458b by assuming that the planet's magnetic field is sufficiently strong to completely inhibit ion escape while neutrals escape at the kinetic rate. This scenario led to an increase in thermospheric temperatures that enhanced the neutral thermal escape rate and as a result, the evaporation rate was reduced only by about 30%. However, he did not consider non-thermal escape processes, the potential escape of ions along open field lines or any interactions with the stellar wind. Also, he did not take into account the slow rotation rate of HD209458b relative to Jupiter, which may imply a weak magnetic field.

Erkaev et al. [2005] presented a more comprehensive study of plasma and magnetic field parameters for close-in EGPs. They argued that, with stellar wind conditions similar to the Sun, the magnetosonic Mach numbers would be less than 1.0 for giant planets like HD209458b orbiting within about 0.1-0.2 AU from the host star and thus there would be no bow shock protecting such planets. Grießmeier et al. [2004] suggested earlier that the magnetic moment of planets like HD209458b can be very weak, less than one tenth of the magnetic moment of Jupiter, due to tidal locking. As these planets are also likely to have an expanded upper atmosphere, both Grießmeier et al. [2004] and Erkaev et al. [2005] concluded that this would give rise to a Venus-like interaction between the ionopause and the stellar wind. Based on such a regime, Erkaev et al. [2005] calculated the production of planetary H^+ ions due to photoionisation, impact ionisation and charge exchange in the exosphere of HD209458b and thus evaluated the ion escape rate due to pick-up by the stellar wind. They deduced mass loss rates in the range of $\sim 10^8$–10^9 g s^{-1}, depending on the number density of hydrogen near the exobase. These values correspond to about 0.5–5

% of the expected thermal escape rate, which is of the order of 2 $\times 10^{10}$ g s^{-1}. These ion escape rates can be enhanced by occasional coronal mass ejections (CMEs), which are a well established feature of solar activity [Khodachenko et al., 2007].

This concludes our discussion of atmospheric escape from short-period exogiants. It appears that evaporation from close-in EGPs takes place primarily in the form of thermal hydrodynamic escape, while non-thermal escape plays only a minor role in comparison, despite the fact that the planets do not seem to be able to establish a bow shock. Of course stellar wind interaction may lead to the heating of the upper atmosphere, and this could contribute to thermal escape. The stellar wind interaction regimes for short-period exoplanets are likely to be both complex and exotic and much more work is needed to characterise them. It is interesting to note that Erkaev et al. [2005] place the boundary between the fast and slow bow shock regimes between 0.1 and 0.2 AU, as this region lies near our stability limit for thermal escape. In another paper Erkaev et al. [2007] explore thermal escape under tidal forces and end up suggesting that EGPs may undergo Jeans escape beyond 0.15 AU. Although their argument is based on the strength of the tidal forces and is thus entirely different to ours, the limit they suggest agrees with this current work. A picture is beginning to emerge, and this picture tells us that the upper atmospheres of giant exoplanets orbiting Sun-like stars become significantly exposed to different erosion processes somewhere between 0.1 and 0.2 AU.

Chapter 6

A Case Study: HD17156b

HD17156b was discovered with the radial velocity method by Fischer et al. [2007] as a part of the N2K program, which is a survey of metal-rich stars, intended to identify short-period planets. It orbits a G0 star with an effective temperature T_{eff} = 6080 K, $R_* = 1.47\ R_{Sun}$, $M_* = 1.2\ M_{Sun}$ and the bolometric luminosity $L_* = 2.6\ L_{Sun}$. The metallicity of the star is [Fe/H] = 0.24 and the age is estimated to be 5.7 Gyr. The Ca II H & K emissions from the star (or rather the lack of them) suggest low chromospheric activity, and the estimated stellar rotation period is approximately 12.8 days [Fischer et al., 2007]. As HD17156 is a G-type star and older than the Sun, the work of Ribas et al. [2005] suggests that the XUV flux it emits should be slightly lower than the solar XUV flux. Low chromospheric activity seems to support this, but the XUV flux is also expected to correlate with the stellar rotation rate. The period of rotation for HD17156b is shorter than that of the Sun, which could indicate a higher XUV flux. Given these characteristics, the XUV emissions from this star are not likely to be exactly the same as for the Sun. However, no observations of these emissions exist, and given the spectral type and the age of the star, it is probably good enough to adopt solar fluxes for the simulations. At least the simulations then demonstrate the response of the upper atmosphere to relative flux variations along the orbit. In this context it is also interesting to note that the conditions in the upper atmosphere of the planet could, with suitable observational or modelling constraints, yield clues to the XUV activity of the star.

According to the radial velocity measurements, the planet has $M \sin i = 3.11\ M_{Jup}$, P = 21.2 days, $e \sim 0.67$ and an orbital semi-major axis $a \sim 0.15$ AU. Soon after the initial discovery, a group of amateur astronomers, forming a part of the *Transitsearch.org* network, discovered that HD17156b is a transiting planet [Barbieri et al., 2007]. Due to the gaps in the initial transit light curve, and the inaccuracy of the data, the planetary and orbital parameters released by Barbieri et al. [2007] are somewhat uncertain. Based on independent ground-based observations, two groups, Gillon et al. [2007] and Irwin et al. [2008] have released improved parameters for the planet. The two latter sets of parameters agree broadly with each other, with some slight quantitative differences, whereas some parameters released by Barbieri et al. [2007] differ significantly from both. For these simulations of HD17156b, the parameters released by Gillon et al. [2007] were adopted, and together with the model input parameters, they are listed in

Table 6.1: Planetary and orbital parameters for HD17156b

Planetary parameters[a]	
M_p (M_{Jup})	3.111
R_p (R_{Jup})	0.964
Orbital parameters	
Eccentricity	0.6717
Semi-major axis (AU)	0.1594
Inclination	88.23^o
Period (days)	21.217
Longitude of periastron	121.23^o
Lower boundary conditions	
T_o (K)	520
p_o (Pa)	0.2
Gravity (ms^{-2})	87.0
Mixing ratio of H	
HD.001	2×10^{-4}
HD.002	0.01

---

[a] The planetary and orbital parameters are taken from Gillon et al. [2007]

Table 6.1.

HD17156b is in many ways a remarkable transiting planet. It is the longest period transiting planet known to date, and with an orbital semi-major axis of 0.16 AU and eccentricity of ~0.67, it moves between 0.27 AU at apastron and 0.053 AU at periastron, facing wildly different irradiation conditions during the orbit. Indeed, the stellar flux is 26 times higher at periastron than at apastron. For our purposes the planet is particularly intriguing because it moves across the stability limit around 0.15 AU, spending some of the time inside the limit and some of the time outside it. It is interesting to examine if the stability of the atmosphere is determined near the periastron, or at other parts of the orbit, and if the atmosphere cools down significantly when it moves away from periastron toward apastron.

However, there are some caveats that come into play here. The planet is three times as massive as Jupiter, although the radius of the planet is comparable to that of Jupiter ($R_p \sim 0.964\ R_J$). This means that the average density of the planet is relatively high, and this is bound to have an impact on the atmosphere. Thus the planet deviates from the Jupiter-like test case that was used to establish the stability limit. Higher gravity, arising from the higher mass, causes scale heights in the atmosphere to shrink. This has an impact on molecular diffusion processes in the thermosphere, and thus the vertical distribution of different species.

Another difference is that a planet on such a highly eccentric orbit as HD17156b is not likely to be rotationally synchronised, and we have already learned that rotational dynamics driven by the Coriolis force has a potentially significant impact on the upper atmosphere. Fortunately, some constraints can be placed on the rotation of the planet around its axis. The planet experiences very strong tidal forces during periastron, and these have almost certainly driven the planet into 'pseudo-synchronous' rotation [Barbieri et al., 2007, Hut, 1981]. This means that the planet is synchronised to the host star (with the same side facing the star) during periastron, but at other parts of the orbit it rotates around its axis asynchronously. According to Hut [1981], the 'pseudo-synchronous' spin angular velocity of the planet is given by:

$$\Omega_{sp} = \frac{1 + (15/2)e^2 + (45/8)e^4 + (5/16)e^6}{[1 + 3e^2 + (3/8)e^4](1 - e^2)^{3/2}}\overline{\Omega} \tag{6.1}$$

where e is the eccentricity, and $\overline{\Omega}$ is the mean orbital angular velocity. Substituting $e \sim 0.67$ yields $\Omega_{sp} \sim 5.6\,\overline{\Omega}$. This means that during one full orbit the planet spins around its axis 4.6 times in the star's frame of reference. The orbital angular velocity at periastron is given by (derived from Kepler's laws):

$$\Omega_p = \frac{(1 + e)^2}{(1 - e^2)^{3/2}}\overline{\Omega} \tag{6.2}$$

Thus in terms of Ω_p, the 'pseudo-synchronous' spin can be expressed as:

$$\Omega_{sp} = \frac{1 + (15/2)e^2 + (45/8)e^4 + (5/16)e^6}{[1 + 3e^2 + (3/8)e^4](1 + e)^2}\Omega_p \tag{6.3}$$

Again using $e \sim 0.67$ yields $\Omega_{sp} \sim 0.818\ \Omega_p$. In other words, during periastron the planet's spin is slower than the orbital angular velocity, and while passing the periastron the planet should therefore revolve backwards with respect to the star compared to normal, faster spin at other parts of the orbit. This behaviour is a curious feature of 'pseudo-synchronisation' and it causes a peculiar jitter in the position of the star in the planet's sky near periastron.

Lastly, the results are affected by the composition at the lower boundary of the model (at 2 μbar), and in particular by the mixing ratio of atomic hydrogen there. The extensive discussions in Chapters 4 and 5 already indicated that this mixing ratio is not easily constrained. In order to explore different options, we have chosen to use two different lower boundary mixing ratios for atomic hydrogen; $\sim 2 \times 10^{-4}$, which is appropriate for Jupiter [Grodent et al., 2001], and 0.01, which may be appropriate for a planet like HD209458b [Liang et al., 2003].

6.1 The Model Orbit

The progress of the planet along the orbit is simulated by changing the irradiation conditions. In order to do this, we need to know the orbital true anomaly, which is the angular separation of the planet from

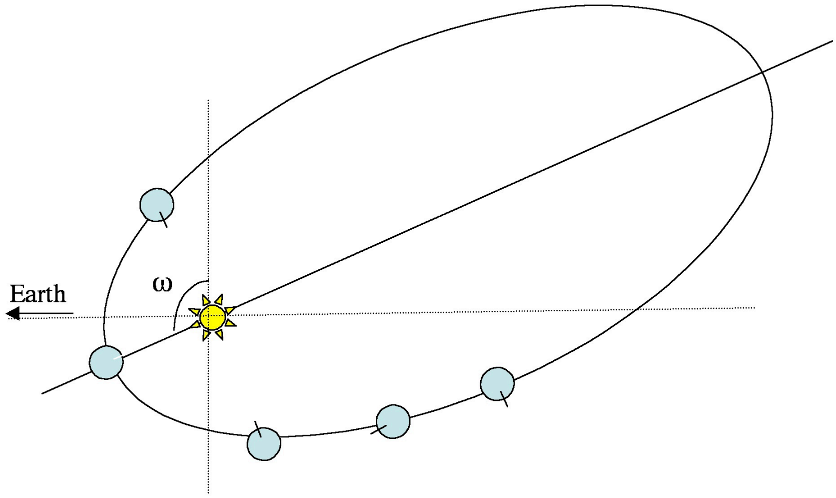

Figure 6.1: Illustration of the orbit of HD17156b. The angle ω is the longitude of the periastron ($\sim$121.23^o). 'Pseudo-synchronisation' during periastron is also illustrated with the planet and the sub-stellar point indicated. The figure is for illustration purposes only, and has not been drawn to scale or with an accurate eccentricity.

periastron, and the distance of the planet from the star as a function of time. Also, we need to account for the planet's spin around its axis by varying the position of the host star in the planet's rotating frame of reference.

Figure 6.1 is an illustration of the orbit of HD17156b that also shows the longitude of the periastron from the point of view of an observer on Earth. The transit is offset clockwise from periastron by 31.23 degrees. The inclination of the orbit is i = 88.23 degrees [Gillon et al., 2007], although this figure has been revised to 86.5 degrees by Irwin et al. [2008]. It is not clear if a secondary eclipse exists. Gillon et al. [2007] suggest that it should be a partial grazing eclipse, but Irwin et al. [2008] ascribe only a 9.2 % chance of this. The probability of a full secondary eclipse is even lower at 6.9 %. In case a secondary eclipse does occur, the angular separation between the antitransit and periastron is 148.77 degrees.

The orbital mean anomaly as a function of time is given by:

$$M(t) = \frac{2\pi}{P}(t - T) \tag{6.4}$$

where P is the orbital period and T is the time of periastron. The mean anomaly is simply the angular distance traversed by the planet in time $(t-T)$ if the orbit was circular. It can be related to the *eccentric anomaly*, E, by using Kepler's second law, which states that the radius vector from the host star to the planet sweeps out equal areas in equal time, and the geometry of an ellipse (see Figure 6.2). The relation is given by Kepler's equation:

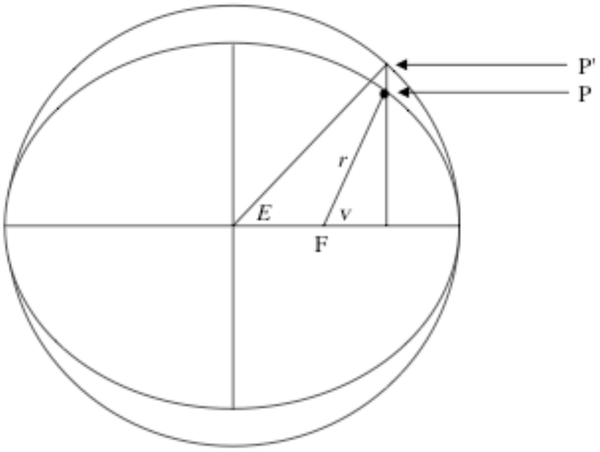

Figure 6.2: Geometry of the ellipse shown together with the *eccentric* or *auxiliary* circle surrounding it. Here F is the focus (corresponding to the location of the host star), P is the position of the planet along the ellipse, and P' is the point on the eccentric circle. E is the eccentric anomaly, and ν is the true anomaly.

$$M = E - e\sin(E) \tag{6.5}$$

The eccentric anomaly is measured along the *eccentric circle*, which is a circle with a diameter equal to the major axis of the ellipse for which true anomaly is calculated. In effect, it is the angle between periastron, the centre of the eccentric circle and point P' along the circle directly above the position of the planet on the elliptic orbit (point P), as shown in Figure 6.2. By using the general equation of an ellipse and geometric relations, it is straightforward to show that true anomaly, θ, is related to the eccentric anomaly by:

$$\cos(\theta) = \frac{\cos(E) - e}{1 - e\cos(E)} \tag{6.6}$$

Once true anomaly is known, it is easy to solve for the orbital distance as a function of time by using:

$$d(t) = \frac{a(1-e^2)}{1 + e\cos[\theta(t)]} \tag{6.7}$$

where a is the semi-major axis of the orbit.

Kepler's equation (6.5) is a transcendental equation, which cannot be solved analytically. Fortunately, it can be solved easily by using Newton-Raphson iteration. For this purpose, the equation is first written as:

$$f(E) = E - e\sin E - M = 0$$

If the initial guess at the solution is given by E_g, then the progressive corrections to this solution are given by:

$$E = E_g - \frac{f(E_g)}{f'(E_g)}$$

where f' is the differential of f with respect to E. The iteration proceeds until an acceptable level of convergence is achieved. In general, the solution converges very quickly and only a few iterations are required. Analytically, it can be shown that for $e < 0.99$ and the initial guess of π, convergence is guaranteed.

In asynchronous rotation, the position of the host star, viewed from a fixed position on the surface of the rotating planet, varies during the orbit. The change in local hour angle in time δt is simply given by the numerical difference of the spin angular velocity and orbital angular velocity multiplied by δt:

$$\delta H_a = [\Omega_{sp} - \Omega(\theta)]\delta t \tag{6.8}$$

where $\Omega(\theta)$ is the orbital angular velocity, which depends on the true anomaly of the planet's position. Note that near periastron, where $\Omega(\theta)$ is faster than Ω_{sp}, δH_a becomes temporarily negative.

The above suite of equations allows us to model the stellar irradiation on the atmosphere at every point along the orbit. During every time step the model calculates a new value for the mean anomaly. This value is then converted into true anomaly by using equations (6.5) and (6.6), and Newton-Raphson iteration. The distance of the planet from the host star can then be calculated by using equation (6.7) and thus the dilution factor for the stellar XUV flux can be determined. Equation (6.8) is used to calculate the position of the star in the planet's sky. Given that this procedure is completed every timestep, it proceeds surprisingly swiftly and does not add much to the overall computation time.

Figure 6.3 shows the orbital true anomaly versus time, Figure 6.4 shows the orbital distance versus true anomaly and Figure 6.5 shows how the hour angle develops during one orbit. All simulations presented in this chapter begin from apastron, with $\theta = 180^o$, and the local zenith for the hour angle calculation is set initially at the substellar point. The plots illustrate that the orbital solution is working as it should and that it makes physical sense. Also, they demonstrate the fact that the orbital angular velocity is faster during periastron, implying that the planet spends most of the time completing the 'far-side' of the orbit.

6.2 Thermospheric Conditions and Evaporation

For parameters appropriate for HD17156b, with $p_o = 2$ μbar, and with the upper boundary at 0.04 nbar, equation (4.1) from Chapter 4 yields exospheric temperatures of 7340 K and $\sim$ 470,000 K for apastron and periastron, respectively, if there is no radiative cooling. With an 80 % cooling function, the corresponding values are 1530 K and 56,213 K, respectively. In both cases the atmosphere would begin to escape hydrodynamically during periastron.

Figure 6.6 shows the globally averaged temperatures at the upper boundary (0.04 nbar) of the EXOTIM model versus orbital true anomaly. The results are shown for two different simulations, one with

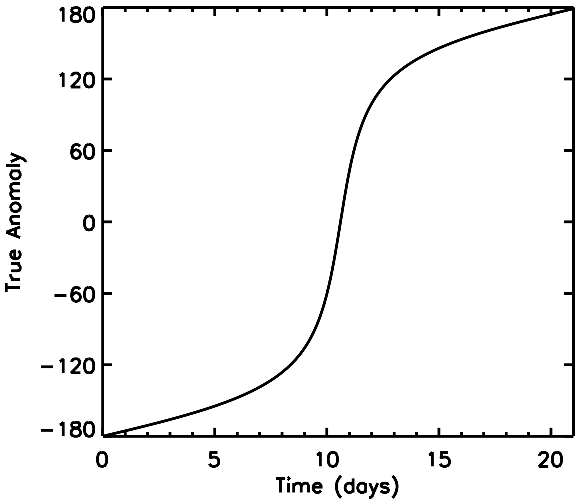

Figure 6.3: True anomaly versus time for HD17156b. The planet spends only around two days of its 21.2-day orbit within 0.1 AU from the host star. All simulated orbits are initiated at apastron with $\theta = \pm\ 180^o$.

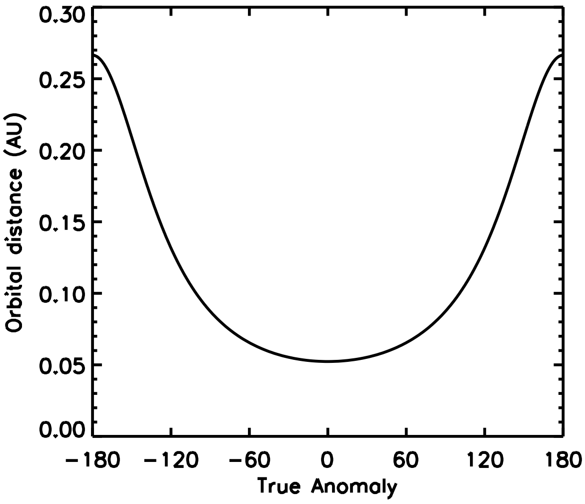

Figure 6.4: Orbital distance versus true anomaly for HD17156b. All simulated orbits are initiated at apastron with $\theta = \pm\ 180^o$.

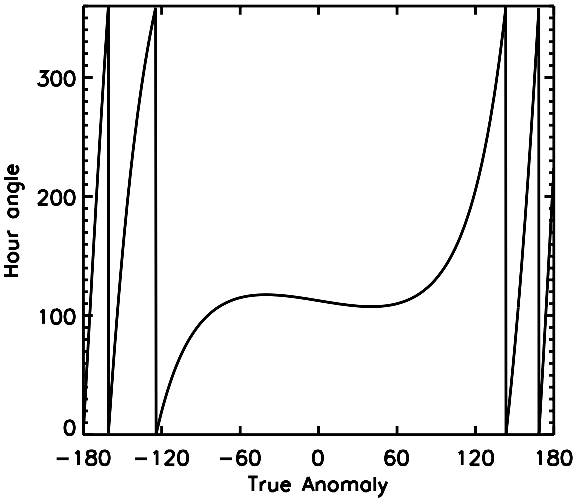

Figure 6.5: Hour angle versus true anomaly. All simulated orbits are initiated at apastron with $\theta = \pm 180^o$. The hour angle is set to zero (substellar point) in the beginning of the simulations, and thus it follows the progress of the initial substellar point as the planet moves along the orbit. The planet completes 4.6 rotations with respect to the star.

a Jupiter-type mixing ratio of atomic hydrogen at the lower boundary (HD.001), and one with 1 % of atomic hydrogen at the lower boundary (HD.002). Due to different amounts of H_2 in these thermospheres, the two types of simulations produce totally different cooling functions, and thus the exospheric temperatures differ significantly. If the mixing ratio of atomic hydrogen at the lower boundary is relatively low, less than $\sim 1.0 \times 10^{-3}$, the H_3^+ cooling function is relatively high. It varies between 72 % and 91 % of the total heating rate, reaching a maximum around $\theta = 153^o$. If the mixing ratio of atomic hydrogen is around 1 % at 2 μbar, the cooling function varies between 0.01 % and 0.24 %, reaching a minimum near periastron. This makes H_3^+ cooling in the HD.002 simulation virtually negligible.

As we pointed out in Chapter 5, the cooling function is linked to the composition of the thermosphere. Figure 6.7 shows the substellar mixing ratios of atomic hydrogen for HD.001 and HD.002 during apastron. The difference between the two simulations is striking. The mixing ratio of atomic hydrogen in HD.001 is relatively low throughout, rising to about 10 % near the exobase. In contrast, HD.002 is dominated by atomic hydrogen, with the transition from the H_2-atmosphere to a H-atmosphere taking place deep in the thermosphere, between 0.1 and 1.0 μbar (50–300 km above the 2 μbar level). Due to strong gravity and more aggressive downward diffusion of heavy molecules, this transition region is deeper in the thermosphere of HD17156b than it would be for a Jupiter-type planet or HD209458b with similar lower boundary conditions.

For HD.001, the globally averaged exobase temperature is around 2000 K at apastron, rising to over 3000 K during periastron. The temperature difference between successive apastron passages is negligible,

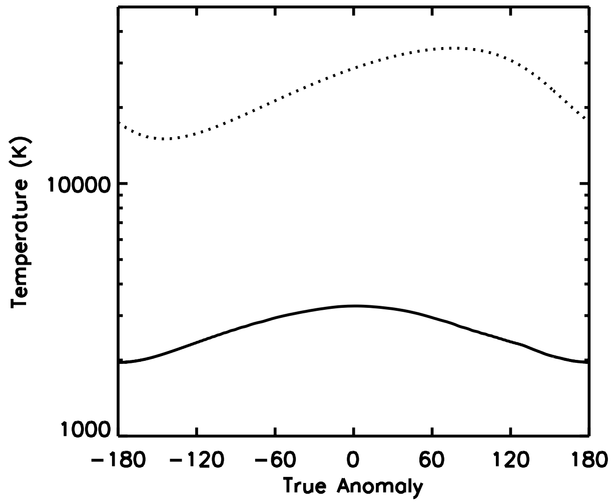

Figure 6.6: Globally averaged temperatures at the upper boundary of the model for the HD.001 (solid line) and HD.002 (dotted line) simulations versus true anomaly. The two simulations are characterised by different thermospheric compositions and thus different radiative cooling functions.

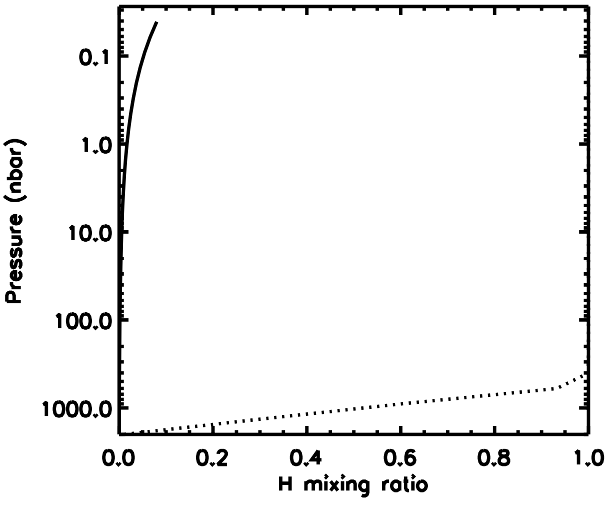

Figure 6.7: Substellar mixing ratios of atomic hydrogen for HD.001 (solid line) and HD.002 (dotted line) during apastron. The lower boundary mixing ratio is 2×10^{-4} for HD.001 and 0.01 for HD.002.

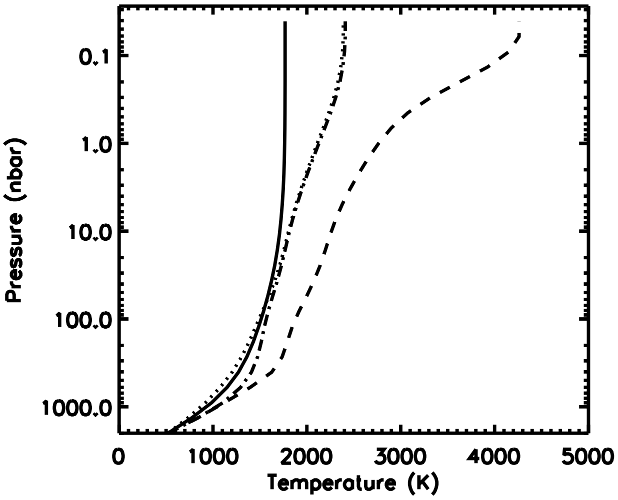

Figure 6.8: Substellar P-T profiles for the HD.001 simulation at apastron (solid line), $\theta = -153^o$ (dotted line), periastron (dashed line), and $\theta = 153^o$ (dash-dotted line).

indicating that the simulations have reached steady state in that they repeat the same behaviour during each orbit. Remarkably, steady state is reached after only three simulated orbits. This is due to the dominance of H_3^+ cooling and the short radiative timescales, which bring the simulation rapidly toward energy balance.

The number of collisions suffered by an escaping particle within one scale height at the upper boundary is approximately 5 throughout the orbit, indicating that the 0.04 nbar level is just slightly below the exobase. Figure 6.8 shows the substellar P-T profiles for the HD.001 simulation at four different orbital positions, corresponding to apastron, a quarter orbit after apastron ($\theta = -153^o$), periastron, and a quarter orbit after periastron ($\theta = 153^o$). If a secondary eclipse takes place, the last orbital position is near (although not exactly at) the longitude of the antitransit.

Outside periastron, the P-T profiles are isothermal at pressures lower than about 0.2 nbar. Generally the temperature increases with altitude, and the gradient is steepest in the lower thermosphere at pressures higher than 0.3 μbar. Overall, the temperatures are highest during periastron, and lowest during apastron. At $\theta = -153^o$ and at $\theta = 153^o$ the P-T profiles are identical in the upper thermosphere, but the lower thermosphere is warmer after periastron. During periastron the temperature rises sharply with altitude towards the upper boundary due to added XUV heating. As the P-T profiles are isothermal near the upper boundary for the most part of the orbit, it is acceptable to calculate the value for the thermal escape parameter at 0.04 nbar in order to estimate the likely evaporation rates.

The thermal escape parameter depends on gravity through the escape velocity. The escape velocity from HD17156b is ~108 km s^{-1}, which compares to 60 km s^{-1} from Jupiter. This means that atmospheric particles require more kinetic energy to escape HD17156b than Jupiter. Thus HD17156b is likely to remain stable even at relatively high exospheric temperatures. Also, due to higher gravity, the thickness of the atmosphere is reduced compared to Jovian-type EGPs. For the HD.001 simulation, the upper boundary altitude varies between ∼800 km at apastron to about 1100 km during periastron. At the same time, the thermal escape parameter varies from 400 to 700, rendering even Jeans escape negligible throughout the orbit. Despite strong heating during periastron, the atmosphere does not escape hydrodynamically because the passage through periastron is relatively fast, and any added heating is quickly balanced by an adjustment in the H_3^+ cooling rate.

For HD.002, the exobase temperatures are considerably higher, over 10,000 K throughout the orbit. The minimum temperature is around 15,000 K, reached at $\theta = -145^o$, and the maximum temperature is 34,000 K, reached after the periastron at $\theta = 76^o$. Atomic hydrogen and H^+ are virtually the only species in the upper thermosphere, and between the minimum and maximum temperature regions the thermal escape parameter ranges from 40 to 15, respectively. This implies that near periastron, Jeans escape could be significant and even some bulk flows are possible. However, according to the thermal escape parameter values, the atmosphere remains stable throughout the orbit. The upper boundary altitude ranges from 13,100 km (1.2 R_p) near the temperature minimum to 27,300 km (1.4 R_p) near the temperature maximum.

The temperature variation between successive apastron passes for HD.002 is ∼130 K after fifteen simulated orbits. This means that the simulations have not reached exact steady state, although it is reasonable to assume that they are near steady state. 130 K is not a particularly significant figure compared to the temperature of the upper boundary (over 15,000 K), and the difference gets smaller during each orbit. Computational constraints mean that we cannot run the HD.002 simulation to exact steady state within a reasonable time period, and thus it is possible that the model keeps heating up slowly during each orbit until it reaches conditions that would lead to hydrodynamic escape. Given the rather swift passage through the periastron, however, this should be unlikely.

Figure 6.9 shows the P-T profiles for the HD.002 simulations at the same orbital positions as for HD.001 above. Outside periastron, the profiles are isothermal at pressures lower than about 0.7 nbar, and during periastron the P-T profile is isothermal at pressures lower than about 0.1 nbar. In the lower thermosphere, the temperature increases steadily with altitude. The temperature in the upper thermosphere increases as the planet moves towards periastron from $\theta = -153^o$. The heating goes on for a while after periastron, but by the time the planet reaches $\theta = 153^o$, the outer layers have started to cool down. Curiously, this does not apply to the region between 3.0 and 100 nbar, where the model is actually warmer at $\theta = 153^o$ than it is during periastron. Towards apastron, the whole thermosphere cools down and this cooling continues until the planet reaches $\theta = -153^o$ again. The number of collisions expected for an escaping particles near the upper boundary ranges from 13 to 16 within one scale height, implying that the upper boundary is significantly below the exobase. However, the isothermality of the P-T profiles means that thermal escape parameter values calculated at 0.04 nbar can be used to estimate the evaporation conditions at the exobase.

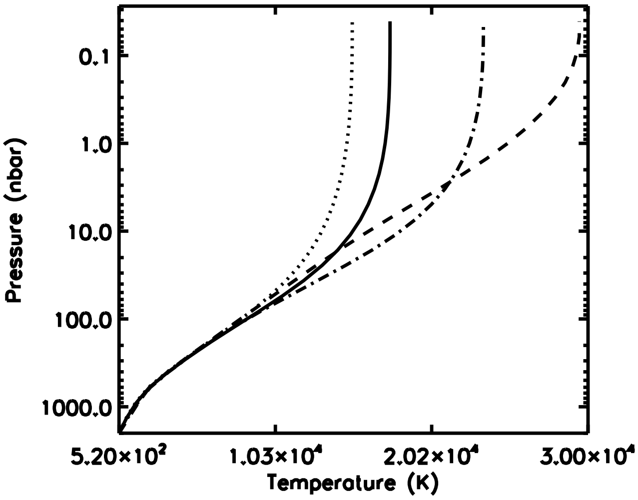

Figure 6.9: Substellar P-T profiles for the HD.002 simulation at apastron (solid line), $\theta = -153^o$ (dotted line), periastron (dashed line), and $\theta = 153^o$ (dash-dotted line).

In general, we have found that the upper atmosphere of HD17156b is likely to be stable throughout the whole orbit, with evaporation being due to Jeans escape, which is likely to be of negligible magnitude, at least in terms of the evolution of the planet. Based on simple arguments, one would expect the atmosphere of HD17156b to escape hydrodynamically at least during periastron. However, due to a delay in response to heating, orbital and thermospheric dynamics, and possibly radiative cooling, this conclusion is premature. The results demonstrate that a scaling law approach to determining the exospheric conditions of an atmosphere in such a complex system would be very misleading.

Both types of simulations produce observable consequences that can be used to differentiate between the two thermospheric composition models, so that actual escape rates can be better estimated. The most definite way of doing this would be to observe infrared emissions from H_3^+. However, the total emission rates are of the order of 10^{15}–10^{16} W for the HD.001 simulation, and of the order of 10^{12}–10^{13} W for the HD.002 simulations. Unfortunately, these emissions are too faint to be observable with current technology [eg. Shkolnik et al., 2006].

The second avenue that could be pursued to constrain the nature of the upper atmosphere of HD17156b would be to observe H Lyman α absorption during transit, following the method used to detect the extended hydrogen cloud around HD209458b [Vidal-Madjar et al., 2003]. If the atmosphere of HD17156b is dominated by atomic hydrogen, it should extend to more than 1.4 R_p during transit, which takes place near periastron. If an extended hydrogen atmosphere is not detected, then infrared cooling may be taking place and this implies that the thermosphere is dominated by H_2. Thus, even if H_3^+ emissions are too faint to be detected directly, their existence can potentially be inferred indirectly and the mixing ratios of H and H_2 in the lower atmosphere can then also be constrained. Unfortunately, the only instrument really capable of performing such observations, i.e. STIS onboard HST, has been taken out of service (Tinetti, G., *personal communication*).

6.3 Circulation

Figure 6.10 shows the upper boundary circulation and temperature distribution for the HD.001 simulation at the four orbital positions described above. The location of the substellar point in each plot is shown by a vertical line drawn along the substellar longitude. At all four orbital positions, the dayside is clearly warmer than the night side. At apastron, the dayside temperature is 2,200–2,300 K, and the temperature peaks at the equator near dawn. The night side temperature, with a minimum close to the dawn terminator, is 1,650–1,750 K. The diurnal temperature difference is thus 500–600 K. The horizontal winds originate in the dayside, and blow across the terminator to the night side. In the night side, the Coriolis force and the geopotential gradients drive the eastward wind towards the equator, into a stream that flows across the antistellar point and faces the westward wind from the dayside near the dawn terminator. Also in the night side, there are two high-latitude vortices that direct the easterly wind from the dayside into the westerly equatorial jet. The maximum zonal wind speed is 1.1–1.3 km s^{-1} at high latitudes, while the maximum equatorial wind speed is $\sim$700 m s^{-1}. Vertical advection is directed upwards in the dayside, accompanied with adiabatic expansion of the atmosphere, and downwards in the night side, accompanied with adiabatic contraction of the atmosphere. The maximum vertical flow speed is only a few m s^{-1}. The thermal escape parameter at the upper boundary is 689, indicating negligible evaporation.

At $\theta = -153$ degrees the distance of the planet from the star is 0.22 AU. The upper boundary temperature and wind pattern is qualitatively identical to the apastron model. However, with added heating, the dayside temperatures are higher, at 2,300–2,450 K. The night side temperature is 1,650–1,850 K, implying a diurnal temperature difference of 600–700 K. The maximum zonal wind speed is also slightly higher at 1.3–1.6 km s^{-1}. The thermal escape parameter is 659, indicating that the atmosphere remains stable.

At periastron, where the orbital distance is 0.052 AU, the near-synchronisation of the planet's spin leads to a more pronounced diurnal temperature difference. Between $\theta = -90^o$ and $\theta = 90^o$, only one hemisphere of the planet is exposed to stellar irradiation. The dayside temperature during periastron is around 4,350 K, while the night side temperature is around 2,200 K. Thus the diurnal temperature difference is over 2,000 K. Large-scale circulation is qualitatively similar to other orbital positions, but the winds are faster, with maximum speeds of 2.6–2.8 km s^{-1}. Vertical advection is also more rigorous, and the maximum vertical wind speed is 8–15 m s^{-1}. However, despite the added heating, the thermal escape parameter is 411, and the atmosphere remains stable. The enhanced XUV heating is balanced by effective H_3^+ cooling, and before the thermosphere has time to heat up significantly, the planet moves away from periastron. At $\theta = 153^o$, the upper boundary is almost identical to the $\theta = -153^o$ model.

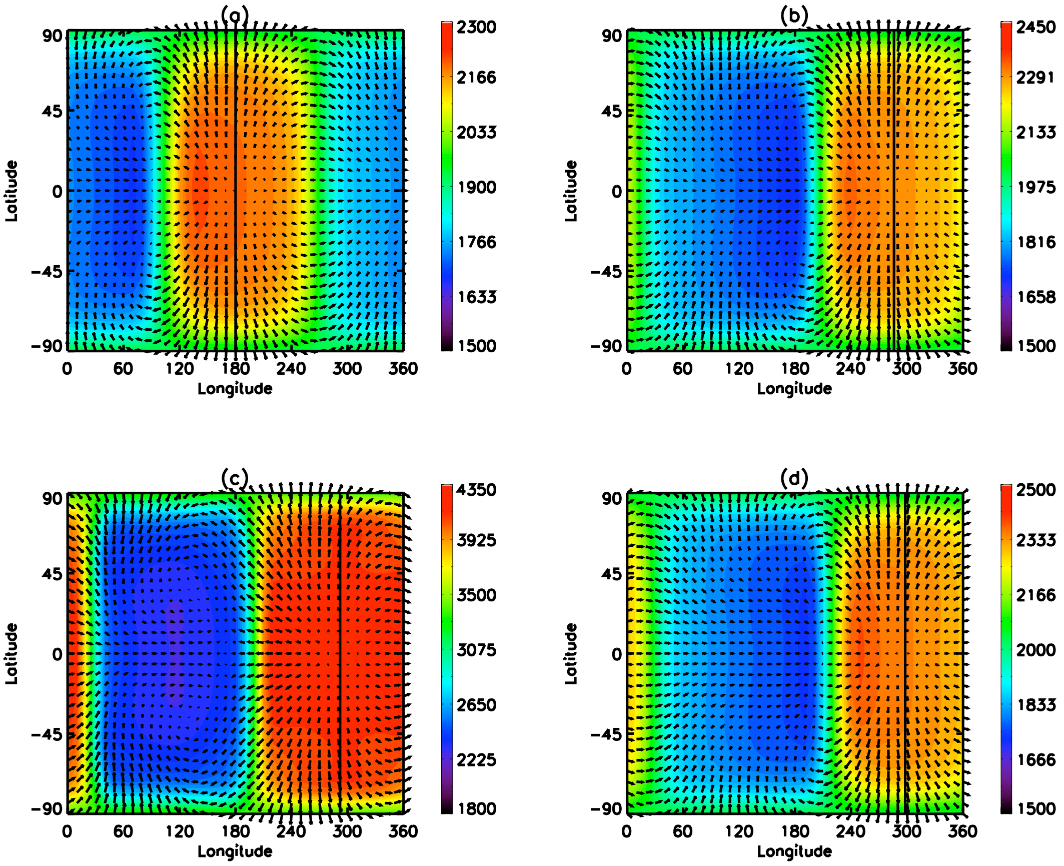

Figure 6.10: Temperatures and winds at the upper boundary of HD.001 at (a) apastron, (b) $\theta = -153^o$, (c) periastron, and (d) $\theta = 153^o$. The substellar longitude is marked in each plot with a vertical line.

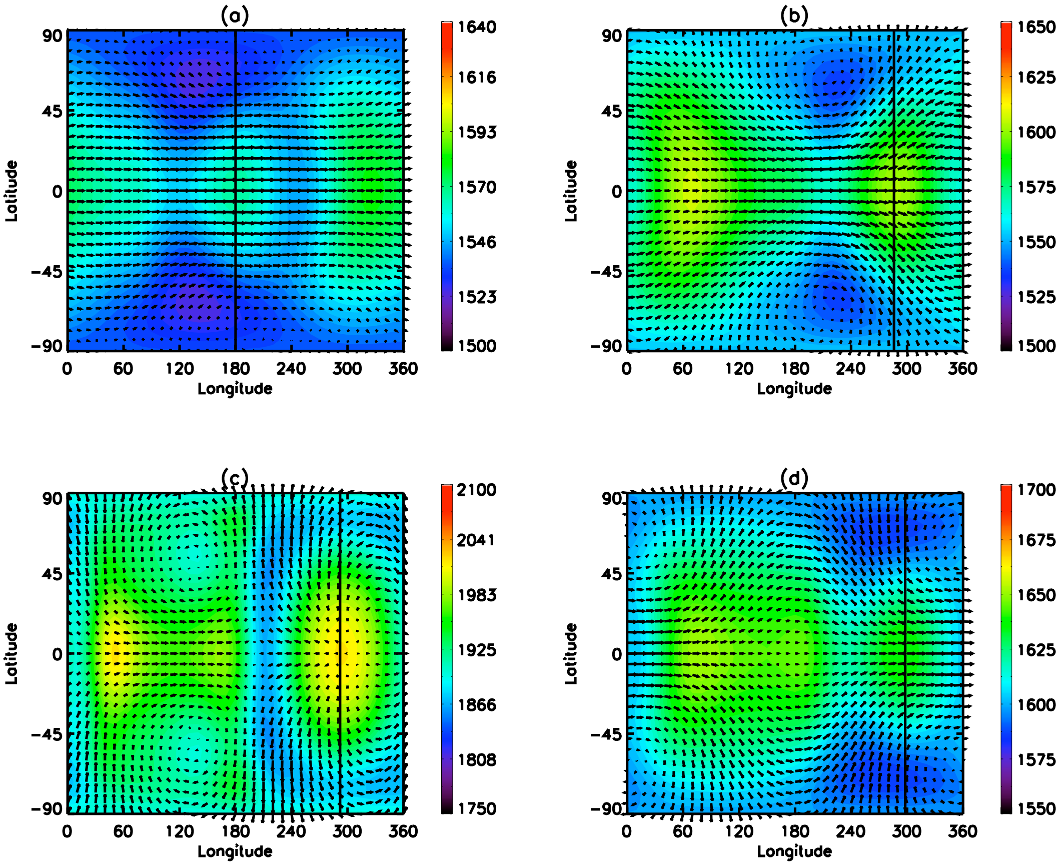

Figure 6.11: Temperatures and winds near the 55 nbar level of HD.001 at (a) apastron, (b) $\theta = -153^o$, (c) periastron, and (d) $\theta = 153^o$. The substellar longitude is marked in each plot with a vertical line.

There are some very slight differences between these models, but those are mostly limited to the lower thermosphere.

Figure 6.11 shows the circulation and horizontal temperature distribution for the same HD.001 simulations at 55 nbar (200–300 km), near the bottom of the modelled region. In all cases, the temperature is nearly uniform. With the exception of periastron, the circulation is characterised by a broad eastward, circumplanetary jet. During apastron, the temperature varies between 1,530 and 1,580 K, and the equator is everywhere slightly warmer than its surroundings, with temperature peaking in the night side. The wind speed in the equatorial jet ranges from 160 to over 220 m s^{-1}. Cyclonic polar vortices circle around the minimum temperature regions near the poles. In general, the circulation in the lower thermosphere is characteristic of Coriolis-driven dynamics, that smoothes out diurnal temperature variations.

At $\theta = -153^o$, the temperature varies between 1,540 and 1,610 K. The equator is still warmer than its surroundings, and there are two temperature peaks, one near the substellar point and one in the night side. The temperature minima are again located near the poles near the dawn terminator, and the cyclonic polar vortices are centred on those. In the equatorial jet, the wind speed ranges from 100 to 220 m s^{-1}.

During periastron the horizontal temperature variations are more pronounced, with the temperature ranging from 1,840 to 2,020 K, but the details of the temperature distribution are confusing. The warm substellar region is surrounded by a cooler ring along the terminator, but the night side is almost as warm as the dayside. The winds diverge from the substellar point, blowing towards the night side. A westerly jet develops in the night side, but it encounters the easterly wind at dawn, and cannot encircle the planet at this pressure level. The two high-latitude vortices direct easterly flows into the equatorial jet. The maximum wind speed is around 800 m s^{-1}. The circulation is qualitatively similar to the topside circulation, and this is a consequence of the near-synchronisation during periastron.

At $\theta = 153^o$, the temperature ranges from 1580 to 1660 K, and the circulation is again characterised by the circumplanetary jet and cyclonic vortices. The wind speed in the equatorial jet ranges from 100 to 400 m s^{-1}. The lower thermosphere is slightly warmer than it was at the symmetric position with $\theta = -153^o$, and it is in the process of cooling down after the periastron passage.

Figure 6.12 shows the top boundary temperatures and circulation for the HD.002 simulation at corresponding orbital locations. The horizontal uniformity of the temperatures in these models is remarkable. During apastron, the dayside temperature is 17,620–17,630 K while the night side temperature is around 17,530 K, and thus the diurnal temperature difference is only of the order of 100 K. The shallow geopotential gradients drive gentle winds from the dayside to the night side with maximum speed of only 200 m s^{-1}. On the night side the eastward flow is directed into an equatorial jet that faces the westward wind from the dayside near dawn. High-latitude vortices are also present, and they turn the westward flow around and into the equatorial jet. On the dayside the temperature peak on the equator is shifted slightly eastward from the substellar point by circulation and rotation. The thermal escape parameter is 33, implying that Jeans escape may become important.

In the absence of strong radiative cooling, the temperatures and circulation in the HD.002 simulation are dynamics-driven. Strong winds develop initially, as the simulation is initiated, and these smooth out any large diurnal temperature differences. This does not happen to the same degree in the HD.001 simulation, which is subject to a strong radiative cooling function. The radiative timescale in the upper thermosphere is shorter than the timescale for advection, and thus relatively steep temperature gradients persist along the terminator.

At $\theta = -153^o$, the temperatures are generally lower than during apastron. The dayside temperature is around 15,180 K and the night side temperature is around 15,030 K. This means that the diurnal temperature difference is of the order of 150 K. The circulation pattern is qualitatively similar to the apastron model, but the high-latitude zonal winds are slightly faster, reaching maxima of over 300 m s^{-1}. The thermal escape parameter increases to $\sim$39.

Moving from $\theta = -153^o$, the model is heated up by the increasing XUV fluxes, which are multiplied by a factor of 18 between $\theta = -153^o$ and periastron. During periastron, the dayside temperature is 29,200–29,500 K and the night side temperature is around 26,800 K. Thus the diurnal temperature difference is $\sim$2500 K. This arises from the near-synchronisation during periastron. The winds blow from the dayside

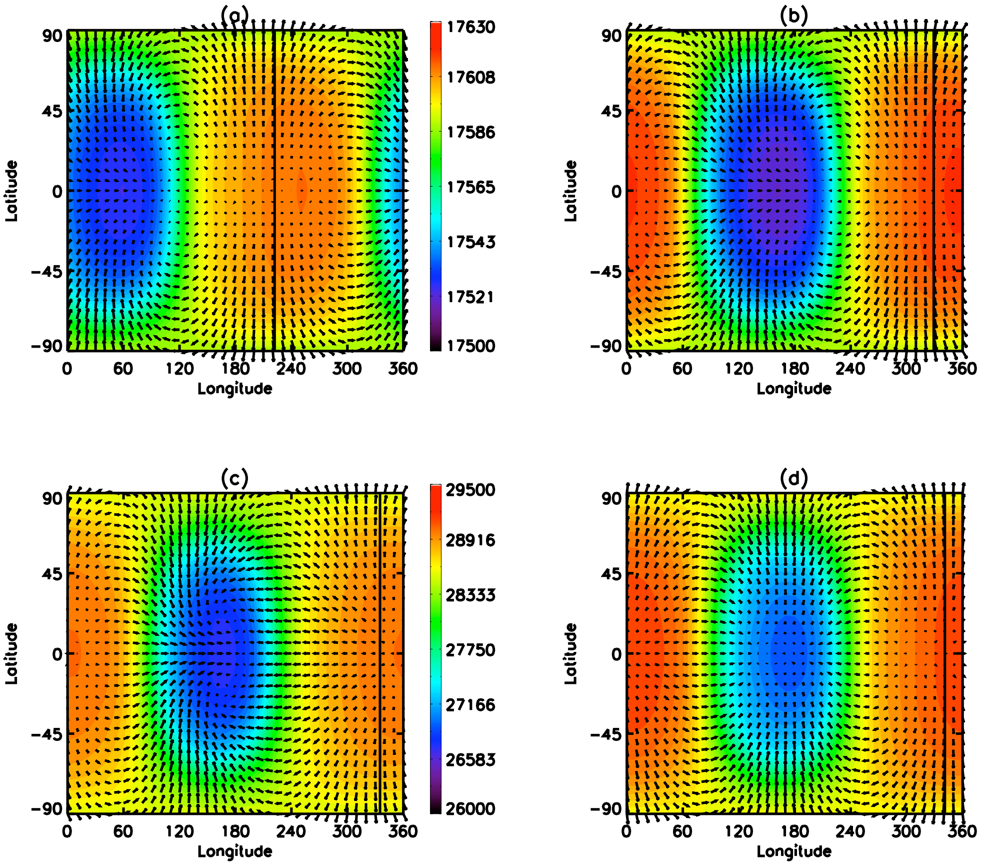

Figure 6.12: Temperatures and winds at the upper boundary of HD.002 at (a) apastron, (b) $\theta = -153^o$, (c) periastron, and (d) $\theta = 153^o$. The substellar longitude is marked in each plot with a vertical line.

to the night side and converge near the anti-stellar point, instead of forming a distinct eastward jet in the night side. The winds are considerably stronger compared to the other orbital positions, with maxima of 2.8–3.2 km s^{-1}. The thermal escape parameter decreases to 19, and this implies potentially significant Jeans escape.

By the time the planet reaches $\theta = -153^o$, the thermosphere has started to cool down. The dayside temperature is around 23,425 K and the night side temperature is around 23,270 K, yielding a diurnal temperature difference of 150 K. Circulation is axisymmetric about an axis connecting the substellar point to the antistellar point, with winds blowing from the dayside to the night side. The maximum wind speed is just over 200 m s^{-1}. The model is recovering from the periastron passage, and rotation relative to the star is picking up. The thermal escape parameter near $\theta = -153^o$ is $\sim$23.

Figure 6.13 shows the circulation and temperatures for the HD.002 simulations at 55 nbar. At apastron, the temperature varies within a few degree interval about 10,790 K. An eastward circumplanetary jet flows around the planet, with wind speeds of 25-35 m s^{-1}. At $\theta = -153^o$, the global temperature is around 10,005 K, with very little variation. Circulation is characterised by similar, weak winds as those seen during apastron. During periastron, the diurnal temperature is slightly more pronounced. The dayside temperature is 10,180–10,190 K and the night side minimum temperature is 10,165 K. The eastward jet persists, accompanied by polar vortices. At $\theta = 153^o$, the global temperature is around 11,200 K, with a 35 K diurnal temperature difference. Notably the temperature here is higher than during periastron, indicating that the heating and cooling timescale is longer in the lower thermosphere than in the upper thermosphere.

The highly uniform global temperatures and isothermal P-T profiles in the outer layers are interesting features of the HD.002 simulation. They arise because the model does not have enough time to cool down, before it heats up again when approaching periastron. The temperatures near apastron are higher than what would be expected from purely radiative considerations. Thus circulation has time to balance the temperatures between the two hemispheres. The prominent cooling mechanism is conduction of heat to layers below the thermosphere, where energy is reradiated. Heat conduction in the thermosphere relies on molecular diffusion, which is a very slow process compared to horizontal advection.

6.4 Composition

Figure 6.14 shows the substellar neutral density profiles for the HD.001 and HD.002 simulations during periastron. The relative concentrations of the species are similar at other orbital positions, which is why only the periastron profiles are shown. For HD.001, H_2 is by far the dominant species at all levels. In the lower thermosphere, there is more helium than atomic hydrogen. The density of atomic hydrogen overtakes helium at pressures lower than about 30 nbar. For HD.002, atomic hydrogen is the dominant species at pressures lower than 1 μbar. Curiously, the density of helium is higher than the density of H_2 between 0.6 μbar and 4 nbar. This is due to the fact that H_2 is removed from the atmosphere by

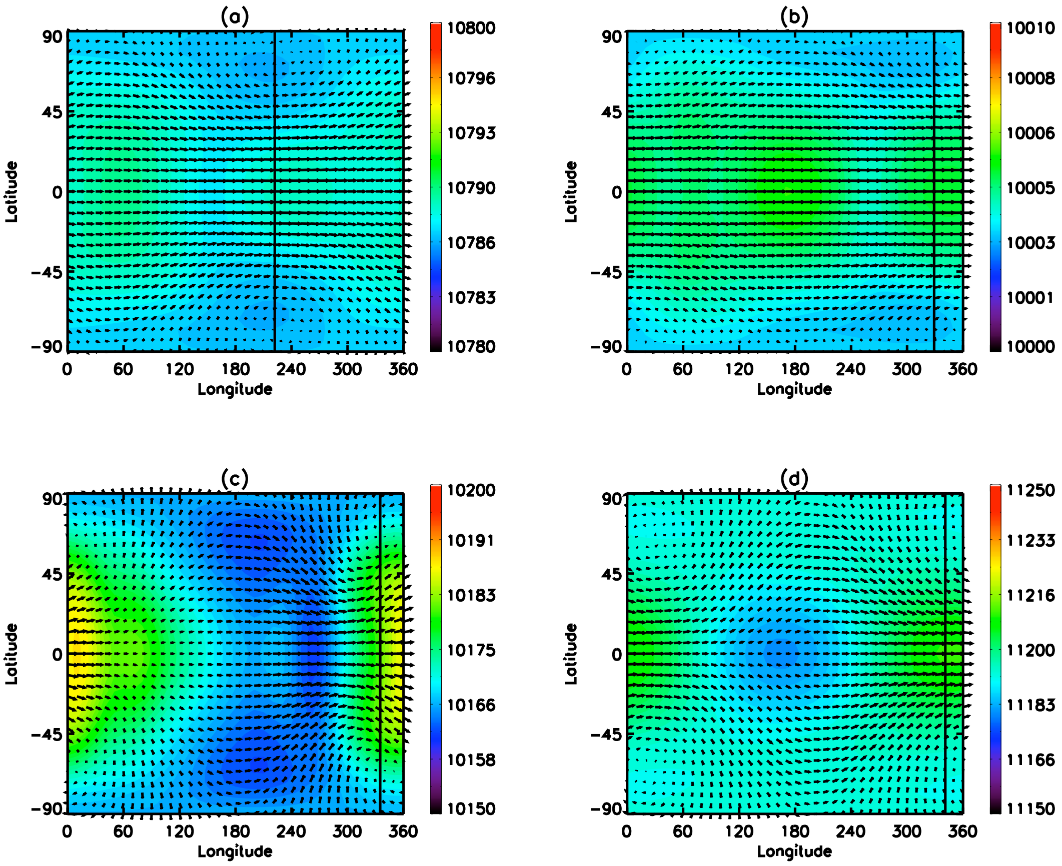

Figure 6.13: Temperatures and winds near the 55 nbar level of HD.002 at (a) apastron, (b) $\theta = -153^o$, (c) periastron, and (d) $\theta = 153^o$. The substellar longitude is marked in each plot with a vertical line.

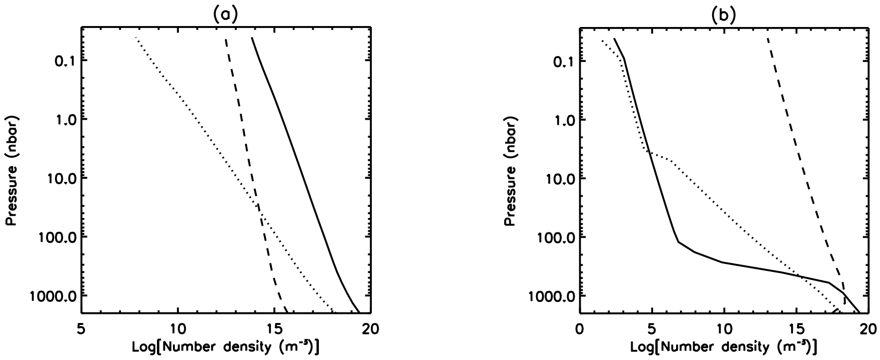

Figure 6.14: Substellar density profiles of the dominant neutral species H_2 (solid line), He (dotted line), and H (dashed line) during periastron for (a) HD.001 and (b) HD.002.

thermal dissociation as well as molecular diffusion.

The neutral densities for the HD.002 simulation may not be entirely reliable because atomic hydrogen is the dominant species. This is because the numerical solution of the species continuity equation treats H_2 as the dominant species. The code first calculates the mass fractions of H and He, taking into account molecular diffusion, advection, convection and neutral chemistry, and then determines the the mass fraction for H_2 by deducting the mass fractions of He and H from unity. This may not make such a big difference, though, because the transition region between the H_2 atmosphere and the H-dominated layers is so thin, and above it, due to thermal dissociation of H_2, H is virtually the only neutral species. Also, the equations themselves do not assume a dominant species. Instead, the diffusion velocities are evaluated by imposing the condition that the net diffusive flux at any given altitude is zero. The matrix of the coefficients of diffusion is symmetric, so the order of diffusion does not matter either.

Figure 6.15 show the substellar ion densities for the HD.001 simulation at the four orbital positions considered above. Substellar electron densities are also shown in Figure 6.16. In general, H^+ is by far the dominant ion. He^+ and H_2^+ densities are relatively insignificant throughout the thermosphere, although H_2^+ densities are comparable to H_3^+ densities near the upper boundary of the model. At apastron, the substellar column densities of H_3^+ and H^+ are 3.5×10^{16} m^{-2} and 7.9×10^{18} m^{-2}, respectively. There are two peaks in the H_3^+ density profile, one near the lower boundary with a density of 3.2×10^{11} m^{-3}, and the other around 3 nbar with a density of 6.3×10^{10} m^{-3}. Overall, the density of H^+ is a few orders of magnitude higher than the density of H_3^+. The H^+ peak is located between 100 and 10 nbar, with a density of 1.7×10^{13} m^{-3}. The electron density profile follows the density profile of H^+ closely, and at all levels ion densities are negligible compared to neutral densities.

The density of H^+ is fairly uniform horizontally in the upper thermosphere, with a significant plasma density surviving in the night side. This is because the lifetime of H^+ against recombination in the outer layers is ~40 hours, which is comparable to the timescale of planetary rotation. In the lower thermosphere the lifetime of H^+ is of the order of one hour, whereas the timescale for rotation is 40 hours and the

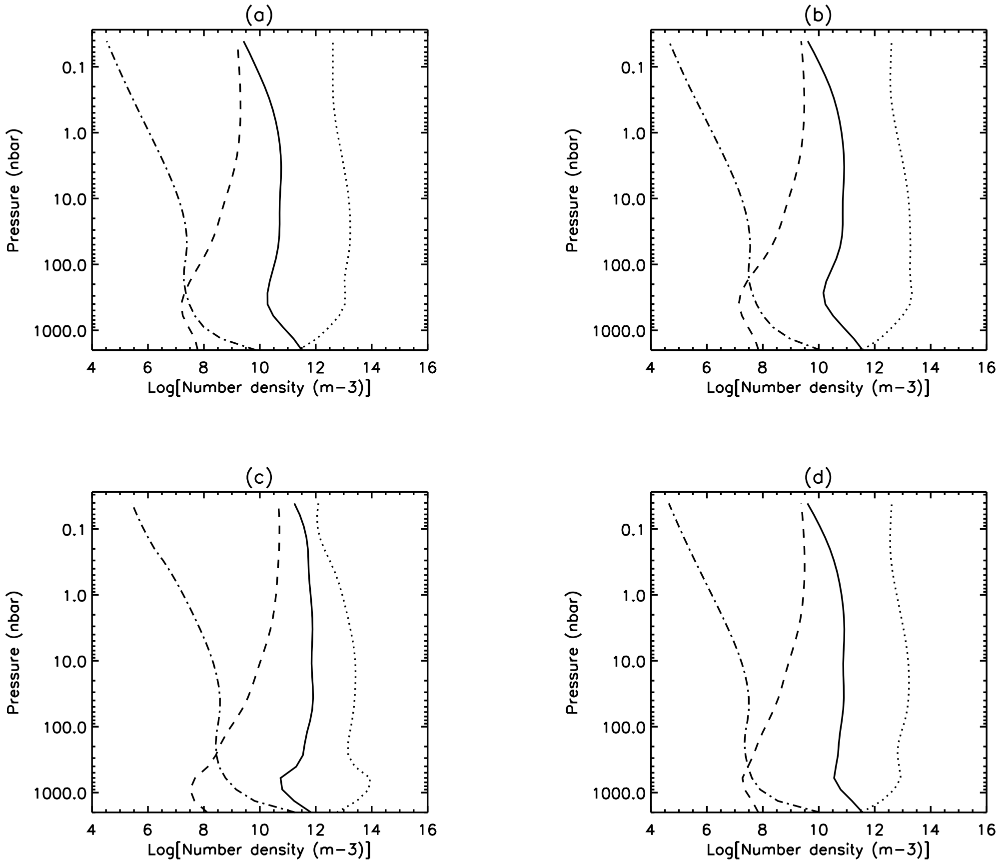

Figure 6.15: Substellar density profiles of the ions H_3^+ (solid line), H^+ (dotted line), H_2^+ (dashed line), and He^+ (dash-dotted line) for the HD.001 simulation at (a) apastron, (b) $\theta = -153^o$, (c) periastron, and (d) $\theta = 153^o$.

timescale for horizontal advection is several days. This is reflected by the H^+ density distribution in the lower thermosphere, which shows a steep drop along the terminator. The lifetimes of H_3^+ and He^+ in the upper thermosphere are a few seconds and around one minute, respectively. The lifetime, on the other hand, of H_2^+ is generally shorter than the lifetime of H_3^+. In the lower thermosphere the lifetimes of H_3^+ and He^+ are less than a second. Thus photochemical equilibrium is likely to be a good approximation in the lower and middle thermosphere, but in the outer layers transport of H^+ is likely to be important. This is a similarity with Jupiter, where the deviation from photochemical equilibrium is also due to the long lifetime of H^+ in the upper atmosphere.

At $\theta = -153^o$, the substellar column densities of H_3^+ and H^+ are 4.7×10^{16} m^{-2} and 9.3×10^{18} m^{-2}, respectively. The ion density profiles are similar to the apastron model. During periastron, the substellar column densities of H_3^+ and H^+ are 6.3×10^{17} m^{-2} and 2.0×10^{19} m^{-2}, respectively. There is a sharp peak in the density of H^+ around 0.7 μbar, where the density of H^+ is almost 10^{14} m^{-3}. The density of H_3^+ is higher at all levels, compared to the other orbital positions. Intriguingly, the density of H^+ in the upper thermosphere is lower than at apastron. This is because the temperature in the outer layers

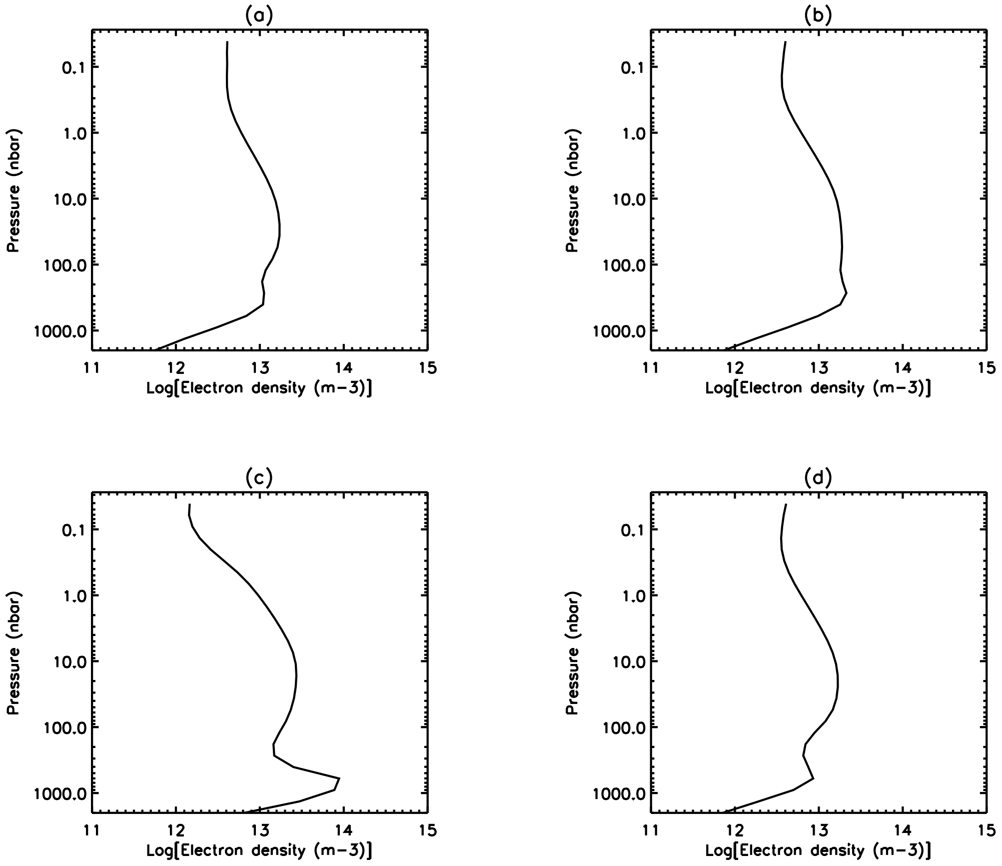

Figure 6.16: Substellar electron densities for the HD.001 simulation at (a) apastron, (b) $\theta = -153^o$, (c) periastron, and (d) $\theta = 153^o$.

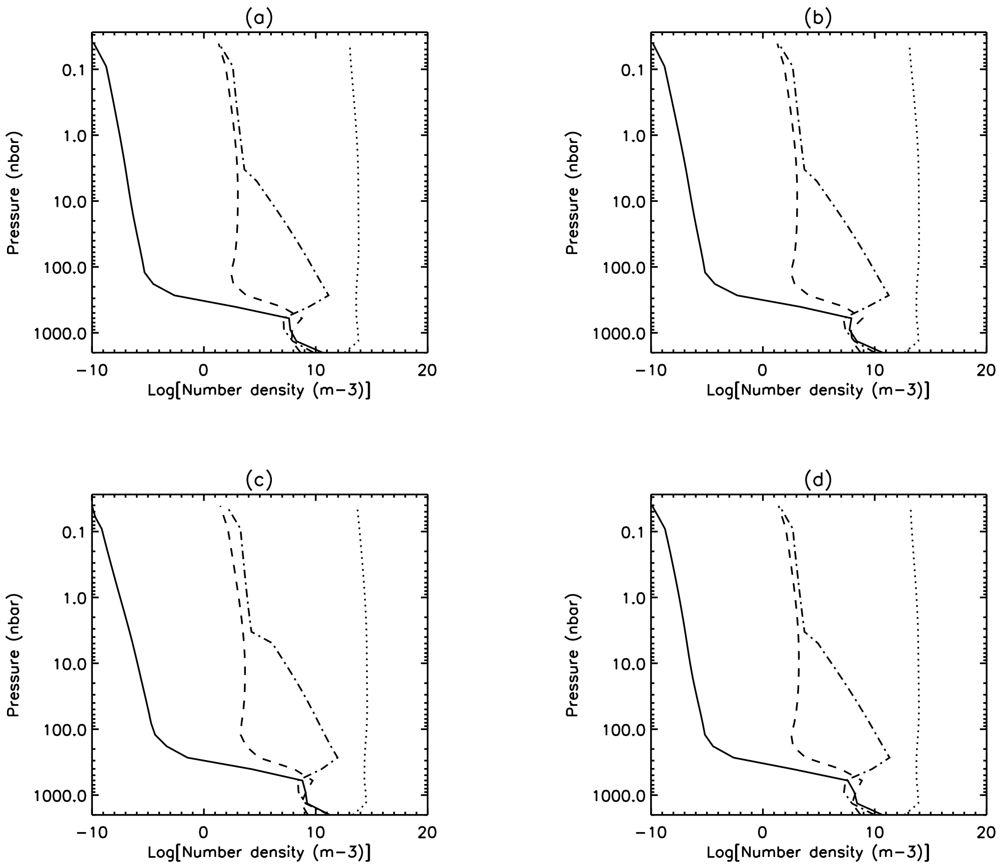

Figure 6.17: Substellar density profiles of the ions H_3^+ (solid line), H^+ (dotted line), H_2^+ (dashed line), and He^+ (dash-dotted line) for the HD.002 simulation at (a) apastron, (b) $\theta = -153^o$, (c) periastron, and (d) $\theta = 153^o$.

is higher, and thus the overall density is lower, and because the near-synchronisation of the planet's spin leads to enhanced day-night circulation that increases the mixing ratio of H_2 in the dayside. At $\theta =$ 153 degrees, the substellar column densities of H_3^+ and H^+ are 5.0×10^{16} m^{-2} and 7.9×10^{18} m^{-2}, respectively. The ion density profiles are qualitatively similar to the periastron model, but of course the densities are lower.

Figures 6.17 and 6.18 show the corresponding ion and electron density profiles for the HD.002 simulation. For this simulation, H^+ is virtually the only ion species at pressures lower than about 0.7 μbar, while the density of H_3^+ in the outer layers is negligible. Following neutral densities, there is more He^+ in the thermosphere than either H_2^+ or H_3^+. The density of H_2^+ is generally higher than the density of H_3^+, because there is not enough H_2 in the thermosphere to convert H_2^+ into H_3^+. However, overall the densities of these secondary ions are vanishingly small compared to H^+ or H. The H^+ density profile peaks around 60 nbar, with a density of 7.0×10^{13} m^{-3}, and the substellar column density of H^+ is 7.9×10^{20} m^{-2}. The density of neutral hydrogen is higher at all levels than the density of H^+. Naturally, the electron density profile is nearly perfectly aligned with the H^+ profile.

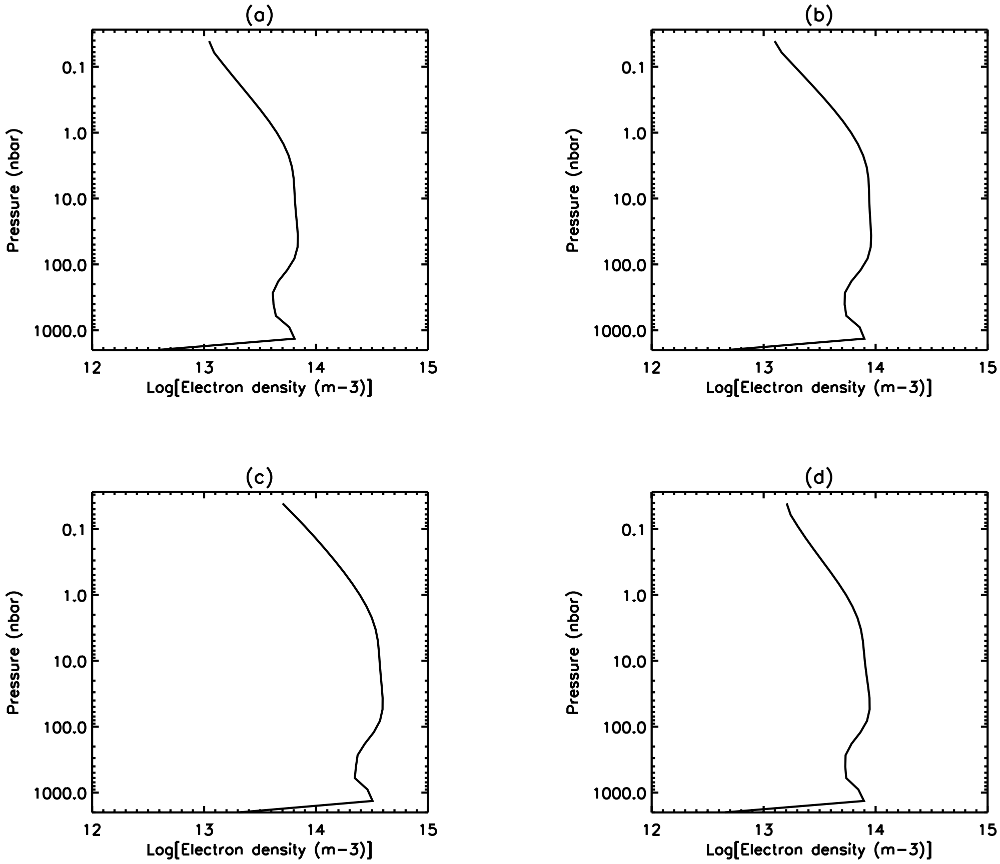

Figure 6.18: Substellar electron densities for the HD.002 simulation at (a) apastron, (b) $\theta = -153^o$, (c) periastron, and (d) $\theta = 153^o$.

At $\theta = -153^o$, the substellar column density of H^+ is still around 7.9×10^{20} m^{-2}, and the H^+ density profile is virtually unchanged from apastron. During periastron, the substellar column density increases to 5.0×10^{21} m^{-2}, and the peak density near 60 nbar is around 4.0×10^{14} m^{-3}. The density of He^+ in the lower thermosphere is also relatively high, even compared to the HD.001 simulation. This is because in the atomic hydrogen thermosphere, reactions between H_2 and He^+, that remove He^+ from the ionosphere, do not take place (see Table 3.1). H^+ overtakes neutral hydrogen as the dominant species at pressures lower than 0.7 nbar, and near the upper boundary the mixing ratio of neutral hydrogen is only about 30 % compared to the H^+ density. The assumption that photoionisation has negligible direct impact on the neutral mass fractions, and that the overall neutral density can be calculated from the ideal gas law, is therefore inaccurate. As a consequence, the periastron ion plots should be treated with suspicion.

At $\theta = 153^o$, the substellar column density of H^+ is 10^{21} m^{-2}. The density of H^+ is higher than the density of neutral hydrogen at pressures lower than 0.06 nbar. This should not be the case, if the planet stayed at 0.22 AU from the host star. The relatively high density of H^+ here arises because the lifetime of the ion against recombination is long, and lot of the H^+ that was created during periastron survives in the outer layers. Both factors, the relatively long lifetime of H^+ and it being the dominant species, render our ion profiles unreliable in the upper thermosphere.

6.5 Energy Balance

The terms in the energy equation reflect the composition of the thermosphere-ionosphere system. Figure 6.19 shows the substellar volume heating and cooling rates for the HD.001 simulation at the four orbital positions considered above, and Figure 6.20 shows similar plots for the antistellar point. Figures 6.21 and 6.22 show the corresponding heating and cooling rates for the HD.002 simulation.

For the HD.001 simulation, the dayside XUV heating is balanced effectively by H_3^+ cooling in the middle and upper thermosphere, where the net heating rate is thus close to zero at all orbital positions. At pressures lower than about 1.0 nbar, radiative cooling is less important due to non-LTE conditions, and heating is mainly balanced by heat conduction. The lower thermosphere is cooled by upwelling vertical winds, adiabatic expansion and heat conduction. In general, the net heating rate deviates from zero according to the orbital position. During apastron, the lower thermosphere is cooling down, mainly due to enhanced heat conduction, following its passage through periastron. By the time the planet reaches $\theta = -153^o$, the net cooling rate is close to zero. Between this point and periastron, the lower thermosphere heats up, and net heating takes place during periastron. This net heating turns into net cooling by the time the planet reaches $\theta = 153^o$.

On the night side, the heating is generally due to downwelling winds and adiabatic contraction of the atmospheric gas. This heating is balanced by vertical heat conduction. The net heating and cooling effects follow the developments po the dayside of the planet. During periastron, there is a small heating

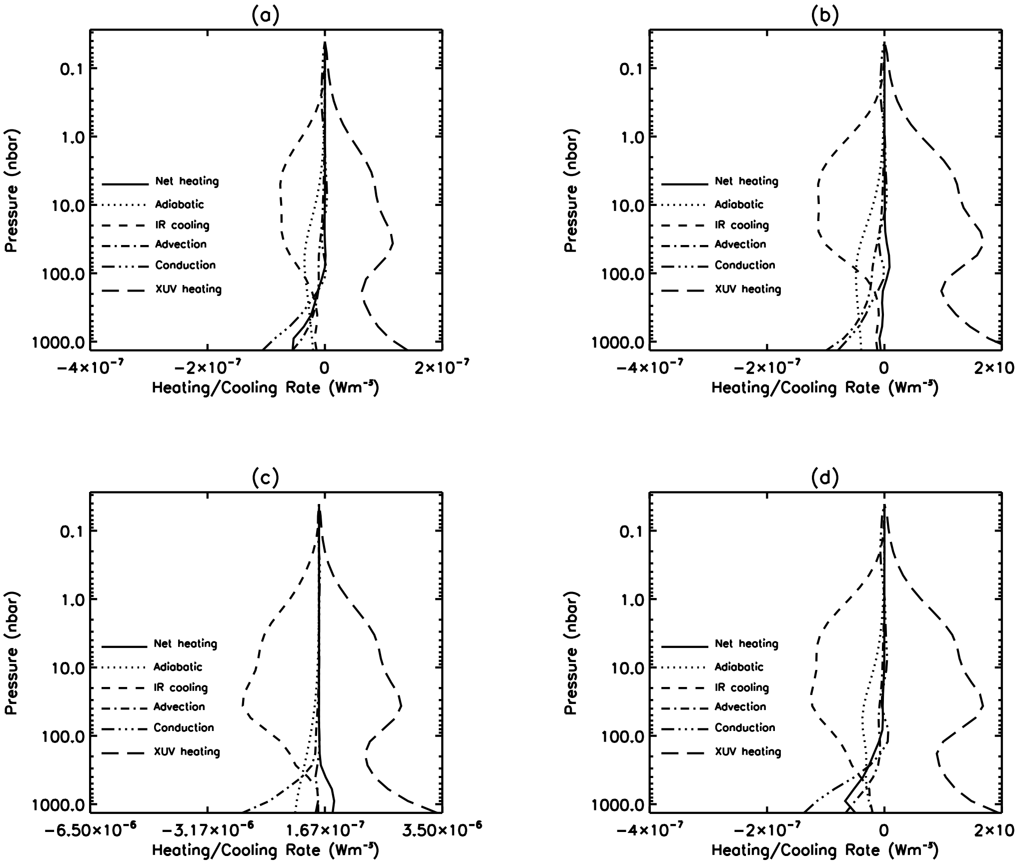

Figure 6.19: Substellar volume heating and cooling terms for the HD.001 simulation at (a) apastron, (b) $\theta = -153^o$, (c) periastron, and (d) $\theta = 153^o$. The net heating term is the sum of all the energy equation terms.

effect by zonal advection that brings warm gas from the dayside to the night side.

We define the radiative cooling function as the ratio of the total H_3^+ emission rate to the total XUV heating rate. During apastron for HD.001, this cooling function is 78 % and the total H_3^+ infrared cooling rate (in all spectral lines) is 6.1 $\times 10^{14}$ W. At $\theta = -153^o$, the corresponding figures are 72 % and 8.5 $\times 10^{14}$ W, respectively. During periastron, the cooling function is 85 % and the total emission rate is 1.7 $\times 10^{16}$ W. Near antitransit at $\theta = 153^o$, the cooling function is 91 % and the emission rate is 1.1 $\times 10^{15}$ W.

For HD.002, the dayside XUV heating (by volume) is concentrated in the lower thermosphere. This is because the atomic hydrogen envelope is not particularly effective in absorbing the XUV radiation, and the heating efficiency for atomic hydrogen is only 10 %. The radiation thus penetrates to the lower thermosphere where it is also absorbed by H_2 and He and where the heating efficiency is 50 %. However, despite this concentration, the upper thermosphere is much hotter because the lower thermosphere is denser and heats up sluggishly, whereas even relatively inefficient heating is capable of producing high temperatures in the outer layers.

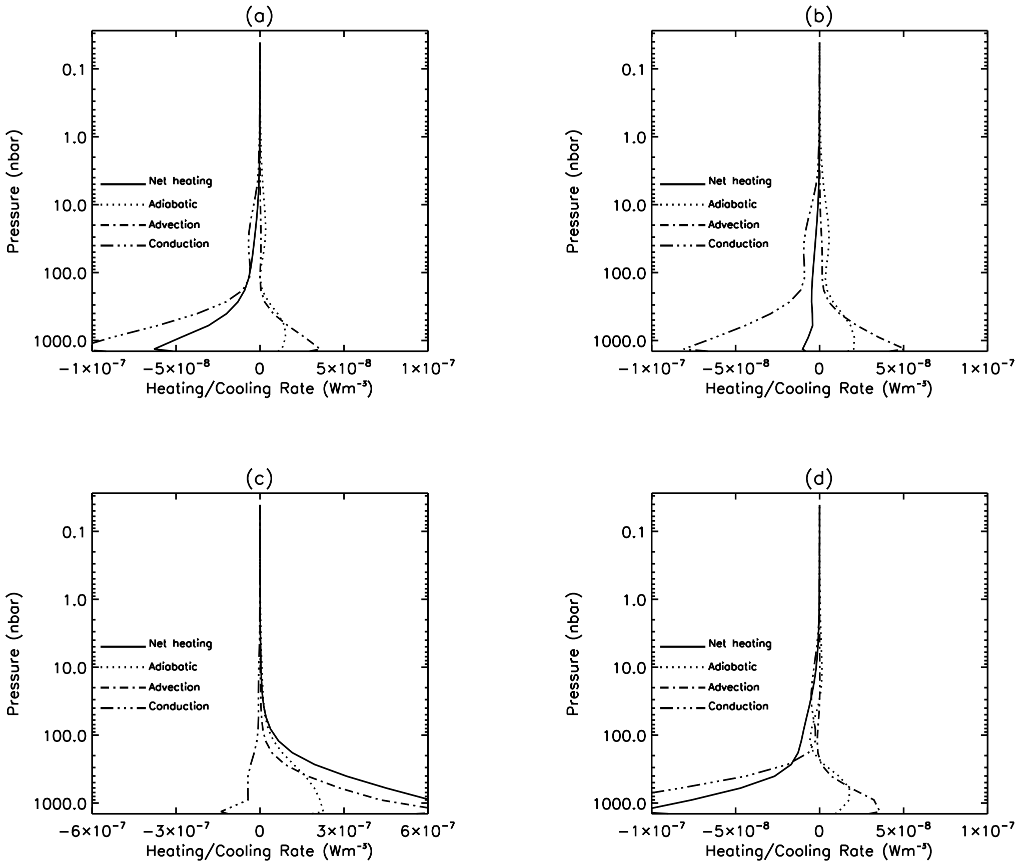

Figure 6.20: Antistellar volume heating and cooling terms for the HD.001 simulation at (a) apastron, (b) $\theta = -153^o$, (c) periastron, and (d) $\theta = 153^o$. The net heating term is the sum of all the energy equation terms.

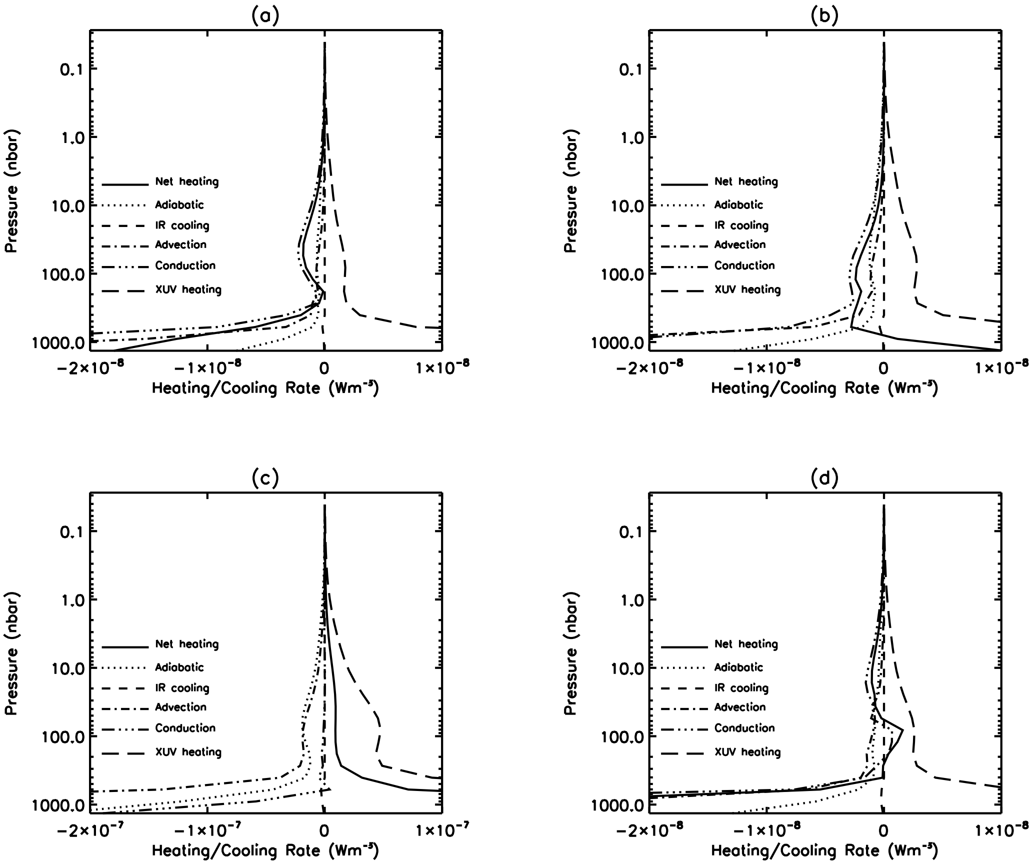

Figure 6.21: Substellar volume heating and cooling terms for the HD.002 simulation at (a) apastron, (b) $\theta = -153^o$, (c) periastron, and (d) $\theta = 153^o$. The net heating term is the sum of all the energy equation terms. The heating and cooling terms in the lower thermosphere are so strong that for clarity it was necessary to exclude the peaks. This enables the terms for the upper atmosphere to be seen.

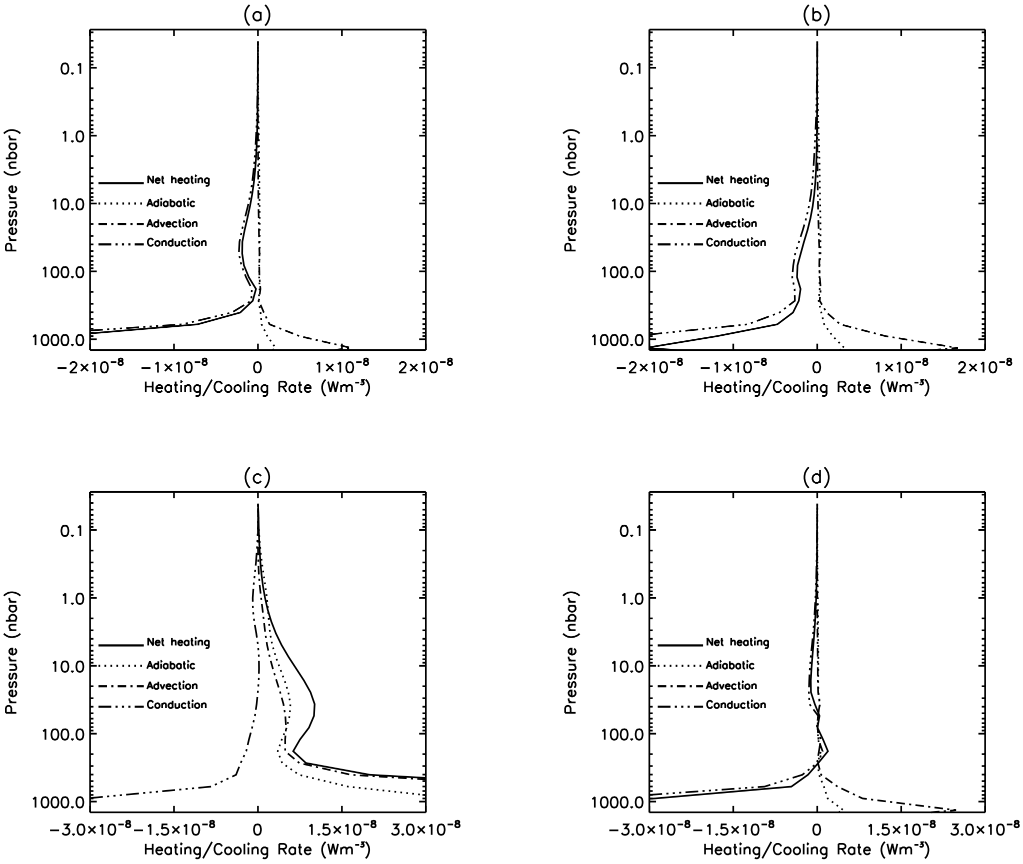

Figure 6.22: Antistellar volume heating and cooling terms for the HD.002 simulation at (a) apastron, (b) $\theta = -153^o$, (c) periastron, and (d) $\theta = 153^o$. The net heating term is the sum of all the energy equation terms.

Generally, the XUV heating is balanced by vertical conduction, advection and adiabatic expansion. On the night side, again, the heating is due to downwelling winds and adiabatic contraction, and this heating is balanced by vertical heat conduction. H_3^+ cooling is negligible compared to other energy equation terms in the dayside, and radiative cooling only occurs near the lower boundary. The thermosphere heats up as it approaches periastron from $\theta = -153^o$, with the heating first occurring in the lower thermosphere. The temperature reaches a maximum after periastron, and by the time the planet reaches $\theta = 153^o$, the upper and lower thermosphere have started cooling down. Curiously, XUV heating and vertical conduction heat the region near the 100 nbar level at $\theta = 153^o$. The radiative cooling function varies between 0.1 to 0.23 % for these four orbital position, with a minimum cooling function reached during periastron (0.1 %). The total infrared emissions for apastron, $\theta = -153^o$, periastron and $\theta = 153^o$ are 4.9×10^{11} W, 7.6×10^{11} W, 5.6×10^{12} W and 6.3×10^{11} W, respectively.

6.6 Conclusions

The simulations of the upper atmosphere and ionosphere of HD17156b are a first application of the model to a specific exoplanet. They are also the first three-dimensional upper atmospheric simulations presented for a known EGP in the literature. In order to achieve these simulations, we have updated the original model and introduced a numerical method for simulating planets with highly eccentric orbits that is generally applicable and not limited to thermosphere-ionosphere modelling. We have generated simulations with two possible compositions, one dominated by H_2 and the other by H and H^+. These simulations point to variable characteristics that can potentially be verified by observations.

In both cases we find that the atmosphere of HD17156b is likely to be stable against hydrodynamic escape throughout the orbit, despite intense heating during periastron. If the thermosphere is dominated by H and H^+, we expect the hydrogen envelope to extend beyond 1.4 R_p during transit, with a temperature of over 20,000 K. The detection or non-detection of such an envelope would not only constrain the nature and composition of the thermosphere, but also the composition in the lower atmosphere. The observations would also place constraints on the evaporation rate of the atmosphere.

We have also predicted total H_3^+ emission rates from the planet at different orbital positions. If H_3^+ cooling is significant, we expect evaporation due to Jeans escape with negligible magnitude. If, on the other hand, the atmosphere is dominated by H and H^+, the outer layers are sufficiently hot to drive potentially significant Jeans escape. Nevertheless, based on the discussion in Section 5.5, evaporation from HD17156b should be predominantly non-thermal.

Chapter 7

The Future

Our investigation has allowed us to characterise the upper atmospheres and ionospheres of extrasolar giant planets for the first time by making use of a three-dimensional, coupled thermosphere-ionosphere circulation model. It has produced many interesting findings, but it has also been at least as effective in identifying the shortcomings and omissions of the model and the method in general. In particular, we have been able to isolate a few ongoing themes. Chief among these is the possibility of hydrodynamic escape, and thus the potential breakdown of hydrostatic equilibrium. The implications of this breakdown, and the amendments necessary to the model are discussed extensively in Section 7.1. It introduces a new model that relies on altitude as a vertical coordinate and explains some early stages in the development of such a model that have already been undertaken.

In Chapter 4 we concentrated on modelling the thermospheres and ionospheres of extrasolar giant planets between 0.2 AU and 1.0 AU. We also presented some simulations for Jupiter's thermosphere. Our assumptions, and the model in general, are particularly suitable for modelling gas giants between 0.2 AU and 1.0 AU, at least in terms of the neutral thermosphere. In this range the prominent heating source is likely to be stellar XUV radiation, and the ion densities are likely to be several orders of magnitude lower than the overall neutral density. Also, the lifetimes of the ions are relatively short at least in the lower and middle thermosphere, broadly justifying the assumption of photochemical equilibrium. However, even in these models we have ignored the transport of the long-lived H^+ ion in the upper thermosphere, the possibility of a planetary magnetic field, and the interaction of the atmosphere with the impinging stellar wind. These aspects of the modelling are discussed in Section 7.2.

In Chapter 5 we saw that the stability limit against hydrodynamic escape for the atmosphere of a Jupiter-type planet orbiting the Sun is somewhere between 0.1 AU and 0.2 AU. Our results imply that most Hot Jupiters, which orbit their host stars within 0.1 AU, undergo hydrodynamic escape almost certainly. For most of these planets, photoionisation rates are also sufficiently high to ensure that H^+ is the dominant species in the upper thermosphere. Under these conditions the assumption that the neutral ideal gas law can be used as the equation of state in the simulations, while photoionisation does not directly affect the densities of H, H_2, and He, is inappropriate. The alterations needed, and suggestions of a new modelling approach are included in Section 7.2. Finally, Hot Jupiters are also affected by tidal forces between the planet and the host star. This feature is discussed briefly in Section 7.3.

7.1 Hydrodynamic Escape

One of the frustration of this project has been our inability to develop realistic models of the so-called Hot Jupiters, as their atmospheres are likely to escape hydrodynamically. We have already begun the development of a three-dimensional, non-hydrostatic model, and this is an important next stage in modelling the atmospheres of close-in EGPs. The non-hydrostatic formulation is conceptually simpler than the pressure coordinate formulation, and it avoids many of the approximations that are necessary in the derivation of the primitive equations for numerical use. However, the new formulation adds to the computation time and it is also particularly prone to numerical instabilities.

7.1.1 Continuity Equation

In the non-hydrostatic formulation, the continuity equation cannot be converted into the pressure coordinate system. Instead, altitude is used as the vertical coordinate, and the number densities for the different species are solved explicitly from the standard continuity equation:

$$\frac{\partial n_i}{\partial t} + \nabla \cdot (n_i \mathbf{u}) = \sum_j R_{ji} \tag{7.1}$$

where n_i is the number density of species i, and R_{ji} is the chemical source term for reaction j. The vector operators should be expressed in spherical polar coordinates, and they are listed in Appendix A. In the vertical direction, the divergence term of this equation is given by:

$$div_r = \frac{1}{r^2}\frac{\partial}{\partial r}[r^2 n_i (u_r + w_i)] \tag{7.2}$$

where u_r is the bulk vertical velocity, and w_i is the vertical diffusion velocity of species i.

7.1.2 Momentum Equation

In order to achieve a convenient numerical formulation, it is useful to cast the momentum equation into the flux-conservative form with the aid of the continuity equation (1.19). This form of the momentum equation, including viscosity and the Coriolis force, is:

$$\frac{\partial(\rho \mathbf{u})}{\partial t} + \nabla \cdot (\rho \mathbf{u}\mathbf{u}) = \rho \mathbf{g}' - \nabla p - 2\rho \mathbf{\Omega} \times \mathbf{u} + \mathbf{F_v} + \mathbf{u}\psi \tag{7.3}$$

The second term on the left-hand side is the advective, or Eulerian term, while the terms on the right-hand side describe accelerations due to gravity, pressure gradients, the Coriolis force, viscosity, and momentum generation, respectively. All the terms on the right-hand side are Lagrangian terms. The vertical component of the momentum equation is:

$$\frac{\partial(\rho u_r)}{\partial t} = -\rho g - \frac{\partial p}{\partial r} + 2\rho\Omega u_\phi \sin\theta + F_{vr} + u_r\psi \tag{7.4}$$

where the vertical component of the viscous force is given by:

$$F_{vr} = \mu(\nabla^2 u_r - \frac{2u_r}{r^2} - \frac{2}{r^2}\frac{\partial u_\theta}{\partial\theta} - \frac{2\cot\theta u_\theta}{r^2} - \frac{2}{r^2\sin\theta}\frac{\partial u_\phi}{\partial\phi}) + 2\frac{\partial\mu}{\partial r}\frac{\partial u_r}{\partial r} \tag{7.5}$$

where μ is the coefficient of viscosity.

7.1.3 Energy Equation

It is also necessary to express the energy equation in the flux-conservative form. Similarly to the momentum equation, this form of the energy equation is derived with the aid of the continuity equation, and it is given by:

$$\frac{\partial(\rho e)}{\partial t} + \nabla\cdot(\rho e\mathbf{u}) = \rho(Q_{xuv} + Q_{ir}) + \nabla\cdot(\kappa\nabla T) - p\nabla\cdot\mathbf{u} + \Phi + e\psi \tag{7.6}$$

where $e = c_v T$ is the internal thermal energy, and Φ is the dissipation functional. The second term on the left-hand side describes the advection of heat by circulation, and the terms on the right-hand side describe heating by stellar XUV radiation, infrared cooling, heat conduction, viscous heating, and generation of heat by chemical reactions, respectively.

7.1.4 Numerical Formulation

The above suite of equations can be used to calculate the number densities of individual species, the bulk flow velocities within the atmosphere, and the temperature of the fluid. The equations assume that the atmosphere can be treated as a single fluid that consists of various components. The formulation is suitable for modelling the neutral thermosphere if ion densities are negligible compared to the neutral density. Strictly speaking, the formulation is not appropriate for plasmas, and depending on the degree of ionisation, some alterations may be necessary. Once temperature and number densities have been solved, pressure is calculated from the equation of state that relates it to the temperature and density within the atmosphere (see Section 7.2). This is different to the hydrostatic formulation, in which constant pressure levels were used, and the overall number density was solved from the ideal gas law.

As we noted before, the non-hydrostatic formulation is particularly prone to suffer from numerical instabilities. For instance, the hydrostatic formulation filters out vertically propagating acoustic waves from the solution, while the non-hydrostatic formulation does not [Jacobson, 1999]. Including these waves requires fine spatial and temporal resolutions, and they are often a source of instability in non-hydrostatic models. Also, steep vertical gradients near the bottom of the thermosphere produce instabilities in the dynamical calculations. In order to pre-empt potential sources of instabilities, several precautions can be taken in developing the numerical model. To begin with, operator splitting techniques can be used to separate the Lagrangian and Eulerian terms in the equations of motion. The two components can then be solved separately so that during a single time step, the Lagrangian terms are calculated first, the solution is updated and then the Eulerian terms are added to this solution [Dobbs-Dixon and Lin, 2008, Hawley et al., 1984]. In addition to improving the stability of the model, this method allows for easier tracking of the numerical problems while the solution proceeds. The Lagrangian terms are more likely to integrate stably, while the Eulerian terms cause most of the problems.

As we mentioned briefly in Chapter 3, one of the sources of instability in numerical models is the fact that the flux of momentum and energy is not conserved. In order to aid flux conservation, we have chosen the flux-conservative formulation of the equations of motion and adopted the staggered Arakawa C grid [Arakawa and Lamb, 1977], which places scalar quantities at the centre of the grid cell and vectors at the grid cell boundaries. In addition, we have chosen to use the stable formulation of the Wilson transport scheme to integrate the Eulerian parts of the equations of motion [Hawley et al., 1984]. This scheme aims to conserve flux at least globally, and controls instabilities arising from the inevitable occurrence of artificial numerical diffusion.

As we mentioned, we have already created the first version of the non-hydrostatic code. Perhaps not surprisingly, we have not managed to stabilise the numerical scheme yet. The test runs imply that the horizontal solution may be working while problems arise in the vertical direction. Starting from hydrostatic equilibrium, the model begins to exhibit vertically propagating waves that manifest themselves in the temperature, density, and vertical velocity profiles. These waves quickly grow out of proportion and destabilise the solution. Notably, we did not adopt the Arakawa C grid in the vertical direction, and instead placed the vertical velocity components at the centre of the grid cells. Also, we did not use the Wilson transport scheme in the vertical Eulerian transport differencing. The fact that these features were only adopted in the horizontal directions may contribute to the instabilities. In addition, the steep vertical gradient of density and pressure is difficult to deal with numerically. We may have to use logarithmic variables in pressure and density and modify the equations appropriately. Improving the model, and ensuring that it runs stably is an important part of the future development of this work.

7.1.5 The Use of the Non-Hydrostatic Model

The non-hydrostatic model is primarily needed to simulate the upper atmospheres and ionospheres of Hot Jupiters. For these planets, it is the basis on which other effects such as magnetic fields, stellar wind interaction, and tidal forces can be added. Once such a model is available, it can be employed in realistic modelling of the observable features of EGP thermospheres at close-in orbits. For instance, models of HD209458b can be used to predict the in-transit Lyman α absorption signal, and such predictions can be compared to actual observations. It is likely that three-dimensional modelling will also help in constraining other properties of the hydrodynamicallly escaping part of the atmosphere of HD209458b and other Hot Jupiters. One particularly interesting aspect of such studies is exploring the hydrocarbon and oxygen chemistry of EGP upper atmospheres in the context of 3D hydrodynamic modelling. Hydrodynamic escape alters the concentrations of the heavier molecules by increasing their mixing ratios in the thermosphere and enabling them to survive at higher altitudes than would be expected in the molecular diffusion regime.

In addition to close-in EGPs, a non-hydrostatic 3D thermosphere model has wide applicability in the Solar System. Hydrostatic equilibrium may not be an adequate approximation in the high-latitude regions of the thermosphere of either Jupiter or the Earth because of the importance of auroral heating. Also, it is believed that the atmospheres of Earth and Venus underwent thermal hydrodynamic escape in the early Solar System. Presumably such conditions can also be studied freshly with a new 3D model.

7.2 Plasma Equation of State and Ion Transport

Pressure is related to the number densities and temperatures of the different species through the equation of state. One of the problems in our model has been the assumption that ion densities are negligible compared to the overall neutral density. Dynamically, we have assumed that the atmosphere can be treated as a single neutral, viscous fluid, and thus we have adopted the ideal gas law as the equation of state. In circumstances where the density of one or more ions species becomes comparable to the neutral density, this approach is no longer appropriate. We have seen that the density of H^+ is comparable to or higher than the density of H in the exosphere of close-in EGPs. In simulating the upper atmospheres and ionospheres of these planets, a plasma equation of state should be adopted. Such an equation can be derived from Dalton's law of partial pressures:

$$p = \sum_i n_i k T_i \tag{7.7}$$

where n_i and T_i are the number density and temperature, respectively, associated with species i. It should be noted that a partly ionised plasma consists of neutrals, ions, and electrons. All these species have different temperatures and densities that enter into the equation of state.

A word of warning is necessary here. The transport properties within a plasma are affected by the electromagnetic forces between ions and electrons, and the way these affect the neutral species. This picture is further complicated by the possible presence of a planetary magnetic field and the potential interaction of the planetary atmosphere with the stellar wind. In particular, diffusion processes within the ionosphere are quite different to the neutral thermosphere. These give rise to ion and electron stress and heat flow, and possible higher order diffusion processes. In addition, plasma dynamics are affected by various electrostatic and electromagnetic wave motions, and hydrodynamic shocks [Schunk and Nagy, 2000]. Developing these aspects in a 3D context is an important next step in the study of close-in EGPs. Models that use either the hydrostatic or non-hydrostatic formulation and include some of the plasma transport properties can be used as templates for further modelling that aims to explore different stellar wind interaction regimes, particle precipitation in the auroral regions and other such phenomena. However, modelling plasma transport on gas giants within a 3D thermospheric circulation model is an immensely complicated project, and only a few such models are available at present [eg.

Achilleos et al., 1998, Bougher et al., 2005]. In general, there is no sense in attempting to use the fully self-consistent formulation of a partly ionised plasma at once. Instead, the model should be built up one component at a time. The first step in this process is to develop a fully functioning neutral model that uses a simplistic ionosphere component, as we have done for the purposes of this thesis by using the hydrostatic formulation. Then other physical effects can be added one at a time to the 'core' model.

Possible global magnetic field configurations for gas giants include a simple dipole field, tilted dipole, or an offset and tilted dipole. In some cases higher order magnetic moments may also be needed. At this stage, when no direct detections of EGP magnetic fields exist, simple configurations can be used to explore the crude effects of planetary magnetism on the atmosphere and ionosphere. According to Grießmeier et al. [2004], the magnetic fields of close-in EGPs should be weak due to their relatively slow spin. In this context it is interesting that detections of radio emissions from EGP magnetospheres have not yet been successful. Nevertheless, there is some evidence for the interaction of planetary magnetospheres with the outer layers of the atmospheres of the host stars in systems such as υ And and HD179949 [Shkolnik et al., 2005, Preusse et al., 2006]. This implies that magnetic fields exist at least on some EGPs, and ignoring them, as we have done in this study, is not a sustainable long-term strategy.

7.3 Tidal Forces

Tidal forces can influence the atmospheres of close-in EGPs significantly, and enhance the thermal escape rate. Atmospheric tides can arise either gravitationally or thermally, and due to the rotation of the planet around its axis, and around the star, they appear as migrating tides. Both thermal and gravitational tides are significant in the atmospheres of Hot Jupiters. The thermospheres of these EGPs are affected by a very strong thermal tide arising from heating by the absorption of stellar XUV radiation. As the dayside thermosphere is heated, it expands and the pressure levels shift to higher altitudes. This tide, which is akin to the solar-driven diurnal tide in Earth's upper atmosphere, is included in our model through the XUV heating term in the energy equation and subsequent density and altitude changes.

Gravitational tides can be induced by satellites such as the Moon on Earth or the Jovian moons on Jupiter, or, as is probably the case for close-in EGPs, the host star. Indeed, the strong tidal forces between close-in EGPs and their host stars do not only drive variability in the atmosphere but they also influence the long-term evolution of the planets themselves. It is, for instance, believed that tidal forces between the planets and the stars have circularised the orbits of these planets and even driven them into synchronous rotation. The tidal interactions also affect the long-term evaporation of the atmospheres of the planets, although new studies indicate that the enhancement of the escape rate arising from tidal forces for a planet like HD209458b is only significant within 0.03 AU from the host star [García Muñoz, 2007].

Gravitational tides can be modelled by parameterising the density and temperature perturbations, and including a gravitational perturbation derived from a specific tidal potential function into the momentum equation [eg. García Muñoz, 2007, Erkaev et al., 2007, Lecavelier Des Etangs, 2007]. Simulating gravitational tides within a 3D model for EGPs would be a novelty, because the existing models that include the tidal potential are one-dimensional, and many of them simply parameterise the effect of gravitational tides on the evaporation rate by including a tidal enhancement factor in the thermal evaporation rate.

Appendix A

Some useful formulae

A.1 Gauss' Theorem

Suppose that τ represents a volume and let σ be the closed surface area of this volume. If $\mathbf{F}$ is a continuously differentiable vector field, defined in the neighbourhood of τ, then Gauss' theorem states that:

$$\iiint_\tau (\nabla \cdot \mathbf{F}) d\tau = \iint_\sigma \mathbf{F} \cdot \hat{\mathbf{n}} d\sigma \tag{A.1}$$

where $\hat{\mathbf{n}}$ is a unit vector perpendicular to the surface and pointing outward.

A.2 Differential Operators

Gradient of a scalar quantity in spherical polar coordinates f is given by:

$$\nabla f = \frac{\partial f}{\partial r}\mathbf{e}_r + \frac{1}{r}\frac{\partial f}{\partial \theta}\mathbf{e}_\theta + \frac{1}{r\sin\theta}\frac{\partial f}{\partial \phi}\mathbf{e}_\phi \tag{A.2}$$

In spherical pressure coordinates we have adopted the following 'horizontal' operator:

$$\nabla_p f = \frac{1}{a}\frac{\partial f}{\partial \theta}\mathbf{e}_\theta + \frac{1}{a\sin\theta}\frac{\partial f}{\partial \phi}\mathbf{e}_\phi \tag{A.3}$$

where $a = a(n, \theta, \phi)$ is the local altitude of pressure level n, and the unit vectors $\mathbf{e}_\theta$ and $\mathbf{e}_\phi$ specify a surface of constant pressure.

Divergence of a vector $\mathbf{F}$ in spherical polar coordinates is given by:

$$\nabla \cdot \mathbf{F} = \frac{1}{r^2}\frac{\partial (r^2 F_r)}{\partial r} + \frac{1}{r\sin\theta}\frac{\partial(\sin\theta F_\theta)}{\partial \theta} + \frac{1}{r\sin\theta}\frac{\partial F_\phi}{\partial \phi} \tag{A.4}$$

In spherical pressure coordinates we have adopted the following 'horizontal' operator:

$$\nabla_p \cdot \mathbf{F} = \frac{1}{a\sin\theta}\frac{\partial(\sin\theta F_\theta)}{\partial \theta} + \frac{1}{a\sin\theta}\frac{\partial F_\phi}{\partial \phi} \tag{A.5}$$

Gradient of a vector is a tensor (or a 'dyadic'), and for velocity **u** it is given in Cartesian coordinates by:

$$(\nabla\mathbf{u})_{ij} = \frac{\partial u_i}{\partial x_j} \tag{A.6}$$

Converting the components of the dyadic into spherical polar coordinates is not straightforward. For a detailed discussion see O'Neill and Chorlton [1989]. The dot product of the above dyadic and the velocity vector **u** is a vector, and in spherical polar coordinates it is given by:

$$\begin{aligned}
(\mathbf{u}\cdot\nabla)\mathbf{u} &= (u_r\frac{\partial u_r}{\partial r} + \frac{u_\theta}{r}\frac{\partial u_r}{\partial \theta} + \frac{u_\phi}{r\sin\theta}\frac{\partial u_r}{\partial \phi} - \frac{u_\theta^2 + u_\phi^2}{r})\mathbf{e}_r \\
&+ (u_r\frac{\partial u_\theta}{\partial r} + \frac{u_\theta}{r}\frac{\partial u_\theta}{\partial \theta} + \frac{u_\phi}{r\sin\theta}\frac{\partial u_\theta}{\partial \phi} + \frac{u_\theta u_r - \cot\theta u_\phi^2}{r})\mathbf{e}_\theta \\
&+ (u_r\frac{\partial u_\phi}{\partial r} + \frac{u_\theta}{r}\frac{\partial u_\phi}{\partial \theta} + \frac{u_\phi}{r\sin\theta}\frac{\partial u_\phi}{\partial \phi} + \frac{u_\phi u_r + \cot\theta u_\phi u_\theta}{r})\mathbf{e}_\phi
\end{aligned}$$

This is the advective term in the momentum equation. In spherical pressure coordinates, we have adopted the following horizontal terms:

$$\begin{aligned}
[(\mathbf{u}\cdot\nabla)\mathbf{u}]_p &= (\omega\frac{\partial u_\theta}{\partial p} + \frac{u_\theta}{a}\frac{\partial u_\theta}{\partial \theta} + \frac{u_\phi}{a\sin\theta}\frac{\partial u_\theta}{\partial \phi} - \frac{u_\theta\omega}{a\rho g} - \frac{\cot\theta u_\theta^2}{a})\mathbf{e}_\theta \\
&+ (\omega\frac{\partial u_\phi}{\partial p} + \frac{u_\theta}{a}\frac{\partial u_\phi}{\partial \theta} + \frac{u_\phi}{a\sin\theta}\frac{\partial u_\phi}{\partial \phi} - \frac{u_\phi\omega}{a\rho g} + \frac{\cot\theta u_\phi u_\theta}{a})\mathbf{e}_\phi
\end{aligned}$$

where ω is the Lagrangian derivative of pressure, and we have assumed that $u_r = -\omega/\rho g$.

The Laplacian of a scalar f in spherical pressure coordinates is given by:

$$\nabla^2 f = \frac{1}{r^2}\frac{\partial}{\partial r}(r^2\frac{\partial f}{\partial r}) + \frac{1}{r^2\sin\theta}\frac{\partial}{\partial\theta}(\sin\theta\frac{\partial f}{\partial\theta}) + \frac{1}{r^2\sin^2\theta}\frac{\partial^2 f}{\partial\phi^2} \tag{A.7}$$

In spherical pressure coordinates, we have adopted the following 'horizontal' operator:

$$\nabla_p^2 f = \frac{1}{a^2}(\frac{\partial^2 f}{\partial\theta^2} + \cot\theta\frac{\partial f}{\partial\theta} + \frac{1}{\sin^2\theta}\frac{\partial^2 f}{\partial\phi^2}) \tag{A.8}$$

The Laplacian of a vector **u** is the vector $\nabla^2\mathbf{u} = \nabla\cdot\nabla\mathbf{u}$. Due to the awkward tensor transformations, the conversion of this operator into spherical polar coordinates is demanding. However, the result is:

$$\begin{aligned}
\nabla^2\mathbf{u} &= [\nabla^2 u_r - \frac{2u_r}{r^2} - \frac{2}{r^2}\frac{\partial u_\theta}{\partial\theta} - \frac{2\cot\theta u_\theta}{r^2} - \frac{2}{r^2\sin\theta}\frac{\partial u_\phi}{\partial\phi}]\mathbf{e}_r \\
&+ [\nabla^2 u_\theta + \frac{2}{r^2}\frac{\partial u_r}{\partial\theta} - \frac{u_\theta}{r^2\sin^2\theta} - \frac{2\cos\theta}{r^2\sin^2\theta}\frac{\partial u_\phi}{\partial\phi}]\mathbf{e}_\theta \\
&+ [\nabla^2 u_\phi - \frac{u_\phi}{r^2\sin^2\theta} + \frac{2}{r^2\sin\theta}\frac{\partial u_r}{\partial\phi} - \frac{2\cos\theta}{r^2\sin^2\theta}\frac{\partial u_\theta}{\partial\phi}]\mathbf{e}_\phi
\end{aligned}$$

In spherical pressure coordinates, we have adopted the following 'horizontal' components:

$$
\begin{aligned}
[\nabla^2 \mathbf{u}]_p &= (\nabla_p^2 u_\theta - \frac{u_\theta}{a^2 \sin^2\theta} - \frac{2\cos\theta}{a^2\sin^2\theta}\frac{\partial u_\phi}{\partial \phi})\mathbf{e}_\theta \\
&+ (\nabla_p^2 u_\phi - \frac{u_\phi}{a^2 \sin^2\theta} - \frac{2\cos\theta}{a^2\sin^2\theta}\frac{\partial u_\phi}{\partial \phi})\mathbf{e}_\phi
\end{aligned}
$$

Appendix B

Solar XUV fluxes and absorption cross sections

Table B.1: Solar XUV fluxes (scaled to 1.0 AU)

Wavelengths (nm)		**Photon flux (cm^{-2}s^{-1})**		**Wavelengths (nm)**		**Photon flux (cm^{-2}s^{-1})**	
λ_1	λ_2	Solar Max[a]	Solar Min[b]	λ_1	λ_2	Solar Max	Solar Min
0.00	1.00	3.0862E+06	2.1329E+05	55.44	55.44	5.0922E+08	5.0922E+08
1.00	2.00	6.4268E+07	4.6969E+06	55.44	59.96	1.3310E+09	8.9063E+08
2.00	3.00	1.8530E+08	1.3754E+07	58.43	58.43	2.1046E+09	1.0929E+09
3.00	4.00	3.6945E+07	3.1560E+06	60.98	60.98	1.1380E+09	5.6764E+08
4.00	5.00	2.6412E+08	4.3300E+07	60.98	64.41	1.9586E+09	9.4793E+08
5.05	10.00	5.4759E+09	1.9848E+09	62.97	62.97	1.5671E+09	1.0643E+09
10.05	14.84	5.6245E+09	2.0894E+09	65.03	70.00	1.5432E+09	8.9239E+08
15.01	19.86	4.2085E+09	1.5849E+09	70.34	70.34	4.7261E+08	4.7261E+08
20.00	24.92	3.5219E+09	1.3013E+09	70.10	75.00	6.2133E+08	4.2513E+08
25.63	25.63	1.8395E+08	7.4226E+07	76.52	76.52	7.1362E+08	4.8097E+08
25.11	29.95	3.5168E+09	1.0664E+09	77.04	77.04	7.6103E+08	5.1293E+08
28.41	28.41	6.6363E+08	1.9757E+08	75.00	80.00	2.8920E+09	1.9492E+09
30.33	30.33	1.5682E+09	4.3773E+08	78.77	78.77	1.5461E+09	1.0420E+09
30.38	30.38	2.9783E+10	1.2887E+10	80.10	85.00	5.6768E+09	3.8261E+09
30.33	34.99	5.6108E+09	1.5686E+09	85.10	90.00	1.3508E+10	9.1042E+09
36.81	36.81	4.5406E+09	1.3051E+09	90.10	95.00	1.3243E+10	8.9258E+09
35.60	39.98	1.3998E+09	3.9014E+08	95.10	100.00	4.7181E+09	3.1800E+09
40.11	43.67	2.3904E+09	6.9127E+08	97.70	97.70	8.1840E+09	5.5160E+09
46.52	46.52	9.0761E+08	3.7995E+08	100.10	105.00	6.4915E+09	5.5386E+09
45.30	49.94	1.4837E+09	6.2113E+08	102.57	102.57	8.4840E+09	4.4619E+09
50.00	55.00	1.6193E+09	1.1852E+09	103.19	103.19	2.2445E+09	2.2445E+09

---

[a] November 1980

[b] January 1996

Table B.2: Photoabsorption cross sections (cm^2)

Wavelength (Å)	Energy (eV)	σ_{H}^{total}	$\sigma_{H_2}^{total}$	σ_{He}^{total}	Reaction 2	Reaction 1a	Reaction 1b	Reaction 1c	Reaction 3[a]
5.00	2479.65	5.35417E-25	1.57758E-24	2.25334E-23	5.35417E-25	1.29160E-24	2.30762E-25	5.52151E-26	2.25334E-23
15.00	826.55	2.15001E-23	6.36216E-23	8.31669E-22	2.15001E-23	5.19175E-23	9.47731E-24	2.22676E-24	8.31669E-22
25.00	495.93	1.16250E-22	3.43001E-22	4.19655E-21	1.16250E-22	2.78986E-22	5.20104E-23	1.20050E-23	4.19655E-21
35.00	354.24	3.48811E-22	1.02171E-21	1.18275E-20	3.48811E-22	8.28314E-22	1.57635E-22	3.57598E-23	1.18275E-20
45.00	275.52	7.86558E-22	2.27717E-21	2.51502E-20	7.86558E-22	1.84014E-21	3.57335E-22	7.97010E-23	2.51502E-20
75.00	165.31	4.01601E-21	1.09638E-20	1.09194E-19	4.01601E-21	8.85608E-21	1.88847E-21	2.19277E-22	1.09194E-19
125.00	99.19	1.98157E-20	4.87914E-20	4.22466E-19	1.98157E-20	3.83882E-20	8.45154E-21	1.95165E-21	4.22466E-19
175.00	70.85	5.55103E-20	1.50986E-19	9.49028E-19	5.55103E-20	1.17682E-19	2.87745E-20	4.52959E-21	9.49028E-19
225.00	55.10	1.18358E-19	3.46703E-19	1.65427E-18	1.18358E-19	2.85352E-19	5.78837E-20	3.46703E-21	1.65427E-18
256.30	48.37	1.74459E-19	5.29520E-19	2.17024E-18	1.74459E-19	4.52968E-19	7.54925E-20	1.05904E-21	2.17024E-18
275.00	45.08	2.14893E-19	6.66891E-19	2.50225E-18	2.14893E-19	5.77395E-19	8.94962E-20	0.00000E+00	2.50225E-18
284.15	43.63	2.36679E-19	7.42920E-19	2.67072E-18	2.36679E-19	6.45456E-19	9.74639E-20	0.00000E+00	2.67072E-18
303.31	40.88	2.86743E-19	9.23027E-19	3.03565E-18	2.86743E-19	8.15395E-19	1.07632E-19	0.00000E+00	3.03565E-18
303.78	40.81	2.88049E-19	9.27824E-19	3.04480E-18	2.88049E-19	8.19633E-19	1.08192E-19	0.00000E+00	3.04480E-18
325.00	38.15	3.50994E-19	1.16511E-18	3.46751E-18	3.50994E-19	1.05727E-18	1.07842E-19	0.00000E+00	3.46751E-18
368.07	33.68	5.04004E-19	1.78979E-18	4.37747E-18	5.04004E-19	1.62266E-18	1.67134E-19	0.00000E+00	4.37747E-18
375.00	33.06	5.31942E-19	1.91095E-18	4.52947E-18	5.31942E-19	1.74356E-18	1.67382E-19	0.00000E+00	4.52947E-18
425.00	29.17	7.62481E-19	2.89591E-18	5.65511E-18	7.62481E-19	2.78185E-18	1.14056E-19	0.00000E+00	5.65511E-18
465.22	26.65	9.86820E-19	3.63930E-18	6.56073E-18	9.86820E-19	3.54708E-18	9.22241E-20	0.00000E+00	6.56073E-18
475.00	26.10	1.04687E-18	3.84158E-18	6.77355E-18	1.04687E-18	3.74789E-18	9.36971E-20	0.00000E+00	6.77355E-18
525.00	23.62	1.38893E-18	5.00170E-18	1.36000E-18	1.38893E-18	4.88924E-18	1.12453E-19	0.00000E+00	1.36000E-18

---

[a] See Table 3.1 for reactions and references.

Wavelength (Å)	Energy (eV)	σ_{H}^{total}	$\sigma_{H_2}^{total}$	σ_{He}^{total}	Reaction 2	Reaction 1a	Reaction 1b	Reaction 1c	Reaction 3[a]
554.37	22.36	1.61814E-18	5.77349E-18	0.00000E+00	1.61814E-18	5.64921E-18	1.24283E-19	0.00000E+00	0.00000E+00
575.00	21.56	1.79209E-18	6.34999E-18	0.00000E+00	1.79209E-18	6.21330E-18	1.36693E-19	0.00000E+00	0.00000E+00
584.37	21.22	1.87469E-18	6.62003E-18	0.00000E+00	1.87469E-18	6.48386E-18	1.36161E-19	0.00000E+00	0.00000E+00
609.76	20.33	2.11001E-18	7.37322E-18	0.00000E+00	2.11001E-18	7.22865E-18	1.44573E-19	0.00000E+00	0.00000E+00
625.00	19.84	2.25943E-18	7.83750E-18	0.00000E+00	2.25943E-18	7.68383E-18	1.53677E-19	0.00000E+00	0.00000E+00
629.73	19.69	2.30706E-18	7.98303E-18	0.00000E+00	2.30706E-18	7.82650E-18	1.56530E-19	0.00000E+00	0.00000E+00
675.00	18.37	2.79372E-18	9.39215E-18	0.00000E+00	2.79372E-18	9.30837E-18	8.37753E-20	0.00000E+00	0.00000E+00
703.36	17.63	3.12751E-18	1.00000E-17	0.00000E+00	3.12751E-18	1.00000E-17	0.00000E+00	0.00000E+00	0.00000E+00
725.00	17.10	3.39751E-18	1.22000E-17	0.00000E+00	3.39751E-18	1.22000E-17	0.00000E+00	0.00000E+00	0.00000E+00
765.15	16.20	3.93423E-18	1.06000E-17	0.00000E+00	3.93423E-18	1.06000E-17	0.00000E+00	0.00000E+00	0.00000E+00
770.41	16.09	4.00803E-18	9.60000E-18	0.00000E+00	4.00803E-18	9.60000E-18	0.00000E+00	0.00000E+00	0.00000E+00
775.00	16.00	4.07311E-18	1.00000E-17	0.00000E+00	4.07311E-18	1.00000E-17	0.00000E+00	0.00000E+00	0.00000E+00
789.36	15.71	4.28072E-18	5.20000E-18	0.00000E+00	4.28072E-18	5.20000E-18	0.00000E+00	0.00000E+00	0.00000E+00
825.00	15.03	4.82268E-18	1.00000E-17	0.00000E+00	4.82268E-18	2.00000E-18	0.00000E+00	0.00000E+00	0.00000E+00
875.00	14.17	5.64825E-18	8.05000E-18	0.00000E+00	5.64825E-18	0.00000E+00	0.00000E+00	0.00000E+00	0.00000E+00
925.00	13.40	1.60250E-18	1.20000E-17	0.00000E+00	1.60250E-18	0.00000E+00	0.00000E+00	0.00000E+00	0.00000E+00
975.00	12.72	0.00000E+00	1.85000E-17	0.00000E+00	0.00000E+00	0.00000E+00	0.00000E+00	0.00000E+00	0.00000E+00
977.62	12.68	0.00000E+00	1.85000E-17	0.00000E+00	0.00000E+00	0.00000E+00	0.00000E+00	0.00000E+00	0.00000E+00
1025.00	12.10	0.00000E+00	1.30000E-17	0.00000E+00	0.00000E+00	0.00000E+00	0.00000E+00	0.00000E+00	0.00000E+00
1025.72	12.09	0.00000E+00	1.30000E-17	0.00000E+00	0.00000E+00	0.00000E+00	0.00000E+00	0.00000E+00	0.00000E+00
1031.91	12.01	0.00000E+00	1.10000E-17	0.00000E+00	0.00000E+00	0.00000E+00	0.00000E+00	0.00000E+00	0.00000E+00

---

[a] See Table 3.1 for reactions and references.

Appendix C

Simulations

Table C.1: Run parameters for different simulations

ID	Distance (AU)	T_o[a] (K)	SW1[b]	Day length[c] (hr)	Period[d] (days)	SW2[e]	κ_τ[f] (cm^2s^{-1})	Runtime[g]	q_H[h]	q_{H_2}	q_{He}
EX10r	1.0	225	off	24	N/A	on	10^7	201 d	1.8×10^{-4}	0.94426	0.05556
EX10rh	1.0	225	off	24	N/A	off	10^7	1500 d	1.8×10^{-4}	0.94426	0.05556
EX08r	0.8	285	off	24	N/A	on	10^7	128 d	1.8×10^{-4}	0.94426	0.05556
EX08rh	0.8	285	off	24	N/A	off	10^7	1500 d	1.8×10^{-4}	0.94426	0.05556
EX07r	0.7	300	off	24	N/A	on	10^7	128 d	1.8×10^{-4}	0.94426	0.05556
EX07rh	0.7	300	off	24	N/A	off	10^7	263 d	1.8×10^{-4}	0.94426	0.05556
EX06r	0.6	300	off	24	N/A	on	10^7	56 d	1.8×10^{-4}	0.94426	0.05556
EX06rh	0.6	300	off	24	N/A	off	10^7	86 d	1.8×10^{-4}	0.94426	0.05556
EX05r	0.5	300	off	24	N/A	on	10^7	57 d	1.8×10^{-4}	0.94426	0.05556
EX05rh	0.5	300	off	24	N/A	off	10^7	87 d	1.8×10^{-4}	0.94426	0.05556
EX04r	0.4	400	off	24	N/A	on	0.0	36 d	1.8×10^{-4}	0.94426	0.05556
EX04rh	0.4	400	off	24	N/A	off	0.0	215 d	1.8×10^{-4}	0.94426	0.05556
EX03r	0.3	400	off	24	N/A	on	0.0	20+ d	1.8×10^{-4}	0.94426	0.05556
EX03rh	0.3	400	off	24	N/A	off	0.0	20+ d	1.8×10^{-4}	0.94426	0.05556

---

[a] Temperature at the lower boundary

[b] Tidal locking switch (on/off)

[c] Does not apply to rotationally synchronised models

[d] Only given for rotationally synchronised models

[e] H_3^+ cooling switch (on/off)

[f] Eddy diffusion coefficient

[g] Given in local days or hours for tidally locked models

[h] Volume mixing ratio of H at the lower boundary

ID	Distance (AU)	T$_o$[a] (K)	SW1[b]	Day length[c] (hr)	Period[d] (days)	SW2[e]	κ_τ[f] (cm^{2}s^{-1})	Runtime[g]	q$_H$[h]	q$_{H_2}$	q$_{He}$
EX024r,w[i]	0.24	520	on	N/A	44	on	0.0	2000 hr	1.8×10^{-4}	0.94426	0.05556
EX02r	0.2	520	on	N/A	35	on	0.0	7000 hr	1.8×10^{-4}	0.94426	0.05556
EX02re1	0.2	520	on	N/A	35	on	10^7	7000 + 500 hr	1.8×10^{-4}	0.94426	0.05556
EX02re2	0.2	520	on	N/A	35	on	10^9	7000 + 3600 hr	1.8×10^{-4}	0.94426	0.05556
EX02rh	0.2	520	on	N/A	35	off	0.0	7000 + 60 hr	1.8×10^{-4}	0.94426	0.05556
EX02rf1	0.2	520	off	48	N/A	on	0.0	7000 hr + 110 d	1.8×10^{-4}	0.94426	0.05556
EX02rf1	0.2	520	off	24	N/A	on	0.0	7000 hr + 125 d	1.8×10^{-4}	0.94426	0.05556
EX02rh1	0.2	520	on	N/A	35	on	0.0	7000 + 100 hr	0.001	0.94343	0.05557
EX02rh2	0.2	520	on	N/A	35	on	0.0	7000 + 100 hr	0.01	0.93443	0.05557
EX02smin[j]	0.2	520	on	N/A	35	on	0.0	7000 + 500 hr	1.8×10^{-4}	0.94426	0.05556
EX02exp[k]	0.2	520	on	N/A	35	on	0.0	7000 + 250 hr	1.8×10^{-4}	0.94426	0.05556
EX02st1-4[l]	0.2	520	on	N/A	35	on	0.0	7000 + 250 hr	1.8×10^{-4}	0.94426	0.05556
EX02st1-4[m]	0.2	520	on	N/A	35	on	0.0	7000 + 250 hr	1.8×10^{-4}	0.94426	0.05556
EX018r	0.18	520	on	N/A	35	on	0.0	5510 hr	1.8×10^{-4}	0.94426	0.0556
EX016r	0.16	520	on	N/A	20	on	0.0	5510 hr	1.8×10^{-4}	0.94426	0.0556
EX014r[n]	0.14	520	on	N/A	20	on	0.0	53460 hr	1.8×10^{-4}	0.94426	0.0556
EX012r	0.12	520	on	N/A	15	on	0.0	10450 hr	1.8×10^{-4}	0.94426	0.0556

---

[a] Temperature at the lower boundary

[b] Tidal locking switch (on/off)

[c] Does not apply to rotationally synchronised models

[d] Only given for rotationally synchronised models

[e] H_3^+ cooling switch (on/off)

[f] Eddy diffusion coefficient

[g] Given in local days or hours for tidally locked models

[h] Volume mixing ratio of H at the lower boundary

[i] EX024w includes lower boundary winds

[j] Solar minimum fluxes used

[k] Experimental non-LTE correction used (see text in Chapter 4)

[l] Different temperature and wind smoothing frequencies used

[m] Different composition smoothing frequencies used. Note that the runtime for EX02st1 is only 7000 + 90 hr.

[n] Onset of hydrodynamic escape

Bibliography

N. Achilleos, S. Miller, J. Tennyson, A. D. Aylward, I. Mueller-Wodarg, and D. Rees. JIM: A time-dependent, three-dimensional model of Jupiter's thermosphere and ionosphere. *J.Geophys.Res.*, 103: 20089–20112, September 1998.

E. Anders and N. Grevesse. Abundances of the elements - Meteoritic and solar. *Geochim. Cosmochim. Acta*, 53:197–214, January 1989.

V. G. Anicich. Evaluated bimolecular ion-molecule gas phase kinetics of positive ions for use in modeling planetary atmospheres, cometary comae, and interstellar clouds. *Journal of Physical and Chemical Reference Data*, 22:1469–1569, 1993.

A. Arakawa. Computational design for long-term numerical integration of the equations of fluid motion: Two-dimensional incompressible flow. *Journal of Computational Physics*, 1:119–143, 1966.

A. Arakawa and V. R. Lamb. *Computational design of the basic dynamical processes of the UCLA general circulation model.*, pages 173–265. Methods in Computational Physics, 1977.

D. Auerbach, R. Cacek, R. Candano, T. D. Gaily, C. J. Keyser, J. W. McGowan, P. M. Mul, and S. F. J. Wilk. Merged electron-ion beam experiments. I. Method and measurement of e+H_2^+ and e+H_3^+ dissociative-recombination cross sections. *J.Phys. B At.Mol.Phys.*, 10:3797–3820, 1977.

G. E. Ballester, D. K. Sing, and F. Herbert. The signature of hot hydrogen in the atmosphere of the extrasolar planet HD 209458b. *Nature*, 445:511–514, February 2007.

P. M. Banks and G. Kockarts. *Aeronomy.* Academic Press, New York, USA, 1973.

I. Baraffe, F. Selsis, G. Chabrier, T. S. Barman, F. Allard, P. H. Hauschildt, and H. Lammer. The effect of evaporation on the evolution of close-in giant planets. *Astron. Astrophys.*, 419:L13–L16, May 2004.

M. Barbieri, R. Alonso, G. Laughlin, J. M. Almenara, R. Bissinger, D. Davies, D. Gasparri, E. Guido, C. Lopresti, F. Manzini, and G. Sostero. HD 17156b: a transiting planet with a 21.2-day period and an eccentric orbit. *Astron. Astrophys.*, 476:L13–L16, December 2007.

T. Barman. Identification of Absorption Features in an Extrasolar Planet Atmosphere. *ApJ*, 661:L191–L194, June 2007.

D. L. Baulch, C. J. Cobos, R. A. Cox, C. Esser, P. Frank, T. Just, J. A. Kerr, M. J. Pilling, J. Troe, R. W. Walker, and J. Warnatz. Evaluated Kinetic Data for Combustion Modelling. *Journal of Physical and Chemical Reference Data*, 21:411–734, May 1992.

J. P. Beaulieu, S. Carey, I. Ribas, and G. Tinetti. Primary Transit of the Planet HD 189733b at 3.6 and 5.8 μm. *ApJ*, 677:1343–1347, April 2008.

S. W. Bougher, J. H. Waite, T. Majeed, and G. R. Gladstone. Jupiter Thermospheric General Circulation Model (JTGCM): Global structure and dynamics driven by auroral and Joule heating. *Journal of Geophysical Research (Planets)*, 110:4008–4033, April 2005.

T. M. Brown. Transmission Spectra as Diagnostics of Extrasolar Giant Planet Atmospheres. *ApJ*, 553: 1006–1026, June 2001.

A. Burkert, D. N. C. Lin, P. H. Bodenheimer, C. A. Jones, and H. W. Yorke. On the Surface Heating of Synchronously Spinning Short-Period Jovian Planets. *ApJ*, 618:512–523, January 2005.

A. Burrows and C. M. Sharp. Chemical Equilibrium Abundances in Brown Dwarf and Extrasolar Giant Planet Atmospheres. *ApJ*, 512:843–863, February 1999.

A. Burrows, I. Hubeny, and D. Sudarsky. A Theoretical Interpretation of the Measurements of the Secondary Eclipses of TrES-1 and HD 209458b. *ApJ*, 625:L135–L138, June 2005.

A. Burrows, D. Sudarsky, and I. Hubeny. Theory for the Secondary Eclipse Fluxes, Spectra, Atmospheres, and Light Curves of Transiting Extrasolar Giant Planets. *ApJ*, 650:1140–1149, October 2006.

A. Burrows, I. Hubeny, J. Budaj, H. A. Knutson, and D. Charbonneau. Theoretical Spectral Models of the Planet HD 209458b with a Thermal Inversion and Water Emission Bands. *ApJ*, 668:L171–L174, October 2007.

S. Chapman and T. G. Cowling. *The Mathematical Theory of Non-Uniform Gases (3rd edition)*. Cambridge University Press, Cambridge, UK, 1970.

D. Charbonneau, T. M. Brown, D. W. Latham, and M. Mayor. Detection of Planetary Transits Across a Sun-like Star. *ApJ*, 529:L45–L48, January 2000.

D. Charbonneau, T. M. Brown, R. W. Noyes, and R. L. Gilliland. Detection of an Extrasolar Planet Atmosphere. *ApJ*, 568:377–384, March 2002.

D. Charbonneau, L. E. Allen, S. T. Megeath, G. Torres, R. Alonso, T. M. Brown, R. L. Gilliland, D. W. Latham, G. Mandushev, F. T. O'Donovan, and A. Sozzetti. Detection of Thermal Emission from an Extrasolar Planet. *ApJ*, 626:523–529, June 2005.

J. Y.-K. Cho and L. M. Polvani. The emergence of jets and vortices in freely evolving, shallow-water turbulence on a sphere. *Physics of Fluids*, 8:1531–1552, June 1996.

J. Y.-K. Cho, K. Menou, B. M. S. Hansen, and S. Seager. The Changing Face of the Extrasolar Giant Planet HD 209458b. *ApJ*, 587:L117–L120, April 2003.

J. Y.-K. Cho, K. Menou, B. M. S. Hansen, and S. Seager. Atmospheric Circulation of Close-in Extrasolar Giant Planets. I. Global, Barotropic, Adiabatic Simulations. *ApJ*, 675:817–845, March 2008.

Y. M. Chung, E.-M. Lee, T. Masuoka, and J. A. R. Samson. Dissociative photoionization of H_2 from 18 to 124 eV. *J.Chem.Phys.*, 99:885–889, July 1993.

C. S. Cooper and A. P. Showman. Dynamic Meteorology at the Photosphere of HD 209458b. *ApJ*, 629: L45–L48, August 2005.

C. S. Cooper and A. P. Showman. Dynamics and Disequilibrium Carbon Chemistry in Hot Jupiter Atmospheres, with Application to HD 209458b. *ApJ*, 649:1048–1063, October 2006.

N. B. Cowan, E. Agol, and D. Charbonneau. Hot nights on extrasolar planets: mid-infrared phase variations of hot Jupiters. *MNRAS*, 379:641–646, August 2007.

S. Datz, G. Sundström, C. Biedermann, L. Broström, H. Danared, S. Mannervik, J. R. Mowat, and M. Larsson. Branching Processes in the Dissociative Recombination of H_3^+. *Physical Review Letters*, 74:4099–+, May 1995.

D. Deming, T. M. Brown, D. Charbonneau, J. Harrington, and L. J. Richardson. A New Search for Carbon Monoxide Absorption in the Transmission Spectrum of the Extrasolar Planet HD 209458b. *ApJ*, 622:1149–1159, April 2005a.

D. Deming, S. Seager, L. J. Richardson, and J. Harrington. Infrared radiation from an extrasolar planet. *Nature*, 434:740–743, March 2005b.

D. Deming, J. Harrington, S. Seager, and L. J. Richardson. Strong Infrared Emission from the Extrasolar Planet HD 189733b. *ApJ*, 644:560–564, June 2006.

D. Deming, J. Harrington, G. Laughlin, S. Seager, S. B. Navarro, W. C. Bowman, and K. Horning. Spitzer Transit and Secondary Eclipse Photometry of GJ 436b. *ApJ*, 667:L199–L202, October 2007.

B.-O. Demory, M. Gillon, T. Barman, X. Bonfils, M. Mayor, T. Mazeh, D. Queloz, S. Udry, F. Bouchy, X. Delfosse, T. Forveille, F. Mallmann, F. Pepe, and C. Perrier. Characterization of the hot Neptune GJ 436 b with Spitzer and ground-based observations. *A & A*, 475:1125–1129, December 2007.

B. M. Dinelli, S. Miller, and J. T. Tennyson. Bands of H_3^+ up to $4\nu_2$: Rovibrational transitions from first principles calculations. *Journal of Molecular Spectroscopy*, 153:718–725, 1992.

I. Dobbs-Dixon and D. N. C. Lin. Atmospheric Dynamics of Short-Period Extrasolar Gas Giant Planets. I. Dependence of Nightside Temperature on Opacity. *ApJ*, 673:513–525, January 2008.

T. E. Dowling, A. S. Fischer, P. J. Gierasch, J. Harrington, R. P. Lebeau, and C. M. Santori. The Explicit Planetary Isentropic-Coordinate (EPIC) Atmospheric Model. *Icarus*, 132:221–238, April 1998.

P. Drossart, J.-P. Maillard, J. Caldwell, S. J. Kim, J. K. G. Watson, W. A. Majewski, J. Tennyson, S. Miller, S. K. Atreya, J. T. Clarke, J. H. Waite, and R. Wagener. Detection of H_3^+ on Jupiter. *Nature*, 340:539–541, August 1989.

P. Drossart, B. Bezard, S. K. Atreya, J. Bishop, J. H. Waite, Jr., and D. Boice. Thermal profiles in the auroral regions of Jupiter. *Journal of Geophysical Research*, 98:18803–+, October 1993.

G. Dujardin, M. J. Besnard, L. Hellner, and Y. Malinovitch. Double photoionization of H_2: An experimental test of electronic-correlation models in molecules. *Phys.Rev.A*, 35:5012–5019, June 1987.

D. Ehrenreich, A. Lecavelier Des Etangs, G. Hébrard, J.-M. Désert, A. Vidal-Madjar, J. C. McConnell, C. D. Parkinson, G. E. Ballester, and R. Ferlet. New observations of the extended hydrogen exosphere of the extrasolar planet HD 209458b. *A & A*, 483:933–937, June 2008.

N. V. Erkaev, T. Penz, H. Lammer, H. I. M. Lichtenegger, H. K. Biernat, P. Wurz, J.-M. Grießmeier, and W. W. Weiss. Plasma and Magnetic Field Parameters in the Vicinity of Short-periodic Giant Exoplanets. *ApJS*, 157:396–401, April 2005.

N. V. Erkaev, Y. N. Kulikov, H. Lammer, F. Selsis, D. Langmayr, G. F. Jaritz, and H. K. Biernat. Roche lobe effects on the atmospheric loss from “Hot Jupiters”. *A & A*, 472:329–334, September 2007.

D. A. Fischer, S. S. Vogt, G. W. Marcy, R. P. Butler, B. Sato, G. W. Henry, S. Robinson, G. Laughlin, S. Ida, E. Toyota, M. Omiya, P. Driscoll, G. Takeda, J. T. Wright, and J. A. Johnson. Five Intermediate-Period Planets from the N2K Sample. *ApJ*, 669:1336–1344, November 2007.

J. J. Fortney and M. S. Marley. Analysis of Spitzer Spectra of Irradiated Planets: Evidence for Water Vapor? *ApJ*, 666:L45–L48, September 2007.

J. J. Fortney, C. S. Cooper, A. P. Showman, M. S. Marley, and R. S. Freedman. The Influence of Atmospheric Dynamics on the Infrared Spectra and Light Curves of Hot Jupiters. *ApJ*, 652:746–757, November 2006a.

J. J. Fortney, D. Saumon, M. S. Marley, K. Lodders, and R. S. Freedman. Atmosphere, Interior, and Evolution of the Metal-rich Transiting Planet HD 149026b. *ApJ*, 642:495–504, May 2006b.

A. García Muñoz. Physical and chemical aeronomy of HD 209458b. *Planetary and Space Science*, 55: 1426–1455, July 2007.

T.R. Geballe, M.-F. Jagod, and T. Oka. Detection of H_3^+ infrared emission lines in Saturn. *ApJL*, 408: L109–, 1993.

M. Gillon, A. H. M. J. Triaud, M. Mayor, D. Queloz, S. Udry, and P. North. Improved parameters for the transiting planet HD 17156b: a high-density giant planet with a very eccentric orbit. *ArXiv e-prints*, 712, December 2007.

J.-M. Grießmeier, A. Stadelmann, T. Penz, H. Lammer, F. Selsis, I. Ribas, E. F. Guinan, U. Motschmann, H. K. Biernat, and W. W. Weiss. The effect of tidal locking on the magnetospheric and atmospheric evolution of "Hot Jupiters". *A & A*, 425:753–762, October 2004.

C. J. Grillmair, D. Charbonneau, A. Burrows, L. Armus, J. Stauffer, V. Meadows, J. Van Cleve, and D. Levine. A Spitzer Spectrum of the Exoplanet HD 189733b. *ApJ*, 658:L115–L118, April 2007.

D. Grodent, Jr. Waite, J. H., and J.-C. Gérard. A self-consistent model of the Jovian auroral thermal structure. *J.Geophys.Res.*, 106:12933–12952, July 2001.

T. Guillot, A. Burrows, W. B. Hubbard, J. I. Lunine, and D. Saumon. Giant Planets at Small Orbital Distances. *ApJ*, 459:L35+, March 1996.

D. O. Ham, D. W. Trainor, and F. Kaufman. Gas Phase Kinetics of $H+H+H_2 \rightarrow 2H_2$. *J.Chem.Phys.*, 53:4395–4396, December 1970.

J. Harrington, B. M. Hansen, S. H. Luszcz, S. Seager, D. Deming, K. Menou, J. Y.-K. Cho, and L. J. Richardson. The Phase-Dependent Infrared Brightness of the Extrasolar Planet υ Andromedae b. *Science*, 314:623–626, October 2006.

J. Harrington, S. Luszcz, S. Seager, D. Deming, and L. J. Richardson. The hottest planet. *Nature*, 447: 691–693, June 2007.

William K. Hartmann. *Moons & Planets, 4th edition.* Wadsworth Publishing Company, Belmont, CA94002, USA, 1999.

J. F. Hawley, L. L. Smarr, and J. R. Wilson. A numerical study of nonspherical black hole accretion. II - Finite differencing and code calibration. *ApJS*, 55:211–246, June 1984.

D. P. Hinson, F. M. Flasar, A. J. Kliore, P. J. Schinder, J. D. Twicken, and R. G. Herrera. Jupiter's ionosphere: Results from the first Galileo radio occultation experiment. *Geophys. Res. Lett.*, 24: 2107–+, September 1997.

M. Holstrom, A. Ekenback, F. Selsis, T. Penz, H. Lammer, and P. Wurz. Energetic neutral atoms as the explanation for the high-velocity hydrogen around HD 209458b. *Nature*, 451:970–972, 2008.

James R. Holton. *An Introduction to Dynamic Meteorology.* Elsevier Academic Press, London, England, 2004.

D. G. Hummer and M. J. Seaton. The ionization structure of planetary nebulae, I. Pure hydrogen nebulae. *MNRAS*, 125:437–459, 1963.

D. M. Hunten. The Escape of Light Gases from Planetary Atmospheres. *Journal of Atmospheric Sciences*, 30:1481–1494, November 1973.

D. M. Hunten. The escape of light gases from planetary atmospheres. *Journal of Atmospheric Sciences*, 30:1481–1494, 1974.

P. Hut. Tidal evolution in close binary systems. *Astron. Astrophys.*, 99:126–140, June 1981.

A. P. Ingersoll, T. E. Dowling, P. J. Gierasch, G. S. Orton, P. L. Read, A. Sánchez-Lavega, A. P. Showman, A. A. Simon-Miller, and A. R. Vasavada. *Dynamics of Jupiter's atmosphere*, pages 105–128. Jupiter. The Planet, Satellites and Magnetosphere, 2004.

N. Iro, B. Bézard, and T. Guillot. A time-dependent radiative model of HD 209458b. *Astron. Astrophys.*, 436:719–727, June 2005.

J. Irwin, D. Charbonneau, P. Nutzman, W. F. Welsh, A. Rajan, M. Hidas, T. M. Brown, T. A. Lister, D. Davies, G. Laughlin, and J. Langton. Parameters and Predictions for the Long-Period Transiting Planet HD 17156b. *ApJ*, 681:636–643, July 2008.

M. Z. Jacobson. *Fundamentals of Atmospheric Modeling.* Cambridge University Press, Cambridge, England, 1999.

Z. Kapras, V. G. Anicich, and W. T. Huntress. An ion cyclotron resonance study of reactions of ions with hydrogen atoms. *J.Chem.Phys.*, 655:2877–2881, January 1979.

F. Keith. *Fluid Mechanics.* CRC Press LLC, Boca Raton, Florida, USA, 2000.

M. L. Khodachenko, H. Lammer, H. I. M. Lichtenegger, D. Langmayr, N. V. Erkaev, J.-M. Grießmeier, M. Leitner, T. Penz, H. K. Biernat, U. Motschmann, and H. O. Rucker. Mass loss of 'Hot Jupiters': Implications for CoRoT discoveries. Part I: The importance of magnetospheric protection of a planet against ion loss caused by coronal mass ejections. *Planetary and Space Science*, 55:631–642, April 2007.

Y. H. Kim and J. L. Fox. The chemistry of hydrocarbon ions in the Jovian ionosphere. *Icarus*, 112: 310–325, December 1994.

H. A. Knutson, D. Charbonneau, L. E. Allen, J. J. Fortney, E. Agol, N. B. Cowan, A. P. Showman, C. S. Cooper, and S. T. Megeath. A map of the day-night contrast of the extrasolar planet HD 189733b. *Nature*, 447:183–186, May 2007a.

H. A. Knutson, D. Charbonneau, R. W. Noyes, T. M. Brown, and R. L. Gilliland. Using Stellar Limb-Darkening to Refine the Properties of HD 209458b. *ApJ*, 655:564–575, January 2007b.

H. A. Knutson, D. Charbonneau, L. E. Allen, A. Burrows, and S. T. Megeath. The 3.6-8.0 μm Broadband Emission Spectrum of HD 209458b: Evidence for an Atmospheric Temperature Inversion. *ApJ*, 673: 526–531, January 2008.

T. T. Koskinen, A. D. Aylward, and S. Miller. A Stability Limit for Giant Exoplanet Atmospheres. *Nature*, 450:845–848, December 2007a.

T. T. Koskinen, A. D. Aylward, C. G. A. Smith, and S. Miller. A Thermospheric Circulation Model for Extrasolar Giant Planets. *ApJ*, 661:515–526, May 2007b.

T. T. Koskinen, A. D. Aylward, and S. Miller. The Upper Atmosphere of HD17156b. *ApJ, submitted*, 2008.

H. Lammer, F. Selsis, I. Ribas, E. F. Guinan, S. J. Bauer, and W. W. Weiss. Atmospheric Loss of Exoplanets Resulting from Stellar X-Ray and Extreme-Ultraviolet Heating. *ApJ*, 598:L121–L124, December 2003.

A. Lecavelier Des Etangs. A diagram to determine the evaporation status of extrasolar planets. *Astron. Astrophys.*, 461:1185–1193, January 2007.

A. Lecavelier des Etangs, A. Vidal-Madjar, J. C. McConnell, and G. Hébrard. Atmospheric escape from hot Jupiters. *Astron. Astrophys.*, 418:L1–L4, April 2004.

M.-C. Liang, C. D. Parkinson, A. Y.-T. Lee, Y. L. Yung, and S. Seager. Source of Atomic Hydrogen in the Atmosphere of HD 209458b. *ApJ*, 596:L247–L250, October 2003.

M.-C. Liang, S. Seager, C. D. Parkinson, A. Y.-T. Lee, and Y. L. Yung. On the Insignificance of Photochemical Hydrocarbon Aerosols in the Atmospheres of Close-in Extrasolar Giant Planets. *ApJ*, 605:L61–L64, April 2004.

J. I. Lunine, A. Coradini, D. Gautier, T. C. Owen, and G. Wuchterl. *The origin of Jupiter*, pages 19–34. Jupiter. The Planet, Satellites and Magnetosphere, 2004.

Mandl, F. *Statistical Physics (2nd edition).* John Wiley & Sons Ltd., Chichester, UK, 1988.

G. Marcy, R. P. Butler, D. Fischer, S. Vogt, J. T. Wright, C. G. Tinney, and H. R. A. Jones. Observed Properties of Exoplanets: Masses, Orbits, and Metallicities. *Progress of Theoretical Physics Supplement*, 158:24–42, 2005.

M. S. Marley, C. Gelino, D. Stephens, J. I. Lunine, and R. Freedman. Reflected Spectra and Albedos of Extrasolar Giant Planets. I. Clear and Cloudy Atmospheres. *ApJ*, 513:879–893, March 1999.

M. S. Marley, J. Fortney, S. Seager, and T. Barman. Atmospheres of Extrasolar Giant Planets. *Protostars and Planets V*, pages 733–747, 2007.

M. Mayor and D. Queloz. A Jupiter-Mass Companion to a Solar-Type Star. *Nature*, 378:355–359, November 1995.

A. E. Metzger, D. A. Gilman, J. L. Luthey, K. C. Hurley, H. W. Schnopper, F. D. Seward, and J. D. Sullivan. The detection of X rays from Jupiter. *Journal of Geophysical Research*, 88:7731–7741, October 1983.

S. Miller, N. Achilleos, G. E. Ballester, T. R. Geballe, R. D. Joseph, R. Prangé, D. Rego, T. Stallard, J. Tennyson, L. M. Trafton, and J. H. Waite, Jr. The role of H_3^+ in planetary atmospheres. In *Astronomy, physics and chemistry of* H_3^+, pages 2485–, 2000.

L. E. Moore, M. Mendillo, I. C. F. Müller-Wodarg, and D. L. Murr. Modeling of global variations and ring shadowing in Saturn's ionosphere. *Icarus*, 172:503–520, December 2004.

J. I. Moses and S. F. Bass. The effects of external material on the chemistry and structure of Saturn's ionosphere. *J.Geophys.Res.*, 105:7013–7052, March 2000.

J. I. Moses, T. Fouchet, R. V. Yelle, A. J. Friedson, G. S. Orton, B. Bézard, P. Drossart, G. R. Gladstone, T. Kostiuk, and T. A. Livengood. *The stratosphere of Jupiter*, pages 129–157. Jupiter. The Planet, Satellites and Magnetosphere, 2004.

I. C. F. Müller-Wodarg, M. Mendillo, R. V. Yelle, and A. D. Aylward. A global circulation model of Saturn's thermosphere. *Icarus*, 180:147–160, January 2006.

L. Neale and J. Tennyson. A High-Temperature Partition Function for H_3^+. *ApJ*, 454:L169+, December 1995.

L. Neale, S. Miller, and J. Tennyson. Spectroscopic Properties of the H_3^+ Molecule: A New Calculated Line List. *ApJ*, 464:516–+, June 1996.

T. Oka and E. Epp. The Nonthermal Rotational Distribution of H_3^+. *ApJ*, 613:349–354, September 2004.

M.E. O'Neill and F. Chorlton. *Viscous and Compressible Fluid Dynamics.* Ellis Horwood Limited, Chichester, England, 1989.

J. C. B. Papaloizou and C. Terquem. Planet formation and migration. *Reports of Progress in Physics*, 69:119–+, 2006.

T. Penz, G. Micela, and H. Lammer. Influence of the evolving stellar X-ray luminosity distribution on exoplanetary mass loss. *A & A*, 477:309–314, January 2008.

N. A. Phillips. *An example of non-linear computational instability*, pages 501–504. The Atmosphere and the Sea in Motion. Scientific contributions to the Rossby memorial volume, 1959.

L. M. Polvani, R. K. Scott, and S. J. Thomas. Numerically Converged Solutions of the Global Primitive Equations for Testing the Dynamical Core of Atmospheric GCMs. *Monthly Weather Review*, 132: 2539–+, 2004.

F. Pont, R. L. Gilliland, C. Moutou, D. Charbonneau, F. Bouchy, T. M. Brown, M. Mayor, D. Queloz, N. Santos, and S. Udry. Hubble Space Telescope time-series photometry of the planetary transit of HD 189733: no moon, no rings, starspots. *A & A*, 476:1347–1355, December 2007.

F. Pont, H. Knutson, R. L. Gilliland, C. Moutou, and D. Charbonneau. Detection of atmospheric haze on an extrasolar planet: the 0.55-1.05 μm transmission spectrum of HD 189733b with the HubbleSpaceTelescope. *MNRAS*, 385:109–118, March 2008.

W. H. Press, S. A. Teukolsky, W. T. Vetterling, and B. P. Flannery. *Numerical Recipes in Fortran: The Art of Scientific Computing (2nd edition).* Cambridge University Press, Cambridge, UK, 1992.

S. Preusse, A. Kopp, J. Büchner, and U. Motschmann. A magnetic communication scenario for hot Jupiters. *A & A*, 460:317–322, December 2006.

S. Redfield, M. Endl, W. D. Cochran, and L. Koesterke. Sodium Absorption from the Exoplanetary Atmosphere of HD 189733b Detected in the Optical Transmission Spectrum. *ApJ*, 673:L87–L90, January 2008.

I. Ribas, E. F. Guinan, M. Güdel, and M. Audard. Evolution of the Solar Activity over Time and Effects on Planetary Atmospheres. I. High-Energy Irradiances (1-1700 Å). *ApJ*, 622:680–694, March 2005.

L. J. Richardson, D. Deming, and S. Seager. Infrared Observations during the Secondary Eclipse of HD 209458b. II. Strong Limits on the Infrared Spectrum Near 2.2 μm. *ApJ*, 597:581–589, November 2003.

L. J. Richardson, D. Deming, K. Horning, S. Seager, and J. Harrington. A spectrum of an extrasolar planet. *Nature*, 445:892–895, February 2007.

A. J. Ridley, Y. Deng, and G. Tóth. The global ionosphere thermosphere model. *Journal of Atmospheric and Solar-Terrestrial Physics*, 68:839–864, May 2006.

J. F. Rowe, J. M. Matthews, S. Seager, R. Kuschnig, D. B. Guenther, A. F. J. Moffat, S. M. Rucinski, D. Sasselov, G. A. H. Walker, and W. W. Weiss. An Upper Limit on the Albedo of HD 209458b: Direct Imaging Photometry with the MOST Satellite. *ApJ*, 646:1241–1251, August 2006.

M. L. Salby. Deep circulations under simple classes of stratification. *Tellus*, 41:48–65, 1989.

M. L. Salby. *Fundamentals of Atmospheric Physics.* Academic Press, Inc., San Diego, California, USA, 1996.

E. M. Schneiter, P. F. Velázquez, A. Esquivel, A. C. Raga, and X. Blanco-Cano. Three-dimensional Hydrodynamical Simulation of the Exoplanet HD 209458b. *ApJ*, 671:L57–L60, December 2007.

R. W. Schunk and A. F. Nagy. *Ionospheres: Physics, Plasma Physics and Chemistry.* Cambridge University Press, Cambridge, UK, 2000.

S. Seager, B. A. Whitney, and D. D. Sasselov. Photometric Light Curves and Polarization of Close-in Extrasolar Giant Planets. *ApJ*, 540:504–520, September 2000.

A. Seiff, D. B. Kirk, T. C. D. Knight, L. A. Young, F. S. Milos, E. Venkatapathy, J. D. Mihalov, R. C. Blanchard, R. E. Young, and G. Schubert. Thermal structure of Jupiter's upper atmosphere derived from the Galileo probe. *Science*, 276:102–104, April 1997.

R. Shapiro. Smoothing, Filtering, and Boundary Effects. *Reviews of Geophysics and Space Physics*, 8: 359–+, May 1970.

E. Shkolnik, G. A. H. Walker, D. A. Bohlender, P.-G. Gu, and M. Kürster. Hot Jupiters and Hot Spots: The Short- and Long-Term Chromospheric Activity on Stars with Giant Planets. *ApJ*, 622:1075–1090, April 2005.

E. Shkolnik, E. Gaidos, and N. Moskovitz. No Detectable H_3^+ Emission from the Atmospheres of Hot Jupiters. *Astronomical Journal*, 132:1267–1274, September 2006.

A. P. Showman and T. Guillot. Atmospheric circulation and tides of "51 Pegasus b-like" planets. *A & A*, 385:166–180, April 2002.

A. P. Showman, K. Menou, and J. Y-K. Cho. Atmospheric Circulation of Hot Jupiters: A Review of Current Understanding. *ArXiv e-prints*, 710, October 2007.

C. G. Smith. *Ph.D thesis*. University of London, London, England, 2006.

C. G. A. Smith, A. D. Aylward, S. Miller, and I. C. F. Muller-Wodarg. Polar Heating in Saturn's Thermosphere. *Ann.Geophys.*, 23:2465–2477, 2005.

C. G. A. Smith, A. D. Aylward, G. H. Millward, S. Miller, and L. E. Moore. An unexpected cooling effect in Saturn's upper atmosphere. *Nature*, 445:399–401, January 2007.

P. J. Storey and D. G. Hummer. Recombination line intensities for hydrogenic ions-IV. Total recombination coefficients and machine-readable tables for Z=1 to 8. *MNRAS*, 272:41–48, January 1995.

D. Sudarsky, A. Burrows, and I. Hubeny. Theoretical Spectra and Atmospheres of Extrasolar Giant Planets. *ApJ*, 588:1121–1148, May 2003.

G. Sundstrom, J. R. Mowat, H. Danared, S. Datz, L. Brostrom, A. Filevich, A. Kallberg, S. Mannervik, K. G. Rensfelt, P. Sigray, M. A. Ugglas, and M. Larsson. Destruction Rate of H_3^++ by Low-Energy Electrons Measured in a Storage-Ring Experiment. *Science*, 263:785–787, February 1994.

M. R. Swain, J. Bouwman, R. L. Akeson, S. Lawler, and C. A. Beichman. The Mid-Infrared Spectrum of the Transiting Exoplanet HD 209458b. *ApJ*, 674:482–497, February 2008a.

M. R. Swain, G. Vasisht, and G. Tinetti. The presence of methane in the atmosphere of an extrasolar planet. *Nature*, 452:329–331, March 2008b.

F. W. Taylor, S. K. Atreya, T. Encrenaz, D. M. Hunten, P. G. J. Irwin, and T. C. Owen. *The composition of the atmosphere of Jupiter*, pages 59–78. Jupiter. The Planet, Satellites and Magnetosphere, 2004.

L. P. Thread and W. P. Huntress. Ion molecule reactions and vibrational deactivation of H_2^+ ions in mixtures of hydrogen and helium. *J.Chem.Phys.*, 60:2840–2848, 1974.

F. Tian, O. B. Toon, A. A. Pavlov, and H. De Sterck. Transonic Hydrodynamic Escape of Hydrogen from Extrasolar Planetary Atmospheres. *ApJ*, 621:1049–1060, March 2005.

G. Tinetti, A. Vidal-Madjar, M.-C. Liang, J.-P. Beaulieu, Y. Yung, S. Carey, R. J. Barber, J. Tennyson, I. Ribas, N. Allard, G. E. Ballester, D. K. Sing, and F. Selsis. Water vapour in the atmosphere of a transiting extrasolar planet. *Nature*, 448:169–171, July 2007.

W. K. Tobiska, T. Woods, F. Eparvier, R. Viereck, L. Floyd, D. Bouwer, G. Rottman, and O. R. White. The SOLAR2000 empirical solar irradiance model and forecast tool. *Journal of Atmospheric and Terrestrial Physics*, 62:1233–1250, September 2000.

L.M. Trafton, T.R. Geballe, J. Tennyson, and G.E. Ballester. Detection of H_3^+ from Uranus. *ApJ*, 405: 761–, 1993.

D. E. Trilling. Tidal Constraints on the Masses of Extrasolar Planets. *ApJ*, 537:L61–L64, July 2000.

S. Udry and N. C. Santos. Statistical Properties of Exoplanets. *Annu.Rev.Astron.Astrophys.*, 45:397–439, September 2007.

A. Vidal-Madjar, A. Lecavelier des Etangs, J.-M. Désert, G. E. Ballester, R. Ferlet, G. Hébrard, and M. Mayor. An extended upper atmosphere around the extrasolar planet HD209458b. *Nature*, 422: 143–146, March 2003.

A. Vidal-Madjar, J.-M. Désert, A. Lecavelier des Etangs, G. Hébrard, G. E. Ballester, D. Ehrenreich, R. Ferlet, J. C. McConnell, M. Mayor, and C. D. Parkinson. Detection of Oxygen and Carbon in the Hydrodynamically Escaping Atmosphere of the Extrasolar Planet HD 209458b. *ApJ*, 604:L69–L72, March 2004.

A. Vidal-Madjar, A. Lecavelier des Etangs, J.-M. Désert, G. E. Ballester, R. Ferlet, G. Hébrard, and M. Mayor. Exoplanet HD 209458b (Osiris): Evaporation Strengthened. *ApJ*, 676:L57–L60, March 2008.

J. H. Waite, T. E. Cravens, J. Kozyra, A. F. Nagy, S. K. Atreya, and R. H. Chen. Electron precipitation and related aeronomy of the Jovian thermosphere and ionosphere. *J.Geophys.Res.*, 88:6143–6163, August 1983.

A. J. Watson, T. M. Donahue, and J. C. G. Walker. The dynamics of a rapidly escaping atmosphere - Applications to the evolution of earth and Venus. *Icarus*, 48:150–166, November 1981.

A. Williams. *Ph.D thesis.* University of London, London, England, 2004.

A. Wolszczan and D. A. Frail. A planetary system around the millisecond pulsar PSR1257 + 12. *Nature*, 355:145–147, January 1992.

M. Yan, H. R. Sadeghpour, and A. Dalgarno. Photoionization Cross Sections of He and H 2. *ApJ*, 496: 1044–+, March 1998.

R. V. Yelle. Aeronomy of extra-solar giant planets at small orbital distances. *Icarus*, 170:167–179, July 2004.

R. V. Yelle. Corrigendum to 'Aeronomy of extra-solar giant planets at small orbital distances' [Icarus 170 (2004) 167 179]. *Icarus*, 183:508–508, August 2006.

R. V. Yelle and S. Miller. *Jupiter's thermosphere and ionosphere*, pages 185–218. Jupiter. The Planet, Satellites and Magnetosphere, 2004.